Studies on Strain Softening Materials using Nonlocal Finite Element and Element-Free Galerkin Methods

A Thesis Submitted
In Partial Fulfillment of the Requirements
for the Degree of

DOCTOR OF PHILOSOPHY

by

S Sai Kumar

(176103019)

Department of Mechanical Engineering

Indian Institute of Technology Guwahati

Guwahati-781039, India

April, 2024


भारतीय प्रौद्योगिकी संस्थान गुवाहाटी
Indian Institute of Technology Guwahati

Dedicated to

Dr. Neelima, Mahesh, Aditya, and Prof. Nelson,

who have been the foundations in constructing this solid structure called "Sai".

Certificate

It is certified that the work contained in the Thesis titled "**Studies on Strain Softening Materials using Nonlocal Finite Element and Element-Free Galerkin Methods**" submitted by **S Sai Kumar** to the Indian Institute of Technology Guwahati for the award of the degree of Doctor of Philosophy has been carried out under my supervision in the Department of Mechanical Engineering, Indian Institute of Technology Guwahati. This work has not been submitted elsewhere for the award of any other degree.

12th April, 2024

Dr. Nelson Muthu

Assistant Professor

Department of Mechanical Engineering

Indian Institute of Technology Guwahati

Guwahati — 781039

Acknowledgements

I extend my heartfelt gratitude to everyone who, in various ways, supported me through this exhilarating, challenging, and uniquely transformative journey of pursuing a Ph.D.

I would like to thank my supervisor, Prof. Nelson, who has given me the freedom to think in the right direction for the progression of our research work. He is the person who discovered the coding culture within me and encouraged me through strong technical discussions. Though our working style and culture are different, our aspiration towards a beautiful research made us learn new theories together, struggled together for years to clear out the technical obstacles and came out together from that. Regardless of where my research endeavors lead me, I will always be proud to be known as "Sai, student of Dr. Nelson." Thank you.

Furthermore, I extend my gratitude to my doctoral committee members, Prof. K.S.R Krishna Murthy, Prof. Satyajit Panda, and Dr. Hrishikesh Sharma, for their valuable suggestions and insightful perspectives throughout the entire journey. Their constructive inputs have greatly benefited the enrichment of the research work.

I also want to thank all my friends, colleagues, and the connections I made during my Ph.D. Each one has played a special part in this journey in their own unique way. I extend my heartfelt gratitude to my lifelong friends, who have walked beside me throughout the years. In the lifes bustling pace, our exchanges may be scarce. However, I place my trust in each of them, knowing they will stand by me whenever I call upon them.

On this note, I would like to take this opportunity to appreciate my PC, "Finite", which has endured numerous rigorous computational runs despite experiencing two major breakdowns, yet has miraculously recovered without any external intervention.

Recalling this journey, I must especially acknowledge my wife, Dr. Neelima, without whom I couldn't have even imagined completing my Ph.D. I am fully aware of the challenges she has faced over the past year, from being pregnant to becoming a mother, while also single-handedly taking care of our son and me. As a doctor, staying away from practice for almost two years, solely because of me, and managing the responsibilities of our child, I understand the sacrifices she has made. Despite it all, she has never shown any sign of distress in front of us. I believe it's time for her to have the freedom she deserves, and that is the best gift I can offer her. Thank you, my love.

My parents never told me what to do in life; I learned from my father how a middle-class family man lives with honesty, and I am just carrying forward that legacy to come this far. We do have personal and financial problems, but my parents never put these things above my research. Seeing all of this, it seems like for one person's strong forward step, there are sacrifices made by many people behind that. Thank you, amma and nanna. Lastly, God, let us keep moving forward together and help me see things through your eyes.

12th April S Sai Kumar

IIT Guwahati

Abstract

The present work simulates the failure phenomenon of various materials in nonlocal finite element (FEM) and element-free Galerkin (EFG) methods. It commences by examining the constraints inherent in conventional FEM, especially in its application to adhesive bonded joints. Subsequently, it introduces the nonlocal integral theories to accurately capture numerically converged structural responses in complex mode-I and mixed-mode problems within a thermodynamic framework, selecting strain as the regularized variable. Building on the limitations of the nonlocal strain approach, including its tendency to underestimate peak loads and high computational time, the study proposes a strain difference-based method to enhance the prediction of failure behaviour and damage/crack propagation in quasi-brittle materials within a thermodynamic framework. The study then delves into ductile materials exploring the concepts of continuum damage mechanics (CDM) to propose a new nonlocal equivalent plastic strain based ductile damage model which is relatively simpler, reduces the number of material parameters, and enhances the understanding of ductile damage behaviour. A nonlocal equivalent plastic strain is integrated with the proposed damage model to address the challenges associated with strain localization.

The work further explores the EFG method's superior performance in describing continuous fields compared to FEM. Its effectiveness in capturing the strain-softening phenomenon, with a particular emphasis on addressing challenges related to both strong (crack propagation) and weak (sudden change in the area) discontinuities are presented. In the context of strong discontinuities, this work investigates the crack propagation in mode I and mode II problems using CZM concept within the proposed modified EFG framework. Furthermore, it also highlights the stability of GDCM in dealing with various material nonlinearity conditions and improving computational efficiency. Regarding the weak discontinuities, it introduces the application of nonlocal integral theories within the EFG framework and presents a comparative study of convergence over FEM. Lastly, the flexibility of EFG method in dealing with large deformation problems associated with hyperelastic materials are explored.


भारतीय प्रौद्योगिकी संस्थान गुवाहाटी
Indian Institute of Technology Guwahati

Contents

List of Figures

List of Tables

Chapter 1

Introduction

When engineering materials are exposed to adverse conditions like different forming processes, mechanical loads, temperature changes, radiation, environmental causes, and so on, microscopic defects and cracks may emerge. In general, cracks are typically caused by the nucleation of micro-cavities within a zone of discontinuities or defects. Internal defects can be viewed as a set of discrete discontinuities. The presence of distributed defects in materials not only initiates cracks and leads to eventual failure but also contributes to various forms of deterioration or damage. These can include reductions in strength, rigidity, toughness, and stability [1].

Understanding the behaviour of microscopic defects and cracks within materials is of interest to researchers in the field of both material science and mechanics. Material scientists aim to comprehend the mechanisms underlying the development of microscopic cracks and devise strategies to enhance the material's microstructure, ultimately improving its overall performance. Researchers in the field of mechanics typically rely on empirical knowledge gained over extended periods to predict material failure. In certain scenarios, failure prediction entails systematically testing physical models under reproduced service conditions in laboratory settings, which can be both time-consuming and expensive [2]. On the other hand, despite the growing understanding of the mechanisms behind progressive damage caused by microscopic defects in various materials, extensive research has been conducted to develop continuum constitutive models capable of accurately describing the internal degradation of solids. This research builds upon the pioneering work of Kachanov [3] and further advancements in applied mechanics.

Over the course of five decades of research, continuum damage mechanics (CDM) has become a prominent approach, introducing new internal state variables into constitutive models. These models operate under the assumption that internal damage can be effectively represented by one or more internal variables, which may take the form of scalars, vectors, or tensors. These variables, termed as damage variables, quantify the degree of defects within a representative volume element (RVE). Their evolution follows constitutive thermodynamic relations, usually expressed through a system of differential equations over time.

1.1 Classification of CDM theories

When considering the physical significance of damage variables, CDM theories can be broadly categorized into two main types: micromechanical and phenomenological models. Micromechanical models necessitate that the damage internal variable represents an average of the microscopic defects characterizing the state of internal deterioration. Despite the conceptual appeal of internal variables such as the reduction of load-bearing area proposed by Rabotnov [4] or the distribution of microcracks as suggested by Krajcinovic [5,6], the challenges in experimentally identifying damaged states and evolution laws currently limit the practical application of most micromechanical theories. This observation is particularly relevant when considering the analysis of large-scale engineering problems for design purposes.

On the contrary, phenomenological models are formulated based on the impact of internal degradation on the material's macroscopic characteristics. This approach considers how properties like elastic moduli, yield stress, and density are significantly influenced by the presence of microscopic cavities or damage. Certainly, quantifying such properties is generally much more straightforward than characterizing the geometry or distribution of micro-defects. Utilizing these concepts, Lemaitre and Chaboche [7] introduced a class of models that primarily rely on the degradation of elastic moduli as the macroscopic measure of damage. In its simplest form, the damage variable is scalar, particularly under ideally isotropic conditions. However, under anisotropic conditions, it transforms into a second-order tensor [8]. Additionally, Gelin and Mrichcha describe a model that relies on volume changes resulting from void growth as a measure of internal degradation [9].

Thus, within a thermodynamic framework, CDM theories encompasses the entire spectrum of damage evolution, from the inception of microscopic defects such as microcavities or microcracks to the eventual fracture arising from the progression of macroscopic cracks. Within the scope of this thesis, the focus lies on the modelling of various engineering materials, with emphasis placed on utilizing the theoretical background offered by the phenomenological approach.

1.2 Challenges in CDM theories

Usually, most of the constitutive laws developed using phenomenological CDM models rely on local continuum theories. These theories inherently assume material homogeneity and continuity at all size scales. However, this assumption becomes invalid when the internal degradation of the material substantially affects the structural response under loading. In other words, strain localizes within specific zones, while the entire structure demonstrates a strain-softening response on a global scale. At this stage, the heterogeneous nature of microstructure becomes instrumental in instigating the failure phenomenon, ultimately leading to the formation of a crack.

As standard continuum theories overlook the impact of the material's microstructure at this stage, they fall short in accurately depicting the localized failure process. Similarly, the mathematical representation of the failure phenomenon using the classical theory is inadequate because it naturally experiences problems with spurious instabilities. In classical multivariable calculus, the partial differential equilibrium equations governing static (or dynamic) problems are classified as elliptic (or hyperbolic). Since the equations are elliptic (or hyperbolic), the solutions to the boundary-value problems are invariably unique. However, the shift from positive to negative in the material tangential modulus initiates a local transition in the nature of the partial differential equations, changing them from elliptic (or hyperbolic) to hyperbolic (or elliptic). This loss of ellipticity results in an ill-posed boundary value problem [10].

On the other hand, within a numerical framework, such as in structural analysis, consider a scenario where there's a localized zone experiencing deformation. This localized zone is represented by finite elements, and its size matches that of the elements within the critical zone, where deformation is significant. Now, as the mesh undergoes refinement, the strain becomes concentrated in an increasingly smaller layer of elements and the total dissipated energy of the deformation process would unrealistically approach zero, which is not reflective of the actual behaviour of the material. Indeed, it can be inferred that the limitation of the local theory arises from its inability to provide information about the size of the localized zone. Considering the problem from a physical perspective, it becomes evident that the actual size of the localized zone is closely linked to the heterogeneous microstructure of the material. Therefore, mathematical and physical interpretations imply that integrating this missing information into continuum theory is deemed essential for obtaining objective and comprehensive descriptions of localized failure processes.

Over the past three decades, numerous regularization strategies have been suggested in an effort to address the problem of spurious localization caused by strain-softening. Some of them are higher order continuum models, gradient based models, polar theories, nonlocal integral approaches, phase-field theories, peridynamics, viscous models or cohesive zone models [11–14]. Among them, the primary focus of this thesis is the nonlocal integral approach. Nonlocal theories are grounded in the concept that the stress at a specific point is not solely determined by the state variables at that point alone; rather, it generally relies on the distribution of state variables throughout the entire body or, at the very least, within a finite neighbourhood surrounding the point (see Fig. 1.1). These theories incorporate an intrinsic length, which can be explicitly controlled, into the classical continuum by utilizing spatially weighted averages through an integral operator. Thus, nonlocal theories offer enhanced continuum models compared to classical theories and have the capability to capture strain-softening phenomena avoiding mesh dependency issues.

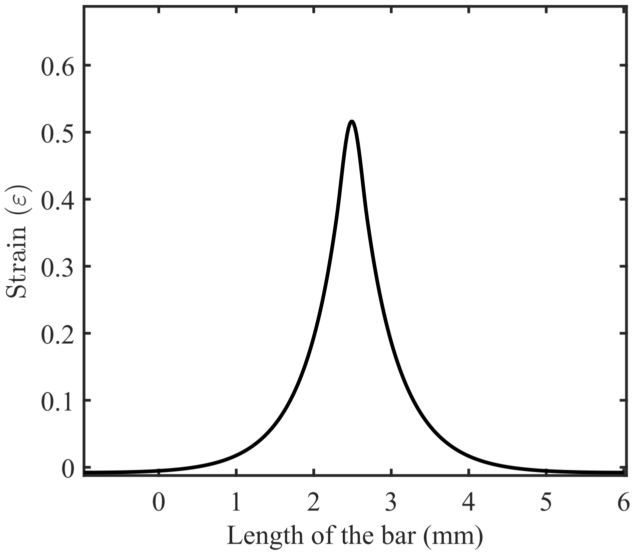

Fig. 1.1. Strain profile in nonlocal integral approach

However, one of the challenges using nonlocal models to accurately represent the fracture process zone (FPZ) is that the element size (or the resolution of discretization in a mesh-free method) must be smaller than the width of the FPZ. This ensures that the model captures the progressive damage across the FPZ accurately. When the element size approaches or exceeds the

FPZ width, the nonlocal effects can be inaccurately averaged over larger areas, causing a loss in resolution of the localized failure and damage evolution, leading to erroneous results. As a result, smaller elements are required, especially near areas of high stress or strain concentration, which significantly increases the number of elements (or nodes) in the model. This not only raises the computational cost in terms of memory and processing power but also increases the computational time for running simulations, particularly for large structures or complex materials.

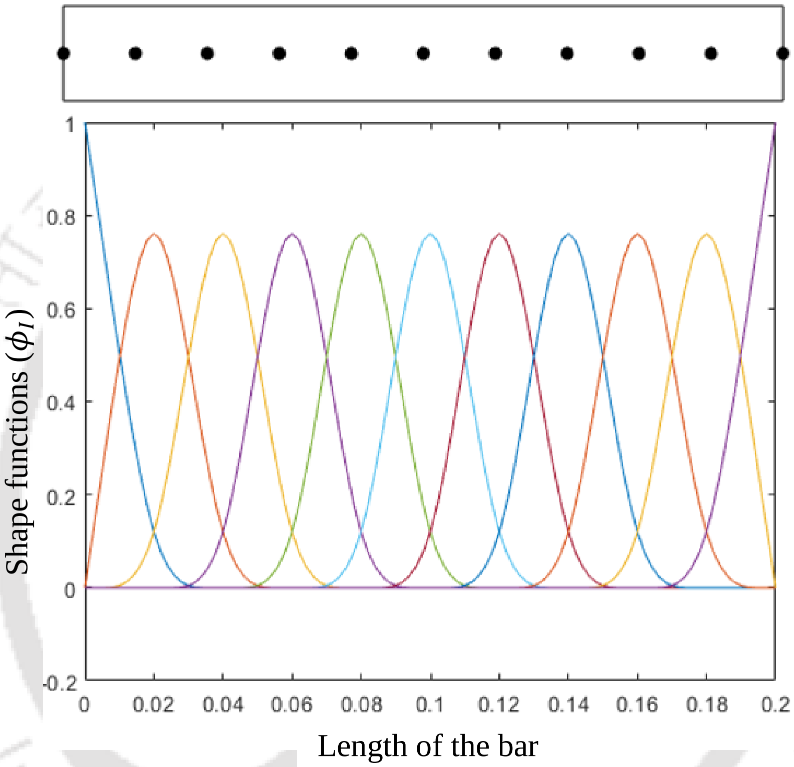

Fig. 1.2. Regular nodal distribution in bar and shape functions distribution in EFG method

On the other hand, meshless methods, unlike FEM, do not associate nodes with specific elements while constructing shape functions. Among different meshless methods, the element-free Galerkin (EFG) method, one of the most popular techniques to solve solid mechanics problems has been used in this thesis. An intriguing characteristic is that the field variables retain continuous differentiability, a feature attributed to the use of higher-order shape functions [15]. Similar to nonlocal theories, the EFG method also employs weight functions through the moving least-square interpolation technique to derive shape functions. This enables the establishment of connectivity between nodes, where each node is influenced by others within the domain (see Fig. 1.2). Given that the nonlocal nature is ingrained in the shape functions, they still impose limitations on their applicability when dealing with discontinuous fields [16]. This can potentially restrict the effectiveness of using EFG methods in scenarios where discontinuous fields need to be accurately represented or captured. Thus, EFG methods encounter similar challenges as FEM when addressing strain localization issues, necessitating the application of regularization theories to effectively manage such challenges. However, the EFG method demonstrates superiority over the FEM in accurately depicting continuous fields. Moreover, the convergence behaviour of the EFG method outperforms that of the FEM, implying that the EFG method achieves higher accuracy per additional degree of freedom [16].

1.3 Motivation

Despite the extensive literature on damage modelling in nonlocal finite element method and EFG method, the efforts are still persist in constructing the constitutive models and respective tangent stiffness matrix that can perform well in any scenario, without compromising the computational cost. The present work aligns with this notion by introducing novel strategies for predicting failure behaviour in both FEM and EFG method.

Research scope in nonlocal FEM framework

This thesis focuses on the regularization of strain-based variables to effectively predict failure behaviours in both quasi-brittle and ductile materials through the application of damage mechanics principles. Furthermore, a nonlinear ductile damage evolution law is proposed to demonstrate its versatility in accurately predicting damage across a variety of ductile materials.

1.3.1 Damage modelling in FEM using nonlocal integral approach

The conventional finite element method (FEM), commonly utilized for predicting failure behaviours in adhesive bonded joints, often yields mesh-dependent results and occasionally fails to converge, especially for complex scenarios such as joints with defects in the adhesive (cohesive cracks) and lap joints with bi-adhesives. Moreover, there is not much existing research addressing the failure analysis of joints with defects and lap joints with bi-adhesives, especially when considering materials with isotropic properties. In this work, the nonlocal integral approach, inspired by Eringen et al.'s work [17], is employed to address these challenges and to capture the numerically converged structural responses within the thermodynamic framework using continuum mixed-mode damage models.

1.3.2 Damage modelling in FEM using strain-difference based nonlocal approach

It has been observed that very few works have considered to enhance the performance of strain-based nonlocal variable in damage mechanics to capture the post-peak behaviour. Indeed, from a physical perspective, it is reasonable to consider strain as a nonlocal variable due to its significant role in deformation processes. Moreover, this approach indirectly incorporates nonlocal effects into the damage variable and the damage energy release rate. In this work, a strain based nonlocal model, adopted from Polizzotto et al.'s [18] linear elastic work, is employed to predict failure behaviour and damage/crack propagation in quasi-brittle materials within the thermodynamic framework of continuum damage mechanics (CDM) theories.

1.3.3 Nonlinear damage model for ductile materials

Several damage models in the context of ductile materials have been developed considering the Lemaitre model as a foundation. Damage evolution laws developed by various researchers have enhanced the accuracy in predicting failure behaviours. However, some of these laws are often limited in their applicability to specific ductile materials, while others pose challenges in determining model parameters. Conversely, Bonora [19], Chandrakanth, and Pandey [20] have formulated models that are analytically derived and demonstrated efficiency in predicting damage across diverse ductile materials. However, they directly leverage the use of the equivalent plastic strain term with hardening exponent in the damage dissipation potential function, implying that plastic strain is entirely attributed to damage. Therefore, the present study introduces a novel ductile damage dissipation potential that incorporates the effects of isotropic hardening and scalar damage, providing an analytical expression that facilitates the straightforward determination of parameters. This formulation offers flexibility in selecting not only the isotropic hardening laws but also the power laws (such as the Ramberg-Osgood model) to contribute to the plasticity process. Moreover, the equivalent plastic strain, which significantly influences the damage evolution of ductile materials, has been treated as the nonlocal variable in the present work.

Research scope in EFG framework

On the other hand, this thesis also focuses on numerical approaches, such as cohesive crack concepts and nonlocal approaches, to address the strain localization problems within the EFG framework. While meshfree methods offer robustness, their computational cost tends to be higher than that of FEM. Particularly, when addressing strain-softening problems that necessitate incremental-iterative techniques, further increases the computational expenses. Although the inherent computation time of EFG cannot be decreased, we can reduce the additional time consumed by iterative methods. This can be accomplished by opting for a nonlinear solver that minimizes the number of iterations while preserving result accuracy.

The EFG method is widely acknowledged for its effectiveness not only in addressing crack propagation problems but also in robustly handling large deformation challenges. Among different categories, hyperelasticity is one class that falls within the realm of large deformations. However, the numerical modelling of hyperelastic materials, which are often nearly incompressible, poses challenges such as volumetric locking. The EFG method efficiently alleviates these challenges compared to FEM. Therefore, before addressing strain-softening in large deformation (hyperelastic) problems, it is essential to employ a robust technique capable of effectively addressing volumetric locking issues within the EFG framework.

1.3.4 Damage modelling in EFG framework using nonlinear solver GDCM

The techniques such as eXtended finite element method (XFEM) [21], and eXtended EFG (XEFG) method [22], which uses branch functions as enrichments at crack-tip nodes are popular in the context of overcoming mesh dependency and stress field singularities. The enriched methods will not be helpful in the absence of analytical solutions from which the branch enrichment functions are inspired. In this work, we combine the modified EFG method with the cohesive zone modelling (CZM) approach that does not necessitate the usage of the branch enrichment functions to simulate the failure phenomenon owing to crack propagation in different geometries and material combinations. In nonlinear separation, whenever the cohesive stress of the FPZs reaches its maximum, the crack gradually begins to open by degrading the stiffness of that region. This nonlinear softening nature was studied using the CZMs by employing various iterative techniques like Newton-Raphson, arc-length control method etc. However, these methods face convergence issues near limit points of softening materials and also fail to predict snapback behaviour [23,24]. Hence, there is a need for the use of an incremental-iterative technique that not only overcomes the convergence issues at limit points but also perform the analysis in fewer increments.

1.3.5 Alleviate locking in EFG framework using mixed displacement-pressure nodes

Most of the hyperelastic materials are nearly incompressible which poses challenges, i.e., volumetric locking during numerical modelling. The mixed displacement-pressure formulations are widely acknowledged as one of the most efficient and robust techniques for addressing volumetric locking issues associated with incompressibility conditions. Nevertheless, these formulations are predominantly applied in standard FE frameworks and have not been extensively explored in EFG frameworks, especially in the context of large deformation problems where challenges such as mesh distortion issues are more prevalent. In this work, a two-field mixed variational formulation employing the perturbed Lagrangian approach is adopted within the EFG framework to tackle the challenge of volumetric locking in hyperelastic materials.

1.4 Objectives

Based on the scope of research identified in the previous section, the objectives of the present work are as follows:

(a) To carry out the performance evaluation of the nonlocal integral approaches over conventional FEM in predicting failure behaviour of complex mode I and mixed-mode problems of adhesive bonded joints.

(b) To develop a nonlocal constitutive equation by regularizing strain-difference within the context of CDM to predict the failure behaviour of quasi-brittle materials.

(c) To develop a novel nonlinear ductile damage model by drawing upon insights from previous models within the context of CDM. Further, to predict the failure behaviour of ductile materials by regularizing the nonlocal equivalent plastic strain.

(d) To incorporate the generalized displacement control method (GDCM) in the modified EFG framework coupled with the CZM to simulate the failure phenomenon in mode I/II fracture problems.

(e) To demonstrate the advantages of EFG method over FEM in addressing large deformation problems associated with hyperelastic materials.

1.5 Organization of the Thesis

The relevant literature is reviewed in chapter 2. This includes the introduction to damage modelling in CDM theories for quasi-brittle and ductile materials. Further, the failure behaviour of adhesive bonded joints through CZM and CDM approaches are explored. Finally, the discussion extends to examining studies on the strain-softening phenomenon within the EFG framework for problems characterized by both strong and weak discontinuities. In Chapter 3, the foundational principles and thermodynamic aspects of CDM theories are elucidated. Subsequently, the basic concepts of CZM are outlined, encompassing their variational formulation, traction-separation laws, damage initiation, and failure criteria. Moreover, the chapter addresses the challenges in classical continuum theories by introducing nonlocal integral approaches and formulations to overcome these issues are derived within the thermodynamic framework. Additionally, it presents theoretical and numerical formulations of hyperelastic materials, along with their respective mathematical preliminaries. Finally, the chapter concludes with an overview of the EFG method, including the key parameters influencing the approach, properties of the shape functions, and the variational formulation for a 2D problem.

Chapter 4 focuses on the application of nonlocal integral theories in predicting the failure behaviour of adhesively bonded joints. It particularly explores complex scenarios where conventional FEM faces challenges, such as joints with defects in the adhesive (cohesive cracks) and single-lap joints with bi-adhesives. While strain regularization achieves physical realism and mesh independence, it still faces challenges in accurately predicting the structural response. To enhance performance, Chapter 5 introduces the strain difference-based nonlocal model, adapted from Polizzotto et al.'s [18] linear elastic work. This model is employed to predict failure behaviour and damage propagation in quasi-brittle materials within the thermodynamic framework of CDM theories. Until now, the absence of permanent strain concepts has allowed the authors to explore various approaches to strain regularization to enhance the performance. However, Chapter 6 focuses on the failure and damage behaviour of ductile materials, where damage is significantly influenced by plastic strain rather than total strain, playing a crucial role in the deformation process. Thus, a scalar variable representing equivalent plastic strain is regularized in this context. Furthermore, the chapter predominantly focuses on devising a new ductile damage evolution law to demonstrate its adaptability in predicting damage across various types of ductile materials.

Given the EFG method's superior performance in describing continuous fields compared to FEM [16], the subsequent portion of the thesis aims to capture the strain-softening phenomenon within the EFG framework, with a particular emphasis on addressing challenges related to both strong (crack propagation) and weak (sudden change in area) discontinuities. Chapter 7 investigates the crack propagation in mode I and mode II problems using CZM concept within the proposed modified EFG framework. While the inherent computation time of EFG cannot be reduced, the study explores the potential to minimize additional time consumption by employing the generalized displacement control method (GDCM), which necessitates fewer increments compared to alternative methods. Whereas, Chapter 8 introduces the application of nonlocal integral theories within the EFG framework, particularly exploring their implementation on a concrete bar with a sudden reduction in area at its central portion. It also presents a comparative study of convergence, evaluating the effectiveness of the nonlocal approach in both FEM and EFG frameworks.

The EFG method is renowned for its ability to effectively handle large deformation problems, particularly in the realm of hyperelasticity. However, the incompressible nature of hyperelastic materials often leads to volumetric locking issues, which the EFG method is adept at alleviating. Therefore, prior to addressing strain-softening phenomena in hyperelastic materials, the authors recognized the need to employ a robust technique within the EFG framework to mitigate locking and mesh distortion issues. Therefore, in Chapter 9, a two-field mixed variational formulation using the perturbed Lagrangian approach within the EFG framework is proposed for modelling nearly incompressible hyperelastic material models. Finally, the main conclusions and future scope of this work are presented in Chapter 10.

Chapter 2

Literature Review

This chapter provides a comprehensive overview of finite element and meshfree methods, followed by a detailed discussion on classical continuum damage models and their significance in quasi-brittle and ductile materials. It delves into how strain localization issues are tackled in the FEM framework using nonlocal theories based on continuum damage mechanics. Further, it explores various research works on addressing strong and weak discontinuity problems within the element-free Galerkin (EFG) framework, employing cohesive zone modelling (CZM) and continuum damage mechanics (CDM). In the end, it highlights the literature on the failure behaviour of adhesive bonded joints using CZM and CDM approaches.

While FEM and Meshfree Methods (MMs) have distinct characteristics and applications, they both play a crucial role in addressing important engineering problems. Both these methods are employed to analyze and model complex physical phenomena, such as structural behaviour, heat transfer, fluid dynamics, and material failure. Despite their differences, FEM and MMs share a common goal: to provide accurate and efficient numerical solutions for a wide range of practical problems. Whether it is simulating the behaviour of a mechanical component under load or predicting the failure of a component, both FEM and MMs contribute significantly to advancing our understanding of physical systems and optimizing engineering designs. The present thesis explored their complementary strengths to make them valuable tools in the field of computational mechanics.

2.1 Finite Element Analysis

Finite element analysis (FEA) is a widely practised numerical procedure for solving a mathematical model driven by differential equations that govern most physical problems in real life. Over time, FEA has found numerous applications in a diverse set of engineering fields, such as solid mechanics, fluid mechanics, biomechanics, electromagnetics, and many more [25]. It has brought a fundamental transformation in the approach to scientific modelling and engineering design, impacting a wide range of applications across various fields of study.

2.1.1 Fundamental insights into FEA

The fundamental steps associated with the FEA process are shown in Fig. 2.1, which offers a comprehensive overview of the different methodological stages in FEA. The physical problem at hand usually involves a real-world structure or its components that experience specific loads. To translate this physical problem into a mathematical model, certain assumptions are made, which ultimately lead to the formulation of differential equations that govern the behaviour of the physical problem. FEA plays a critical role in solving these intricate mathematical models.

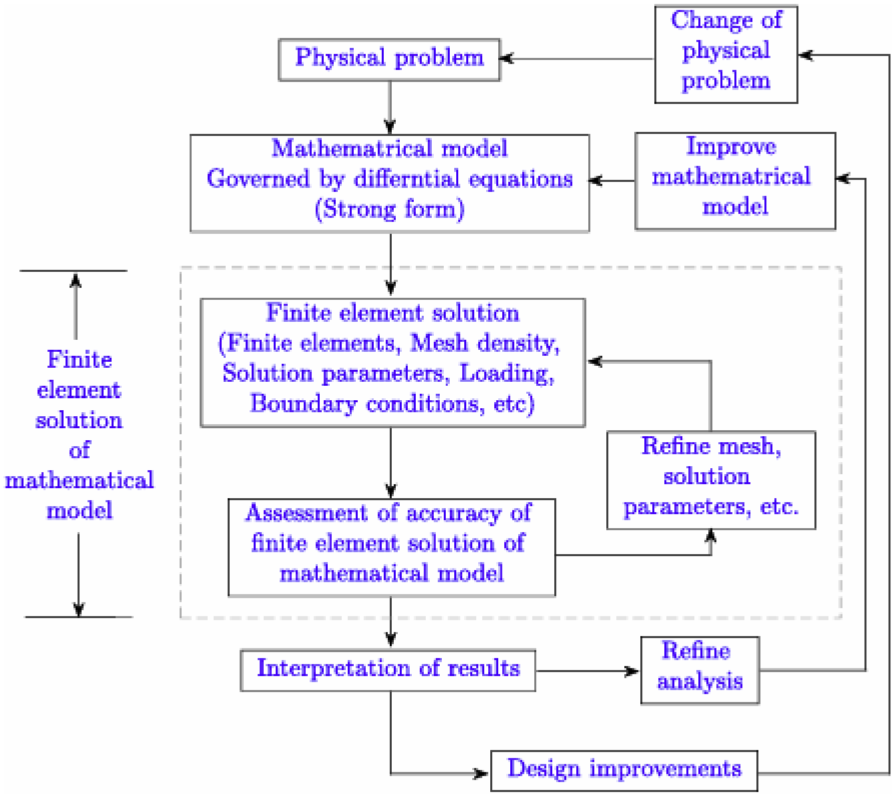

Fig. 2.1. The process of finite element analysis

Conventionally, FEA employs classical variational methods to solve these differential equations that govern physical systems. The fundamental approach involves transforming the governing equations into an equivalent weak form. The solution is then approximated across the domain using a linear combination of suitable chosen interpolation functions (ϕ_j) and unknown coefficients (c_j). The determination of these coefficients (c_j) is carried out to ensure the satisfaction of an integral statement which is the weak form of the original differential equation. Various methods of weighted residuals (MWR), such as Galerkin, collocation, sub-domain and least squares methods, distinguish themselves by their unique choices in integral form by means of the weighted functions. Each method offers a different perspective on how to effectively formulate and solve the mathematical model, providing flexibility in adapting to the characteristics of specific engineering problems [26]. In addition to MWR, one could obtain the system of equations through other techniques such as principle of minimization of potential energy, principle of virtual work or variational methods.

After selecting the suitable variational method, the domain is segmented into sub domains/elements. Within each element, FEA approximate the variation of the primary field variables. This approach leverages the simplicity of representing complex functions as collections of simple polynomials, simplifying the computational process in FEA. Finally, the assembled system of equations is solved to evaluate the solution parameters. As FEA is a numerical procedure, it is imperative to assess the accuracy of the solution. If the predefined accuracy criteria are not met, the numerical solution has to be repeated with refined parameters until a satisfactory level of accuracy is attained. For a comprehensive exploration of this topic, one can refer to standard FEA books such as those by Bathe [27] and Reddy [26].

On the other hand, FEM has certain limitations, such as being somewhat incomplete due to the omission of rotational degrees of freedom in two- and three-dimensional elements. This limitation has roots in the historical development of FEM, where efforts to find closed-form solutions eventually reached a point of exhaustion [28]. This suggests that, despite the advancements and improvements in finite element methods, there still seems to be something missing that prevents it from being a truly dynamic (or fully kinetic) solution to elasticity equations. In other words, FEM may not entirely capture the complete physical behaviour or motion in elastic systems, as it doesn’t fully address all the kinetic aspects that govern elasticity. In biomechanics, FEM faces challenges in accurately simulating the dynamic behaviour of complex biological structures, such as the tooth and its supporting tissues [29]. Due to mesh-based interpolation, distorted or low quality meshes lead to higher errors, necessitate remeshing, a time and human labour consuming task, which is not guaranteed to be feasible in finite time for complex three-dimensional geometries [30].

2.2 Meshfree methods

The FE method has been widely used in various academic and industrial domains, offering effective solutions to numerous challenges. However, it does come with certain limitations. One such limitation arises from mesh-based interpolation, where distorted or low-quality meshes can result in increased errors. Rectifying these issues often requires remeshing, a labour-intensive and time-consuming task, especially challenging for complex three-dimensional geometries and not always feasible within finite time constraints [31].

Mesh-based methods rely on a fixed mesh structure to approximate solutions within a domain. However, they struggle to handle problems with discontinuities that do not align with element edges. Traditional approaches like remeshing or discontinuous enrichment are costly and can degrade accuracy. An alternative is the extended finite element method (XFEM), which enriches the approximation space to capture both weak and strong discontinuities without the need for remeshing [21,32–35].

One prominent formulation of meshfree methods (MM) is smoothed particle hydrodynamics (SPH) [36]. Initially developed for astrophysics, it was later applied to fluid dynamics [37], and solid mechanics to solve impact problems [38]. However, SPH's initial form suffered from numerical instability, leading to various corrective formulations based on the strong form [39].

The diffuse element method (DEM) [40] and the element free Galerkin (EFG) method [41] adopted the Bubnov-Galerkin approach, while the meshless local Petrov-Galerkin (MLPG) method by Atluri and Zhu [42] utilised the local weak form. Although the DEM had some shortcomings, it later became a popular MM in the area of solid mechanics. The reproducing kernel particle method (RKPM) by Liu et al. [43], based on wavelets, followed shortly after the EFG method. These methods (EFG, DEM, and RKPM) necessitate higher-order Gauss integration due to the non-polynomial nature of their shape functions. To address this, Liu [44] introduced the linearly conforming point interpolation method (LC-PIM) leveraging polynomial basis functions.

Other MM variants, such as particle-in-cell (PIC), can utilize both strong and weak forms. The PIC method, when applied to the strong form, is called the finite-volume particle-in-cell method [45], while the weak form version is known as the material point method [46]. Similarly, RKPM offers both collocation strong form [43] and weak form variations [47].

Formulations of these MM variants can be found in review articles [31,48]. Compared to FEM, the EFG method offers advantages in adaptivity and handling complex problems (Nguyen et al., 2008; Liu, 2010): adding nodes in EFG simplifies h and p-adaptivity (mesh refinement and increase in solution order) [49]. This allows for easier treatment of moving boundaries (cracks, waves, phase changes) and large deformations. Additionally, EFG offers higher-order continuity of the shape functions, nonlocal interpolation character, and a simpler post-processing. Unlike FEM, EFG does not require nodes precisely on discontinuities.

However, MMs also have drawbacks: The non-polynomial nature of shape functions necessitate higher-order integration for accurate stiffness matrices. Enforcing essential boundary conditions is challenging due to the lack of the Kronecker delta property in shape functions. Additionally, MMs can be computationally slower than FEM, and the system stiffness matrix is asymmetric depending on the weak form.

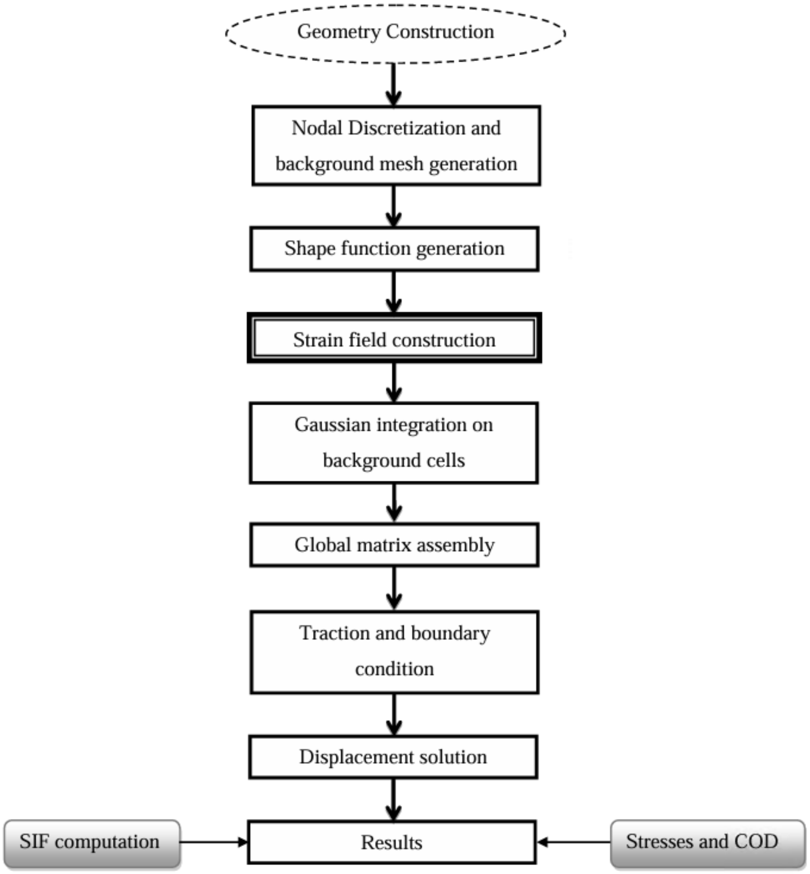

Fig. 2.2. The process of analysis in EFG framework [50]

In this research work, both strong and weak discontinuity problems are addressed using the element-free Galerkin (EFG) method, a popular approach in structural analysis. The process of analysis using the EFG method is shown in Fig. 2.2.

2.3 Numerical approaches for strain localization problems

As discussed in Chapter 1, many structures exhibit a shift from initially uniform strain distribution to highly localized patterns when subjected to extreme loading conditions. In these localized zones, the strains intensify, while the rest of the structure experiences unloading. The size and development of these localized zones are influenced by the material's microstructure, particularly by the presence and characteristics of heterogeneities, and failure mechanisms relative to loading. The evolution and coalescence of the microvoids/cavities in the localized zones may lead to the the formation of stress-free cracks.

On the contrary, in the case of standard FEA, the constitutive laws derived from classical continuum theories often fail to accurately capture the post-peak behaviour of structures containing strong and weak discontinuities including macro-cracks, holes, and other geometric complexities. Mathematically, the loss of ellipticity results in an ill-posed boundary value problem. Furthermore, from a numerical perspective, the results exhibit both mesh size dependence and unrealistic zero-energy dissipation upon mesh refinement [51]. To address these challenges, some of the following approaches are used [52]:

- Strong discontinuities, characterised by a jump in the displacement field, are effectively handled by the cohesive crack model (see Fig. 2.3(a)). It accounts for the softening of the material through a traction-separation law, which correlates the traction transmitted by the crack with the extent of crack opening.
- In structures containing holes, notches, and other defects where the strains become localized, the conventional FEM encounters challenges in preserving continuity within the strain field (see Fig. 2.3(b)). Regularized theories are based on generalized continuum theories, which introduce a characteristic length to inhibit the strain from localizing into infinitesimally small volumes. By enforcing a minimum width for the numerically resolved process zone, these models are referred to as localization limiters.

In contrast to the conventional FEM, regularized theories ensure continuity in both displacement and strain fields. Rather than sudden jumps in strains, these theories generate a strain profile that is elevated in localized zones and gradually decreases as it extends to the surrounding regions of the body, as depicted in Fig. 2.3(c).

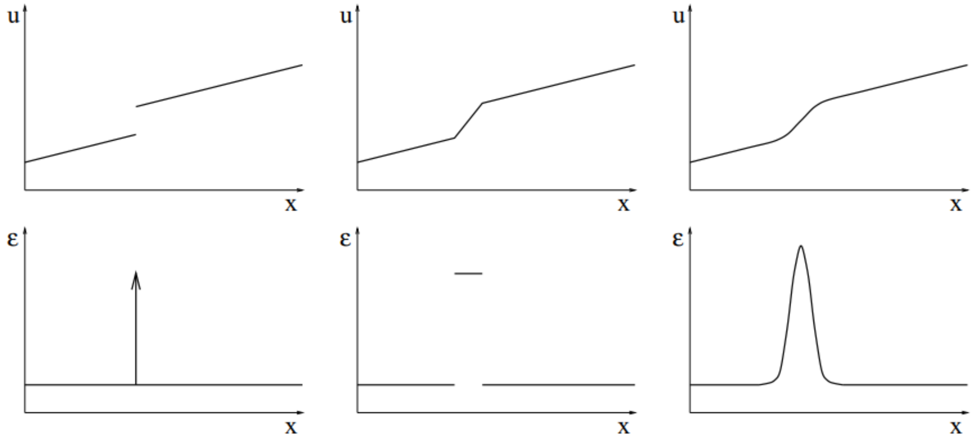

(a) **(b)** **(c)**

Fig. 2.3. Kinematic description with (a) strong discontinuity, (b) weak discontinuities, (c) no discontinuities [52]

2.3.1 Integral based nonlocal approaches

Developing the constitutive law at a specific point through integral-type nonlocal approaches involves integrating weighted averages of a state variable over a certain neighbourhood within a continuum. This approach allows for considering the influence of material behaviour beyond the immediate vicinity of a specific point, providing a more comprehensive representation of the material's response. The approach has been utilized in various branches of physical sciences since early stages. For instance, they have been employed in optimizing slider bearings, modelling liquid crystals [53], studying radiative transfer, and investigating electric wave phenomena in the cortex.

In the domain of solid mechanics, initial models of this kind were introduced during the 1960s, with the aim of refining the understanding of elastic wave dispersion in crystalline structures. Kröner [54] formulated the nonlocal continuum model to investigate the long-range impact of cohesive forces. Subsequently, Eringen and his colleagues [55,56] refined the theory of nonlocal mechanics to its present form. They established attenuation functions to describe the decrease in long-range interactions between particles based on their separation distance. These functions were instrumental in formulating constitutive and balance equations in the continuum theory, which relied on integral functionals of kinematical variables [12]. Eringen [17] applied nonlocal elasticity theories to crack problems, where the abrupt changes in strains near the crack tip region are smoothed out. This smoothing process helps to eliminate stress singularities, highlighting the physical nature of the problem. It indicates that in the vicinity of geometric discontinuities in the body, nonlocal intermolecular forces play a dominant role. Polizzotto [57] revisited Eringen's nonlocal elasticity theory, particularly tailoring it for elastic continua with discontinuities. In this reformulation, Polizzotto derived attenuation functions that consider the geodetic path of the nonlocal field. Polizzotto et al. [18] introduced a nonlocal elasticity model that relies on the strain difference between two distinct points within the continuum. In this model, the stress comprises two components: local and nonlocal. The local contribution is governed by the linear elastic moduli tensor, while the nonlocal contribution is determined by the nonlocal stiffness tensor which is symmetric positive-definite.

In parallel, Eringen extended these theories to include nonlocal elastoplasticity in the early 1980s [58]. It was later observed that specific nonlocal formulations can serve as effective localization limiters, exerting a regularizing influence on issues characterized by strain localization [59], a research topic that will be further explored in Section 2.5.

2.4 Strain-softening phenomenon in FEM framework

This section offers insight into the research efforts dedicated to damage modelling across different materials and applications, utilizing principles from continuum damage mechanics. Moreover, it explores how numerous studies have aimed to overcome mathematical and numerical challenges inherent in classical continuum theories by integrating nonlocal damage mechanics theories within a thermodynamic framework.

2.4.1 Damage modelling using CDM theories

Continuum damage mechanics encompasses various underlying damage mechanisms, including brittle, ductile, creep, fatigue, and spall damage [60]. Here, the modelling theory concerning brittle and ductile damages within the continuum damage mechanics framework is succinctly introduced.

2.4.1.1 *Damage in brittle or quasi-brittle materials*

Brittle damage manifests itself through the disruption of interatomic bonding at the atomic level, culminating in the formation of cracks at the macroscopic level. This damage mechanism is commonly observed in materials like rocks, concrete, and ceramics, often characterised by a smooth crack surface [61]. In many quasi-brittle materials, such as concrete, they exhibit brittle behaviour under tension and greater ductility under compressive loading. In contrast to uniaxial tension, where only a single crack propagates, compression induced by heterogeneities (such as aggregates surrounded by a cement matrix) generates transverse tensile strains, leading to the initiation of mesoscopic cracks perpendicular to the extension direction. These mesoscopic cracks gradually coalesce until they reach a complete rupture. Under high confinement, hydrostatic pressure compacts the porous cement matrix, while shear stress promotes mode II fracture behaviour.

The uniaxial response to tension and compression exhibits different shapes and maximum stresses, indicating different damage kinematics. In the context of continuum mechanics, to simulate the failure behaviour of quasi-brittle materials, the elastic damage [52,62,63] or coupled plastic damage models [64,65] are commonly employed. As damage evolves, stiffness decreases during unloading-reloading cycles, while permanent strains increase.

In the category of elastic-damage models, Mazars [62] introduced an isotropic damage model, which handles both compression and tension. Furthermore, he formulated the damage threshold function as a function of equivalent strains, given by:

$$\tilde{\varepsilon} = \sqrt{\textstyle\sum_i \langle \varepsilon_i \rangle_+^2} \qquad \varepsilon_i = \text{principal strain} \tag{2.1}$$

$$\langle \varepsilon_i \rangle_+ = \varepsilon_i \qquad \text{if } \varepsilon_i \geq 0$$

$$\langle \varepsilon_i \rangle_+ = 0 \qquad \text{if } \varepsilon_i < 0$$

The damage threshold is then defined as

$$f(\varepsilon, \kappa) = \tilde{\varepsilon} - \kappa = 0, \quad \dot{\kappa} \geq 0 \text{ and } f(\varepsilon, \kappa)\dot{\kappa} = 0 \tag{2.2}$$

with $\kappa_0 = \kappa(0) = \varepsilon_{D_0}$ (initial damage threshold). κ is an internal variable that corresponds to the maximum level of equivalent strain ever reached in the previous history of the material.

In the uniaxial case, the damage in tension (D_t) and compression (D_c) are given by:

$$D_t = \mathbf{F}_t(\tilde{\varepsilon}) \quad \text{for tension;} \qquad D_c = \mathbf{F}_c(\tilde{\varepsilon}) \quad \text{for compression} \tag{2.3}$$

The combination of compression and tensile damages for the multiaxial case is expressed as follows:

$$D = \alpha_t D_t + \alpha_c D_c \tag{2.4}$$

here, α_t and α_c shows the contributions of both damages in multiaxial case, which are generally linked to tensile and compressive stresses. Therefore, from several experimental results we can conclude the following.

$$\begin{aligned} D_t(\tilde{\varepsilon}) &= 1 - \frac{\kappa_0(1-A_t)}{\tilde{\varepsilon}} - \frac{A_t}{\exp[B_t(\tilde{\varepsilon}-\kappa_0)]} \\ D_c(\tilde{\varepsilon}) &= 1 - \frac{\kappa_0(1-A_c)}{\tilde{\varepsilon}} - \frac{A_c}{\exp[B_c(\tilde{\varepsilon}-\kappa_0)]} \end{aligned} \tag{2.5}$$

where A_t, B_t, A_c, and B_c are the damage parameters of the material obtained with uniaxial compression tests and flexural tests.

Simo and Ju [63] suggest defining $\bar{\tau}$ as the (undamaged) energy norm of the strain tensor (ψ_0). This definition differs from that used by Mazars and Lemaitre [66], where it represents the J_2-norm of the strain tensor. Consequently,

$$\bar{\tau} = \sqrt{2\psi_0(\boldsymbol{\varepsilon})} \tag{2.6}$$

The damage state of the material is assessed using a damage criterion $g(\bar{\tau}, r) = \bar{\tau}_{i+1} - r_{i+1} \leq 0$, formulated in the strain space. The term r_{i+1} is the damage threshold at the current increment $i + 1$. The damage criterion stipulates that damage initiation occurs when the energy norm of the strain tensor, $\bar{\tau}$, surpasses the initial damage threshold r_0. For the isotropic case, the rate of evolution of the damage variable, D, is defined as

$$\dot{D} = \dot{\lambda} H(\bar{\tau}_{i+1}, D_{i+1}) \tag{2.7}$$

here, $\dot{\lambda}$ represents the damage multiplier, determining the loading/unloading conditions based on Kuhn-Tucker relations, similar to Mazars model. If $H(\bar{\tau}_{i+1}, D_{i+1})$ in the Eq. (2.7) is independent of D_{i+1}, the rate equation may be rephrased as follows. Let $G: \mathbb{R} \rightarrow \mathbb{R}_+$ be such that $H(\bar{\tau}_{i+1}) = \frac{\partial G(\bar{\tau}_{i+1})}{\partial \bar{\tau}_{i+1}}$, assuming $G(.)$ is monotonic. A damage criterion entirely equivalent to condition $g(\bar{\tau}, r) = \bar{\tau}_{i+1} - r_{i+1} \leq 0$ is given by $g(\bar{\tau}, r) = G(\bar{\tau}_{i+1}) - G(r_{i+1}) \leq 0$. The flow rule in Eq. (2.7) then become $\dot{D} = \dot{\lambda} \frac{\partial g(\bar{\tau}, r)}{\partial \bar{\tau}} = \dot{\lambda} \frac{\partial G(\bar{\tau})}{\partial \bar{\tau}}$. According to Kuhn-Tucker relations, when $\dot{\lambda} > 0$, it is determined by the damage consistency condition, given as

$$g(\bar{\tau}, r) = \dot{g}(\bar{\tau}, r) = 0 \Rightarrow \dot{\lambda} = \dot{\bar{\tau}} \tag{2.8}$$

Furthermore, Brekelmans et al. [67] proposed a damage criterion aimed at describing significant differences between tensile and compressive strength. In their study, they introduced a scalar measure of strain known as the damage equivalent strain, $\varepsilon_d = \varepsilon_d(\varepsilon) \geq 0$, which is defined as a function of the principal stresses:

$$\varepsilon_d = \bar{\gamma}\left(\sum_{j=1}^{3}\left(\langle\sigma_i\rangle^2 + \bar{h}^2\langle-\sigma_i\rangle^2\right)\right)^{\frac{1}{2}} \tag{2.9}$$

With σ_i being linear combinations of ε_i, the quantities $\bar{\gamma}$ and $\bar{h}$ are expressed in Poisson's ratio (ν) and a material constant (η)

$$\bar{\gamma} = \frac{1}{(1+\nu)(1-2\nu)}, \quad \bar{h} = \frac{1}{\eta} \tag{2.10}$$

By incorporating the damage equivalent strains into the loading/unloading relations and the power-law based damage evolution equation, a closed-form expression for damage under monotonic loading is derived as follows:

$$D(\varepsilon_d) = 1 - (1 - D_0)\left(\frac{\left(\varepsilon_{d_c}\right)^{m+1} - \left(\varepsilon_d\right)^{m+1}}{\left(\varepsilon_{d_c}\right)^{m+1} - \left(\varepsilon_{d_0}\right)^{m+1}}\right)^{\frac{1}{n+1}} \tag{2.11}$$

where *m* and *n* are the exponents in the damage law, ε_{d_c} and ε_{d_0} are the critical and initial damage equivalent strain thresholds, and D_0 is the initial damage threshold. Comi and Perego [68] introduced an inelastic strain energy function that incorporates a damage hardening variable, which plays a significant role in the damage evolution process, as discussed in detail in Section 5.2.

$$\psi_{in}(\xi) = K(1-\xi)\sum_{j=1}^{N}\frac{N!}{j!}ln^{j}\left(\frac{c^{*}}{1-\xi}\right) \tag{2.12}$$

here, K, c^{*}, and N are the material parameters. The internal scalar variable ξ represents material rearrangements at the microscale resulting from the development of damage. Damage is the only dissipation mechanism considered in this model. Many damage models have been developed based on the aforementioned foundations [69–77].

CDM alone is insufficient for fully describing the constitutive modelling of quasi-brittle materials because it fails to account for the irreversible strain that arises during deformation. To address irreversible strains, the inclusion of plasticity theory becomes necessary. Simo and Ju [63] further developed their work by integrating a thermodynamic framework into the elastoplastic damage model. This is done through a dual approach, employing formulations based on both strain and stress. In these formulations, damage is delineated within the effective stress or strain space, using the hypothesis of strain-stress equivalency. The additive split of stress/strain tensors is the basis of the plastic flow rule. In a stress-based formulation, the complementary energy norm of the stress tensor serves as the foundation. In contrast, in strain-based formulations, an equivalent strain is determined by the second invariant of the strain tensor.

Ibrahimbegović et al. [78] introduced a novel coupled plasticity-damage framework capable of accommodating a diverse range of materials, as demonstrated through its application to porous metal and compacting concrete. The total deformation can be decomposed additively into three distinct components: elastic (ε^{e}), plastic (ε^{p}), and damage (ε^{d}). Accordingly, strain energy as the sum of elastic, damage and plastic is written as

$$\psi(\varepsilon, \varepsilon^{d}, D, \xi^{d}, \varepsilon^{p}, \xi^{p}) = \psi^{e}(\varepsilon^{e}) + \psi^{d}(\varepsilon^{d}, D) + \Xi^{p}(\xi^{p}) + \Xi^{d}(\xi^{d}) \tag{2.13}$$

where ξ^{p} and ξ^{d} are internal variables defining the phenomenon of hardening for plasticity and damage, $\Xi^{p}(\xi^{p})$ and $\Xi^{d}(\xi^{d})$ are the respective hardening functions, and $\psi^{d}$is the damage strain energy.

The novelty of this model compared to standard coupled models lies in its treatment of plasticity and damage as separate entities, each governed by its own distinct yield or damage criteria.

$$\begin{gathered} \phi^{p}(\sigma, q^{p}) = |\sigma| - (\sigma_{y}^{p} - q^{p}) \leq 0 \\ \phi^{d}(\sigma, q^{d}) = |\sigma| - (\sigma_{f}^{d} - q^{d}) \leq 0 \end{gathered} \tag{2.14}$$

where q^{p} and q^{d} are stress-like parameters that describe the hardening phenomenon. σ_{y} is the yield limit and σ_{f} is the fracture limit.

This characteristic can offer notable advantages, particularly when the behaviour of one or both components of the coupled model is thoroughly understood. Subsequently, the plastic and damage models are linked to establish the elastic domain, enabling the parallel implementation of numerical procedures for both. Ultimately, these components can be integrated through a local iteration procedure. More extensive work was done on the coupled damage-plasticity of quasi-brittle materials for various loading conditions [79–86].

2.4.1.2 Damage in ductile materials

This form of damage commonly occurs in ductile metals and is the result of the formation, growth, and coalescence of voids. Typically, the formation of voids is triggered by the separation of the matrix material from the hard inclusions or by the fracture of these inclusions [60]. Subsequently, these voids grow under plastic deformation and eventually coalesce, forming microcracks [87], which often result in dimpled fracture surfaces [88]. The first phenomenological model in the spirit of continuum damage mechanics was proposed by Lemaitre [89]. The integrated model of ductile plastic damage developed on the basis of thermodynamic principles and effective stress concepts, exhibits linearity in strain. To derive constitutive equations for the evolution of dissipative variables, it is assumed that there exists a potential for dissipation, a scalar convex function of flux variables (r, p, D), with the state variables acting as parameters.

$$\begin{gathered} F^{p}(\boldsymbol{\sigma}, R, D) = \frac{\sigma_{\boldsymbol{eq}}}{(1-D)} - \left(\sigma_{\boldsymbol{y_0}} + R\right) \\ F^{D} = \frac{S}{2(1-D)}\left(\frac{Y}{S}\right)^{2} \end{gathered} \tag{2.15}$$

Upon applying the normality laws which will be later discussed in Section 3.1 and performing certain mathematical operations to determine the evolution of plastic strain, isotropic hardening and damage.

$$\dot{p} = \left(\frac{2}{3}\dot{\boldsymbol{\varepsilon}}^p : \dot{\boldsymbol{\varepsilon}}^p\right)^{\frac{1}{2}} = \frac{\dot{\lambda}}{(1-D)}; \qquad \dot{r} = -\dot{\lambda}\frac{\partial F^p}{\partial R} = \dot{\lambda} = (1-D)\dot{p}$$

$$\dot{D} = \dot{\lambda}\frac{\partial F^D}{\partial Y} = \left(\frac{Y}{S}\right)\dot{p} \tag{2.16}$$

here, F^p and F^D represents plastic and damage dissipation potential functions, $\boldsymbol{\sigma_{eq}}$ and R are the von Mises equivalent stress and thermodynamic conjugate to the isotropic hardening variable, $\dot{\lambda}$ and S are plastic multiplier and damage parameter, Y is defined as damage energy release rate which includes the effects of stress triaxiality. The stress triaxiality is an important quantity governing the fracture mode of material, and the larger the value of σ_H/σ_{eq} the more brittle is the fracture.

Tai and Yang [90] proposed a plastic damage model for ductile materials along with a damage mechanics criterion for ductile fracture. They are utilized to analyze the effects of plastic damage on localized deformation and mechanical properties of materials, as well as to predict the initiation of ductile fracture. The damage potential function is expressed as

$$F^D = \frac{S}{2(1-D)}\left(\frac{Y}{S}\right)^2 D \tag{2.17}$$

Using the normality laws and Ramberg-Osgood hardening law coupled with damage, the evolution of damage is given by the following:

$$\dot{D} = m\left(\frac{1}{\varepsilon_r^m - \epsilon_0^m}\right)\ln\left(\frac{D_c}{D_0}\right) f\left(\frac{\sigma_H}{\sigma_{eq}}\right) p^{\frac{2}{n}} D\dot{p} \tag{2.18}$$

Tai and Yang's model is found to be suitable for low-carbon steel. It is observed that the model is suitable only for a small range of triaxiality ratio. Chandrakanth and Pandey [20] have proposed a ductile damage model that shows a nonlinear variation with respect to plastic strain. The damage potential function is expressed as

$$F^D = \frac{S}{2(1-D)D^{\frac{\alpha}{n}}p^{\frac{2}{n}}}\left(\frac{Y}{S}\right)^2 \tag{2.19}$$

Similarly to Tai and Yang's work, the damage evolution equation is derived by substituting the Ramberg-Osgood hardening law and is given by

$$\dot{D} = m\left(\frac{D_c^m - D_0^m}{\varepsilon_r^m - \epsilon_0^m}\right)\left(\frac{n}{\alpha+n}\right)f\left(\frac{\sigma_H}{\sigma_{eq}}\right)D^{-\frac{\alpha}{n}}\dot{p} \tag{2.20}$$

This nonlinearity is not completely represented by a linear or a parabolic model except in a few cases like aluminium. Each model can represent only a limited family of damage evolution patterns. It should also be noted that each model is only suitable for a specific material or class of materials. This indicates a need for a more generalized damage model, which can represent damage evolution in a wider range of materials and consider nonlinear accumulation of plastic strain.

Building upon these findings, Bonora [19] proposed a novel nonlinear continuum damage mechanics (CDM) plasticity damage model. This model is formulated on the basis of experimental observations that indicate that the accumulation of damage exhibits nonlinear behaviour alongside plastic deformation, particularly as a result of microvoid growth. Three basic possible damage evolution trends are identified and considered by a single damage model. Thus, the damage dissipation function is given by

$$F^D = \frac{S}{2(1-D)}\left(\frac{Y}{S}\right)^2\left(\frac{(D_c-D)^{\frac{\alpha-1}{\alpha}}}{p^{\frac{2+n}{n}}}\right) \tag{2.21}$$

The damage exponent α, from a phenomenological perspective, considers the overall impact of growth phases within the RVE under a specific accumulated plastic strain p. Thus, the damage evolution equation is written as follows.

$$\dot{D} = \left(\frac{K^2}{2ES}\right)\left(\frac{(D_c-D)^{\frac{\alpha-1}{\alpha}}}{p}\right)f\left(\frac{\sigma_H}{\sigma_{eq}}\right)\dot{p} \tag{2.22}$$

The overall influence of the three stages of void growth on decreased material stiffness can be accurately depicted by a group of four material parameters: $\varepsilon_0, \varepsilon_r, D_0$, and D_c, in addition to a damage exponent α. These parameters can be easily determined through tensile tests. The proposed model has been successfully applied to seven different materials, each clearly exhibiting the three distinct trends of damage evolution.

These damage growth laws have played a useful role in predicting the initiation of fractures in some engineering materials. However, most of these assume that the triaxiality remaining constant is not valid after necking as it keeps changing after the necking due to the triaxial state of stress. In Kumar and Dixit's work [91], an expression for the damage potential is proposed, leading to a nonlinear ductile damage growth law. This law comprises only two material constants and simplifies to a linear damage growth law when one of the constants is zero. These material constants are not defined in relation to the threshold and fracture values of the equivalent plastic strain and damage. Therefore, there is no requirement to assume constant triaxiality. The damage potential expression by Lemaitre (Eq. (2.5)) is refined to adopt an exponential form in terms of (Y) rather than a quadratic structure. Furthermore, the notation for the material constant $2S$ is updated to b_0 for enhanced clarity. Furthermore, a second material constant, denoted as a_0, is introduced to accommodate linear variation. Thus, the following expression is proposed for the damage potential (F^D)

$$F^D = \frac{a_0}{b_0(1-D)} exp(b_0 Y) \qquad (2.23)$$

However, the model can represent only one family of damage evolution patterns.

On the other hand, instead of a damage law applicable to various materials, many works have also been carried out in developing damage laws that suitable for various stress triaxiality ratios of same material. In this context, Malcher and Mamiya [92] introduced a damage evolution law within the framework of CDM. This law incorporates dependencies on hydrostatic pressure, stress triaxiality, and the third invariant of the deviatoric stress tensor, referred to as the normalized third invariant.

In the original Lemaitre model, high stress triaxiality ($\eta > 0.33$) leads to delayed fracture onset, as observed in notched cylindrical bar specimens. On the contrary, under loading conditions with low stress triaxiality, such as pure shear ($\eta = 0$), the model predicts the appearance of premature fracture. However, with the new formulation, the model enhances its predictive consistency, reducing its sensitivity to variations between operational and calibration conditions. Cao et al. [93] suggested a modification to the stress triaxiality-based Lemaitre damage model to predict ductile fracture under low stress triaxiality and shear-dominated loads. This modification introduces the influence of the third stress invariant on the evolution of damage through the Lode parameter, resulting in the Lode-dependent Enhanced Lemaitre (LEL) model.

2.4.2 Nonlocal damage mechanics

FEM simulations of strain-softening materials often converge to physically unreasonable solutions as the inelastic strain localizes in a narrow band of vanishing thickness with increasing mesh refinement. Therefore, this section reviews how integral-based nonlocal theories successfully address the challenges encountered in predicting the failure behaviour of quasi-brittle and ductile materials.

These approaches introduce spatial terms into constitutive relations, using a length parameter that corresponds to the material's characteristic length or length scale. This length parameter, l_c, governs the spatial interaction between material points in non-local continuum models. It is essential for distributing fracture energy over a finite region, thus addressing the mesh sensitivity problem commonly encountered in conventional local models. The parameter l_c is related to the theoretical width w_t of the fracture process zone [94]. Nguyen and Houlsby [95] observed that the relationship between l_c and w_t is nonlinear and influenced by several parameters within the non-local model, and thus introduced a procedure for establishing the relationship between the length parameter (or the non-local radius R) and the crack band width w_t. In brittle fracture, the length-scale parameter l_c is calibrated by using the relation with the maximum stress obtained from a homogenous solution of a bar in uniaxial traction tests [96,97]. However, the calibrated l_c may have a fairly large value relative to the specimen size, and thus an overly diffusive damage/crack can be obtained from the numerical simulation [98]. For this reason, Wu and Nguyen [99]developed a novel length-scale insensitive model to simulate brittle fracture. They defined a complicated degradation function that encompasses the commonly used quadratic degradation as a special case.

2.4.2.1 Damage in brittle or quasi-brittle materials

In Jirásek's work [100], variables associated with material degradation until complete failure were individually regularized. Notably, formulations regarding nonlocal damage energy release rate and nonlocal strain share similarities, as the damage energy release rate can be interpreted as the square of a generalized strain norm. It suggests that, while both methods yield similar results, there are differences in computational efficiency and versatility. The average of the damage energy release rate is computationally less expensive as it involves a scalar quantity. On the other hand, the approach using nonlocal strain formulation is considered more versatile, as it can be extended to various constitutive laws. Alternatively, the nonlocal formulation of the inelastic and damage variables, γ and D requires an even larger amount of computational work than averaging of the strain. However, the work has not paid too much attention to the thermodynamic aspects of nonlocal models or to the physical interpretation of the averaging.

Continuing from there, Comi and Perego [101] revised the nonlocal model, building upon the methodology proposed earlier in [59], by adopting the elastic energy release rate as the nonlocal variable. The explicit expression of the consistent tangent matrix is derived, ensuring symmetry under the assumption of associative evolutions for both the damage and the internal variables. This restricts the usage of different dissipation potential functions to predict the structural response with less computational time. Jirásek [102] introduced a nonlocal damage formulation in which damage evolves based on the symmetric gradient of the nonlocal displacement field, serving as a localization limiter. However, the weight function needs to be designed to ensure that the averaging operator conserves not only a constant field but also a linear field. The load-displacement responses predicted by the nonlocal displacement approach are compared with those obtained from a damage model based on nonlocal strains, revealing a similar trend between the two. The nonlocal strain model often results in stress oscillations within particular regions of the process zone. The oscillations are caused by the unbalanced quality of the approximation of the local and nonlocal strain. However, employing nonlocal displacements helps alleviate this issue.

Nguyen [103] by regularizing the damage variable proposed a consistent thermo-mechanical approach for the formulation of nonlocal constitutive models. In particular, the study presented an explicit connection between the dissipation potential and the damage function, along with a method to incorporate a nonlocal damage function with desired characteristics into the proposed nonlocal approach. Thus, developing a nonlocal model based on this approach simply involves two energy potentials and adhering to a set of pre-established procedures consistently. This simplification in formulation helps prevent potential violations of the laws of thermodynamics that may arise when developing complex nonlocal constitutive models.

Giry et al. [104] proposed the stress-based nonlocal damage model, where each point influences its surrounding region based on the magnitude and direction of its principal stresses, and the model also tailors the regularization near free boundaries. In this context, He et al. [105] regularized the equivalent strain and adopted the spatial wight function of Borino et al.'s [106] to mitigate boundary effects. However, it requires finer mesh sizes in regions with strain localization, limiting large-scale applicability.

Furthermore, Onate [107] presented a robust nonlocal isotropic damage model for quasi-brittle materials that works in a small deformation regime, along with an adaptive mesh finite element technique that permits adapting the spatial discretization in an optimal manner. It is known that nonlocal models lead to smooth solutions with a continuous variation of strain. However, to address narrow bands of highly localized strains in the finite element method, fine computational grids are required. The advantage lies in the need for a finer mesh primarily in the damage progression zone, while the rest of the structure can be adequately represented by a coarser mesh. Typically, the localization pattern is not predetermined, making it challenging to manually design refined meshes. To streamline this process, an adaptive mesh refinement technique can significantly improve analysis efficiency by automating the entire process.

Parallely, research on nonlocal damage in quasi-brittle materials was extended by including plasticity effects. Grassl and Jirásek [108] proposed a framework for nonlocal damage-plastic models, combining local plasticity with integral-type nonlocal damage. The evolution of damage is driven by plastic stress. In this work, two approaches are analysed that enforce a continuous strain profile of inelastic strain. (a) The plastic hardening modulus is larger than the critical plastic hardening modulus, and the local damage-driving variable is replaced by its nonlocal counterpart. (b) The local damage-driving variable is replaced by a linear combination of its local and nonlocal value, with a suitable value of the parameter m ($m > 1$). It is shown that the nonlocal damage-plastic model for concrete can provide a mesh-independent description of various combinations of tensile and compressive failure, even in situations where the traditional approach, relying on a local formulation with adjustments to the softening modulus based on fracture energy, falls short.

Substantial progress has been made in integrating nonlocality into both elastic damage [107,109–111] and plasticity coupled damage models [112,113] to better understand the intricate behaviour of quasi-brittle materials.

2.4.2.2 Damage in ductile materials

Andrade et al. [114] formulated and implemented a constitutive model of ductile damage enriched with a thermodynamically consistent nonlocal integral theory accounting for finite strains to describe ductile deformation. The thermodynamic framework entails regularization of the thermodynamic force conjugated with damage, leading to a dual averaging characteristic. The degradation of the material is captured by the Lemaitre damage evolution law. The use of the exponential map backward integration scheme, coupled with the logarithmic strain measure, facilitates the formulation of the constitutive problem in a format similar to small strain. This enables the attainment of a nonlocal solution through a modified Newton-Raphson strategy. The results obtained from the nonlocal damage model are compared with those from the classical approach, revealing that the nonlocal model exhibits a greater diffusive effect on damage evolution compared to the local model due to the additional averaging of the energy release rate.

Andrade et al. [115] addressed the question of which variable to regularize to achieve mesh-insensitive results under strain-softening regimes. Hence, various nonlocal models grounded in the constitutive theories of Lemaitre and Gurson have been developed. For the case of Lemaitre based models, four variables are opted for regularization: damage ($\bar{D}$), isotropic hardening variable ($\bar{r}$), damage energy release rate ($\bar{Y}$), and both $\bar{D}$ and $\bar{r}$ simultaneously. The summarized results of their work for Lemaitre model are shown in Table 2.1.

The η_0 and ξ_{avg} are mean values of stress triaxiality ratio and the normalized third invariant. Moreover, the assessment results indicate that the varying third invariant of the deviatoric stress, rather than the triaxiality, may have a more significant impact on addressing pathological mesh dependency. Review of the findings suggests that, in both Lemaitre- and Gurson-based models, the damage variable stands out as the most suitable option for the nonlocal variable. It appears that this is an inherent trait of implicit damage models. However, for explicit damage models commonly employed in quasi-brittle material modelling, the conclusion is markedly different. According to Jirásek and Rolshoven [116], the damage variable is deemed unsuitable as a nonlocal variable for such explicit damage models and is advised against.

Table 2.1 Summary of results [115]

Analysis	$\boldsymbol{\eta_0}$	$\boldsymbol{\xi_{avg}}$	$\boldsymbol{\bar{D}}$	$\boldsymbol{\bar{r}}$	$\boldsymbol{\bar{Y}}$	$\boldsymbol{\bar{D}\bar{r}}$
Notched	0.8	1.0	++	- -	++	++
Plane strain	0.7	0.0	++	- -	-	+
Perforated plate	1/3	-	++	- -	-	++
Shear	0.0	0.0	++	- -	+	++

(++ Full regularization, - Poor/little regularization, + Partial but acceptable regularization, - - No regularization)

Nguyen et al. [117] devised a thermodynamics-based nonlocal constitutive model aimed at encompassing both pre-peak hardening and post-peak softening behaviours, along with the material's stiffness reduction throughout deformation and fracture phases. The authors attempted to improve the proposed coupled damage-plasticity model by regularizing the equivalent plastic strain and addressing challenges related to softening in constitutive modelling and failure analysis. Considering the work as the preliminary step towards nonlocal ductile damage modelling, they choose a simple linear energy-based damage dissipation potential function and neglect the effects of triaxiality. The study demonstrates the accurate calibration of model parameters using both the proposed procedure and experimental data, indicating that the model is well suited for real-world applications.

Indeed, besides regularizing constitutive variables, there are other studies conducted within the nonlocal regime aimed at accurately predicting ductile damage. Shutov and Klyuchantsev [118] explored stress-based and strain-based modifications of the delocalization kernels to improve the analysis of mixed-mode damage and fracture. They used a fully coupled model of ductile damage for their investigation. These modified kernels offer enhanced control over the shape of the $K_I - K_{II}$ diagrams. Unlike conventional Bažant kernels, modified kernels incorporate an additional fitting parameter (h_{stress} or h_{strain}), enabling a more precise description of mixed-mode damage and fracture. Furthermore, numerous recent studies have effectively utilized nonlocal damage models to analyze the failure behaviour of ductile materials under various loading conditions [119–122].

2.4.3 Adhesive-bonded joints

The increasing complexity of the manufacturing of single-piece components highlights the urgent need to develop effective joining techniques. In recent years, there has been a growing interest in the use of adhesive joints due to their numerous advantages over traditional bonding techniques, such as lighter structures and reduced stress concentrations [123]. Consequently, there has been extensive research on predicting the strength of adhesive joints. When assessing the failure of adhesive joints using numerical methods, various approaches are available, including continuum mechanics, fracture mechanics, damage mechanics (CDM), cohesive zone modelling (CZM), extended finite element method (XFEM), and meshfree methods. This section provides a concise overview of two widely used approaches, namely cohesive zone modelling (CZM) and continuum damage models (CDM), for predicting the strength of adhesive joints.

2.4.3.1 Cohesive zone modelling

This approach is commonly implemented using the FEM, where special cohesive elements are utilized. These cohesive elements feature paired nodes that adhere to established cohesive laws. These cohesive elements incorporate fracture criteria that dictate crack propagation and stress criteria that govern the onset of damage. CZM offers the advantage of mesh-independent strength prediction, as validated by several studies on mesh dependency [124,125]. This results from the definition of damage growth being based on an energetic criterion averaged over an area, rather than relying on values from individual points.

There are two primary approaches to cohesive zone modelling (CZM): the local approach and the continuum approach. In the local approach, cohesive elements connect superimposed nodes of elements, effectively representing a zero-thickness interface. On the other hand, the continuum approach utilizes cohesive elements to simulate the entire adhesive bond, which has a finite thickness, connecting the two adherends. O'Mahoney et al. [126] conducted a Taguchi analysis on single-lap joint (SLJ) using the local approach, which employs zero-thickness cohesive elements at the adherend/adhesive interface and continuum damage elements within the adhesive. Through their analysis, they concluded that adhesive strength, interface fracture toughness, and adhesive ductility are the most influential factors affecting the strength of SLJ. Sugiman et al. [127] examined the impact of employing zero-thickness cohesive elements either in the middle of the adhesive layer or at the adhesive/adherend interface, while the remaining adhesive elements were modelled as continuum elements. They observed that cohesive elements positioned in the middle provided slightly more accurate results for SLJ compared to those positioned at the adhesive/adherend interface. Geleta et al. [128] adopted a unique approach distinct from both local and continuum approaches. They discretized the adhesive layer using continuum elements and then inserted cohesive elements between each of these elements. An advantage of this approach, compared to conventional CZM methods, is its lack of restriction on the crack path, allowing more flexibility in modelling crack propagation.

The cohesive law can assume various shapes, such as triangular, linear-parabolic, polynomial, exponential, and trapezoidal [129]. Among these, the triangular shape is the simplest and most commonly employed [130]. The detailed explanation of cohesive formulations and traction-separation laws will be discussed in Chapter 3. Fernandes and Campilho [131] investigated DCB samples to determine how the shape and parameters of the cohesive law influence the prediction of the strength of joints under pure mode I traction. They observed that triangular and trapezoidal law shapes yield similar and accurate strength predictions for both brittle and ductile adhesives. In a similar investigation focused on mode II loading, Fernandes and Campilho [132] explored ENF samples. They observed that the triangular law performed better for brittle adhesives, whereas its accuracy decreased with increasing adhesive ductility, where the trapezoidal law proved to be more accurate. Campilho et al. [133] compared the predictive accuracy of different cohesive law shapes by varying overlap length (L_o) of single-lap joints (SLJ). They observed that triangular laws are more appropriate for brittle adhesives, while trapezoidal laws yielded better results for ductile adhesives. However, the variance in strength prediction between triangular and trapezoidal laws for ductile adhesives was less than 10%. Therefore, for simplicity, the triangular law may be favoured in such scenarios. For $L_o \leq 50$ mm, the choice of cohesive law shape will have minimal influence on the results. Thus, selecting any shape will not significantly affect the results in these scenarios [134].

Other authors focused on the influence of CZM parameters on strength predictions. Teixeira et al. [135] investigated the effect of CZM parameters on strength predictions, finding that variations in t_n^0 had a minor influence under pure mode I loading with DCB specimens. Conversely, reducing t_n^0 resulted in a notable decrease in strength. A higher or lower G_{Ic} led to more significant strength increases or decreases, respectively, highlighting the importance of selecting the appropriate G_{Ic} value in CZM. Azevedo et al. [136] demonstrated that in pure mode II loading, specifically in the ENF test, a substantially lower t_s^0 had the most significant impact on joint strength, resulting in a reduction regardless of adhesive ductility. Changing G_{IIc} had an effect on the joint strength, but it did not alter the stiffness of the load-displacement curve, unlike changes in t_s^0. Campilho et al. [137] investigated the impact of CZM parameters on SLJ using a triangular cohesive law shape. He found that lower values of G_c in numerical models for single-lap joints led to significant decreases in joint strength, while higher G_c values resulted in minor increases in strength. Higher values of t_n^0 had minimal impact on joint strength, while lower values led to a moderate decrease. Additionally, smaller or larger values of t_s^0 resulted in significant decreases or increases in strength, respectively.

2.4.3.2 Continuum damage mechanics approach

The damage mechanics approach enables the simulation of gradual material degradation in the adhesive, in which the stiffness diminishes progressively until failure, resulting in a complete loss of stiffness. This approach allows for the determination of crack paths without being restricted by predefined paths set by cohesive elements, as is the case in CZM.

de Moura and Chousal [138] conducted a numerical analysis focussing on fracture characterization in adhesive joints. They utilized a triangular traction-separation law to simulate fracture propagation in DCB and ENF tests, employing a pure mode damage criterion. To convert the strains obtained from the FE analysis to relative displacements in the continuum model, they introduced a characteristic length l_c. One advantage of CDM over CZM is its capability to predict non-negligible stress components in the fracture process zone (FPZ) during asymmetrical propagation. Hua et al. [139] developed a continuum damage modelling method to simulate the cohesive failure of single lap joints bonded with EA9321 adhesive, subjected to various environmental conditions. Unlike traditional models that rely on strain-based failure criteria, this method employs a damage parameter based on equivalent plastic displacement, offering mesh independence. This parameter not only indicates the failure path, but also quantifies the extent of damage within elements. As a result, the model allows for a more gradual accumulation of damage, leading to a more realistic representation of the joint behaviour.

García et al. [140] used a continuum damage model to investigate the initiation and propagation of cracks in a joint typically employed in wind turbines. The joint was bonded using a tough and ductile adhesive. Their model employed the Drucker-Prager exponential criterion to characterize the elasto-plastic behaviour of the adhesive, with softening described in a linear manner. They accurately determined both the crack path and the joint strength, as validated against experimental tests. Chousal and de Moura [141] introduced a mixed mode damage model employing continuum elements with a triangular traction separation law. They utilized a quadratic stress and fracture energy criterions to derive the mode I/II stress components leading to damage onset and relative mixed-mode displacements. Validating their model with DCB and ENF specimens, they successfully predicted crack paths and the fracture process zone. Stapleton et al. [142] proposed an enhanced FEM formulation featuring adaptive shape functions and mesh, based on their earlier work [143]. The shape functions of this method are obtained through analytical solutions of the governing equations, resulting in a computational approach that demands fewer elements and offers faster processing compared to a CZM for similar problems. Joint failure is evaluated using a progressive damage model, reminiscent of the approach in CZM.

Sugiman and Ahmad [144] conducted a comparison between CZM and CDM featuring linear softening. While the CZM yielded slightly more precise strength predictions, it lacked the ability to determine the path of the crack, a capability accurately predicted by the CDM. This work also demonstrated the importance of maintaining an aspect ratio of 1 for adhesive elements. Riccio et al. [145] evaluated the effectiveness of a damage model featuring a linear softening phase in Scarf joints and joints subjected to three-point bending. Their model accurately identified crack paths and damage locations in both scenarios. Zhang et al. [146] applied linear softening CDM to predict the strength of the composite metal scarf joint. In their work, they investigated the impact of employing different metals and composite stacking sequences on joint strength. Kim and Hong [147] proposed a mixed-mode damage model that accounts for both the hardening and softening behaviours of various adhesives. They utilized an exponential hardening section to capture the ductility of the adhesives effectively and complemented it with an exponential softening section, with a distinct formula, ensuring a comprehensive representation of material behaviour. They employed the Benzeggagh-Kenane criterion to assess damage propagation, while a second-order criterion was used to determine damage initiation. The effectiveness of the model is evaluated in single-lap joints with varying adhesive thickness (t_A) and adherend thickness (t_p), both with and without adhesive fillets. The study demonstrated that joint strength increased with the inclusion of fillets and t_p. In the absence of fillets, the joint strength decreased with t_a, but in their presence, t_a contributed to an increase in joint strength.

2.4.3.3 Bi-adhesives and adhesive/cohesive failure problems

Employing bi-adhesive joints reduces shear and peel stress concentrations at the ends of the overlap, while elevating stress levels in the middle of the joint, particularly when a brittle adhesive is utilized [148–150]. This implies a more uniform distribution of loads along the bondline. The decrease in stress concentration in these critical areas, which are prone to causing adhesive joint failure, leads to an overall increase in joint strength, thus delaying failure [151]. Moreover, in bi-adhesive joints, stress concentrations are present not only at the bonding ends (primary peak) but also in the gap regions (secondary peak) where the adherends remain unbonded. These stress concentrations at the boundaries of the two adhesives arise from differences in mechanical properties or from the presence of a gap between ductile and brittle adhesives [150].

Jairaja and Naik [152] investigated the impact of using bi-adhesive joints on failure modes, using AV138 and Araldite 2015 as brittle and ductile adhesives, respectively. They found that single-adhesive joints typically experience adhesive failure, while the bi-adhesive joints show cohesive failure. Length ratio $\left(d = \frac{\text{length of the ductile adhesive}}{\text{length of the brittle adhesive}}\right)$, elasticity ratio $\left(E = \frac{\text{elasticity modulus of the ductile adhesive}}{\text{elasticity modulus of the brittle adhesive}}\right)$ are one of the most important variables that influence the strength of the joints. Research works [148,149,153,154] indicate that as the d ratio increases, there is a corresponding increase in maximum stress at the joint ends, while shear stress at the adhesive boundaries decreases. Therefore, the distribution of stress becomes more uniform, with lower stress at the overlap ends and higher stress in the centre, improving the strength of the joint. On the other hand, a decrease in adhesive stiffness correlates with a reduced stress concentration at the joint ends, often resulting in increased joint strength [153].

Regarding cohesive and adhesive failures, Belnoue and Hallett [155] proposed a new methodology for the finite element (FE) modelling of failure in adhesively bonded joint. The deformation of the adhesive, representing cohesive failure, is simulated using a smeared-crack approach. This method enables crack propagation without requiring prior knowledge of the crack path and is well suited for modelling situations involving both plasticity and damage [156]. Many studies have highlighted the significant influence of adhesive plasticity and its response to hydrostatic pressure on the failure mechanisms observed in the structural adhesive used in their work [157–159]. On the basis of these observations, authors have chosen smeared crack models to address adhesive plasticity, incorporating a pressure-dependent yield criterion. In contrast, adhesive failure is represented by incorporating a layer of cohesive elements at the interface between the adhesive and the adherends.

2.5 Strain softening in EFG framework

2.5.1 Cohesive zone modelling

Belytschko et al. [160] explored the feasibility of CZM within the EFG framework for simulating dynamic crack growth in concrete. It builds on recognizing the limitations of LEFM for concrete due to the FPZ (a zone of microcracks and weakened material). The conclusive results suggest that the CZM-EFG approach is a reliable tool for simulating dynamic crack growth in concrete. However, authors suggest for further research and development are necessary to explore alternative material models or utilizing adaptivity within the EFG framework to improve computational efficiency. Rabczuk and Belytschko [161] introduced a novel approach for modelling cohesive cracks within the EFG framework. This method treats the crack as a collection of discrete particles, eliminating the need for pre-defined crack topology. The computed crack speed adheres to the established physical limit of the Rayleigh wave speed. Furthermore, the method qualitatively captures the intricate branching patterns observed in pre-notched specimens under sudden loading. However, the dependence of the method on specific quadrature schemes and their convergence behaviour in the presence of cracks need further investigation.

Rabczuk and Zi [22] broadened the eXtended EFG (XEFG) method proposed by Ventura et al., [162] to model cohesive and dynamic cracks. The XEFG method, which uses branch functions as enrichments at crack-tip nodes, was found to be much more effective than the cracking particle method. Rabczuk et al. [163] introduced a three-dimensional reinforced concrete model with geometrical and material nonlinearity, wherein cracking is simulated using the extended element-free Galerkin (XEFG) method, explicitly introducing the crack. Nodes whose domain of influence was cut by the crack were enriched with the step function or a near top function. After the crack initiation, a cohesive model ensured proper energy dissipation as the crack propagated. Additionally, both the prestressing tendons and conventional reinforcement were simulated using finite elements, employing standard J_2 plasticity with isotropic hardening.

Chong [164] demonstrates the use of the EFG method to analyze cohesive crack growth in 2D domains. The cohesive curved crack is simulated by connecting straight-line interface elements to form the crack. As a result, the crack is represented by a piecewise linear line. The relative displacement increments between the two opposing surfaces of the interface elements represent the crack displacement increments. These increments are expressed in terms of the nodal displacement increments through EFG shape functions, which adhere to the visibility criterion. The visibility criterion is essential for constructing the shape functions near a crack. It involves treating domain boundaries and crack lines as opaque objects during the construction of weight functions. The methodology avoids the need for iterative processes by directly integrating a term related to energy dissipation along the interface elements into the stiffness equation of the domain within the weak form of the global system equation. The constitutive law of cohesive cracks is then considered through this energy term.

Ghosh and Chaudhuri [165] presented a multi-scale approach for fracture in concrete materials. The XEFG method, a modelling technique, has been applied to simulate concrete behaviour at both macroscopic and mesoscopic levels. In this work, the material behaviour of the cement paste is described using a nonlinear isotropic damage model to account for its response under tensile loading. Additionally, a cohesive crack model is introduced to accurately capture complex mixed-mode fracture phenomena. The interface behaviour between the cement and aggregates is further modelled using a phenomenological approach. Goudarzi and Mohammadi [166] utilized the element-free Galerkin (EFG) approach, for modelling cohesive crack propagation through extrinsically enrichment strategy based on the partition of unity property of MLS shape functions. The study focuses on fully saturated porous media subjected to external mechanical loads within the small deformation regime. Fractures are treated as cohesive cracks with significant permeability, enabling the flow of water inside. The governing equations for a fully coupled saturated state are discretized using enriched moving least squares (MLS) shape functions. Various coupled and uncoupled fracturing problems, including mode I and mixed-mode scenarios in porous materials, are investigated. Significant advancements have been achieved in modelling cohesive crack growth within the EFG framework, building upon the approaches mentioned earlier [167–170].

2.5.2 Continuum damage mechanics

In his work, Milan Jirásek [171] explores the suitability of the element-free Galerkin (EFG) method for problems involving strain localization. He discusses why the EFG method struggles with standard local continuum problems, even when adjustments are made to ensure correct energy dissipation. Jirásek analyzes the source of stress oscillations leading to multiple softening bands using a simple uniaxial example. He demonstrates that these oscillations are significantly reduced when the model is reformulated as nonlocal (Integral approach), provided that the radius of influence in the EFG formulation is appropriately scaled compared to the internal length of the nonlocal continuum. Additionally, highlights that for problems involving regularized localization, the accuracy of the EFG solution can surpass that of the finite element method.

Askes et al. [16] employed the EFG method to discretize structures governed by gradient based nonlocal damage models. Many research works [172,173] have highlighted that incorporating fourth- and higher-order derivatives significantly alters the solution. However, incorporating fourth-order derivatives poses computational challenges, particularly when using the FEM, as it requires either C^1 shape functions or mixed finite elements, which can increase the computational burden. On the contrary, ensuring higher-order continuity of the EFG shape functions is comparatively straightforward, rendering the method suitable for capturing higher-order strain fields present in gradient damage models. Certainly, the EFG method facilitates a straightforward comparison of various gradient based damage formulations. Further, they observed that both the second-order implicit model and the fourth-order implicit model capture the characteristics of the integral based nonlocal damage model adequately, suggesting that the inclusion of fourth-order terms does not significantly affect the response.

The study conducted by Rabczuk and Eibl [174] focused on analyzing prestressed concrete beams subjected to quasistatic loading through the coupled FE-EFG approach for their analysis. In their model, concrete was represented using particles, while reinforcement was represented using beam elements. The steel reinforcement was modelled using an elastoplastic constitutive law with isotropic hardening and a tension cutoff. Additionally, a continuum damage model was employed to simulate the behaviour of concrete in tension, incorporating an anisotropic tensile damage variable for this purpose. Yang and Misra [175,176] introduced a higher-order theory that incorporates strain gradients and their conjugate higher-order stresses. The higher-order gradient models are discretized using the EFG method, combined with a penalty method for enforcing essential boundary conditions.

Pan and Yuan [15,177] introduced a modified gradient-based nonlocal damage model derived from the well-known Gurson-Tvergaard-Needleman (GTN) model within the framework of the EFG method. The EFG algorithm computes nodal equivalent plastic strain. It involves interpolating strain values at integration points and using MLS (Moving Least Squares) shape functions to compute high-order spatial derivatives directly from the interpolated nodal plastic strain. This approach avoids the need for additional plastic strain boundary conditions. The proposed algorithm allows for the analysis of shear band localization, and the results indicate that the dependence of damage localization on mesh resolution is eliminated by employing the gradient regulator. Luca et al. [178] devised a non-standard variational approach to simultaneously derive the second-gradient equilibrium equations and the Karush–Kuhn–Tucker conditions for the 2D scenario in EFG framework. It is observed that the damage begins at the boundary due to specific boundary conditions. These boundary effects can impact the interpretation of experimental measurements, potentially influencing results by interacting with material defects or affecting the control of boundary conditions. The developed variational approach enables the recovery of not just the pertinent governing equations and the relationship governing damage evolution, but also ensures the determination of clear and unambiguous boundary conditions.

The study confirms that the nonlocal damage model, coupled with the element-free Galerkin method, is effective in simulating damage phenomena and predicting size effects.

2.6 Summary

The literature extensively covers strain-softening phenomena using CZM and CDM approaches within both FEM and EFG frameworks. Additionally, there is widespread discussion on the application of nonlocal integral approaches for addressing strain localization problems across various materials. In the realm of adhesive bonded joints, a wide range of studies have focused on failure analysis utilizing CZM and CDM approaches, showcasing a diverse range of works in this area.

Certain aspects of adhesive bonded joints remain relatively underexplored in the literature, particularly regarding failure analysis involving adhesive and cohesive crack problems, where conventional FEM often yields highly mesh-sensitive results. Additionally, in the quest to mitigate stress concentrations in single-lap joints, the adoption of biadhesives has emerged as a popular approach. However, there is limited research on failure analysis conducted on these joints, and numerical analysis using FEM often encounter abrupt discontinuities in stress distributions, leading to simulation abortion, further highlighting the need for more comprehensive investigations in this area. Hence, nonlocal integral approaches have been employed in conjunction with CDM theories to address the aforementioned challenges.

Nevertheless, while the nonlocal strain approach achieves mesh-independent results, it often lacks accuracy. Consequently, there has been limited research aimed at improving the performance of the nonlocal strain approach. To address this gap, the strain difference-based nonlocal constitutive law proposed by Polizzotto et al. [18] is employed in conjunction with Continuum Damage Mechanics (CDM) theories. This combined approach is utilized to predict the structural response of quasi-brittle materials, aiming to enhance accuracy and reliability in capturing the complex behaviour of such materials under loading conditions.

In ductile materials, plastic strain significantly influences damage evolution. However, while many research works treat damage as the nonlocal variable, the consideration of equivalent plastic strain remains relatively unexplored. On the other hand, the models introduced by Bonora [19] and Thakkar and Pandey [179] exhibit versatility in predicting damage across diverse ductile materials. However, this approach can impose limitations when plasticity-related internal variables, including isotropic and kinematic hardening, are present. In such cases, it becomes crucial to differentiate the contributions of hardening to the plastic strain, highlighting a potential constraint in the application of these models. Therefore, a novel ductile damage dissipation potential is proposed, which integrates the effects of isotropic hardening and scalar damage.

EFG methods with higher-order shape functions possess mathematical nonlocality but may not adequately capture mechanical nonlocality, especially when solving problems related to strong and weak discontinuities. It is widely acknowledged that cohesive crack concepts are effective in solving strong discontinuities, such as crack propagation problems. Many research works have employed these concepts within the EFG framework, enriched with the methodology of XFEM, referred to as XEFG. However, methods like eXtended EFG (XEFG) and extrinsically enriched EFG methods will not be helpful in the absence of analytical solutions from which the branch enrichment functions are inspired. Therefore, there remains a research gap in simulating crack propagation within the EFG framework without relying on these functions.

On the other hand, when addressing weak discontinuities such as holes, notches, and sudden changes in area, gradient theories are commonly employed within the EFG framework. However, to the best of the authors' knowledge, there has been relatively little exploration of integral-based nonlocal theories in the EFG method. Moreover, due to their simplicity, ease of implementation, and reduced mathematical complexity, these methods can be effectively extended to address large deformations, such as those encountered in hyperelasticity. Indeed, the EFG shape functions' ability to readily satisfy higher-order continuity requirements enables the method to effectively alleviate phenomena such as locking [16]. Therefore, before addressing strain localization in large deformation (hyperelastic) problems, the authors identified a research gap concerning the effective handling of volumetric locking issue in nearly incompressible hyperelastic materials within the EFG framework.

Chapter 3

Mathematical Formulations and Methodology

This chapter explores the physical significance of the damage phenomenon and its modelling approaches, which address damage at both meso and macroscopic levels while adhering to specific principles. Further, it explores nonlocal integral approaches, focusing on challenges encountered by classical continuum theories. Fundamentals of both local and nonlocal continuum theories are discussed, covering dissipation inequalities and step-wise procedures for deriving constitutive equations. Additionally, it covers the core concepts of hyperelasticity and its mathematical terminology, providing a detailed description of its finite element implementation procedure. Finally, the chapter provides an overview of the EFG method, encompassing key parameters influencing the method, shape functions and their properties, as well as techniques for imposing boundary conditions.

3.1 Damage phenomenon and its modelling approaches

In the context of Fig. 3.1, depicting body B under the influence of an external loading displacement causing the development of a crack of length a_c, the examination of an arbitrary point $P(\mathbf{x})$ near the crack tip reveals the presence of numerous microscopic cavities or microcracks within the surrounding region. These cavities typically nucleate from the breakage of atomic bonds or defects in the atomic arrangement.

The fracture of materials is a complex process involving multiple scales of observation. At the microscopic level, it entails the nucleation of microcavities or microcracks due to the rupture of atomic bonds. On a macroscopic scale, it manifests as the propagation of cracks resulting from the coalescence of these microstructural defects. However, an intermediate mesoscopic process exists, where the interplay of nucleation, growth, and coalescence of microcavities drives the initiation and progression of macroscopic cracks.

The formation of cavities across microscopic, mesoscopic, and macroscopic stages of material fracture, along with consequent degradation in mechanical properties, collectively constitutes damage [6,180,181].

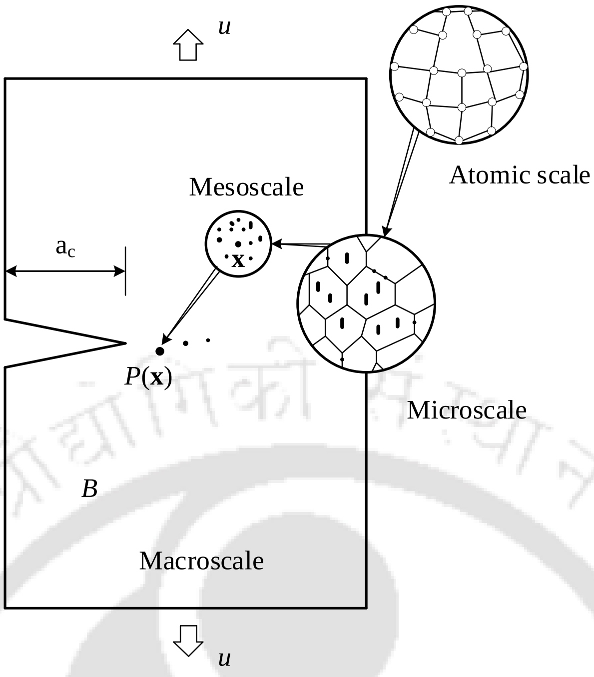

Fig. 3.1. Notion of representative volume element and continuum damage mechanics

3.1.1 Continuum damage mechanics (CDM)

The mechanics concerning the discussion of material damage and its mechanical consequences within the framework of continuum mechanics is known as continuum damage mechanics (CDM) [182–184]. Hence, the problem of damage and fracture induced by the formation of distributed cavities can be analyzed within the framework of continuum mechanics through the following procedures [60]:

(a) Characterising the damage state through a damage variable denoted as $\boldsymbol{D}(\mathbf{x})$.

(b) Establishing an equation governing the evolution of the damage variable, termed as the evolution equation.

(c) Developing an equation delineating the mechanical response of the damaged material, known as the constitutive equation.

(d) Resolving the initial and boundary value problems utilizing these equations.

3.1.1.1 *Effective stress concept*

This section examines the damage mechanism in a cylindrical bar when subjected to tensile loading, as illustrated in Fig. 3.2. Consider a scenario where the bar depicted in Fig. 3.2(a), featuring a cross-sectional area of $\mathrm{d}A$, experiences a tensile load denoted as $\mathrm{d}F$, while being in a state of damage characterised by D. In this context, the effective load-carrying cross-sectional area is represented by $\mathrm{d}\tilde{A}$, which differs from the apparent area $\mathrm{d}A$. Hence, the effective area $\mathrm{d}\tilde{A}$ is given by [182],

$$\mathrm{d}\tilde{A} = (1 - D)\mathrm{d}A \tag{3.1}$$

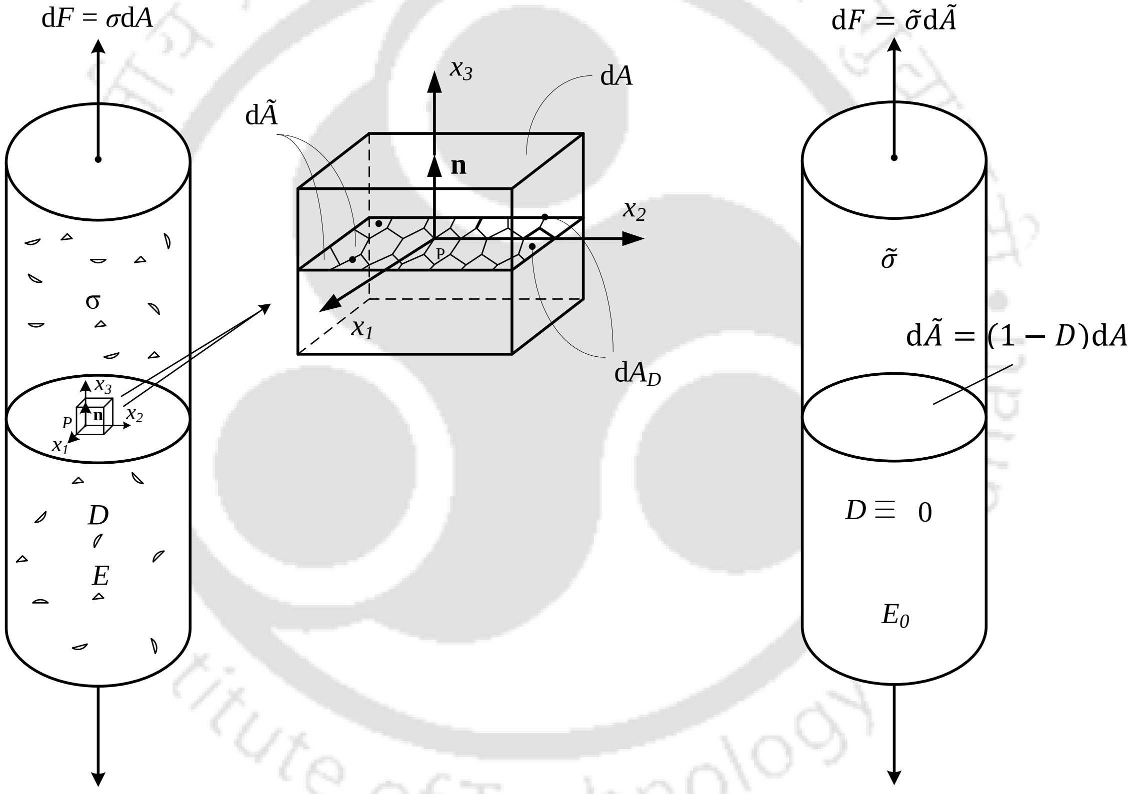

(a) **(b)**

Fig. 3.2. Deformation and damage of a bar under tensile load

The reduction in the load-carrying area amplifies the effect of the stress σ induced by the external force $\mathrm{d}F$. According to Eq. (3.1), the effective stress, denoted as $\tilde{\sigma}$, is determined by:

$$\tilde{\sigma} = \frac{\mathrm{d}F}{\mathrm{d}\tilde{A}} = \frac{\sigma}{1 - D} \tag{3.2}$$

The concept of effective stress, as delineated in Eq. (3.2), is designed to encapsulate not just the impact of diminished geometrical area owing to damage but also to account for stress concentration effects occurring at voids, as well as the interactions between voids. The actual phenomena of material damage, however, exhibit a complexity beyond the scope postulated in Kachanov's model, and as such, the model may possess limited validity [185,186].

3.1.1.2 Variation of elastic modulus

We now apply another concept of the effective stress to the bars shown in Fig. 3.2(a) and 3.2(b). Let us assume that bar (a) and (b) is in a damaged and the fictitious undamaged state, respectively. In this context, the elastic strain ε experienced by bar (b) due to the stress $\tilde{\sigma}$ should be equal to that ε experienced by bar (a) under stress σ.

$$\tilde{\sigma} = E_0\varepsilon, \quad \sigma = E(D)\varepsilon \tag{3.3}$$

(or)

$$\varepsilon = \frac{\tilde{\sigma}}{E_0} = \frac{\sigma}{E(D)} \tag{3.4}$$

here, E_0 and $E(D)$ represent Young's modulus of the material in the initial undamaged state and in the damaged state after loading, respectively. Eq. (3.4) thus defines another form of effective stress.

$$\tilde{\sigma} = \frac{E_0}{E(D)}\sigma \tag{3.5}$$

By combining Eqs. (3.2) and (3.5), we have

$$\begin{gathered} E(D) = (1 - \mathrm{D})\mathrm{E}_0 \\ D = 1 - \frac{E(D)}{E_0} \end{gathered} \tag{3.6}$$

3.1.1.3 Principle of strain equivalence

The statement asserts that the strain constitutive equations of a damaged material are formulated using the same framework as for an undamaged material, with the exception that the stress is substituted by the effective stress [187].

Chaboche and Lemaitre extended this concept to encompass the broader scope of inelastic deformation by introducing constitutive equations for both damaged and undamaged materials, defined as [180,188]:

$$\boldsymbol{\varepsilon} = F_0(\tilde{\boldsymbol{\sigma}}, \boldsymbol{\alpha}) = F(\boldsymbol{\sigma}, \boldsymbol{D}, \boldsymbol{\alpha}) \tag{3.7}$$

where $\boldsymbol{\alpha}$ is an internal variable representing the internal structural change other than the damage, and $\boldsymbol{D}$ is the damage tensor.

3.1.1.4 Thermodynamic aspects of damaged material

When the thermodynamic state, and consequently the state variables, of a system remain constant over time, the system is deemed to be in thermodynamic equilibrium. Conversely, if the state of a system undergoes alteration due to external agencies, this alteration in the state is termed a thermodynamic process. The state variables that autonomously drive changes in the system state are designated as independent variables. Conversely, variables determined by single-valued functions of these independent variables are termed dependent variables. It should be noted that the selection of independent variables is not unique.

In general, the thermodynamic state of a material is typically non-uniform and resides in a non-equilibrium condition, resulting in irreversible processes. Classical thermodynamics, formulated under the assumption of uniform and equilibrium states, fails to adequately describe such non-equilibrium phenomena. To address this challenge, the principle of local state is introduced [189,190]

This hypothesis posits that a material element within a continuum, even when in a non-equilibrium state, exhibits an identical thermodynamic response to that of the same element in the corresponding equilibrium state. Therefore, this postulate remains valid under the condition that the response time of the material element to reach its equilibrium state is significantly shorter compared to the characteristic time of the kinematic and thermodynamic evolution of the continuum.

The second law of thermodynamics asserts that the rate of entropy increase within a system is always greater than or equal to the rate of entropy increase resulting from heat sources and heat flux. Therefore, the irreversibility of entropy production is expressed by means of:

$$\rho\dot{s} + \operatorname{div}\left(\frac{\mathbf{q}}{T}\right) - \frac{r}{T} \geq 0 \tag{3.8}$$

here $\rho, s, T, r,$ and $\mathbf{q}$ represents mass density, entropy per unit mass, absolute temperature, rate of heat generation per unit volume and the outward heat flux vector on boundaries of the volume V.

By substituting $r = \rho\dot{e} - \boldsymbol{\sigma}:\dot{\boldsymbol{\varepsilon}} + \operatorname{div}(\mathbf{q})$ from the first law of thermodynamics, where e is the internal energy per unit mass, and using the Helmholtz free energy $\psi = e - Ts$, into Eq. (3.8) and performing mathematical derivations gives,

$$\boldsymbol{\sigma}:\dot{\boldsymbol{\varepsilon}} - \rho(\dot{\psi} - \dot{T}s) - \mathbf{q}.\frac{\operatorname{grad}(T)}{T} \geq 0 \tag{3.9}$$

Eq. (3.9) is known as the Claussius-Duhem inequality, and must be satisfied for every possible process [189,191].

<u>Constitutive equations</u>

Let's consider that at any given time *t*, the thermodynamic state at a point is defined by a set of state variables, denoted as follows:

$$\{\boldsymbol{\varepsilon}, \boldsymbol{V}_k, \mathbf{q}, T\} \tag{3.10}$$

The term $\boldsymbol{V}_k$ represents the set of internal variables that are scalar, vector, and tensor nature associated with dissipative mechanisms. Following that, the Helmholtz free energy defined as $\psi = \psi(\boldsymbol{\varepsilon}, \boldsymbol{V}_k, T)$, has it rate form as:

$$\dot{\psi} = \frac{\partial\psi}{\partial\boldsymbol{\varepsilon}}:\dot{\boldsymbol{\varepsilon}} + \frac{\partial\psi}{\partial\boldsymbol{V}_k}:\dot{\boldsymbol{V}}_k + \frac{\partial\psi}{\partial T}\dot{T} \tag{3.11}$$

Substituting the Eq. (3.11) in Eq. (3.9), we obtain:

$$\left(\boldsymbol{\sigma} - \rho\frac{\partial\psi}{\partial\boldsymbol{\varepsilon}}\right):\dot{\boldsymbol{\varepsilon}} - \rho\frac{\partial\psi}{\partial\boldsymbol{V}_k}:\dot{\boldsymbol{V}}_k - \rho\left(s + \frac{\partial\psi}{\partial T}\right)\dot{T} - \mathbf{q}.\frac{\operatorname{grad}(T)}{T} \geq 0 \tag{3.12}$$

Eq. (3.12) must hold true for any pair of functions $\{\dot{\boldsymbol{\varepsilon}}, \dot{T}\}$. This implies the well-known constitutive equations:

$$\boldsymbol{\sigma} = \rho\frac{\partial\psi}{\partial\boldsymbol{\varepsilon}}, \qquad s = -\frac{\partial\psi}{\partial T} \tag{3.13}$$

By defining new variables,

$$\boldsymbol{A}_k \equiv -\rho\frac{\partial\psi}{\partial\boldsymbol{V}_k}, \qquad \mathbf{g} \equiv -\mathrm{grad}(T) \tag{3.14}$$

and substituting them into Eq. (3.12), the Claussius-Duhem inequality reduces to

$$\phi = \boldsymbol{A}_k\!:\!\dot{\boldsymbol{V}}_k + \mathbf{q}.\frac{\mathbf{g}}{T} \geq 0 \tag{3.15}$$

here $\boldsymbol{A}_k$ is defined as the conjugate thermodynamic force for each internal variable $\boldsymbol{V}_k$**,** and $\mathbf{g}$ represents the temperature gradient.

Evolution equations

The Eq. (3.15) indicates that dissipation ϕ is determined by the products of the generalized flux vector and the generalized force vector. However, when considering the vector of rates of internal variables$\{\dot{\boldsymbol{V}}_k, \mathbf{g}\}$ and their associated variables $\{\boldsymbol{A}_k, \mathbf{q}\}$, there's no unique selection for which variables constitute the generalized flux vector and which constitute the generalized force vector. Conventionally, it's often simpler to interpret that the force drives the flux. Henceforth, we will designate the generalized force vector as $\{\boldsymbol{A}_k, \mathbf{q}\}$ and the associated generalized flux vector as $\{\dot{\boldsymbol{V}}_k, \mathbf{g}\}$.

In cases where the dissipation ϕ is expressible in the form delineated by Eq. (3.15), particularly, the evolution equations of $\{\dot{\boldsymbol{V}}_k, \mathbf{g}\}$ can be derived from a potential function defined as a function of $\{\boldsymbol{A}_k, \mathbf{q}\}$ [180,189,192]. Then postulating the existence of a scalar-valued dissipation potential function of the form:

$$F = F\left(\boldsymbol{A}_k, \mathbf{q}; \dot{\boldsymbol{V}}_k, \frac{\mathbf{g}}{T}\right) \tag{3.16}$$

The function F in Eq. (3.16) is assumed to be a non-negative convex function, and it satisfies $F = 0$ for $\{\boldsymbol{A}_k, \mathbf{q}\} = \{\mathbf{0}\}$. In other words, the constitutive equations governing the heat flux vector $\mathbf{q}$, and the evolution of the internal variable $\boldsymbol{V}_k$ are determined by the outward normal vectors to the potential surface $F = 0$ within the space of generalized force. This principle is formally known as a normality law. Therefore, the evolution equations of the flux variables are given by,

$$\dot{\boldsymbol{V}}_k = \dot{\lambda}\frac{\partial F}{\partial\boldsymbol{A}_k}; \qquad \mathbf{q} = \dot{\lambda}\frac{\partial F}{\partial\left(\frac{\mathbf{g}}{T}\right)} \tag{3.17}$$

here, $\dot{\lambda}$ in the above equation represents the indeterminate multiplier.

3.1.2 Cohesive zone modelling

The cohesive crack model, a simplified representation of the process zone, is often viewed as a specialized form of more general approaches. In the cohesive zone model proposed by Dugdale [193], it is postulated that a plastic zone exists near the crack tip. Within this zone, a stress equivalent to the yield strength σ_y is assumed to act across the crack. On the other hand, the Barenblatt model [194] resembles the Dugdale model but incorporates variations in stress with deformation. However, the Barenblatt model is not commonly employed in finite element analysis [195].

Hillerborg [195] proposed the cohesive crack concept, which shares similarities with the Barenblatt model. In this model, initiation of the crack propagation occurs when the stress at the crack tip reaches the tensile strength t_{max}. Unlike the assumption of an abrupt drop to zero stress, the stress is considered to decrease gradually with increasing crack width w, as illustrated in Fig. 2.3.

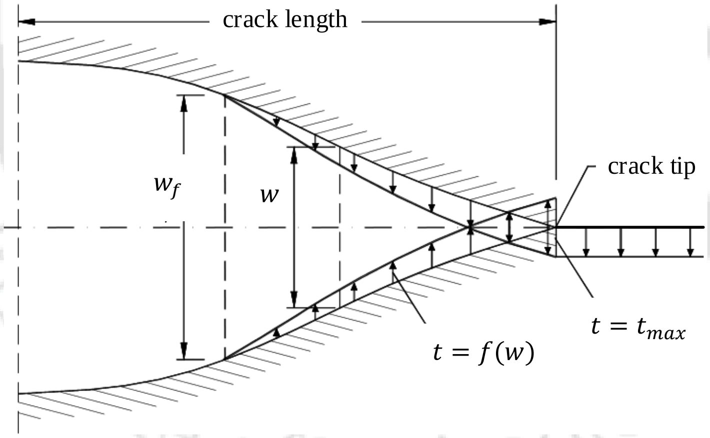

Fig. 3.3. Cohesive crack concept

At the crack width w_f, the stress reaches to zero. In regions where $w < w_f$, the "crack" actually corresponds to a microcracked zone with remaining ligaments responsible for stress transfer. Since there is a stress required to initiate crack opening, energy is absorbed. The energy absorbed per unit crack area in widening the crack from zero to w is:

$$G = \int_0^w t \mathrm{d}w \tag{3.18}$$

here, G also corresponds to the area under the cohesive traction (t)-separation (w) curve. When stress reaches zero at w_f, then the area under the curve is expressed as,

$$G_c = \int_0^{w_f} t\mathrm{d}w \qquad (3.19)$$

where G_c means the critical absorbed energy required for the crack to propagate. In implementing the cohesive crack concept, different shapes of $t - w$ curves are available, typically categorized as intrinsic and extrinsic traction-separation or cohesive laws, as shown in Fig. 3.4.

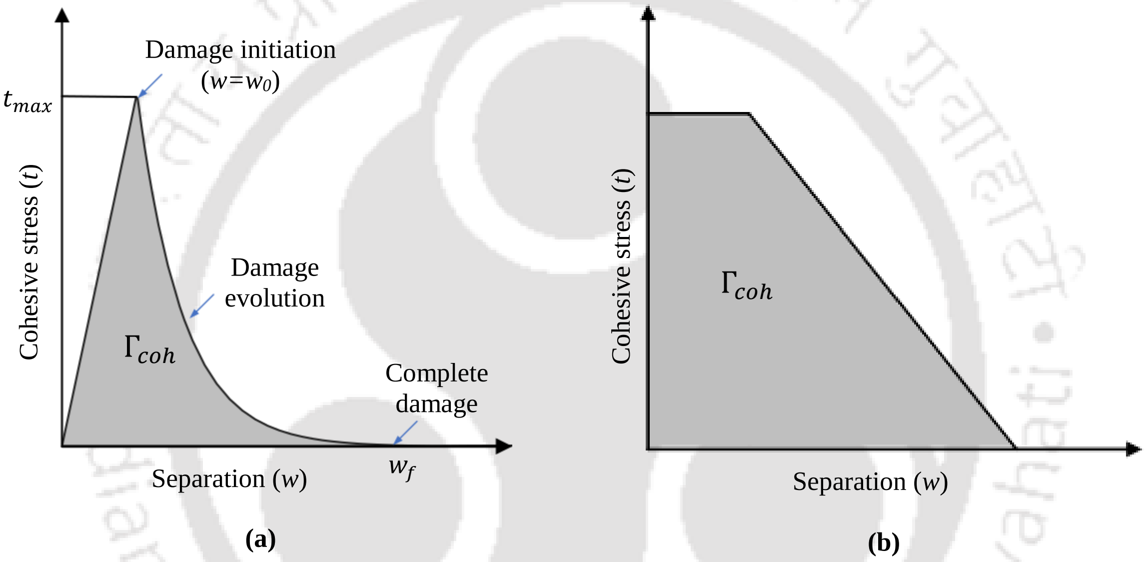

Fig. 3.4. (a) Intrinsic and **(b)** extrinsic traction-separation laws

Various shapes of cohesive zone model (CZM) laws have been proposed in the literature, tailored to simulate different material or interface behaviours. The triangular, exponential, and trapezoidal shapes, are among the most frequently employed for predicting the strength of typical materials. Thus, the constitutive law expressed in terms of cohesive stress and separation, or crack width w is given as,

$$t = K(1 - D)w \qquad (3.20)$$

where, D represents the damage variable, which is determined through the damage evolution equations specified by cohesive laws. Some of the commonly used damage evolution equations are [196]:

Triangular law: $$D = \frac{w_f}{w}\left(\frac{w - w_0}{w_f - w_0}\right) \tag{3.21}$$

Exponential law: $$D = 1 - \left\{\frac{w_0}{w}\right\}\left\{1 - \frac{1 - \exp\left(-\alpha\left(\frac{w - w_0}{w_f - w_0}\right)\right)}{1 - \exp(-\alpha)}\right\} \tag{3.22}$$

here, the separation at damage initiation and complete failure are represented by w_0 and w_f, α is a non-dimensional material parameter that defines the rate of damage evolution.

The aforementioned damage evolution equations are applicable only when the stresses or strains at a material point meet specific damage initiation criteria, signaling the onset of material degradation. Several damage initiation criteria are available such as:

Maximum stress criterion: $$\max\left\{\frac{\langle t_n \rangle}{t_n^{max}}, \frac{t_s}{t_s^{max}}, \frac{t_t}{t_t^{max}}\right\} = 1 \tag{3.23a}$$

Maximum strain criterion: $$\max\left\{\frac{\langle \varepsilon_n \rangle}{\varepsilon_n^{max}}, \frac{\varepsilon_s}{\varepsilon_s^{max}}, \frac{\varepsilon_t}{\varepsilon_t^{max}}\right\} = 1 \tag{3.23b}$$

Quadratic stress criterion: $$\left\{\frac{\langle t_n \rangle}{t_n^{max}}\right\}^2 + \left\{\frac{\langle t_s \rangle}{t_s^{max}}\right\}^2 + \left\{\frac{\langle t_t \rangle}{t_t^{max}}\right\}^2 = 1 \tag{3.23c}$$

Quadratic strain criterion: $$\left\{\frac{\langle \varepsilon_n \rangle}{\varepsilon_n^{max}}\right\}^2 + \left\{\frac{\langle \varepsilon_s \rangle}{\varepsilon_s^{max}}\right\}^2 + \left\{\frac{\langle \varepsilon_t \rangle}{\varepsilon_t^{max}}\right\}^2 = 1 \tag{3.23d}$$

where, t_n^{max}, t_s^{max}, and t_t^{max} represent peak nominal stresses for normal and shear deformations, while ε_n^{max}, ε_s^{max}, and ε_t^{max} represent peak nominal strains for the same respective deformations. On the other hand, the failure under mixed-mode conditions or the criteria for crack propagation are determined by a power law interaction between the energies required for failure in the individual modes—normal and shear. This is formulated as:

$$\left\{\frac{G_n}{G_n^C}\right\}^\alpha + \left\{\frac{G_s}{G_s^C}\right\}^\alpha + \left\{\frac{G_t}{G_t^C}\right\}^\alpha = 1 \tag{3.24}$$

here, the quantities G_n, G_s, and G_t represent the work done by traction and its conjugate relative displacement in the normal, first shear, and second shear directions. Meanwhile, the quantities

G_n^C, G_s^C, and G_t^C denote the critical fracture energies needed to induce failure for the same respective deformations.

3.1.2.1 Variational formulations

Let us consider that the domain Ω with a crack Γ_c, as shown in Fig. 3.5, which has displacement constraints, $\mathbf{u}_\Gamma$, on Γ_u and subject to tractions, $\mathbf{T}$, on the boundary Γ_F. It contains an active cohesive zone, Γ_{coh}, within the crack surface where the upper and lower edges are subjected to tractions, $\mathbf{t}^+$and $\mathbf{t}^-$, respectively.

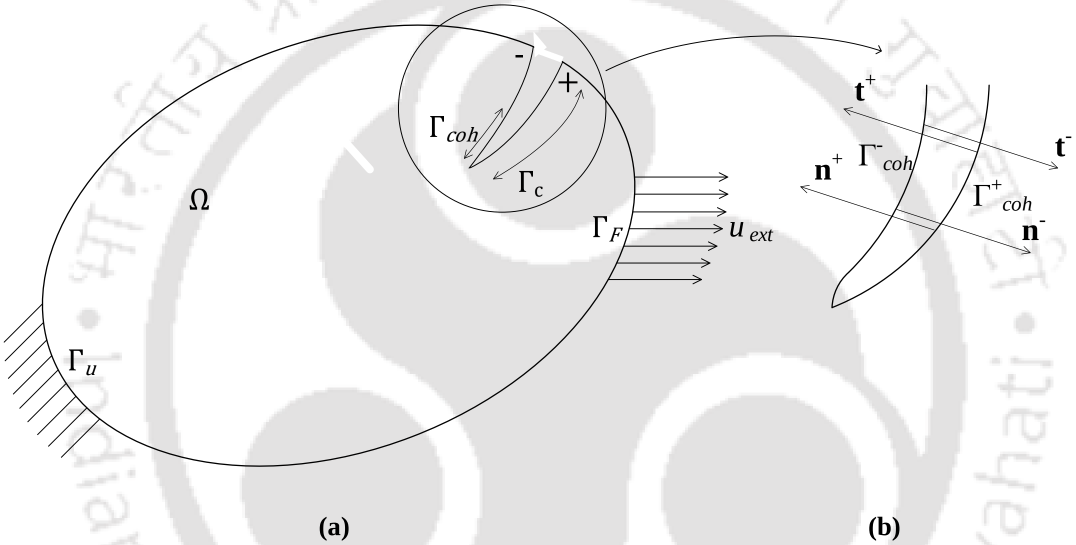

Fig. 3.5. (a) Domain with crack involving cohesive zone, and **(b)** zoom in the region of cohesive zone

The equilibrium equations of this problem are given by

$$\nabla.\boldsymbol{\sigma} = 0 \text{ on } \Omega \tag{3.25}$$

$$\boldsymbol{\sigma}.\mathbf{n}^+ = -\boldsymbol{\sigma}.\mathbf{n}^- = \mathbf{t}^+ = -\mathbf{t}^- = \mathbf{t} \text{ on } \Gamma_{coh} \tag{3.26}$$

where $\boldsymbol{n}^+$ and $\boldsymbol{n}^-$ are the normals at the crack surface. Assuming infinitesimal strains, the kinematic equations will be

Strain-displacement relation: $\boldsymbol{\varepsilon} = \frac{1}{2}(\nabla\mathbf{u} + (\nabla\mathbf{u})^{\mathrm{T}})$ on Ω (3.27)

Cohesive separation: $\mathbf{w} = (\mathbf{u}^- - \mathbf{u}^+)$ on Γ_{coh} (3.28)

The obtained displacement solution should satisfy the following relations:

$$\mathbf{u} = \mathbf{u}_{\Gamma} \text{ on } \Gamma_u \in \Gamma, \text{ and } \boldsymbol{\sigma}.\mathbf{n} = \mathbf{T} \text{ on } \Gamma_F \in \Gamma \tag{3.29}$$

There will be two constitutive laws, one for the cohesive zone and another for the entire domain, which are expressed as

$$\mathbf{t} = \mathbf{t}(\mathbf{w}) \text{ on } \Gamma_{coh} \in \Gamma, \quad \boldsymbol{\sigma} = \mathbf{C}{:}\,\boldsymbol{\varepsilon} \text{ on } \Omega \tag{3.30}$$

where $\mathbf{C}$ is the elasticity tensor. The strong form of the equilibrium equations is now transformed into the Galerkin weak form to construct the discrete system of equations in the FEM framework. The displacement $\mathbf{u}$ must be a member of the set $\boldsymbol{U}$ comprising kinematically admissible displacement fields.

$$\mathbf{u} \in \boldsymbol{U} = \{\overline{\mathbf{u}} \in \overline{\boldsymbol{U}}{:}\,\overline{\mathbf{u}} = \mathbf{0} \text{ on } \Gamma_u\} \tag{3.31}$$

In the $\overline{\boldsymbol{U}}$ space, discontinuous displacements across the crack boundary Γ_c are permitted. Therefore, the weak form of governing equations is given as,

$$\int_{\Omega} \boldsymbol{\sigma}{:}\,\boldsymbol{\varepsilon}(\overline{\mathbf{u}})\, \mathrm{d}\Omega = \int_{\Gamma_F} \mathbf{T}.\overline{\mathbf{u}}\, \mathrm{d}\Gamma + \int_{\Gamma_{coh}^{+}} \mathbf{t}^{+}.\overline{\mathbf{u}}^{+}\, \mathrm{d}\Gamma + \int_{\Gamma_{coh}^{-}} \mathbf{t}^{-}.\overline{\mathbf{u}}^{-}\, \mathrm{d}\Gamma \tag{3.32}$$

Using Eqs. (3.26) and (3.28), the above equation can be rewritten as,

$$\int_{\Omega} \boldsymbol{\sigma}{:}\,\boldsymbol{\varepsilon}(\overline{\mathbf{u}})\, \mathrm{d}\Omega + \int_{\Gamma_{coh}} \mathbf{t}.\mathbf{w}(\overline{\mathbf{u}})\, \mathrm{d}\Gamma = \int_{\Gamma_F} \mathbf{T}.\overline{\mathbf{u}}\, \mathrm{d}\Gamma \tag{3.33}$$

3.2 Nonlocal Integral theory

The formulation of any nonlocal theory commences with the selection of the variable to be enriched by nonlocal effects. Common selections include the regularization of external independent variables (such as strain and strain difference tensors), the regularization of internal variables (such as isotropic hardening and damage), or the regularization of the conjugate thermodynamic forces of the internal forces (damage energy release rate). Considering the multitude of possibilities available, it can initially be challenging to determine which option is the most effective and suitable for use. The selection of a nonlocal variable is intricately linked to thematerial type being modelled and the specific problem at hand, tailored to meet the demands and objectives of the study.

It has been observed that very few works have considered to enhance the performance of the strain-based nonlocal variable in damage mechanics to enhance its performance to capture the post-peak behaviour. Indeed, from a physical perspective, it is reasonable to consider strain as a nonlocal variable due to its significant role in deformation processes and directly linked to the localization phenomenon. Moreover, this approach indirectly incorporates nonlocal effects into the internal variables (damage) and their thermodynamic conjugate forces (damage energy release rate). Hence, in this study, strain-based variables are selected to investigate the damage phenomenon and mechanical behaviour of quasi-brittle and ductile materials.

Let the strain tensor ($\boldsymbol{\varepsilon}$), a local field variable, is subjected to regularization process through integral-type approach. Accordingly, the nonlocal variable ($\bar{\boldsymbol{\varepsilon}}$) is defined as [17]:

$$\bar{\boldsymbol{\varepsilon}}(\mathbf{x}) = \int_V g(\mathbf{x}, \mathbf{x}')\, \boldsymbol{\varepsilon}(\mathbf{x}') \mathrm{d}V(\mathbf{x}') \tag{3.34}$$

where, $\mathbf{x}$ and $\mathbf{x}'$ are target and neighbouring points, $g(\mathbf{x}, \mathbf{x}')$ is the symmetric influence or weight function which describes the mutual nonlocal interactions and is positive definite.

The weight function attains its maximum value at a distance of $r = \|\mathbf{x}' - \mathbf{x}\| = 0$, and its value diminishes as r increases, approaching zero. This indicates that nonlocal effects become significant within a specific region known as the influence radius ($r \leq R$), beyond which the regularized field variables exhibit behaviour equivalent to their local counterparts. In practice, attenuation functions are frequently represented using Gaussian and quartic/bell-shaped functions (see Fig. 3.6), defined as follows:

$$\begin{gathered} g(\mathbf{x}, \mathbf{x}') = c\mathrm{e}^{\left(-\frac{r^2}{l^2}\right)} \\ g(\mathbf{x}, \mathbf{x}') = c\langle 1 - (r^2/R^2)\rangle^2 \end{gathered} \tag{3.35}$$

where l and R are internal characteristic length and influence radius that are interrelated, generally referred as material parameters. However, the determination of these parameters is still under research [197–199]. The Macaulay symbol is defined as $\langle x \rangle = \frac{(x+|x|)}{2}$.

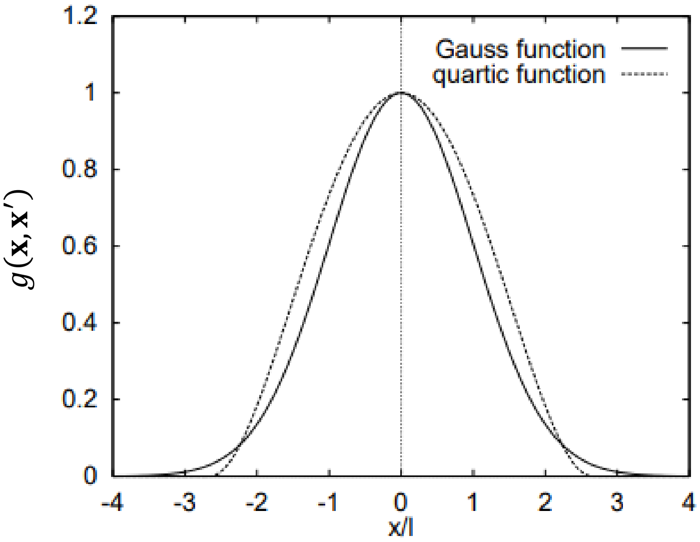

Fig. 3.6. Normalized nonlocal weight functions α_0 [200]

The quartic function is defined within a finite support, specifically for $r \leq R$, where it yields $g(\mathbf{x},\mathbf{x}') = 0$ beyond this limit. In contrast, the exponential function has an unbounded support, with $R = \infty$, but it exhibits a monotonically decreasing behaviour as r increases, eventually approximating zero at larger distances.

Furthermore, the influence function must adhere to the normalization condition, a fundamental criterion in nonlocal integral approaches to ensure the preservation of uniform fields.

$$\gamma(\mathbf{x}) = \int_V g(\mathbf{x},\mathbf{x}')\,\mathrm{d}V(\mathbf{x}') = 1 \tag{3.36}$$

Using Eq. (3.36) the constant 'c' of Eq. (3.35) can be determined [201]. Following this, Eq. (3.34) falls short of satisfying the fundamental requirement because nonlocal effects cease only at points far from the boundary, whereas they persist near the boundaries where $\gamma(\mathbf{x}) < 1$. To overcome this limitation, $g(\mathbf{x},\mathbf{x}')$ in Eq. (3.34) is replaced with [202]:

$$W(\mathbf{x},\mathbf{x}') = \frac{g(\mathbf{x},\mathbf{x}')}{\int_V g(\mathbf{x},\mathbf{x}')\,\mathrm{d}V(\mathbf{x}')} \tag{3.37}$$

While the influence function in the form depicted in Eq. (3.37) lacks symmetry and results in an asymmetric tangent stiffness matrix which does not adversely impact the accuracy of results across various case studies.

3.2.1 Thermodynamic framework

To maintain the integrity of strain-based nonlocal formulations while modelling damage, it is essential that these formulations adhere to the foundational principles of thermodynamics. Hence, following the first and second laws of thermodynamics expressed in a pointwise form as follows:

$$\begin{gathered}\dot{U} = \boldsymbol{\sigma}:\dot{\boldsymbol{\varepsilon}} + P \\ T\dot{\eta} = \boldsymbol{\sigma}:\dot{\boldsymbol{\varepsilon}} - \dot{\psi} + P \geq 0 \ \text{ in } V\end{gathered} \tag{3.38}$$

where, U is internal energy potential for the assumed nonlocal material which is expressed as a function of averaged strain and damage (assuming that plasticity effects are neglected). P signifies the energy density an individual particle acquires through the long-range interactions with neighbouring particles distributed within the body [203–205]. The expression $\psi = \psi(\bar{\boldsymbol{\varepsilon}}, D)$ represents Helmholtz free energy function defined as $\psi = U - T\eta$, with η as entropy and absolute temperature $T > 0$.

In this scenario, the dissipation inequality $(\phi = \dot{\eta} > 0)$ does not apply on a pointwise basis, unlike in the local approach $(\boldsymbol{\sigma}:\dot{\boldsymbol{\varepsilon}} - \dot{\psi} \geq 0)$. Therefore, extending the application of the dissipation inequality to the entire volume V is crucial for upholding second principle of thermodynamics. Consequently, the overall immediate body energy dissipation is given as:

$$\int_V \left(\boldsymbol{\sigma}:\dot{\boldsymbol{\varepsilon}} - \dot{\psi}\right) dV \geq 0 \tag{3.39}$$

where the term, $\int_V P \, \mathrm{d}V = 0$ represents the insulation condition, implying that, under any deformation mechanism $\dot{\boldsymbol{\varepsilon}}$**,** the domain should remain unaffected by long-range energy transfer from the external environment.

This implies that during irreversible processes, it is acceptable for the local violation of the inequality to occur. Expanding Eq. (3.38),

$$\phi = \boldsymbol{\sigma}:\dot{\boldsymbol{\varepsilon}} - \frac{\partial \psi}{\partial \bar{\boldsymbol{\varepsilon}}}:\dot{\bar{\boldsymbol{\varepsilon}}} - \frac{\partial \psi}{\partial D}\dot{D} + P \geq 0 \tag{3.40}$$

3.2.2 Constitutive law and determination of *P*

Remembering the Onsager reciprocity principle, which suggests that the energy dissipation density exhibits a bilinear form in terms of independent local variables driving deformation mechanisms and their associated thermodynamic forces, whether they are local or nonlocal in nature [18,203].

$$\phi = \boldsymbol{X} \colon \dot{\boldsymbol{\varepsilon}} + Y\dot{D} \geq 0 \quad \text{in } V \tag{3.41}$$

where, the damage energy release rate $\left(Y = -\frac{\partial \psi}{\partial D}\right)$ act as the conjugate for the damage (D) variable. Comparing Eqs. (3.40) and (3.41), the energy residual P is obtained as,

$$P = \boldsymbol{X} \colon \dot{\boldsymbol{\varepsilon}} - \boldsymbol{\sigma} \colon \dot{\boldsymbol{\varepsilon}} + \frac{\partial \psi}{\partial \bar{\boldsymbol{\varepsilon}}} \colon \dot{\bar{\boldsymbol{\varepsilon}}} \quad \text{in } V \tag{3.42}$$

Applying the insulation condition to Eq. (3.42), gives

$$\int_V \left(\boldsymbol{X} \colon \dot{\boldsymbol{\varepsilon}} - \boldsymbol{\sigma} \colon \dot{\boldsymbol{\varepsilon}} + \frac{\partial \psi}{\partial \bar{\boldsymbol{\varepsilon}}} \colon \dot{\bar{\boldsymbol{\varepsilon}}} \right) \mathrm{d}V = 0 \tag{3.43}$$

In relation to the third term presented in Eq. (3.43), it can be easily confirmed that the Green-type identity remains valid:

$$\int_V \frac{\partial \psi}{\partial \bar{\boldsymbol{\varepsilon}}} \colon \dot{\bar{\boldsymbol{\varepsilon}}} \, \mathrm{d}V = \int_V \overline{\frac{\partial \psi}{\partial \bar{\boldsymbol{\varepsilon}}}} \colon \dot{\boldsymbol{\varepsilon}} \, \mathrm{d}V \tag{3.44}$$

Substituting Eq. (3.44) in Eq. (3.43) gives,

$$\int_V \left(\boldsymbol{X} \colon \dot{\boldsymbol{\varepsilon}} - \boldsymbol{\sigma} \colon \dot{\boldsymbol{\varepsilon}} + \overline{\frac{\partial \psi}{\partial \bar{\boldsymbol{\varepsilon}}}} \colon \dot{\boldsymbol{\varepsilon}} \right) \mathrm{d}V = 0 \tag{3.45}$$

Therefore, for any deformation mechanism, $\dot{\boldsymbol{\varepsilon}}$, the nonlocal associated variable $\boldsymbol{X}$, is defined as,

$$\boldsymbol{X} = \boldsymbol{\sigma} - \overline{\frac{\partial \psi}{\partial \bar{\boldsymbol{\varepsilon}}}} \quad \text{in } V \tag{3.46}$$

Using Eq. (3.46) in Eq. (3.41) gives,

$$\phi = \left(\boldsymbol{\sigma} - \overline{\frac{\partial \psi}{\partial \bar{\boldsymbol{\varepsilon}}}} \right) \colon \dot{\boldsymbol{\varepsilon}} + Y\dot{D} \geq 0 \tag{3.47}$$

Following the established procedures [206], assuming the reversible processes the constitutive law is defined as,

$$\boldsymbol{\sigma} = \frac{\overline{\partial \psi}}{\partial \bar{\boldsymbol{\varepsilon}}} \qquad \text{in } V \tag{3.48}$$

On the other hand, by substituting Eq. (3.46) in Eq. (3.42), P is determined as,

$$P = \frac{\partial \psi}{\partial \bar{\boldsymbol{\varepsilon}}} : \dot{\bar{\boldsymbol{\varepsilon}}} - \frac{\overline{\partial \psi}}{\partial \bar{\boldsymbol{\varepsilon}}} : \dot{\boldsymbol{\varepsilon}} \qquad \text{in } V \tag{3.49}$$

Finally, the dissipation inequality is given by

$$\phi = Y\dot{D} \geq 0 \tag{3.50}$$

3.3 Hyperelasticity

Hyperelastic materials like rubber are widely used in a variety of structural applications spanning from automotive to aerospace. These materials experience large deformations for very small loads and preserve their original configuration without any permanent deformation after unloading. Fig. 3.7 shows their nonlinear stress-strain response, where a linear elastic modulus is no longer adequate. As a result, it is essential to study the behaviour of these highly nonlinear materials.

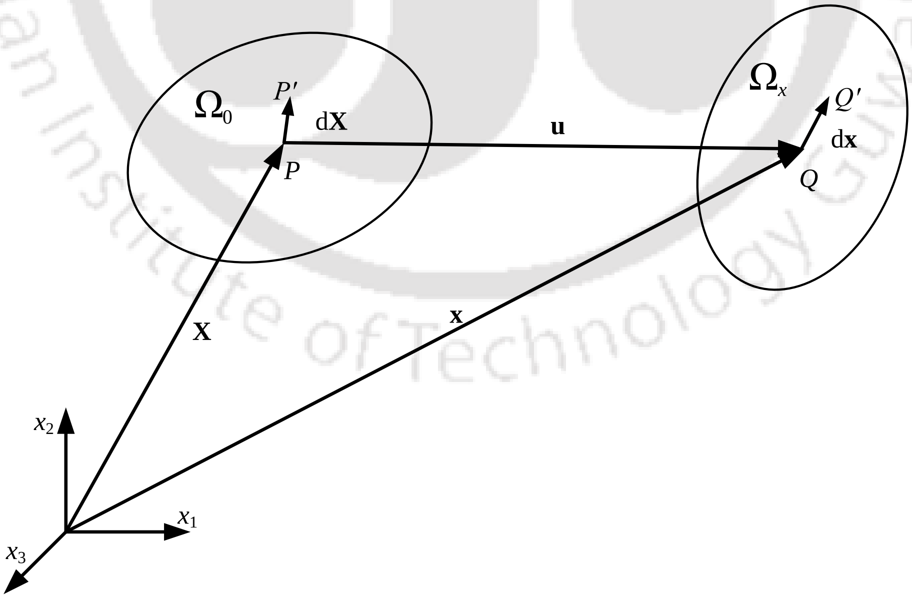

Fig. 3.7. Undeformed and deformed geometries of a body

The properties and the behaviour of these materials are represented by the strain energy density function, which cannot be determined directly from the established behaviours like linear elastic cases. Instead, it requires knowledge of the material's behaviour. Thus, knowledge of the energy function is the key challenge where the increased deformation induces an increase in nonlinearity, which leads to complex stress-stretch relations [207].

3.3.1 Stress and strain measures

In the case of infinitesimal deformation, the distinction between the undeformed and deformed geometries becomes imperceptible. As a result, all quantities, including stresses, strains, and displacements, are considered with respect to the initial geometry. While in reality, structures attain equilibrium after deformation. But the conventional approach often assumes equilibrium based on the undeformed geometry, particularly when dealing with infinitesimal deformations.

On the other hand, this distinction between the undeformed and deformed geometries becomes substantial and cannot be disregarded for large deformation problems. Thus, it is essential to understand the methodology for representing large deformations of material and defining stress and strain accordingly.

3.3.1.1 Deformation gradient

The elastic body, when subjected to various forces (body forces, traction, point loads, etc.) and displacements, changes its geometry from undeformed to deformed state, i.e., from the initial to the current configuration, as shown in Fig. 3.7. The material points in the reference configuration, represented by $\mathbf{X}$, are mapped onto the spatial points in the deformed/Eulerian configuration, denoted by $\mathbf{x}$, and expressed as,

$$\begin{aligned} \mathbf{x}_1 &= \mathbf{x}_1(\mathbf{X}_1, \mathbf{X}_2, \mathbf{X}_3) \\ \mathbf{x}_2 &= \mathbf{x}_2(\mathbf{X}_1, \mathbf{X}_2, \mathbf{X}_3) \\ \mathbf{x}_3 &= \mathbf{x}_3(\mathbf{X}_1, \mathbf{X}_2, \mathbf{X}_3) \end{aligned} \tag{3.51}$$

or,

$$\mathbf{x} = \varphi(\mathbf{X}, t)$$

where φ represents the mapping function. The above equation states that each material point in the initial/ Lagrangian configuration has a unique spatial point in the current/Eulerian configuration. Eq. (3.51) can also be written as,

$$\mathbf{x} = \mathbf{X} + \mathbf{u}(\mathbf{X}, t) \tag{3.52}$$

where $\mathbf{u}(\mathbf{X}, t)$ is the displacement of a material point.

The variation of the vector field, i.e., from reference to a deformed configuration via infinitesimal line segments ($\mathrm{d}\mathbf{X}$ and $\mathrm{d}\mathbf{x}$) of a solid body, is measured by the concept of the deformation gradient. The line segment, which is straight in the reference configuration, will also be (nearly) straight in the current geometry. Therefore, the infinitesimal line segments are stretched and rotated by deformation even though the body is subject to large deformations [208]. The line segments $\mathrm{d}\mathbf{X}$ and $\mathrm{d}\mathbf{x}$ are associated by

$$\mathrm{d}\mathbf{x} = \boldsymbol{F}\mathrm{d}\mathbf{X} \quad \text{or,} \quad \boldsymbol{F} = \frac{\partial \mathrm{x}}{\partial \mathbf{X}} \tag{3.53}$$

Substituting Eq. (3.52) in Eq. (3.53), the deformation gradient ($\boldsymbol{F}$) can be expressed as,

$$\boldsymbol{F} = 1 + \frac{\partial \mathbf{u}}{\partial \mathbf{X}} = 1 + \nabla_0 \mathbf{u} \tag{3.54}$$

here ∇_0 represents the gradient operator in the reference/Lagrangian configuration.

3.3.1.2 Strains in large deformations

Given that the definition of strain incorporates derivatives of displacement relative to the reference frame coordinates, it is necessary to use either the undeformed or deformed geometry as a reference.

Green-Lagrangian strain

The Green-Lagrangian strain utilizes the undeformed geometry as a reference. In Fig. 3.7, considering the two differential elements, where the vector $\mathrm{d}\mathbf{X}$ is deformed to $\mathrm{d}\mathbf{x}$, the change in squares of the length of these two vectors can be expressed as follows:

$$\begin{aligned} \|\mathrm{d}\mathbf{x}\|^2 - \|\mathrm{d}\mathbf{X}\|^2 &= \mathrm{d}\mathbf{x}^{\mathbf{T}}\mathrm{d}\mathbf{x} - \mathrm{d}\mathbf{X}^{\mathrm{T}}\mathrm{d}\mathbf{X} \\ &= \mathrm{d}\mathbf{X}^{\mathrm{T}}(\boldsymbol{F}^{\mathrm{T}}\boldsymbol{F} - \boldsymbol{I})\mathrm{d}\mathbf{X} \end{aligned} \tag{3.55}$$

where $\boldsymbol{I}$ is a identity tensor. The quantity $(\boldsymbol{F}^{\mathrm{T}}\boldsymbol{F} - \mathbf{1})$ quantifies the change in squared lengths relative to the square of the initial length. The term $\boldsymbol{F}^{\mathrm{T}}\boldsymbol{F}$ is a essential quantity known as right Cauchy–Green deformation tensor:

$$\boldsymbol{C} = \boldsymbol{F}^{\mathrm{T}}\boldsymbol{F} \tag{3.56}$$

Thus, the Green-Lagrangian strain ($\boldsymbol{E}$) is defined as,

$$\boldsymbol{E} = \frac{\mathbf{1}}{\mathbf{2}}(\boldsymbol{C} - \boldsymbol{I}) \tag{3.57}$$

The factor $\frac{1}{2}$ is included to align the definition with engineering strains, particularly in the case of infinitesimal strains. The Eq. (3.57) can be reformulated in terms of displacement gradient as:

$$\boldsymbol{E} = \frac{1}{2}(\nabla_0\mathbf{u} + \nabla_0\mathbf{u}^{\mathrm{T}} + \nabla_0\mathbf{u}^{\mathrm{T}}\nabla_0\mathbf{u}) \tag{3.58}$$

<u>Eulerian strain</u>

By using the deformed differential element, $\mathrm{d}\mathbf{x}$, as a reference, one can calculate the change in squares of the two vectors:

$$\begin{aligned}\|\mathrm{d}\mathbf{x}\|^2 - \|\mathrm{d}\mathbf{X}\|^2 &= \mathrm{d}\mathbf{x}^{\mathbf{T}}\mathrm{d}\mathbf{x} - \mathrm{d}\mathbf{X}^{\mathrm{T}}\mathrm{d}\mathbf{X} \\ &= \mathrm{d}\mathbf{x}^{\mathrm{T}}(\boldsymbol{I} - \boldsymbol{F}^{-\mathrm{T}}\boldsymbol{F}^{-1})\mathrm{d}\mathbf{x}\end{aligned} \tag{3.59}$$

where, $\boldsymbol{b} = \boldsymbol{F}^{-\mathrm{T}}\boldsymbol{F}^{-1}$ is defined as left Cauchy-Green deformation tensor. Using that the Eulerian strain tensor is expressed as,

$$\boldsymbol{e} = \frac{1}{2}(\boldsymbol{I} - \boldsymbol{b}^{-1}) \tag{3.60}$$

The Eq. (3.60) can be reformulated in terms of displacement gradient as:

$$\boldsymbol{e} = \frac{1}{2}(\nabla_x\mathbf{u} + \nabla_x\mathbf{u}^{\mathrm{T}} - \nabla_x\mathbf{u}^{\mathrm{T}}\nabla_x\mathbf{u}) \tag{3.61}$$

Where $\nabla_x = \frac{\partial}{\partial\mathbf{x}}$ represents the gradient operator at the deformed geometry.

3.3.1.3 Deformation of volume

It is notable that various materials exhibit different responses to volume-changing and volume-preserving deformations. Thus, it is essential to express the volume changes in terms of deformations. The transition of an infinitesimal volume element from its undeformed state $\mathrm{d}V_0$ to its deformed state $\mathrm{d}V_x$ involves three vectors in both their respective references, denoted by $\mathrm{d}X_1, \mathrm{d}X_2, \mathrm{d}X_3$ and $\mathrm{d}x_1, \mathrm{d}x_2, \mathrm{d}x_3$. Using the definition $\mathrm{d}\mathbf{x} = \boldsymbol{F}\mathrm{d}\mathbf{X}$, the volume change is expressed as,

$$\mathrm{d}V_x = J\mathrm{d}V_0 \tag{3.62}$$

here, $J = \det(\boldsymbol{F})$ contains all the effects of changing geometry.

3.3.1.4 Stresses in large deformations

In general, stress is described as the resisting force exerted on an infinitesimal area. In linear analysis, similar to strain measures, there is no need to differentiate between the deformed and undeformed areas. However, in case of involving large deformation, it is important to clarify which area is being considered when defining stress. The definition of stress can vary depending on the chosen area. Since both the undeformed and deformed geometries serve as frames of reference, stress is defined with respect to the areas associated with these two geometries.

In Fig. 3.7, the stress vector at point Q in the deformed geometry can be calculated using the differential element's area (ΔS_x), force ($\Delta\mathbf{f}$), and unit normal ($\mathbf{n}$).

$$\mathbf{t} = \lim_{\Delta S_x \to 0} \frac{\Delta\mathbf{f}}{\Delta S_x} = \boldsymbol{\sigma}\mathbf{n}, \tag{3.63}$$

The Cauchy stress tensor ($\boldsymbol{\sigma}$), also known as true stress, uses the present deformed geometry as a reference for force and area. With the same force $\Delta\mathbf{f}$ but the differential area ΔS_0, the unit normal $\mathbf{N}$ in the undeformed geometry and using the relations of change in surface area to establish a new stress tensor defined as,

$$\boldsymbol{P} = J\boldsymbol{F}^{-1}\boldsymbol{\sigma} \tag{3.64}$$

One drawback of the first Piola-Kirchhoff stress tensor ($\boldsymbol{P}$) is its lack of symmetry. One can construct a symmetric tensor by post-multiplying $\boldsymbol{P}$ with the transpose of the inverse of the deformation gradient. This modified stress tensor is referred to as the second Piola-Kirchhoff stress tensor ($\boldsymbol{S}$) defined as,

$$\boldsymbol{S} = \boldsymbol{P}\boldsymbol{F}^{-\mathrm{T}} = J\boldsymbol{F}^{-1}\boldsymbol{\sigma}\boldsymbol{F}^{-\mathrm{T}} \tag{3.65}$$

It is important to note that the Piola-Kirchhoff stresses are merely convenient mathematical quantities. Unlike Cauchy stresses, they are not directly associated with surface tractions in deformed geometry.

3.3.2 Principle of minimum potential energy

Consider the 2D domain Ω subjected to traction load ($\mathbf{T}$) and body forces ($\mathbf{f}^b$) on boundary Γ_F and essential boundary conditions on the boundary Γ_u. The potential energy function, using strain energy and external work, can be obtained as:

$$\begin{aligned}\Pi(\mathbf{u}) &= \Pi^{int}(\mathbf{u}) - \Pi^{ext}(\mathbf{u}) \\ &= \iint_{\Omega_{\mathbf{0}}} W(\boldsymbol{E})\,\mathrm{d}\Omega - \iint_{\Omega_0} \mathbf{u}^{\mathrm{T}}\mathbf{f}^b \mathrm{d}\Omega - \int_{\Gamma_0} \mathbf{u}^{\mathrm{T}}\mathbf{T}\mathrm{d}\Gamma\end{aligned} \tag{3.66}$$

To determine the displacement at the minimum potential energy, it is assumed that $\mathbf{u}$ is perturbed in the direction of $\bar{\mathbf{u}}$**.** Thus, taking the first variation of $\Pi(\mathbf{u})$ in the direction of $\bar{\mathbf{u}}$ gives,

$$\begin{aligned}\bar{\Pi}(\mathbf{u},\bar{\mathbf{u}}) &= \frac{\mathrm{d}}{\mathrm{d}\tau}\Pi(\mathbf{u}+\tau\bar{\mathbf{u}})|_{\tau=0} \\ &= \iint_{\Omega_{\mathbf{0}}} \frac{\partial W(\boldsymbol{E})}{\partial \boldsymbol{E}} : \bar{\boldsymbol{E}}\,\mathrm{d}\Omega - \iint_{\Omega_{\mathbf{0}}} \bar{\mathbf{u}}^{\mathrm{T}}\mathbf{f}^b\,\mathrm{d}\Omega - \int_{\Gamma_0} \bar{\mathbf{u}}^{\mathrm{T}}\mathbf{T}\,\mathrm{d}\Gamma\end{aligned} \tag{3.67}$$

Thus, the variational equation for the present nonlinear elastic system can be written as

$$a(\mathbf{u},\bar{\mathbf{u}}) = l(\bar{\mathbf{u}}), \qquad \forall \bar{\mathbf{u}} \in \mathbb{Z} \tag{3.68}$$

here $a(\mathbf{u},\bar{\mathbf{u}})$ and $l(\bar{\mathbf{u}})$ are the energy and load forms, defined as

$$a(\mathbf{u},\bar{\mathbf{u}}) = \iint_{\Omega_{\mathbf{0}}} \boldsymbol{S}:\bar{\boldsymbol{E}}\,\mathrm{d}\Omega, \qquad l(\bar{\mathbf{u}}) = \iint_{\Omega_{\mathbf{0}}} \bar{\mathbf{u}}^{\mathrm{T}}\mathbf{f}^b\,\mathrm{d}\Omega + \int_{\Gamma_0} \bar{\mathbf{u}}^{\mathrm{T}}\mathbf{T}\,\mathrm{d}\Gamma \tag{3.69}$$

where $\boldsymbol{S} = \frac{\partial W(\boldsymbol{E})}{\partial \boldsymbol{E}}$ is the constitutive relation between second Piola-kirchoff stress and Lagrangian strain tensors, and the first variation of Lagrangian strain tensor is defined as $\bar{\boldsymbol{E}} = \frac{1}{2}(\nabla_0\bar{\mathbf{u}}^{\mathrm{T}}\boldsymbol{F} + \boldsymbol{F}^{\mathrm{T}}\nabla_0\mathbf{u})$. It should be noted that the variational form of Eq. (3.68) is the weak form of nonlinear elastic systems.

3.3.3 Linearization process

Because of its nonlinear relationship between strain and displacement, Eq. (3.68) cannot be directly solved. Instead, it requires a linearization process, wherein the Newton-Raphson iterative scheme is employed to solve the nonlinear variational form. Its residual form is given by,

$$\mathbf{R} = a(\mathbf{u},\bar{\mathbf{u}}) - l(\bar{\mathbf{u}}) \tag{3.70}$$

Applying Taylor’s theorem to the residual function and neglecting the higher order terms leads to,

$$\mathbf{R}^{k+1} = \mathbf{R}^{k} + \frac{\partial \mathbf{R}^{k}}{\partial \mathbf{u}} \Delta \mathbf{u} \tag{3.71}$$

here, k is denoted by the iteration counter. At equilibrium, when the residual $\mathbf{R}^{k+1}$ vanishes, the above equation simplifies to

$$\left[\frac{\partial \mathbf{R}^{k}}{\partial \mathbf{u}}\right] \Delta \mathbf{u}^{k} = -\mathbf{R}^{k} \tag{3.72}$$

where, $$\frac{\partial \mathbf{R}}{\partial \mathbf{u}} = \frac{\partial a(\mathbf{u}, \bar{\mathbf{u}})}{\partial \mathbf{u}} = \iint_{\Omega_0} [\Delta \boldsymbol{S} \colon \bar{\boldsymbol{E}} + \boldsymbol{S} \colon \Delta \bar{\boldsymbol{E}}] \mathrm{d}\Omega \tag{3.73}$$

Since, the load form is independent of displacements, only the energy form is linearized. The increments of stress and first variation strain can be written as

$$\Delta \boldsymbol{S} = \frac{\partial \boldsymbol{S}}{\partial \boldsymbol{E}} \colon \Delta \boldsymbol{E} = \boldsymbol{D} \colon \Delta \boldsymbol{E} \tag{3.74a}$$

$$\Delta \boldsymbol{E} = \frac{1}{2} (\nabla_0 \Delta \mathbf{u}^{\mathrm{T}} \boldsymbol{F} + \boldsymbol{F}^{\mathrm{T}} \nabla_0 \Delta \mathbf{u}) \tag{3.74b}$$

$$\Delta \bar{\boldsymbol{E}} = \frac{1}{2} (\nabla_0 \Delta \mathbf{u}^{\mathrm{T}} \nabla_0 \bar{\mathbf{u}} + \nabla_0 \bar{\mathbf{u}}^{\mathrm{T}} \nabla_0 \Delta \mathbf{u}) \tag{3.74c}$$

Substituting Eqs. (3.74a) in Eq. (3.73) and the linearized equation is rewritten as,

$$\frac{\partial \mathbf{R}}{\partial \mathbf{u}} = \iint_{\Omega_0} [\bar{\boldsymbol{E}} \colon \boldsymbol{D} \colon \Delta \boldsymbol{E} + \boldsymbol{S} \colon \Delta \bar{\boldsymbol{E}}] \mathrm{d}\Omega \tag{3.75}$$

The linearized energy form is discretized into finite elements and expressed as,

$$\{\bar{\mathbf{u}}\}^{\mathrm{T}} [\boldsymbol{K}_T] = \{\bar{\mathbf{u}}\}^{\mathrm{T}} \left[\iint_{\Omega_0} [\boldsymbol{B}_N]^{\mathrm{T}} [\boldsymbol{D}] [\boldsymbol{B}_N] + [\boldsymbol{B}_G]^{\mathrm{T}} [\boldsymbol{\Sigma}] [\boldsymbol{B}_G] \, \mathrm{d}\Omega \right] \tag{3.76}$$

where$[\boldsymbol{B}_N]$ *and* $[\boldsymbol{B}_G]$ are defined as nonlinear and linear strain displacement matrix expressed as:

$$\boldsymbol{B}_N = [R_1][R_2][R_3]; \qquad \boldsymbol{B}_G = [R_2][R_3] \tag{3.77}$$

$$R_1 = \begin{bmatrix} F_{11} & 0 & F_{21} & 0 \\ 0 & F_{12} & 0 & F_{22} \\ F_{12} & F_{11} & F_{22} & F_{21} \end{bmatrix}; R_2 = \begin{bmatrix} J_{11}^{-1} & J_{12}^{-1} & 0 & 0 \\ J_{21}^{-1} & J_{22}^{-1} & 0 & 0 \\ 0 & 0 & J_{11}^{-1} & J_{12}^{-1} \\ 0 & 0 & J_{21}^{-1} & J_{22}^{-1} \end{bmatrix}$$

$$R_3 = \begin{bmatrix} N_{1,\xi} & 0 & N_{2,\xi} & 0 & N_{3,\xi} & 0 & N_{4,\xi} & 0 \\ N_{1,\eta} & 0 & N_{2,\eta} & 0 & N_{3,\eta} & 0 & N_{4,\eta} & 0 \\ 0 & N_{1,\xi} & 0 & N_{2,\xi} & 0 & N_{3,\xi} & 0 & N_{4,\xi} \\ 0 & N_{1,\eta} & 0 & N_{2,\eta} & 0 & N_{3,\eta} & 0 & N_{4,\eta} \end{bmatrix}$$

N and J represent the shape functions and jacobian involved in mapping the master coordinates to the local coordinates (ξ, η).

$$[\boldsymbol{\Sigma}] = \begin{bmatrix} S_{11} & S_{12} & 0 & 0 \\ S_{21} & S_{22} & 0 & 0 \\ 0 & 0 & S_{11} & S_{12} \\ 0 & 0 & S_{21} & S_{22} \end{bmatrix}$$

On the other hand, the terms on the right-hand side of Eq. (3.72) are also discretized and written as

$$a(\mathbf{u}, \bar{\mathbf{u}}) = \iint_{\Omega_0} \boldsymbol{S} : \bar{\boldsymbol{E}}\, \mathrm{d}\Omega = \{\bar{\mathbf{u}}\}^{\mathrm{T}} \left\{ \iint_{\Omega_0} [\boldsymbol{B}_N]^{\mathrm{T}} \{\boldsymbol{S}\}\, \mathrm{d}\Omega \right\} \equiv \{\bar{\mathbf{u}}\}^{\mathrm{T}} \{\mathbf{f}^{int}\} \tag{3.78}$$

$$\begin{aligned} l(\bar{\mathbf{u}}) &= \iint_{\Omega_0} \bar{\mathbf{u}}^{\mathrm{T}} \mathbf{f}^{b}\, \mathrm{d}\Omega + \int_{\Gamma_0} \bar{\mathbf{u}}^{\mathrm{T}} \mathbf{T}\, \mathrm{d}\Gamma \\ &= \{\bar{\mathbf{u}}\}^{\mathrm{T}} \left\{ \iint_{\Omega_0} \boldsymbol{N}^{\mathrm{T}} \mathbf{f}^{b}\, \mathrm{d}\Omega + \int_{\Gamma_0} \boldsymbol{N}^{\mathrm{T}} \mathbf{T}\, \mathrm{d}\Gamma \right\} = \{\bar{\mathbf{u}}\}^{\mathrm{T}} \{\mathbf{f}^{ext}\} \end{aligned} \tag{3.79}$$

Using Eqs. (3.76), (3.78), and (3.79), the incremental form in Eq. (3.72) can now be expressed as a linear algebraic system of equation, as follows:

$$\{\bar{\mathbf{u}}\}^{\mathrm{T}} [\boldsymbol{K}_T] \{\mathrm{d}\mathbf{u}\} = \{\bar{\mathbf{u}}\}^{\mathrm{T}} \{\mathbf{f}^{ext} - \mathbf{f}^{int}\} \tag{3.80}$$

The equation above must be solved iteratively using the Newton-Raphson method until the residual force diminishes.

3.4 Overview of element free Galerkin method

This section offers a comprehensive overview of the key parameters influencing the element-free Galerkin (EFG) method, with a focus on the properties of shape functions derived using the moving least-squares technique. Despite being termed a meshfree method, the EFG method still requires a background mesh for integration purposes, which is discussed herein. Furthermore, various techniques to impose boundary conditions are explored in detail.

3.4.1 Parameters in the EFG method

The EFG method's solution is significantly influenced by key parameters such as the domain of influence, nodal density, and the order of Gauss integration. A thorough study of these parameters is essential for understanding and effectively managing the approximating errors inherent in the method.

3.4.1.1 Domain of influence

The domain of influence is analogous to the element size in the FEM, which is defined as the spatial region where a node applies its influence [209]. Fig. 3.8(a) visually represents this concept, displaying two nodes with their respective circular domains of influence characterised by sizes d_1 and d_I. A larger domain of influence results in a larger bandwidth of the stiffness matrix and artificially smooth out the solution. In general, d_I is maintained at an intermediate size, neither too large nor too small; it is typically related to the average nodal spacing (δ) by the expression $d_I = \alpha\delta$.

The size of the domain of influence can be either constant or varied within a domain. For instance, the nodal domain of influence tends to be relatively small when a node is located near a crack tip or within a region where the gradient in the field variable (e.g., displacement) is notably high. This adjustment is made to accurately capture the variation in displacement.

3.4.1.2 Weight function

Weight functions, also referred to as window or kernel functions, are indispensable for deriving the shape functions, providing a localized behaviour to the solution. With compact support, they remain continuous and positive within their associated range. Weight functions are typically utilized in conjunction with a support domain linked to a specific point of interest, while a domain of influence is associated with a node.

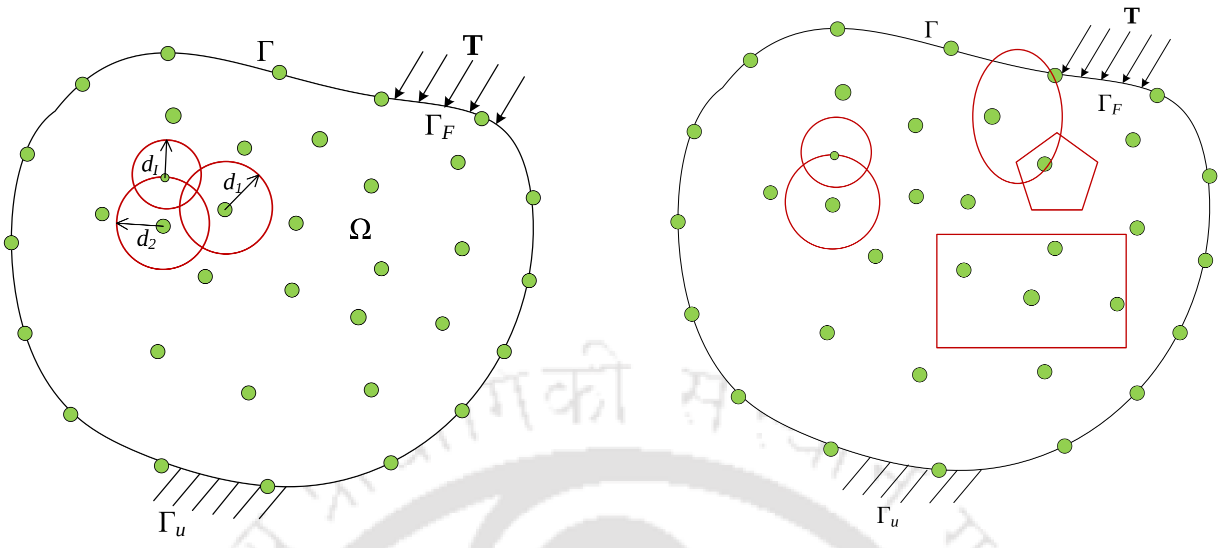

(a) **(b)**

Fig. 3.8. **(a)** Domain of influence, and **(b)** Shape of the domain of influence.

Commonly employed functional forms of weight functions for interpolation include [210] :

Cubic spline

$$W(\mathbf{x}-\mathbf{x}_I)=\begin{cases}\frac{2}{3}-4r^2+4r^3 & \text{for } r\le\frac{1}{2}\\ \frac{4}{3}-4r+4r^2-\frac{4}{3}r^3 & \text{for } \frac{1}{2}\le r\le 1\\ 0 & \text{for } r>1\end{cases}\qquad(3.81)$$

Quartic spline

$$W(\mathbf{x}-\mathbf{x}_I)=\begin{cases}1-6r^2+8r^3-3r^4 & \text{for } r\le 1\\ 0 & \text{for } r>1\end{cases}\qquad(3.82)$$

Conical formula

$$W(\mathbf{x}-\mathbf{x}_I)=\begin{cases}1-r^2 & \text{for } r\le 1\\ 0 & \text{for } r>1\end{cases}\qquad(3.83)$$

Exponential function

$$W(\mathbf{x}-\mathbf{x}_I)=\begin{cases}e^{-\left(\frac{r}{h}\right)^2} & \text{for } r\le 1\\ 0 & \text{for } r>1\end{cases}\qquad(3.84)$$

Negative exponential function

$$W(\mathbf{x}-\mathbf{x}_I)=\begin{cases}\dfrac{e^{-(rh)^2}-e^{-h^2}}{1-e^{-h^2}} & \text{for } r\leq 1\\ 0 & \text{for } r>1\end{cases} \tag{3.85}$$

where $r=\frac{d_{mI}}{d_I}$ and $d_{mI}=\|\mathbf{x}-\mathbf{x}_I\|$. The parameter h affects the shape of exponential functions. In this study, we employ the circular shape of d_I, along with cubic spline weight functions, commonly used in the literature.

3.4.1.3 Nodal density and Gaussian integration

From the works of Xiaoying et al. [211], it is observed that augmenting the nodal density leads to an increase in the order of the approximating nodal shape functions. In contrast to the FEM, the EFG method offers both h-adaptivity and p-adaptivity with the escalation of nodal density. Hence, controlling error in the EFG method proves challenging. Furthermore, the shape functions, being rational, exhibit behaviour akin to non-polynomial functions, particularly in scenarios involving non-uniformly distributed nodes.

To illustrate this phenomenon, Dolbow and Belytschko [212] examined a 1D problem with an irregular nodal distribution. Their findings revealed that the derivative and square of the derivative of the shape function exhibit complex behaviour, necessitating a higher order of Gauss integration for precise evaluation of the stiffness matrix. Fries and Matthies [48] conducted a comparative analysis of the computational efforts involved in integrating the derivatives of shape functions within regular and irregular nodal distributions. Their findings suggest that a regular nodal distribution, facilitating smooth variations of shape functions and their derivatives, is generally favoured over non-uniform distributions.

3.4.2 Shape function

The shape functions in the EFG method are determined through the moving least-squares (MLS) interpolation technique, introduced by Lancaster and Salkauskas [213]. In MLS, the term 'moving' denotes coefficients that dynamically adjust with spatial coordinates. Various variants of least squares methods exist for data interpolation, as outlined by Oñate et al. [214]: these include the standard least squares method, the fixed least squares method, and the multiple fixed least squares method. These techniques operate by minimizing the residual, which represents the weighted square of the error at any given point. The residual is given by,

$$\mathbf{J} = \sum_{I=1}^{N} w\left(u^h(\boldsymbol{x}_I) - u(\boldsymbol{x}_I)\right)^2 \tag{3.86}$$

where $u(\boldsymbol{x}_I)$ is the actual value at node I and $u^h(\boldsymbol{x}_I)$ is the approximated value, N is the total number of nodes that influence the node $\boldsymbol{x}_I$, and w is the weight function. For simplicity, let's consider the 1D formulation of the EFG method, which can be extended to higher dimensions. The approximated field variable at any arbitrary point x can be represented by:

$$u^h(x, x_I) = \boldsymbol{P}^{\mathrm{T}}(x_I)\boldsymbol{k}(x) \tag{3.87}$$

where $\mathbf{P}(x)$ is a complete polynomial basis of order m, given by $\mathbf{P}^{\mathrm{T}}(x) = [P_0(x)P_1(x)P_2(x) \dots P_m(x)] = [1\ \ x\ \ x^2\ \ x^3 \ \dots\ x^m\ ]$ and $\boldsymbol{k}(x)$ is the coefficient vector given by $\boldsymbol{k}^{\mathrm{T}}(x) = [k_0(x)\ \ k_1(x)\ \ k_2(x) \dots . k_m(x)]$. By substituting $\mathbf{P}(x)$ and $\boldsymbol{k}(x)$ into Eq. (3.86) and minimizing the residual ($\mathbf{J}$) with respect to each unknown coefficient, we obtain:

$$\begin{gathered}
\frac{\partial \mathbf{J}\big(\boldsymbol{k}(x)\big)}{\partial k_0} = 0;\ \sum_{I=1}^{N} w(x - x_I) 2P_0(x_I)[\mathbf{P}^{\mathrm{T}}(x_I)\boldsymbol{k}(x) - u_I] = 0 \\
\frac{\partial \mathbf{J}(\boldsymbol{k}(x))}{\partial k_1} = 0;\ \sum_{I=1}^{N} w(x - x_I) 2P_1(x_I)[\mathbf{P}^{\mathrm{T}}(x_I)\boldsymbol{k}(x) - u_I] = 0 \\
\vdots \\
\frac{\partial \mathbf{J}(\boldsymbol{k}(x))}{\partial k_m} = 0;\ \sum_{I=1}^{N} w(x - x_I) 2P_m(x_I)[\mathbf{P}^{\mathrm{T}}(x_I)\boldsymbol{k}(x) - u_I] = 0
\end{gathered} \tag{3.88}$$

Eq. (3.88) can be rearranged to yield,

$$\begin{gathered}
\sum_{I=1}^{N} w(x - x_I)\, \boldsymbol{P}(x_I)\boldsymbol{P}^{\mathrm{T}}(x_I)\boldsymbol{k}(x) = \sum_{I=1}^{N} w(x - x_I)\, \boldsymbol{P}(x_I)u_I \\
\mathbf{A}(x)\boldsymbol{k}(x) = \mathbf{B}(x)\mathbf{u}
\end{gathered} \tag{3.89}$$

where,

$$\boldsymbol{A}(x) = \sum_{I=1}^{N} w(x - x_I)\, \boldsymbol{P}(x_I)\boldsymbol{P}^{\mathrm{T}}(x_I)$$

$$\mathbf{B}(x) = [w(x - x_1)\mathbf{P}(\boldsymbol{x}_1)\ \ w(x - x_2)\mathbf{P}(x_2)\ \dots w(x - x_N)\mathbf{P}(x_N)]$$

$$\mathbf{u} = \{u_1 \quad u_2 \quad \cdots \quad u_N\}^{\mathrm{T}}$$

For a 1D system the linear basis will be $\boldsymbol{P}^{\mathrm{T}}(x) = [1 \quad x]$, $\boldsymbol{A}(x)$ and $\boldsymbol{B}(x)$ will be

$$\begin{gathered}
\boldsymbol{A}(x) = w(x - x_1)\begin{bmatrix} 1 & x_1 \\ x_1 & x_1^2 \end{bmatrix} + w(x - x_2)\begin{bmatrix} 1 & x_2 \\ x_2 & x_2^2 \end{bmatrix} + \ldots + w(x - x_N)\begin{bmatrix} 1 & x_N \\ x_N & x_N^2 \end{bmatrix} \\
\mathbf{B}(x) = \left[w(x - x_1)\begin{Bmatrix} 1 \\ x_1 \end{Bmatrix} \quad w(x - x_2)\begin{Bmatrix} 1 \\ x_2 \end{Bmatrix} \;\ldots\; w(x - x_N)\begin{Bmatrix} 1 \\ x_N \end{Bmatrix} \right]
\end{gathered} \tag{3.90}$$

Replacing the term $\boldsymbol{k}(x)$ in Eq. (3.87) with the solution obtained from Eq. (3.89), we get:

$$u^h(x) = \boldsymbol{\Phi}^{\mathrm{T}}(x)\boldsymbol{u} = \sum_{I=1}^{N} \Phi_I(x)\, u_I \tag{3.91}$$

where $\boldsymbol{\Phi}^{\mathrm{T}}(x) = \mathbf{P}^{\mathrm{T}}(x)[\boldsymbol{A}(x)]^{-1}\boldsymbol{B}(x)$. Here, $\Phi_I(x)$ is the MLS shape function associated with node I.

Due to the necessity of inverting the moment matrix $\boldsymbol{A}(x)$ at each Gauss point during the computation of the global stiffness matrix, the computational cost of the EFG method becomes considerable. Additionally, the domain of influence d_I needs to be increased in proportion to the size of the polynomial $\mathbf{P}^{\mathrm{T}}(x)$ vector. This adjustment is necessary to prevent the occurrence of a singular moment matrix. For instance, if $m = 2$, the number of nodes (N) within a domain of influence must be at least equal to m $(N \geq 2)$. As N increases, so does the bandwidth of the stiffness matrix. Consequently, the computational costs increase significantly with the expansion of the polynomial basis. Therefore, in this study, a linear basis is adopted, aiming to enhance accuracy while minimizing computational costs.

3.4.2.1 Properties of shape functions

Approximants

Unlike FEM, shape functions derived from the MLS technique, while rooted in the partition of unity concept, do not exhibit the Kronecker delta property. At each node, multiple shape functions have non-zero values, complicating the imposition of essential boundary conditions (EBC) and resulting in increased computational costs.

Non-polynomial nature of the shape functions

Despite the polynomial nature of weight functions, resulting shape functions are non-polynomial, with their derivatives exhibiting even more non-polynomial behaviour [215].This presents challenges when integrating the weak form expressions [216]. However, for regular nodal discretization, shape functions and their derivatives can be approximated as polynomial-like functions (Section 3.4.1.3).

3.4.3 Imposition of essential boundary conditions

Previously, it was discussed that the absence of the Kronecker delta property in shape functions poses challenges in enforcing Dirichlet or EBCs. Several techniques have been proposed to address this issue; however, it's important to note that most imposition techniques result in a loss of convergence order.

3.4.3.1 Boundary collocation

This approach, as outlined by Mukherjee and Mukherjee [217], offers a straightforward method for imposing EBCs within the context of meshfree methods. However, it lacks the capability to enforce EBCs at points other than nodal locations, as noted by Atluri and Shen [218]. If imposing the displacement value u_I at node I, located at position x_I, an additional row and column will be appended to the global stiffness matrix $[\boldsymbol{K}]$, resulting in:

$$\begin{bmatrix} & & \cdots & & \\ \cdots & \Phi_{i-1}(x_I) & \Phi_i(x_I) & \Phi_{i+1}(x_I) & \cdots \\ & & \cdots & & \end{bmatrix} \rightarrow \begin{Bmatrix} \cdots \\ u_I \\ \cdots \end{Bmatrix} \qquad (3.92)$$

where $\Phi_i(x_I): i = 1,2, \dots, N$ are shape functions of the N nodes that influence the point x_I.

3.4.3.2 Lagrange multiplier approach

The Lagrange multipliers, denoted as λ, can be conceptualized as 'smart forces' with the role of enforcing the system's constraints [30]. The introduction of Lagrange multipliers adds unknown functions, consequently increasing the total number of field functions within the system. As part of the process to obtain discretized system equations, Lagrange multipliers also need to be approximated akin to field functions. This results in an increase in the total number of nodal unknowns within the discretized system equation. As a result, the final structure $\begin{bmatrix} \boldsymbol{K} & \boldsymbol{G} \\ \boldsymbol{G} & 0 \end{bmatrix}$, comprising the global stiffness matrix $(\boldsymbol{K})$ and the contributions from the Lagrange multipliers $(\boldsymbol{G})$, loses its positive definiteness (because of zeros on the main diagonal).

3.4.3.3 *Finite element coupling*

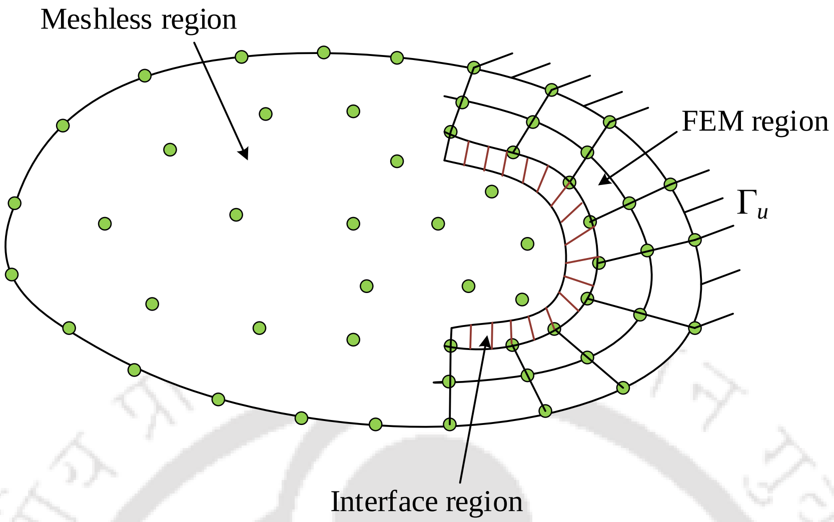

Fig. 3.9. Coupled meshless finite element method.

Although FE shape functions possess the Kronecker delta property, suggesting the effectiveness of this coupling, challenges arise in modelling interfaces, as illustrated in Fig. 3.9 due to the discontinuous nature of derivatives. Numerous approaches to address this challenge have been proposed [219], including the master-slave coupling approach [160,220], compatibility coupling [221], the bridging domain coupling method [222] coupling with Lagrange parameters [216,219], and hybrid approximation [223]. Coupling would incur even higher computational costs if a point falls within a domain where EBCs must be enforced.

Aside from the previously mentioned approaches, there are also more intricate methods such as the Transformation method [48,224,225], singular weighting functions [226], and D'Alembert's principle [227], aimed at addressing the challenges associated with enforcing EBCs.

3.4.4 EFG formulations for linear elastic problems

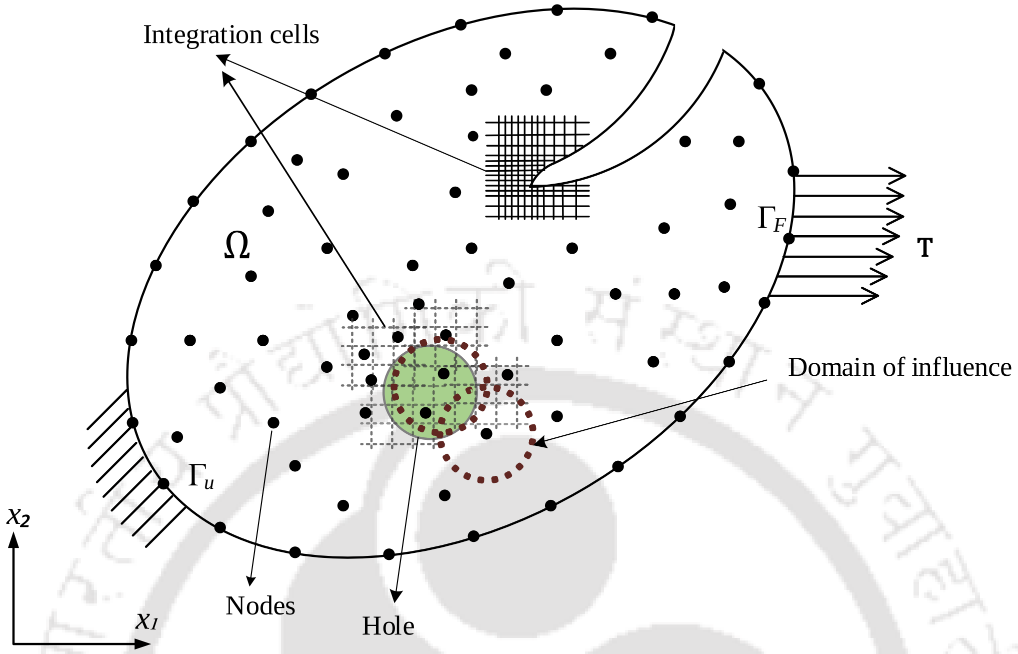

Fig. 3.10. EFG method discretization with background mesh for integration

To illustrate the process of formulating discrete system equations using the EFG method, a two-dimensional (2D) linear solid mechanics problem is employed (see Fig. 3.10). The associated partial differential equation and boundary conditions for this 2D solid mechanics problem can be succinctly expressed as:

$$\mathbf{L}_d^{\mathrm{T}}\boldsymbol{\sigma} + \mathbf{b} = 0 \quad \text{on} \quad \Omega \tag{3.93}$$

$$\begin{aligned} \mathbf{u} &= \mathbf{u}_\Gamma && \text{on} \quad \Gamma_u \\ \mathbf{L}_n^{\mathrm{T}}\boldsymbol{\sigma} &= \mathbf{t} && \text{on} \quad \Gamma_F \end{aligned} \tag{3.94}$$

where $\mathbf{L}_d = \begin{bmatrix} \frac{\partial}{\partial x_1} & 0 \\ 0 & \frac{\partial}{\partial x_2} \\ \frac{\partial}{\partial x_2} & \frac{\partial}{\partial x_1} \end{bmatrix}$, **b** is the body force vector defined as $\{b_1\ b_2\}^{\mathrm{T}}$ and $\boldsymbol{\sigma} = \{\sigma_{11}\ \sigma_{22}\ \sigma_{12}\}^{\mathrm{T}}$ is the stress in voigt form. For this 2D problem, the Galerkin weak form in the presence of Lagrange multipliers (λ) for the constraints is given by,

$$\int_{\Omega} \delta(\mathbf{L}_d\mathbf{u})^{\mathrm{T}}\mathbf{C}(\mathbf{L}_d\mathbf{u})\mathrm{d}\Omega \, - \int_{\Omega} \delta\mathbf{u}^{\mathrm{T}}\mathbf{b}\, \mathrm{d}\Omega \, - \int_{\Gamma_F} \delta\mathbf{u}^{\mathrm{T}}\mathbf{t}\, \mathrm{d}\Gamma \, - \int_{\Gamma_u} \delta\lambda^{\mathrm{T}}(\mathbf{u}-\mathbf{u}_{\Gamma})\, \mathrm{d}\Gamma \, - \int_{\Gamma_u} \delta\mathbf{u}^{\mathrm{T}}\lambda\, \mathrm{d}\Gamma \, = 0 \tag{3.95}$$

The inclusion of the last two terms in Eq. (3.95) arises from the utilization of Lagrange multipliers, specifically to manage essential boundary conditions in situations where $\mathbf{u} \neq \mathbf{u}_{\Gamma}$. Now, we utilize the MLS approximation to express both the trial and test functions at any given point **x**, leveraging the nodes within **x**'s support domain.

Specifically, for the displacement component **u**, we obtain:

$$\boldsymbol{u}^h(\boldsymbol{x}) = \begin{Bmatrix} u \\ v \end{Bmatrix}^h = \sum_{I\in S_N} \underbrace{\begin{bmatrix} \Phi_I & 0 \\ 0 & \Phi_I \end{bmatrix}}_{\boldsymbol{\Phi}_I} \underbrace{\begin{Bmatrix} u_I \\ v_I \end{Bmatrix}}_{\boldsymbol{u}_I} = \sum_{I\in S_N} \boldsymbol{\Phi}_I^H \mathbf{u}_I \tag{3.96}$$

where S_N is the set that contains the nodes in the support domain of point **x.** It's crucial to note that at the node location $\mathbf{x}_I$, $\boldsymbol{u}^h(\boldsymbol{x}_I) = \mathbf{u}_I$**.** This discrepancy arises from the MLS shape functions lacking the Kronecker delta property. Furthermore, $\mathbf{L}_d\mathbf{u}$ can be simplified further using Eq. (3.96) as follows:

$$\mathbf{L}_d\mathbf{u}^h = \sum\nolimits_{I\in S_N} \begin{bmatrix} \frac{\partial}{\partial x_1} & 0 \\ 0 & \frac{\partial}{\partial x_2} \\ \frac{\partial}{\partial x_2} & \frac{\partial}{\partial x_1} \end{bmatrix} \begin{bmatrix} \Phi_I & 0 \\ 0 & \Phi_I \end{bmatrix} \mathbf{u}_I = \sum\nolimits_{I\in S_N} \underbrace{\begin{bmatrix} \Phi_{I,x_1} & 0 \\ 0 & \Phi_{I,x_2} \\ \Phi_{I,x_2} & \Phi_{I,x_1} \end{bmatrix}}_{\boldsymbol{B}_I} \mathbf{u}_I = \sum\nolimits_{I\in S_N} \boldsymbol{B}_I \mathbf{u}_I \tag{3.97}$$

In order to impose the boundary conditions, the Lagrange multiplier is expressed by,

$$\lambda(\boldsymbol{x}) = \sum_{I\in S_\lambda} N_I(\boldsymbol{x})\lambda_I \qquad\qquad \boldsymbol{x} \in \Gamma_u \tag{3.98}$$

where S_λ is the set containing the nodes whose shape functions are used to interpolate at the location **x,** and N_I represents the Lagrange interpolant used in the FEM.

Substituting Eqs. (3.96), (3.97), and (3.98) in Eq. (3.95) obtains,

$$\begin{aligned}&\underbrace{\int_{\Omega} \delta\left(\sum_{I\in S_N} \boldsymbol{B}_I \mathbf{u}_I\right)^{\mathrm{T}} \mathbf{C}\left(\sum_{I\in S_N} \boldsymbol{B}_I \mathbf{u}_I\right) \mathrm{d}\Omega}_{\boldsymbol{\delta}\mathbf{U}^{\mathrm{T}}\boldsymbol{K}\mathbf{U}} - \underbrace{\int_{\Omega} \delta\left(\sum_{I\in S_N} \boldsymbol{\Phi}_I^H \mathbf{u}_I\right)^{\mathrm{T}} \mathbf{b}\, \mathrm{d}\Omega - \int_{\Gamma_F} \delta\left(\sum_{I\in S_N} \boldsymbol{\Phi}_I^H \mathbf{u}_I\right)^{\mathrm{T}} \mathbf{t}\, \mathrm{d}\Gamma}_{\boldsymbol{\delta}\mathbf{U}^{\mathrm{T}}\mathbf{F}} \\ &- \underbrace{\int_{\Gamma_u} \delta\lambda^{\mathrm{T}}\left(\left(\sum_{I\in S_N} \boldsymbol{\Phi}_I^H \mathbf{u}_I\right) - \mathbf{u}_{\Gamma}\right) \mathrm{d}\Gamma}_{\boldsymbol{\delta}\lambda^{\mathrm{T}}[\boldsymbol{G}^{\mathrm{T}}\mathbf{U}-\mathbf{q}]} - \underbrace{\int_{\Gamma_u} \delta\left(\sum_{I\in S_N} \boldsymbol{\Phi}_I^H \mathbf{u}_I\right)^{\mathrm{T}} \lambda\, \mathrm{d}\Gamma}_{\boldsymbol{\delta}\mathbf{U}^{\mathrm{T}}\boldsymbol{G}\lambda} = 0\end{aligned} \tag{3.99}$$

Rewriting Eq. (3.99) in form of algebraic system of equations,

$$\begin{bmatrix} \mathbf{K} & \mathbf{G} \\ \mathbf{G} & 0 \end{bmatrix} \begin{Bmatrix} \mathbf{U} \\ \lambda \end{Bmatrix} = \begin{Bmatrix} \mathbf{F} \\ \mathbf{q} \end{Bmatrix} \tag{3.100}$$

where,

$$\begin{gathered} \boldsymbol{K}_{IJ} = \int_{\Omega} \boldsymbol{B}_I{}^{\mathrm{T}} \mathbf{C} \boldsymbol{B}_I \,\mathrm{d}\Omega \\ \boldsymbol{G}_{IJ} = -\int_{\Gamma_u} \boldsymbol{N}_I^{\mathrm{T}} \boldsymbol{\Phi}_J \,\mathrm{d}\Gamma \\ \boldsymbol{N}_I = \begin{bmatrix} N_I & 0 \\ 0 & N_I \end{bmatrix} \\ \mathbf{F}_I = \int_{\Omega} \boldsymbol{\Phi}_I{}^{\mathrm{T}} \mathbf{b}\, \mathrm{d}\Omega + \int_{\Gamma_F} \boldsymbol{\Phi}_I^{\mathrm{T}} \mathbf{t}\, \mathrm{d}\Gamma \\ \mathbf{q} = \int_{\Gamma_u} \boldsymbol{N}_I^{\mathrm{T}} \mathbf{u}_{\Gamma} \,\mathrm{d}\Gamma \end{gathered} \tag{3.101}$$

Chapter 4

Damage Modelling in Adhesive Bonded Joints using Nonlocal FEM

This chapter introduces the application of nonlocal integral theories for the failure analysis of adhesive bonded joints, focusing on cohesive crack mode I problems and biadhesive single-lap joint problems. The continuum mixed-mode damage models proposed by Chousal and de Moura [141] are employed to illustrate material degradation within the nonlocal framework. The tangent stiffness matrix derived based on the proposed nonlocal constitutive model is also presented.

4.1 Introduction

According to the literature discussed in Chapter 2, it is observed that among the two primary CZM approaches, zero-thickness interface elements exhibit greater accuracy in comparison to cohesive elements employed throughout the adhesive region (conventional approach). Comparatively, these elements offer better flexibility in modelling unknown crack paths than the traditional CZM approach [127]. However, accurately predicting the unknown crack path within the adhesive region necessitates the discretization of a large number of continuum elements, with cohesive elements inserted between them [128]. The limitation in CZM is circumvented by continuum damage models (CDM), where employing only continuum elements is sufficient to predict the crack paths. In this approach, traction-separation laws (TSL) are directly applied to the continuum elements to capture the damage state within each element. In addition to TSLs, there is also ease in utilizing alternative damage models and integrating plasticity effects through continuum theories [144].

Studies on varying adhesive thicknesses, overlap lengths, and cohesive parameters, as well as comparison of TSLs for mode I, mode II, and mixed-mode problems, are well explored through both CZM and CDM in the FEM framework. However, there are certain case studies in adhesive bonded joints where FEM face challenges. These challenges include results that are highly mesh-sensitive, especially when dealing with adhesive cracks featuring sharp pre-cracks at the interface and cohesive cracks with sharp pre-cracks within the adhesive region, assuming these pre-cracks as defects. Additionally, FEM often lacks iterative convergence and requires extensive mesh refinement. This is particularly apparent in biadhesive single lap joints, where abrupt changes in material within the adhesive region lead to discontinuous strains, further complicating the convergence process, especially for medium-sized meshes.

As previously discussed in the literature, the aforementioned issues are addressed by the nonlocal integral theories. These theories efficiently produce mesh-independent results by ensuring the continuity of strain distributions, particularly in cases involving weak discontinuities. Therefore, in the present work, integral-based nonlocal strain theories are applied to analyze the failure behaviour of problems across various modes where FEM faces challenges. In this context, to highlight the mesh independence and iterative convergence by maintaining strain continuity for relatively medium-sized meshes, double cantilever beam (DCB) with a sharp pre-crack in the adhesive region (cohesive crack) and biadhesive bonded single lap joint problems are solved.

4.2 Nonlocal Strain Approach

Damage in adhesive bonded joints is typically characterised using TSLs, which indirectly rely on strains via relative displacements. Additionally, adhesive joints constitute a multi-material system, where the interface is influenced by both materials. Therefore, to accurately represent their influence at the interface while maintaining c^1 continuity, and from a physical standpoint, it is reasonable to regard strain as a nonlocal variable due to its crucial role in deformation processes.

$$\bar{\boldsymbol{\varepsilon}}(\mathbf{x}) = \int_V W(\mathbf{x}, \mathbf{x}')\, \boldsymbol{\varepsilon}(\mathbf{x}') \mathrm{d}V(\mathbf{x}') \tag{4.1}$$

Recalling the integration of nonlocal effects within the thermodynamic framework and the development of formulations for dissipation inequality, leading to the derivation of the constitutive law as discussed in Section 3.2, is summarized as follows:

$$\phi = Y\dot{D} \geq 0 \tag{4.2}$$

$$\boldsymbol{\sigma} = \overline{\frac{\partial \psi}{\partial \bar{\boldsymbol{\varepsilon}}}} \qquad \text{in } V \tag{4.3}$$

Following the conditions such as constant strain distribution over the uniform field, the elastic strain energy density function for a damaged material is expressed as:

$$\psi = \frac{1}{2} \bar{\boldsymbol{\varepsilon}} : (1 - D)\mathbb{C}_0 : \bar{\boldsymbol{\varepsilon}} \tag{4.4}$$

By substituting Eq. (4.4) into Eq. (4.3) and conducting the requisite mathematical and regularization operations, we obtain:

$$\boldsymbol{\sigma} = \int_V \int_V W(\mathbf{x},\mathbf{z})W(\mathbf{x}',\mathbf{z})\big(1-D(\mathbf{z})\big)\mathbb{C}_0(\mathbf{z}):\boldsymbol{\varepsilon}(\mathbf{x}')\mathrm{d}V(\mathbf{z})\mathrm{d}V(\mathbf{x}') \qquad (4.5)$$

This constitutive equation not only accounts for the influence of state variables at points $\mathbf{x}$ and $\mathbf{x}'$ but also factors in the cumulative influence of points $\mathbf{z}$, which are the common neighbours of both $\mathbf{x}$ and $\mathbf{x}'$.

4.3 Continuum Damage Model

The objective of the damage model is to simulate the failure behaviour of the adhesive in adhesively bonded structures. This is accomplished by representing the adhesive region with continuum elements, utilizing a bilinear mixed-mode traction-separation law (TSL). This approach incorporates criteria for damage initiation, indicating the onset of material degradation, and predicts damage evolution through a fracture energy criterion. The critical fracture energy for the respective mode is expressed as,

$$G_{i,c} = \frac{\sigma_{u,i}\varepsilon_{u,i}l_c}{2} \qquad (4.6)$$

$$l_{c_i} = \frac{\delta_i}{\varepsilon_i}, \quad i = I, II \qquad (4.7)$$

where l_c is defined as characteristic length that establishes the relation between opening (δ_I) or shear (δ_{II}) displacements and the corresponding strain ($\varepsilon_i, i = I, II$). The quadratic stress criterion is considered to simulate the damage onset

$$\left(\frac{\sigma_I}{\sigma_u}\right)^2 + \left(\frac{\tau}{\tau_u}\right)^2 = 1 \qquad (4.8)$$

where σ_I and τ are the normal (mode I) and shear (mode II) stresses respectively and σ_u , τ_u are their corresponding ultimate stresses. Based on Eq. (4.8), the mode I stress component that lead to damage onset (σ_{eI}, σ_{eII}) under mixed-mode loading can be defined as follows:

If $\sigma_I > 0$,

$$\sigma_{eI} = \frac{\sigma_u \tau_u}{\sqrt{{\tau_u}^2 + {\beta_s}^2\, {\sigma_u}^2}} \qquad (4.9)$$

If $\sigma_I < 0$,
$$\sigma_{eII} = \frac{\sigma_u \tau_u}{\tau_u \sqrt{\left(\frac{1}{{\beta_s}^2} + \frac{{\alpha_s}^2}{{\beta_s}^2}\right) + \ {\sigma_u}^2}} \tag{4.10}$$

In standard continuum approaches, the relative displacements for damage initiation under mixed-mode loading are directly obtained from the constitutive or Hooke's law (see Fig. 4.1). However, in this particular work, due to the presence of nonlocal effects in the constitutive law (as shown in Eq. (4.5)), deriving these displacements becomes challenging. Since damage has not initiated at this stage and strain localization effects are not significant, the authors believe that employing Hooke's law to compute the relative mixed-mode displacements for damage initiation is a reasonable choice. Nevertheless, the stresses are still calculated from Eq. (4.5) and subsequently employed in the following expressions.

If $\sigma_I > 0$,
$$\delta_{o,Im} = \frac{\sigma_{eI}}{E}\,(1 - \nu\alpha_s)l_c; \qquad \delta_{0,IIm} = \frac{2\sigma_{eI}(1 + \nu)}{E}\,\beta_s l_c \tag{4.11}$$

If $\sigma_I < 0$,
$$\delta_{o,Im} = \frac{\sigma_{eII}}{E\ \beta_s}\,(1 - \nu\alpha_s)l_c; \qquad \delta_{0,IIm} = \frac{2\sigma_{eII}(1 + \nu)}{E}\,l_c \tag{4.12}$$

here, σ_{eI} and σ_{eII} are the equivalent stresses in mode I and II responsible for damage onset, E and ν are the elastic modulus and Poisson's ratio of the adhesive, $\beta_s = \frac{|\tau|}{\sigma_I}$, and α_s is the ratio between x and y direction stresses, where mode I component among two will be in the denominator.

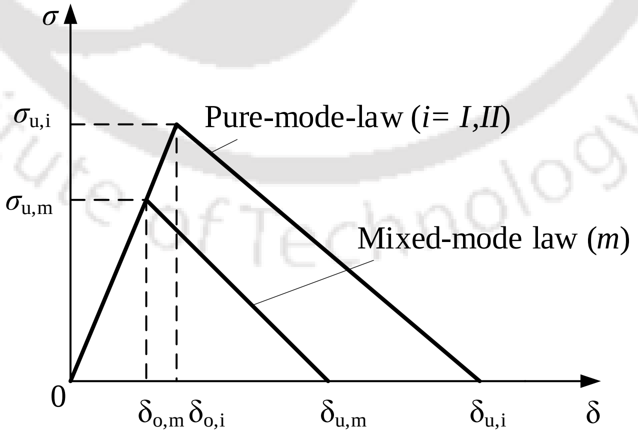

Fig. 4.1. Mixed mode traction-separation law

The equivalent relative displacement at damage onset is given by

$$\delta_{o,m} = \sqrt{{\delta_{o,Im}}^2 + {\delta_{o,IIm}}^2} \tag{4.13}$$

The evolution of damage is simulated using the linear fracture energy criterion.

$$\frac{G_I}{G_{Ic}} + \frac{G_{II}}{G_{IIc}} = 1 \tag{4.14}$$

where the energy components G_I and G_{II} are given by

$$\text{If } \sigma_I > 0, \qquad G_I = \frac{\sigma_{eI}\delta_{u,Im}}{2}; \qquad G_{II} = \frac{|\tau|\delta_{u,IIm}}{2} \tag{4.15}$$

$$\text{If } \sigma_I < 0, \qquad G_I = \frac{\sigma_I\delta_{u,Im}}{2}; \qquad G_{II} = \frac{\sigma_{eII}\delta_{u,IIm}}{2} \tag{4.16}$$

where $\delta_{u,Im}$ and $\delta_{u,IIm}$ represent the ultimate relative displacements in each mode leading to failure under mixed mode loading. Therefore, equivalent ultimate relative displacement under mixed-mode loading to total failure is given by,

$$\delta_{u,m} = \sqrt{{\delta_{u,Im}}^2 + {\delta_{u,IIm}}^2} \tag{4.17}$$

Recreating Eq. (3.21) involves replacing the pure mode relative displacements ($\delta_i, \delta_{o,i}, \delta_{u,i}$), with their equivalent mixed-mode counterparts ($\delta_m, \delta_{o,m}, \delta_{u,m}$). This substitution leads to the revised expression for damage.

$$D = D_m = \frac{\delta_{um}(\delta_m - \delta_{om})}{\delta_m(\delta_{um} - \delta_{om})} \tag{4.18}$$

4.4 Tangent Stiffness Matrix

In structures composed of a single material, the failure behaviour can typically be captured by employing either the secant stiffness or tangent stiffness matrix. However, for structures comprising multiple materials, only the tangent stiffness matrix can accurately predict the global load-displacement behaviour. The use of secant stiffness in such cases fails to demonstrate softening behaviour. Hence, implementing the tangent stiffness matrix is the most efficient choice. The internal force vector is given by,

$$\mathbf{F}^{int} = \int_{V} \boldsymbol{B}^{\mathrm{T}}\,(\mathbf{x})\boldsymbol{\sigma}(\mathbf{x})\mathrm{d}V(\mathbf{x}) = \int_{V_p} \boldsymbol{B}_p^{\mathrm{T}}\,\boldsymbol{\sigma}_p \mathrm{d}V_p \tag{4.19}$$

Tangent Stiffness

$$\boldsymbol{K}_T = \frac{\partial \mathbf{F}^{int}}{\partial \mathbf{U}} = \frac{\partial}{\partial \mathbf{U}}\left(\int_{V_p} \boldsymbol{B}_p^{\mathrm{T}}\,\boldsymbol{\sigma}_p \mathrm{d}V_p \right) \tag{4.20}$$

With the inclusion of nonlocal effects in the constitutive law, expressing stress as a function of damage and strains from neighboring points becomes more intricate. Consequently, deriving the tangent stiffness matrix is less straightforward compared to local theories.

$$\frac{\partial \boldsymbol{\sigma}}{\partial \mathbf{U}} = \int_{V_q}\int_{V_z} W_{pq}W_{qz}\big(\mathbb{C}_0(1-D_z)\big)^{\mathrm{T}}\left(\frac{\partial \boldsymbol{\varepsilon}_q}{\partial \mathbf{U}}\right) - (\mathbb{C}_0)^{\mathrm{T}}\boldsymbol{\varepsilon}_q \frac{\partial D_z}{\partial \mathbf{U}} \mathrm{d}V_q \mathrm{d}V_z \tag{4.21}$$

where,

$$\frac{\partial D_z}{\partial \mathbf{U}} = \left(\frac{\partial D}{\partial \delta_m}\right)_z \left(\frac{\partial \delta_m}{\partial \boldsymbol{\varepsilon}}\right)_z^{\mathrm{T}} \frac{\partial \boldsymbol{\varepsilon}_z}{\partial \mathbf{U}} \tag{4.22}$$

Substituting Eqs. (4.21) and Eq. (4.22) in (4.20) and applying the numerical integration process to tangent stiffness matrix is shown as,

$$\begin{aligned}\boldsymbol{K}_T = \sum_{p=1}^{ngp}\sum_{q=1}^{ngp}\sum_{z=1}^{ngp} w_p w_q w_z W_{pq} W_{qz} \Bigg(\big(\mathbb{C}_0(1-D_z)\big)^{\mathrm{T}}\left(\frac{\partial \boldsymbol{\varepsilon}_q}{\partial \mathbf{U}}\right) \\ - (\mathbb{C}_0)^{\mathrm{T}}\boldsymbol{\varepsilon}_q \left(\frac{\partial D}{\partial \delta_m}\right)_z \left(\frac{\partial \delta_m}{\partial \boldsymbol{\varepsilon}}\right)_z^{\mathrm{T}} \frac{\partial \boldsymbol{\varepsilon}_z}{\partial \mathbf{U}} \Bigg) detJ_z detJ_q detJ_p\end{aligned} \tag{4.23}$$

In adhesive bonded problems, it is established that damage propagation occurs exclusively within the adhesive region. Consequently, the elements in the adherends that are not influenced by damage in the adhesive region do not experience any change in their stiffness during the deformation process. Therefore, it is only necessary to construct the stiffness (secant) matrix for these regions once before commencing the incremental-iterative (Newton-Raphson) procedure. This approach significantly reduces the computational burden, even when employing refined meshes.

4.5 Numerical Examples

In this section, initially, a mode I problem is solved to validate the formulations and procedures of the proposed nonlocal approach in this work. Following this, the subsequent two examples are addressed to emphasize the advantages of utilizing the nonlocal integral approaches over conventional FEM.

4.5.1 Double cantilever beam test

The continuum mixed-mode damage model is employed in the analysis of a double cantilever beam (DCB), subjected to pure mode I loading. This selection of the problem aims to validate the nonlocal formulations and their implementation procedures. The geometry of the double cantilever beam (DCB), as depicted in Fig. 4.2, is adopted from [141], with dimensions specified as follows: $L = 100$ mm, $a_0 = 30$ mm, $h = 1.5$ mm, $t = 0.2$ mm and width $B = 10$ mm. The properties of both the adherend and adhesive materials are provided in Table 4.1 for numerical analysis.

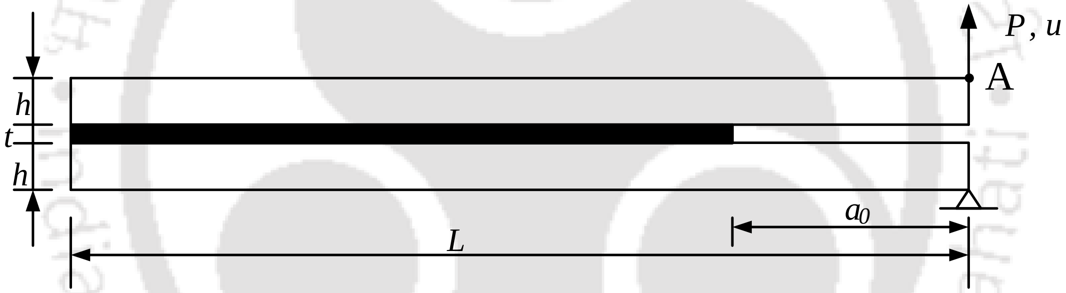

Fig. 4.2. Adhesively bonded DCB specimen: geometry, dimensions, loading and boundary conditions

Numerical simulations are carried out using four-node quadrilateral elements in both adherend and adhesive. Plane stress conditions are assumed. The mesh related details are provided in Table 4.2. The influence radius (R), that covers the neighbouring elements to participate in process of finding stresses is taken as 0.1 mm. Quartic functions are used as weight functions for all the case studies in this work.

Table 4.1 Material properties used for DCB test

	E (GPa)	ν	σ_u (MPa)	τ_u (MPa)	G_{Ic} (N/mm)	G_{IIc} (N/mm)
Adhesive	4.0	0.3	20	20	0.3	0.6
Adherend	210.0	0.3	–	–	–	–

Fig. 4.3 displays the load-displacement response obtained through both nonlocal and local FEM, which is then compared with the reference results. It can be observed that the nonlocal results align closely with conventional FEM results and exhibit good agreement with the reference data. This demonstrates the accuracy of the numerical procedure, nonlocal constitutive law and the implementation procedure of tangent stiffness matrix. Consequently, these validated procedures can be reliably applied to subsequent case studies. Two meshes, labeled as A and B, are utilized to demonstrate the mesh independence achieved by the nonlocal FEM.

Table 4.2 Material properties used for DCB test

Mesh	Adherend (mm)	Adhesive (mm)	Total no.of elements
A	0.25×0.75	0.25×0.2	1880
B	0.1×0.75	0.1×0.2	4700

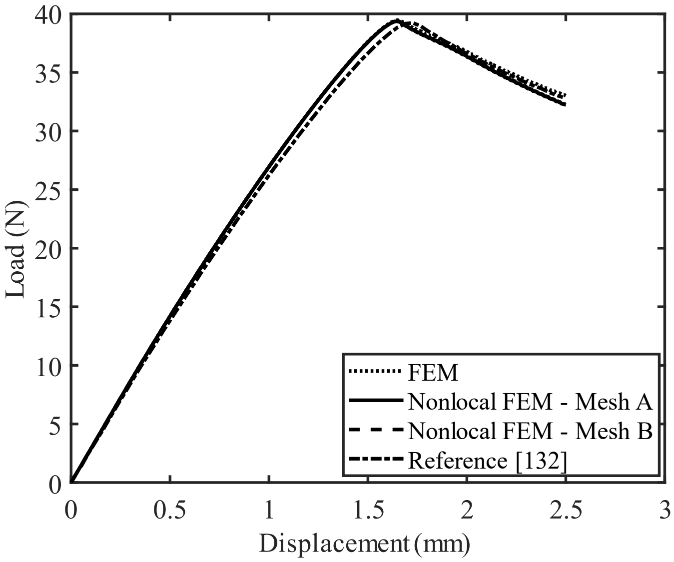

Fig. 4.3. Load-displacement response: comparison of FEM, nonlocal FEM with reference results

In Fig. 4.4(a) and 4.4(b), stress contours in the mode I direction are presented at displacements of $u = 0.55$ mm and $u = 1.65$ mm, respectively. The former depicts the stress distribution within the linear elastic region, while the latter illustrates the stress distribution at the peak load. Fig. 4.4(a) shows maximum stresses within the adhesive element adjacent to the notch, coinciding with the initiation of damage. Subsequent loading induces progressive damage evolution, leading to a gradual reduction in stress within that element. This reduction ultimately tends towards zero when the element is entirely damaged, as depicted in Fig. 4.4(b). On the contrary, there is an observable phenomenon where the maximum stresses gradually shift away from the notch as the loading progresses, suggesting the initiation of damage within that particular element.

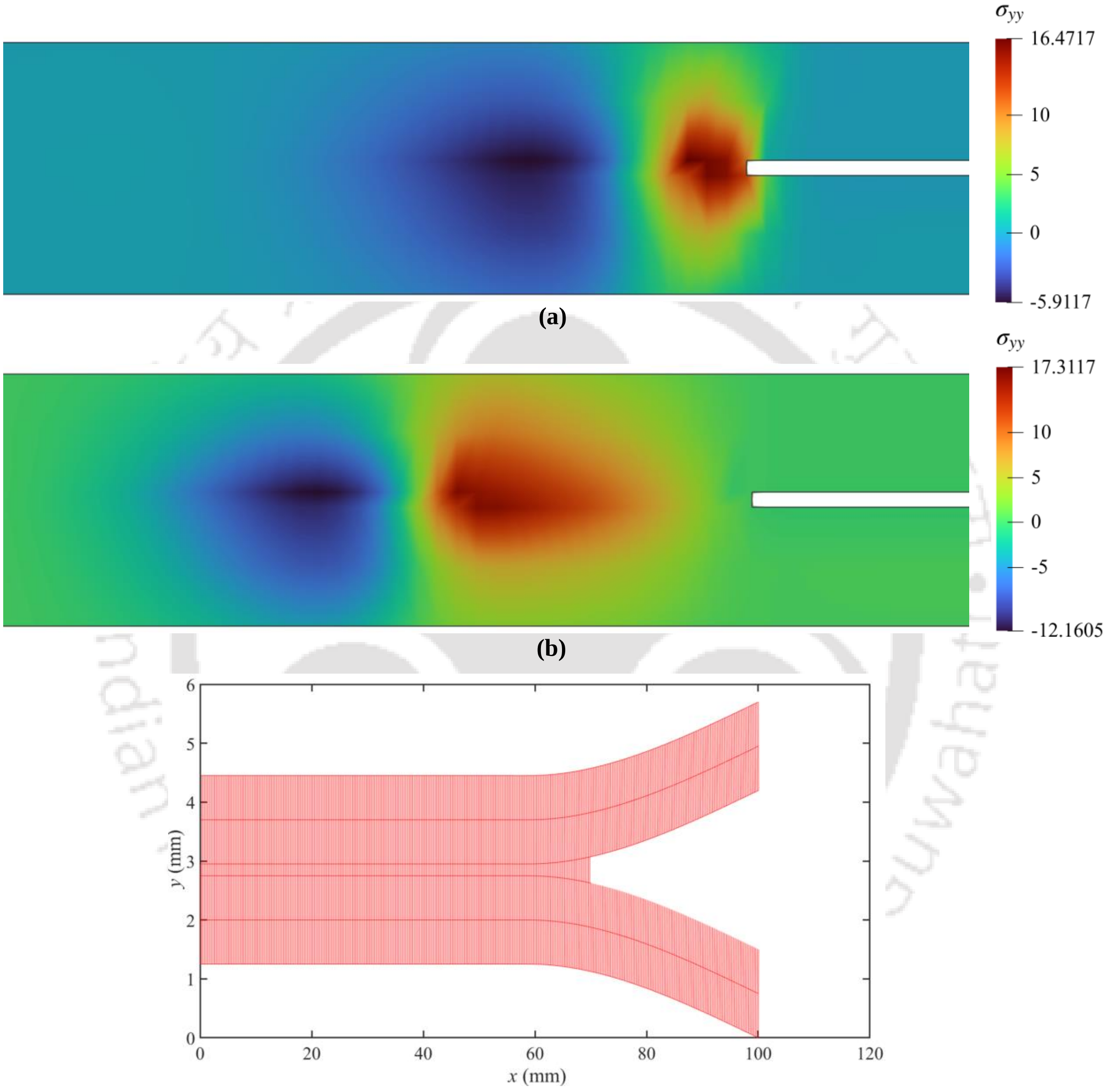

(a)

(b)

(c)

Fig. 4.4. (a) Contour plots of stresses in y-direction at $u = 0.55$ mm, **(b)** $u = 1.65$ mm for the DCB test, and **(c)** Deformed plot of adhesively bonded DCB specimen for mesh A

Fig. 4.4(a) and 4.4(b) also illustrates that as the peeling/loading process progresses, compressive stresses emerge in the vicinity of the crack propagation area. When a load is applied at the free end, the notched portion of the top adherend displaces vertically, as shown in Fig. 4.4(c).

This movement leads to the imposition of compressive loads on the region adjacent to the crack propagation area causing compressive stresses there. Moreover, it is evident from the Fig. 4.4(b) that there exists a positive correlation between the level of displacement loading and the corresponding increase in compressive stresses.

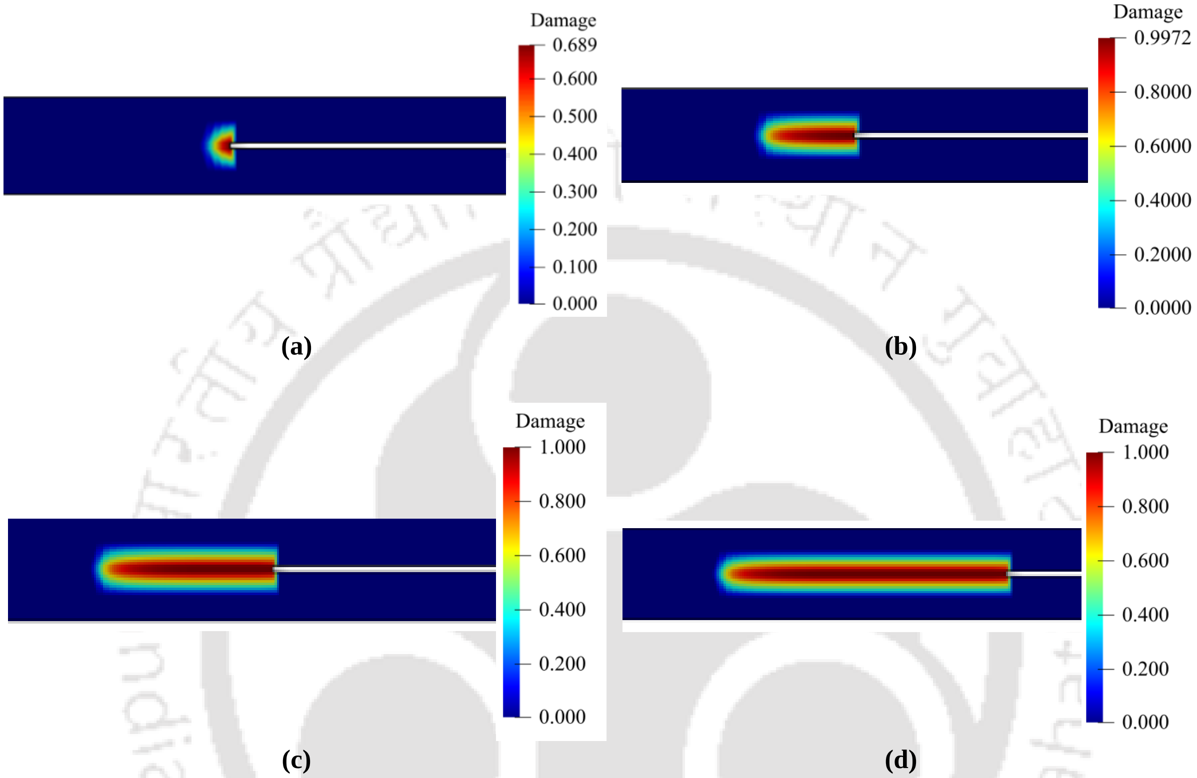

(a) **(b)**

(c) **(d)**

Fig. 4.5. Damage evolution in the adhesive region at a displacement of (a) 0.55 mm, (b) 1.65 mm, (c) 2.00 mm and (d) 2.50 mm

Fig. 4.5 presents the damage evolution in the refined mesh, illustrated through contour plots. During the analysis, damage in the adhesive elements begins at a displacement of 0.27 mm and progresses from there. Fig. 4a shows the damage evolution at a displacement of 0.55 mm, with a maximum damage of 0.689. In Fig. 4b, at the peak load and a displacement of 1.65 mm, the maximum damage reaches 0.9972, after which stiffness begins to decrease. Fig. 4c illustrates the damage evolution at a displacement of 2.00 mm, where some adhesive elements have reached a damage level of 1, indicating that their stiffness has become zero.

4.5.2 Double cantilever beam with sharp crack

In this example, numerical analysis is conducted to investigate the mode I failure of a notched DCB specimen featuring a sharp crack within the adhesive, which is considered as a defect. The primary objective is to showcase the importance of utilizing a strain-based nonlocal model in capturing the strain-softening behaviour exhibited by the material. The geometry, boundary and loading conditions, and material properties for this analysis follow those utilized in the previous example.

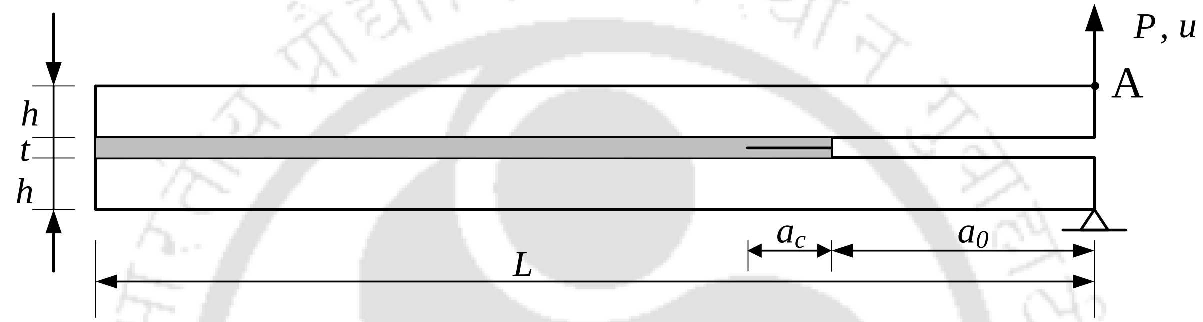

Fig. 4.6. Adhesively bonded DCB specimen with sharp crack: geometry, dimensions, loading and boundary conditions

Due to the presence of a cohesive crack, as illustrated in Fig. 4.6, the adhesive material is discretized into two elements in the thickness direction, while the mesh size in the length direction is varied. Table 4.3 presents the different mesh sizes utilized for the convergence study.

Table 4.3. Mesh sizes used for DCB with sharp crack

Mesh size	**Adherend (mm)**	**Adhesive (mm)**	**Total no.of elements**
A	0.1×0.75	0.1×0.1	5400
B	0.05×0.75	0.05×0.1	7742
C	0.025×0.75	0.025×0.1	10880

The selection of the influence radius is guided by two primary considerations. Firstly, the radius should be chosen to ensure that the stiffness of the load-displacement response remains unchanged when compared with the reference/conventional FEM results, thereby preserving the integrity of the analysis results. Secondly, to minimize computational time while still providing accurate and reliable results. Based on these considerations, the influence radius has been set at 0.025 mm.

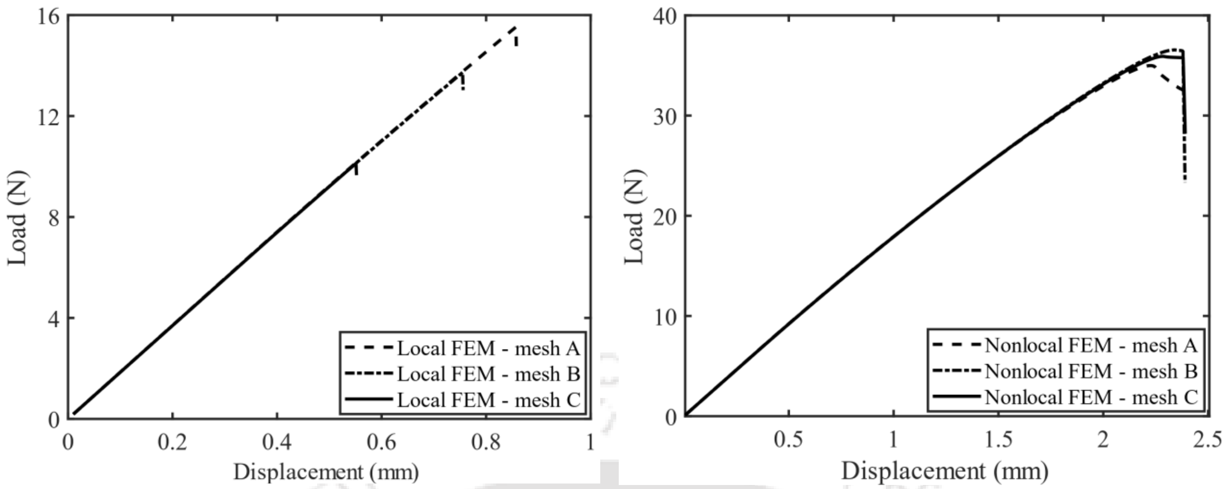

(a) **(b)**

Fig. 4.7. Load-displacement response: **(a)** Local FEM, and **(b)** Nonlocal FEM

Fig. 4.7(a) and 4.7(b) illustrate the load-displacement responses obtained for various meshes within both local and nonlocal finite element method (FEM) frameworks. Notably, it is observed that results obtained via conventional FEM exhibit high sensitivity to mesh resolution, a characteristic commonly associated with the solution of problems involving sharp cracks. In contrast, the proposed nonlocal constitutive model demonstrates significantly reduced variation in peak loads across different mesh configurations, indicating its mesh independence.

(a) $u = 0.5$ mm

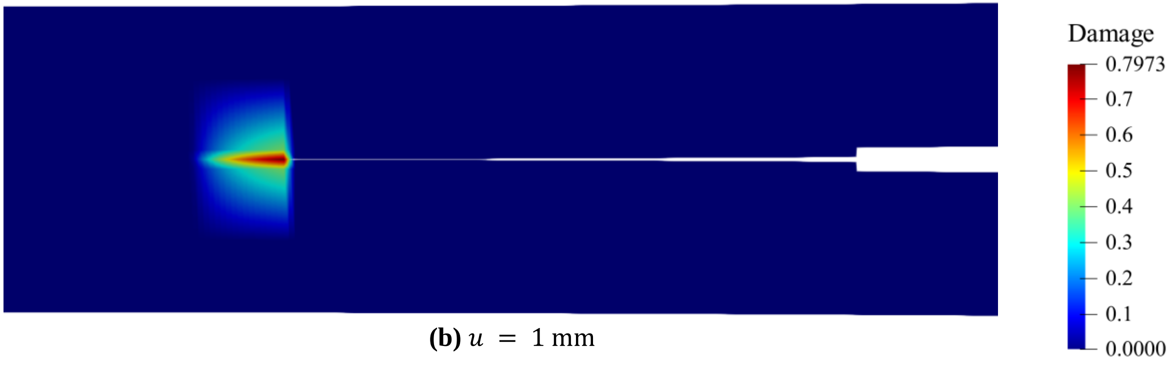

(b) $u = 1$ mm

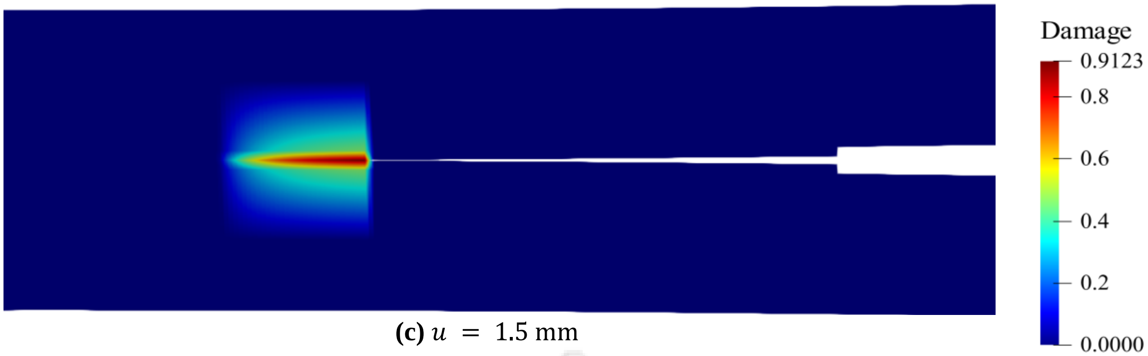

(c) $u = 1.5$ mm

Fig. 4.8. Damage contour plots at respective displacements for mesh B

Fig. 4.8 displays the damage contours at different displacements within the deformed configuration. The inclusion of deformed plots serves the purpose of illustrating how damage evolves as the sharp crack within the adhesive elongates. From Fig. 4.8(a), it is evident that damage initiation occurs near the crack tip, coinciding with the separation of the adhesive material adjacent to the notch. Moreover, Fig. 4.8(b) illustrates the uniform propagation of damage within the adhesive region, accompanied by its uniform spreading to the surrounding areas. On the other hand, when the loading is applied to the top adherend, the initiation of damage occurs initially in the upper portion of the adhesive elements. Subsequently, this damage gradually spreads to the lower portion of elements within that region while concurrently propagating along the crack path, as depicted in Fig. 4.8(c). Nevertheless, it is noteworthy that the damage spread near the top portion of the adhesive layer is not uniform. In a particular location, there is a lesser influence of damage, leading to localized variations in damage distribution. However, beyond these specific locations, the damage propagation resumes its uniform pattern. Indeed, the observed non-uniformity in damage spread near the top portion of the adhesive layer appears to be more of a numerical artifact rather than a physical phenomenon. It is possible that this effect is negligible, as it does not manifest as a significant difference in the load-displacement responses or their convergence. Sometimes, this might also be due to the choice of the increment size, which in this case is taken as 0.01 mm for the numerical analysis on mesh B. Opting for a smaller increment size can potentially yield a more stable and accurate representation of damage propagation. However, this comes at the expense of increased computational time.

4.5.3 Biadhesive single-lap joint

The stress concentrations at the ends of the overlap are influenced by the stiffness of the adhesive used in the bonded joints. Stress concentrations at ends of overlap can be reduced by using fillets, gradual reduction of adherend material, biadhesives and several other methods can be used of all the methods, use of biadhesive is the effective and easier way. The lower the stiffness of the adhesive used, the lower will be the stress concentrations which leads to higher joint strength. A low modulus adhesive is used at the ends of the overlap and a structural adhesive is used in the middle (see Fig. 4.9). The adhesive properties and overlap length details are adopted from [152]: $L_0 = 2L_1 + L_2$ where $L_1 = 6.25$ mm, $L_2 = 12.5$ mm i.e., $L_1/L_2 = 0.5$. Young's modulus is reduced by 60% i.e., $E1/E2 = 0.4$. The adherend and adhesive material properties are mentioned in Table 4.4 for numerical analysis. The adherends used are of aluminium and adhesives used are brittle epoxy araldite AV138 and Araldite 2015.

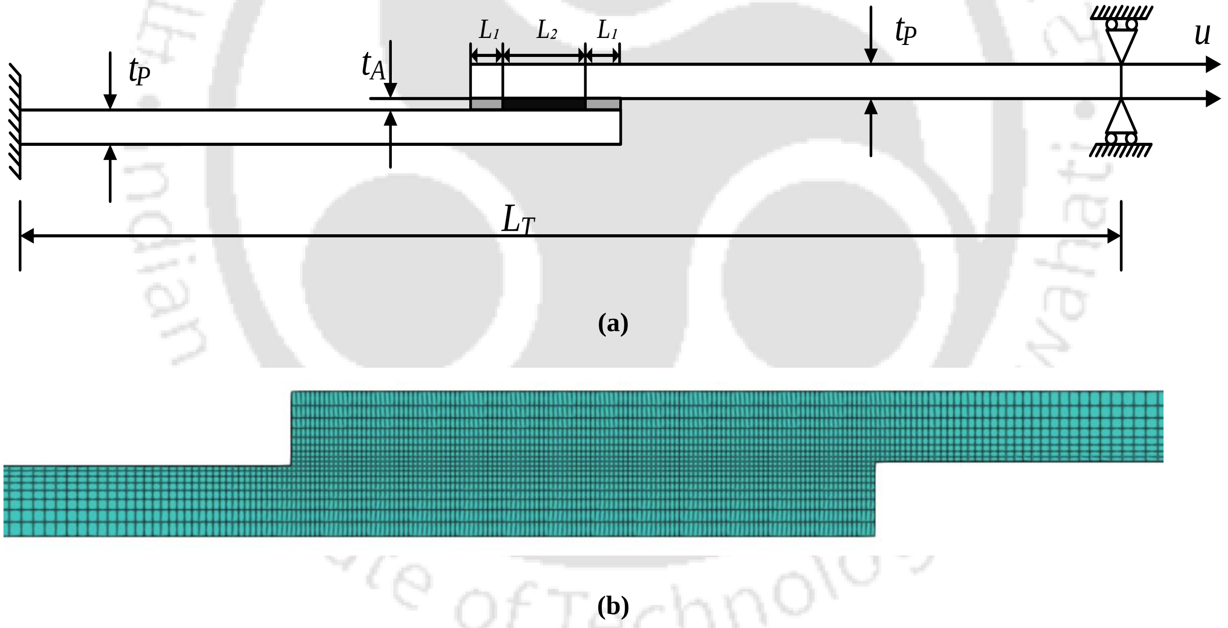

Fig. 4.9. Biadhesive single-lap joint specimen: **(a)** geometry, dimensions, loading and boundary conditions, and (b) mesh (3773 elements)

The plane strain condition is assumed. Regarding the mesh, uniform pattern of elements are followed in adhesive region, while biased meshing is employed in the adherends to optimize computational time. Four meshes are employed to study the mesh convergence of the proposed nonlocal constitutive model. The mesh details are given in Table 4.5.

Table 4.4. Material properties of biadhesive single lap joint

	E (GPa)	ν	σ_u (MPa)	τ_u (MPa)	G_{Ic} (N/mm)	G_{IIc} (N/mm)
AV138	4.89	0.35	39.45	30.2	0.2	0.38
Araldite 2015	1.85	0.33	21.63	17.9	0.43	4.70
Aluminium	70	0.34	–	–	–	–

Table 4.5. Mesh sizes in biadhesive region

Mesh	Adhesive (mm)	Total no.of elements
A	0.2 × 0.2	3773
B	0.1 × 0.2	6670
C	0.05 × 0.2	10692
D	0.025 × 0.2	19496

Fig. 4.10(a) and 4.10(b) illustrates the load-displacement responses obtained for various meshes through local and nonlocal FEM. It is evident that the load-displacement results obtained through conventional FEM encounter iterative convergence issues and abruptly abort from the numerical analysis for the first three meshes. However, the analysis completes successfully for the refined mesh consisting of 19496 elements. An intriguing aspect is that, since the mesh A is relatively coarser than the others, there are no neighboring elements within the influence radius. Consequently, the only neighbor element is the specific element itself, resembling standard FEM analysis. Nonetheless, the nonlocal approach effectively completes the entire analysis.

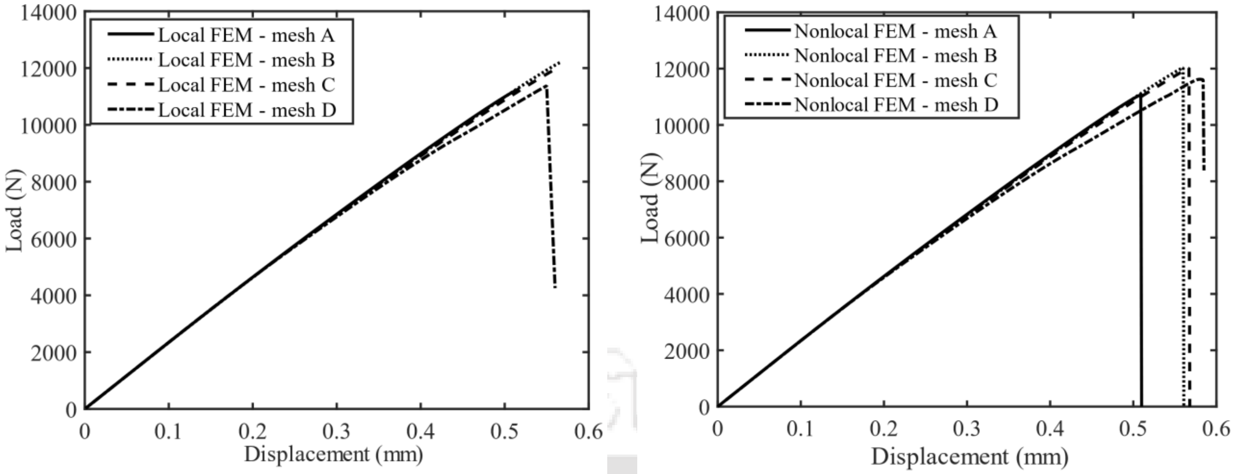

(a) **(b)**

Fig. 4.10. Load-displacement response: **(a)** Local FEM, and **(b)** Nonlocal FEM

Though we cannot say the proposed approach achieves complete mesh independence, it is noteworthy that there is not a significant difference in the peak loads between meshes B, C, and D. There is a slight decrease in stiffness observed in the refined mesh D, possibly due to the mesh size of 0.2 mm x 0.025 mm. It is worth mentioning that Sugiman and Ahmad [144] in his works recommended maintaining an aspect ratio of 1. However, following this increases the number of elements and consequently the computational time when employing the nonlocal approach. Moreover, the proposed approach yields reasonably close responses for both relatively medium and refined meshes.

Fig. 4.11 displays the stress distributions in the yy and xy directions along the overlap length at $u = 0.35$ mm. Due to the local FEM aborting from the analysis abruptly, the stress distributions are plotted immediately after damage initiation to facilitate a smooth comparison between the local and nonlocal approaches. Given that all meshes yield reasonably close peak load values, mesh C is selected to plot the stress distributions. The regularization process applied to the constitutive law results in stresses at the boundaries or corners of the overlap region being slightly lower than those obtained with the local approach (see Fig. 4.11(a) and 4.11(c)). This regularization effectively controls the stresses and mitigates instability, unlike traditional FEM methods.

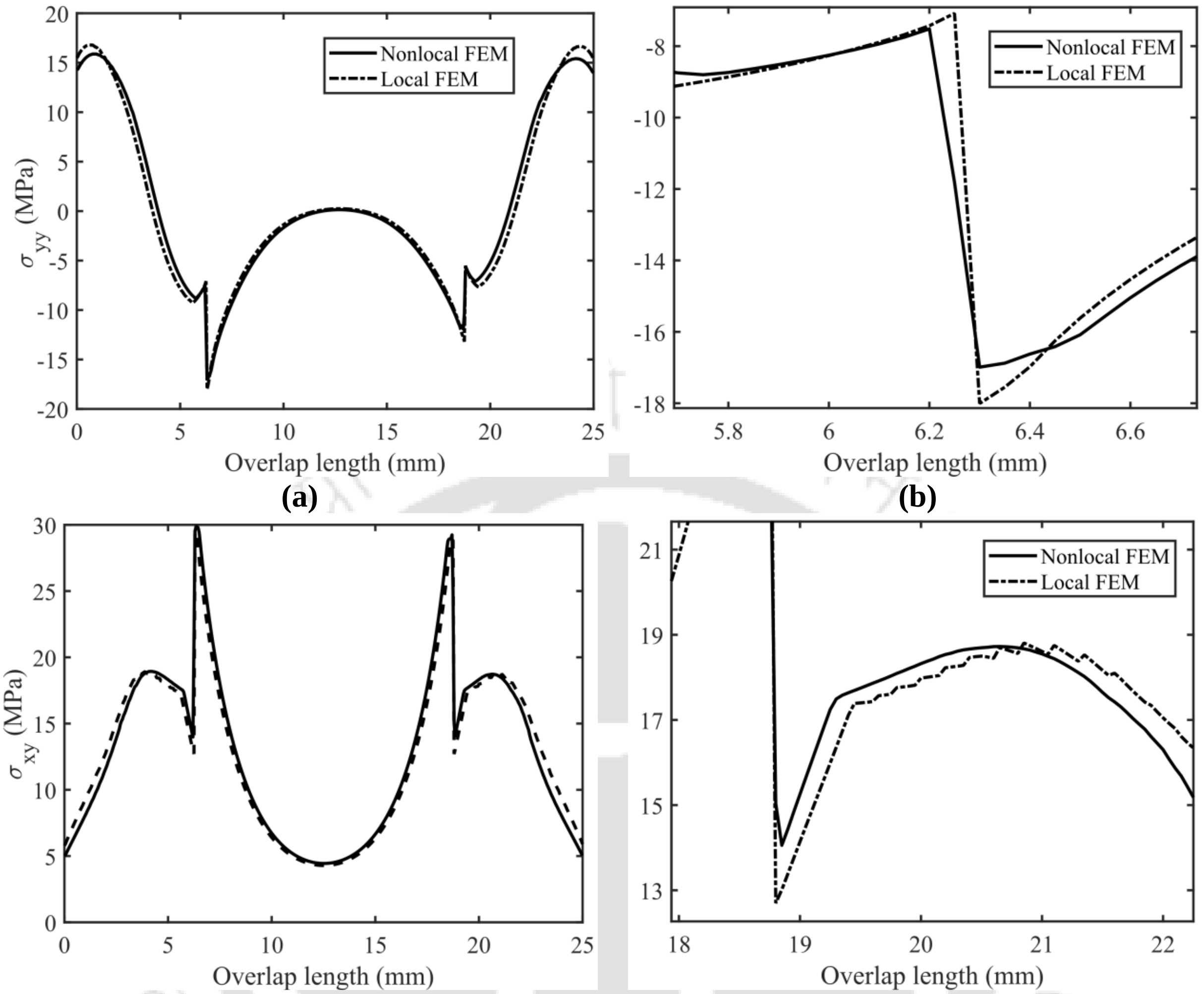

(a) (b)

(c) (d)

Fig. 4.11. Stress distributions along the overlap length for mesh C: **(a)** σ_{yy} distribution, **(b)** zoomed view of σ_{yy}, **(c)** σ_{xy} distribution, and **(d)** zoomed view of σ_{xy} at the upper region of adhesive interface

Fig. 4.11(b) illustrates the comparative behaviour of both local and nonlocal approaches at the interface of the adhesives. As discussed previously, the local FEM exhibits a sudden drop at the interface, whereas the proposed nonlocal model displays intermediate values between the transition from the lower Young's modulus adhesive to the higher one. This continuous nature of stresses significantly contributes to the efficient completion of the entire analysis. On the contrary, the shear stresses exhibit a smooth behaviour immediately after the interface region in the proposed nonlocal model (see Fig. 4.11(d)), whereas local FEM begins to display a discontinuous nature even in the uniform material. This behaviour is observed just after the damage initiation, and as the load progresses, these effects may further intensify, potentially contributing to its failure to achieve iterative convergence.

This analysis represents an initial stage. However, a more thorough study is required, taking into consideration essential parameters for optimizing the design of the biadhesive joint. Such an extensive investigation can better ensure the production of mesh-independent results and contribute to a deeper understanding, as well as improved design methodologies.

4.6 Summary

This work highlights the application of nonlocal integral theories in capturing the failure behaviour of adhesively bonded joints. Numerical analysis to assess the performance of the proposed methodology is conducted using continuum damage models proposed by Chousal and de Moura (2013) within a nonlocal FEM framework. The total strain is employed as the nonlocal variable, and ensuring thermodynamic consistency for successful derivation of a nonlocal constitutive law is achieved. Utilizing this proposed constitutive law, the construction and efficient implementation of the tangent stiffness matrix, crucial for capturing the material nonlinear behaviour of multimaterial system, is demonstrated. To reduce the computational time and effectively utilize the proposed constitutive law, the tangent stiffness is computed for every iteration only in the adhesive and adhered regions influenced by them. The stiffness of the rest of the geometry remains constant throughout as they remain in the linear elastic regime. Upon analysis, the nonlocal approach showcases mesh-independent results with minimal variation in peak loads across all employed meshes.

Chapter 5

Damage Modelling in Quasi-brittle Materials using Strain Difference -based Nonlocal Approach

The present chapter extends the strain difference-based nonlocal approach to continuum damage mechanics (CDM) theories for predicting the failure behaviour of quasi-brittle materials. The strain difference approach is adopted for two reasons: (i) similar to strain, it also maintains physical realism and indirectly incorporates nonlocal effects while computing both the damage variable and the damage energy release rate, and (ii) the constitutive model maintains a symmetry nature in constructing the nonlocal part of the stiffness matrix, reducing the computational cost in strain-softening problems. The state and damage evolution equations for the present nonlocal approach are formulated within the thermodynamic framework. Additionally, the chapter demonstrates the effectiveness of the proposed approach with the treatment of several 2D and 3D examples, and comparing the obtained numerical results with experimental data from the literature.

5.1 Introduction

In nonlocal theories, despite the physical realism and mesh independence achieved through strain regularization, it still struggles to accurately predict the structural response (shown and discussed in the numerical examples section). On the other hand, as discussed in Section 3.2, the attenuation function of Eq. (3.34) is symmetric but cannot alleviate boundary effects. Conversely, the weight function of Eq. (3.37) overcomes boundary effects but introduces a nonsymmetric stiffness matrix, posing a computational burden. At the same time, researchers have regularized the several variables responsible for the irreversible processes to ensure a well-posed boundary value problem in the softening regimes.

Jirásek [100] opted for averaging the damage energy release rate for computationally efficiency and explicitly constructed a nonsymmetric consistent tangent stiffness matrix. Continuing from there, Comi and Perego [101] utilized dual nonlocal variables, incorporating damage and its conjugate thermodynamic force. They derived the symmetric consistent tangent matrix, highlighting its symmetry only when both the damage and internal variables follow associative evolutions. Similarly, Borino et al.[228], employing the concept of dual nonlocal variables, redefined the spatial weight function by incorporating local and nonlocal contributions, enabling the derivation of a symmetric tangent operator, with the damage variable considered as the nonlocal component. Giry et al. [104] proposed the stress-based nonlocal damage model, where each point influences its surrounding region based on the magnitude and direction of its principal stresses, and the model also tailors the regularization near free boundaries. In this context, He et al. [229] regularized the equivalent strain and adopted Borino et al.'s [228] spatial weight function to mitigate boundary effects. However, it requires finer mesh sizes in regions with strain localization, limiting large-scale applicability.

To the best of the authors' knowledge, there have been limited efforts to enhance the performance of strain-based nonlocal approaches in damage mechanics for capturing post-peak behaviour. Indeed, from a physical perspective, it is reasonable to consider strain as a nonlocal variable due to its significant role in deformation processes. Moreover, this approach indirectly incorporates nonlocal effects into the damage variable and the damage energy release rate. In this work, for the first time, the strain difference-based nonlocal model, adopted from Polizzotto et al.'s [18] linear elastic work, is employed to predict failure behaviour and damage/crack propagation in quasi-brittle materials within the thermodynamic framework of continuum damage mechanics (CDM) theories.

In most of the works, the nonlocal elemental stiffness matrices exhibit asymmetry, i.e., $k_{pq} \neq \left(k_{qp}\right)^{\mathrm{T}}$, resulting in the computation and assembly of the stiffness matrix for each neighbouring element (q) relative to the current element (p), incurring significant computational costs. The strain difference-based nonlocal constitutive model inherently produces a symmetric cross-stiffness element matrix $\left(k_{pq} = \left(k_{qp}\right)^{\mathrm{T}}\right)$, thus alleviating the computational burden. This reduction is particularly valuable in strain-softening problems where incremental-iterative techniques are employed until specimen failure. Furthermore, under certain assumptions, the thermodynamic formulation of the present model demonstrates that the energy residual function is independent of both reversible and irreversible processes. Various 2D and 3D numerical examples are solved: (i) to study the influence of nonlocal parameter 'α' on the damage distribution for the same interaction radius, and (ii) to show the effectiveness of the present approach in capturing the failure behaviour and damage/crack paths of quasi brittle materials while maintaining the mesh independency with significantly fewer iterations using secant stiffness matrix.

5.2 Strain difference-based nonlocal integral approach

To ensure compliance with the normalization condition throughout the volume and enhance computational efficiency, Polizzotto et al., [18,230] introduced a nonlocal model based on strain differences, as follows:

$$\mathcal{R}\big(\boldsymbol{\varepsilon}(\mathbf{x})\big) = \int_V g(\mathbf{x}, \mathbf{x}')\,\big(\boldsymbol{\varepsilon}(\mathbf{x}') - \boldsymbol{\varepsilon}(\mathbf{x})\big)\mathrm{d}V(\mathbf{x}') \qquad \forall \mathbf{x} \in V \tag{5.1}$$

which represents the excess of strain at neighbouring point with respect to the target point. The internal energy potential for the assumed nonlocal material is expressed as a function of local strain and averaged strain difference, given by

$$U = U(\boldsymbol{\varepsilon}, \mathcal{R}(\boldsymbol{\varepsilon}), D) \tag{5.2}$$

5.2.1 Thermodynamic framework

It is to be noted that in many research works, when incorporating damage or other internal variables for regularization, the commonly held view is that nonlocality becomes active only when irreversible processes occur [205,228]. Alternatively, by integrating nonlocality into the first law of thermodynamics, it can also be physically interpreted as the result of long-range energy exchange among particles, which underlies the material's nonlocal behaviour regardless of whether processes are reversible or irreversible. In other words, during reversible process the material at point **x** transmits energy to the neighbouring points within volume *V*. However, in the irreversible case, only a portion of this energy is conveyed to the neighbouring points, with the remainder dissipating outside. Though the mathematical formulations of all the works are identical, the interpretation of the underlying physics can vary [203]. Referring to the consequence of the nonlocal nature of the material, the authors felt that choosing strain, which is the source of deformation and damage evolution processes, as the nonlocal variable is a reasonable choice.

As discussed earlier in Section 3.2.1, nonlocal theories necessitate extending the application of the dissipation inequality to the entire volume V to maintain consistency with the second law of thermodynamics (refer to Eq. (3.38)). However, it remains acceptable to violate the local form of the inequality by introducing the nonlocal energy residual. Thus, the dissipation inequality in the present context can be expressed as follows:

$$\phi = \boldsymbol{\sigma}:\dot{\boldsymbol{\varepsilon}} - \frac{\partial\psi}{\partial\boldsymbol{\varepsilon}}:\dot{\boldsymbol{\varepsilon}} - \frac{\partial\psi}{\partial\mathcal{R}(\boldsymbol{\varepsilon})}:\mathcal{R}(\dot{\boldsymbol{\varepsilon}}) - \frac{\partial\psi}{\partial D}\dot{D} - \frac{\partial\psi}{\partial\xi}\dot{\xi} + P \geq 0 \quad \text{in } V \tag{5.3}$$

The bilinear form in terms of independent local variables is given by,

$$\phi = \boldsymbol{X}:\dot{\boldsymbol{\varepsilon}} + Y\dot{D} - \chi\dot{\xi} \geq 0 \quad \text{in } V \tag{5.4}$$

where, the damage energy release rate $\left(Y = -\frac{\partial\psi}{\partial D}\right)$ and the associated force $\left(\chi = \frac{\partial\psi}{\partial\xi}\right)$ act as the conjugates for the damage (D) and damage hardening (ξ) variables. Comparing Eqs. (2.1) and (5.4), the energy residual P is obtained as

$$P = \boldsymbol{X}:\dot{\boldsymbol{\varepsilon}} - \boldsymbol{\sigma}:\dot{\boldsymbol{\varepsilon}} + \frac{\partial\psi}{\partial\boldsymbol{\varepsilon}}:\dot{\boldsymbol{\varepsilon}} + \frac{\partial\psi}{\partial\mathcal{R}(\boldsymbol{\varepsilon})}:\mathcal{R}(\dot{\boldsymbol{\varepsilon}}) \quad \text{in } V \tag{5.5}$$

Recalling both the insulation condition and Green's identity, we proceed by defining the nonlocal associated variable $\boldsymbol{X}$, which allows for the rewriting of the dissipation inequality of Eq. (5.4) as,

$$\phi = \left(\boldsymbol{\sigma} - \frac{\partial\psi}{\partial\boldsymbol{\varepsilon}} - \mathcal{R}\left(\frac{\partial\psi}{\partial\mathcal{R}(\boldsymbol{\varepsilon})}\right)\right):\dot{\boldsymbol{\varepsilon}} + Y\dot{D} - \chi\dot{\xi} \geq 0 \tag{5.6}$$

Following the established procedures [231], assuming the reversible processes the constitutive law is defined as,

$$\boldsymbol{\sigma} = \frac{\partial\psi}{\partial\boldsymbol{\varepsilon}} + \mathcal{R}\left(\frac{\partial\psi}{\partial\mathcal{R}(\boldsymbol{\varepsilon})}\right) \qquad \text{in } V \tag{5.7}$$

Thus,

$$P = \frac{\partial\psi}{\partial\mathcal{R}(\boldsymbol{\varepsilon})}:\mathcal{R}(\dot{\boldsymbol{\varepsilon}}) - \mathcal{R}\left(\frac{\partial\psi}{\partial\mathcal{R}(\boldsymbol{\varepsilon})}\right):\dot{\boldsymbol{\varepsilon}} \qquad \text{in } V \tag{5.8}$$

It is evident that the expressions derived for stress and nonlocal energy residual are the same as those achieved through a reversible process, as demonstrated in the works of Polizzotto et al. [18]. This similarity arises because damage alone cannot account for the irreversible strains [205]. Consequently, it is assumed that the unloading of material from a damaged state follows a reversible path, resulting in strains that are themselves reversible. Therefore, the state equations and the determination of 'P' can also be alternatively obtained using Eq. (2.1) while considering reversible conditions. Finally, the dissipation inequality is given by

$$\phi = Y\dot{D} - \chi\dot{\xi} \geq 0 \tag{5.9}$$

5.2.2 Damage evolution laws – continuum approach

Considering the inelasticity effects by introducing the damage hardening variable (ξ), the Helmholtz free energy potential can be expressed now as,

$$\psi = \psi_e(\boldsymbol{\varepsilon}, \mathcal{R}(\boldsymbol{\varepsilon}), D) + \psi_{in}(\xi) \tag{5.10}$$

here, ψ_e stands for the strain energy density of damaged material, while ψ_{in} pertains to the inelastic component of free energy. In the case of ψ_{in}, it encapsulates the energy stored in the microstructure, reflecting changes in the material's internal characteristics [204].

Following the conditions provided by Polizzotto *et al.* [18], the elastic strain energy density function for a damaged material is expressed as:

$$\psi_e = \frac{1}{2}\boldsymbol{\varepsilon}:(1-D)\mathbb{C}_0:\boldsymbol{\varepsilon} + \frac{\alpha}{2}\mathcal{R}(\boldsymbol{\varepsilon}):(1-D)\mathbb{C}_0:\mathcal{R}(\boldsymbol{\varepsilon}) \tag{5.11}$$

$$Y = -\frac{\partial \psi_e}{\partial D} = \frac{1}{2}\boldsymbol{\varepsilon}:\mathbb{C}_0:\boldsymbol{\varepsilon} + \frac{\alpha}{2}\mathcal{R}(\boldsymbol{\varepsilon}):\mathbb{C}_0:\mathcal{R}(\boldsymbol{\varepsilon}); \text{ and } \chi = \frac{\partial \psi_{in}}{\partial \xi} \tag{5.12}$$

Building upon the dissipation inequality as described in Eq. (5.9), it is postulated that a damage dissipation potential function (F^D) exists. This function operates in relation to thermodynamic forces Y and ξ, serving the purpose of determining whether damage activation has occurred and, if so, whether the body is in a loading or unloading state through the application of Kuhn-Tucker conditions.

$$F^D(Y,\chi) = Y - \chi \tag{5.13}$$

$$F^D(Y,\chi) \leq 0, \ \ \dot{\lambda} \geq 0, \ \ F^D(Y,\chi)\dot{\lambda} = 0 \qquad in \ \ V \tag{5.14}$$

Recalling normality laws, the evolution equations are defined as,

$$\dot{D} = \dot{\lambda}\frac{\partial F^D(Y,\chi)}{\partial Y}, \text{ and } \ \dot{\xi} = -\dot{\lambda}\frac{\partial F^D(Y,\chi)}{\partial \chi} \tag{5.15}$$

where $\dot{\lambda}$ represents the indeterminate multiplier that needs to be determined through the consistency condition $\dot{F^D} = 0$ by using Eqs. (5.12) and (5.15) and performing necessary operations leads to,

$$\dot{\lambda} = \frac{1}{h}\dot{Y} \tag{5.16}$$

where, $\dot{Y} = \boldsymbol{\varepsilon}:\mathbb{C}_0:\dot{\boldsymbol{\varepsilon}} + \alpha\big(\mathcal{R}(\boldsymbol{\varepsilon}):\mathbb{C}_0:\mathcal{R}(\dot{\boldsymbol{\varepsilon}})\big);$ $\quad h = \frac{\partial^2 \psi_{in}}{\partial \xi^2}$

5.3 Implementation – Secant stiffness matrix and Numerical algorithm

In this section, the derivation and advantages of secant stiffness method is discussed. Further, the numerical algorithm to implement the proposed methodology in FEM is presented.

5.3.1 Secant stiffness matrix

Applying the free energy potential and Eq. (5.1) to the constitutive law, Eq. (5.7), rearranges and forms as:

$$\boldsymbol{\sigma}(\mathbf{x}) = [1 + \alpha\gamma^2(\mathbf{x})](1 - D)\mathbb{C}_0:\boldsymbol{\varepsilon}(\mathbf{x}) - \alpha \int_V \boldsymbol{J}_D(\mathbf{x},\mathbf{x}'):\boldsymbol{\varepsilon}(\mathbf{x}')\mathrm{d}V(\mathbf{x}') \tag{5.17}$$

where,

$$\begin{aligned} \boldsymbol{J}_D(\mathbf{x},\mathbf{x}') &= [\gamma(\mathbf{x})(1 - D(\mathbf{x}))\mathbb{C}_0 + \gamma(\mathbf{x}')(1 - D(\mathbf{x}'))\mathbb{C}_0]g(\mathbf{x},\mathbf{x}') - \boldsymbol{k}_D(\mathbf{x},\mathbf{x}') \\ \boldsymbol{k}_D(\mathbf{x},\mathbf{x}') &= \int_V g(\mathbf{x},\mathbf{z})g(\mathbf{x}',\mathbf{z})(1 - D(\mathbf{z}))\mathbb{C}_0 \,\mathrm{d}V(\boldsymbol{z}) \end{aligned} \tag{5.18}$$

It is known that, in the field of FEA, capturing material nonlinearity typically involves the adoption of a consistent tangent stiffness matrix. This approach is favoured for its efficiency in achieving quadratic convergence while minimizing the number of iterations within incremental-iterative schemes. The equilibrium equation in the standard finite element discretized form is expressed as:

$$\begin{aligned} &\mathbf{F}^{int} = \int_V \boldsymbol{B}^{\mathrm{T}}(\mathbf{x})\boldsymbol{\sigma}(\mathbf{x})\mathrm{d}V(\mathbf{x}) \\ \text{Tangent Stiffness} \qquad &\boldsymbol{K}_T = \frac{\partial \mathbf{F}^{int}}{\partial \mathbf{U}} = \frac{\partial}{\partial \mathbf{U}}\left(\int_V \boldsymbol{B}^{\mathrm{T}}(\mathbf{x})\boldsymbol{\sigma}(\mathbf{x})\mathrm{d}V(\mathbf{x})\right) \end{aligned} \tag{5.19}$$

However, it can be seen from Eq. (5.17) that the relation between stress and strains is nonlocal, where building the tangent stiffness is not as straightforward as the local theories for which the tangent moduli tensor is directly derived. While it is technically possible to construct a nonlocal tangent stiffness matrix, it may not be a preferable option due to the computational resources it demands. The difficulty arises from the second term on the right-hand side of Eq. (5.17), denoted as $\boldsymbol{J}_D$. This term not only incorporates the damage derivatives at points $\mathbf{x}$ and $\mathbf{x}'$ but also factors in the cumulative influence of points **z**, which are the common neighbours of both $\mathbf{x}$ and $\mathbf{x}'$, present in $\boldsymbol{k}_D(\mathbf{x}, \mathbf{x}')$**.** Hence, opting for the secant stiffness is the alternative and preferable choice, as integrating the terms in $\boldsymbol{k}_D(\mathbf{x}, \mathbf{x}')$ is computationally better than its derivatives.

Using Eq. (5.17) in Eq. (5.19) forms,

$$\mathbf{F}^{int} = \boldsymbol{K}_{sec}\mathbf{U} \tag{5.20}$$

$$\begin{aligned}\boldsymbol{k}_{sec} &= \sum_{n=1}^{ngp} w_n(1+\alpha\gamma_n^2)\boldsymbol{B}_n^{\mathrm{T}}(1-D_n)\mathbb{C}_0\boldsymbol{B}_n \det J_n \\ &\quad - \sum_{n=1}^{ngp}\sum_{m=1}^{ngp} w_n w_m \boldsymbol{B}_n^{\mathrm{T}}\boldsymbol{J}_D\boldsymbol{B}_m \det J_m \det J_n\end{aligned}$$

where $\boldsymbol{K}_{sec}$ and $\boldsymbol{k}_{sec}$ are the global and elemental secant stiffness matrix, n and m used for defining strain-displacement matrix, damage variables at target and neighbouring gauss points $\mathbf{x}$ and $\mathbf{x}'$.

The strain difference-based nonlocal approach addresses not only the elimination of undesired boundary effects, facilitating the use of symmetric geometries, but also introduces the symmetric nonlocal tensor $\boldsymbol{J}_D(\mathbf{x}, \mathbf{x}')$ within the constitutive equation. From a computational perspective, this feature contributes to further cost reduction by generating a symmetric nonlocal stiffness matrix (the second part of k_{sec}), where calculating the upper and diagonal cross-stiffness element matrices is adequate. The implementation procedure for nonlocal part of stiffness matrix is given in the form of pseudo-code in Box 5.1.

Box 5.1. Pseudo-code for nonlocal part of stiffness matrix from Eq. (5.20)

```
Call $m_{ele}$, each neighbour of current element $n_{ele}$
if $[m_{ele} \geq n_{ele}]$      // Initiates for symmetry
        Calculate coordinates, gdofs of current neighbour element $m_{ele}$
        Calculate common neighbour elements, $z_{ele}$, of $m_{ele}$ and $n_{ele}$
        For $n = 1, \ldots\ldots, ngp$
            Calculate $\mathbf{x}$, $J_n$, and $\boldsymbol{B}_n$ at n
            Call $D_n$
            For $m = 1, \ldots\ldots, ngp$
                Calculate $\mathbf{x}'$, and $r_{nm}$
```

```
                        if [$r_{nm} \le R$]
                          Call $D_m$ and calculate $J_m, \boldsymbol{B}_m$ at m
                          For $z_{ele} = 1, \ldots \ldots,$ common neighbour elements
                              For $z = 1, \ldots,$ ngp
                                  Calculate $g(\mathbf{x},\mathbf{z}), g(\mathbf{x}',\mathbf{z})$, and $\boldsymbol{k}_D(\mathbf{x},\mathbf{x}')$
                                  from Eqs. (3.35) and (5.18).
                              end
                          end
                          Calculate $\boldsymbol{J}_D$ from Eq. (5.18)
                          $\boldsymbol{k}^{nonloc} = \boldsymbol{k}^{nonloc} + w_n w_m \boldsymbol{B}_n^{\mathrm{T}} \boldsymbol{J}_D \boldsymbol{B}_m \det J_m \det J_n$
                        end
                    end
                end
                $\boldsymbol{K}(ngdofs, mgdofs) = \boldsymbol{K}(ngdofs, mgdofs) - \boldsymbol{k}^{nonloc}$
        else
                $\boldsymbol{K}(mgdofs, ngdofs) = \boldsymbol{K}(mgdofs, ngdofs) - (\boldsymbol{k}^{nonloc})^{\mathbf{T}}$
        end
```

5.3.2 Numerical algorithm

Owing to the presence of material nonlinearity, this paper employs an incremental-iterative solution approach, specifically the displacement-controlled Newton-Raphson technique for solving the system of equations. The employment of path-dependent constitutive models inherently necessitates the development of algorithms to numerically integrate the evolution equations. At the commencement of each time step, denoted as t_i, the strains, stresses, and damage variable are known. The time step then concludes at t_{i+1}, with updates to the stresses and internal variables in accordance with the specified incremental strain tensor. Hence, the discretization of the rate constitutive equations over a time interval $[t_i, t_{i+1}]$ was carried out using the backward Euler scheme.

Box 5.2. Numerical integration algorithm for continuum based linear damage evolution law with internal variable ξ.

(a) *Elastic state:* with the known values of D, ξ at time step t_i and the incremental strain $\Delta\boldsymbol{\varepsilon}$

- $\boldsymbol{\varepsilon}_{i+1} = \boldsymbol{\varepsilon}_i + \Delta\boldsymbol{\varepsilon};$ $\quad \xi_{i+1}^{trial} = \xi_i;$ $\quad \chi_{i+1}^{trial} = \chi_i.$
- $\mathcal{R}\big(\boldsymbol{\varepsilon}(\mathbf{x})\big)_{i+1} = \sum_{j=1}^{ngp} w_j g(\mathbf{x},\mathbf{x}')\big(\boldsymbol{\varepsilon}(\mathbf{x}') - \boldsymbol{\varepsilon}(\mathbf{x})\big) detJ(\mathbf{x}');$
- $\mathcal{R}\big(\Delta\boldsymbol{\varepsilon}(\mathbf{x})\big)_{i+1} = \sum_{j=1}^{ngp} w_j g(\mathbf{x},\mathbf{x}')\big(\Delta\boldsymbol{\varepsilon}(\mathbf{x}') - \Delta\boldsymbol{\varepsilon}(\mathbf{x})\big) detJ(\mathbf{x}')$
- $Y_{i+1} = \frac{1}{2}\Big(\boldsymbol{\varepsilon}_{i+1} : \mathbb{C}_0 : \boldsymbol{\varepsilon}_{i+1} + \alpha\big(\mathcal{R}(\boldsymbol{\varepsilon}) : \mathbb{C}_0 : \mathcal{R}(\boldsymbol{\varepsilon})\big)_{i+1}\Big)$

(b) *Damage activation function:*

$If\ \phi^{trial} = Y_{i+1} - \chi_{i+1}^{trial} \leq 0$, then

$(.)_{i+1} = (.)_{i+1}^{trial}$ (***elastic step***) go to *EXIT*

Else go to (c)

(c) *Damage corrector:*

- $\Delta Y_{i+1} = \boldsymbol{\varepsilon}_{i+1}\colon \mathbb{C}_0\colon \Delta\boldsymbol{\varepsilon}_{i+1} + \alpha\big(\mathcal{R}(\boldsymbol{\varepsilon})\colon \mathbb{C}_0\colon \mathcal{R}(\Delta\boldsymbol{\varepsilon})\big)_{i+1};\quad h_{i+1} = \frac{\partial^2\psi_{in}}{\partial\xi_{i+1}^2},$
- $\Delta\lambda_{i+1} = \frac{1}{h_{i+1}}\Delta Y_{i+1}.$

(d) *Update the internal variables and their associates:*

- $D_{i+1} = \Delta\lambda_{i+1};\quad \xi_{i+1} = \Delta\lambda_{i+1},$
- $\chi_{i+1} = \chi_i + h_{i+1}\Delta\lambda_{i+1}.$

Exit

In many research studies, it is a common practice to divide the problem into two distinct stages. First, the elastic predictor stage assumes the problem to be elastic, while in the second stage, known as the damage corrector, various parameters such as the damage hardening modulus (h), incremental damage energy release rate ($\dot{Y}$), and indeterminate multiplier ($\dot{\lambda}$) are calculated. These calculations are based on the results obtained in the elastic predictor stage, which serve as initial conditions. If the damage activation condition is violated, the damage corrector stage must be initiated. Notably, this stage directly computes the multiplier without the need for iterative schemes, as the linear damage evolution law is chosen. A concise explanation of the numerical integration algorithm is provided in Box 5.2.

5.4 Numerical studies – Results and Discussions

In this section, three case studies are presented: (i) to study the influence of nonlocal parameter 'α' in the damage distribution while capturing the post-peak behaviours, (ii) to demonstrate the effectiveness of the strain difference-based nonlocal damage model by obtaining mesh-independent results and accurately predicting damage evolution regions, and (iii) comparison between experimental results and numerical structural response for coarse mesh, highlighting both computational efficiency and reduction of mesh-bias dependency.

The inelastic part of Helmholtz free energy in the present work is referred from Comi & Perego [101] and the same are followed for all the examples. The inelastic energy is given by:

$$\psi_{in}(\xi) = K(1-\xi)\sum_{j=1}^{N}\frac{N!}{j!}ln^{j}\left(\frac{c^*}{1-\xi}\right) \tag{5.21}$$

5.4.1 Concrete block with a through hole

In this example, studies are carried out on the nonlocal parameter 'α' to illustrate its significance in the strain difference-based nonlocal model while capturing the strain softening behaviour. The radius of the hole (r) in the specimen is 0.05m, and the length (L) of the block is obtained from $L/r = 10$. The specimen is subjected to displacement loading on both of its vertical ends, as shown in Fig. 4.1(a). The material properties used are as follows [232]: $E = 36$ GPa, $\nu = 0.15$, and the damage parameters are given by $K = 5.8 \times 10^{-14}$ MPa, $c^* = 405$, $N = 12$. Due to symmetry, the analysis is conducted for the upper right quarter of the block, with boundary conditions specified as shown in Fig. 4.1(b).

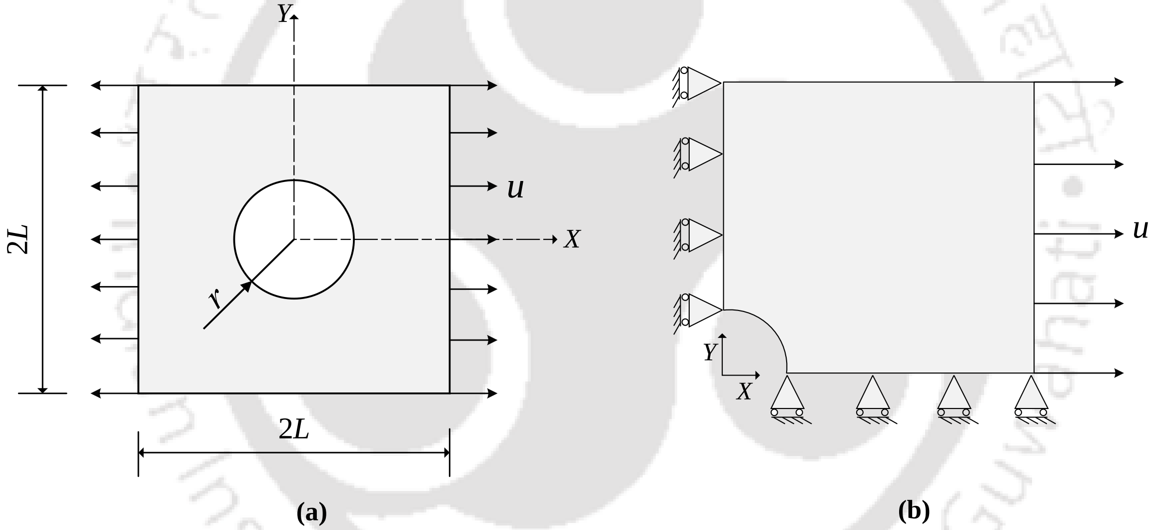

Fig. 5.1. **(a)** Two-dimensional geometry and loading conditions of concrete block with through hole, and **(b)** quarter symmetry portion with boundary conditions.

The quarter of the geometry under analysis is divided into four-node quadrilateral plane strain elements. To examine mesh sensitivity for various α's $(1, 10, 50, 100)$ for characteristic length ($l_c = 0.005$ m), five different meshes, shown in Fig. 5.2(a)-5.2(e), are used to discretize the displacement field. These meshes have varying element sizes, with finer elements concentrated in regions of the geometry, i.e., in the vicinity of the hole, where high strain gradients and damage are anticipated. Here, different mesh densities are chosen in particular to showcase the effectiveness of the proposed methodology in reducing the mesh-bias dependency. Further, the mesh dependency issues often encountered when using standard/local FEM are addressed.

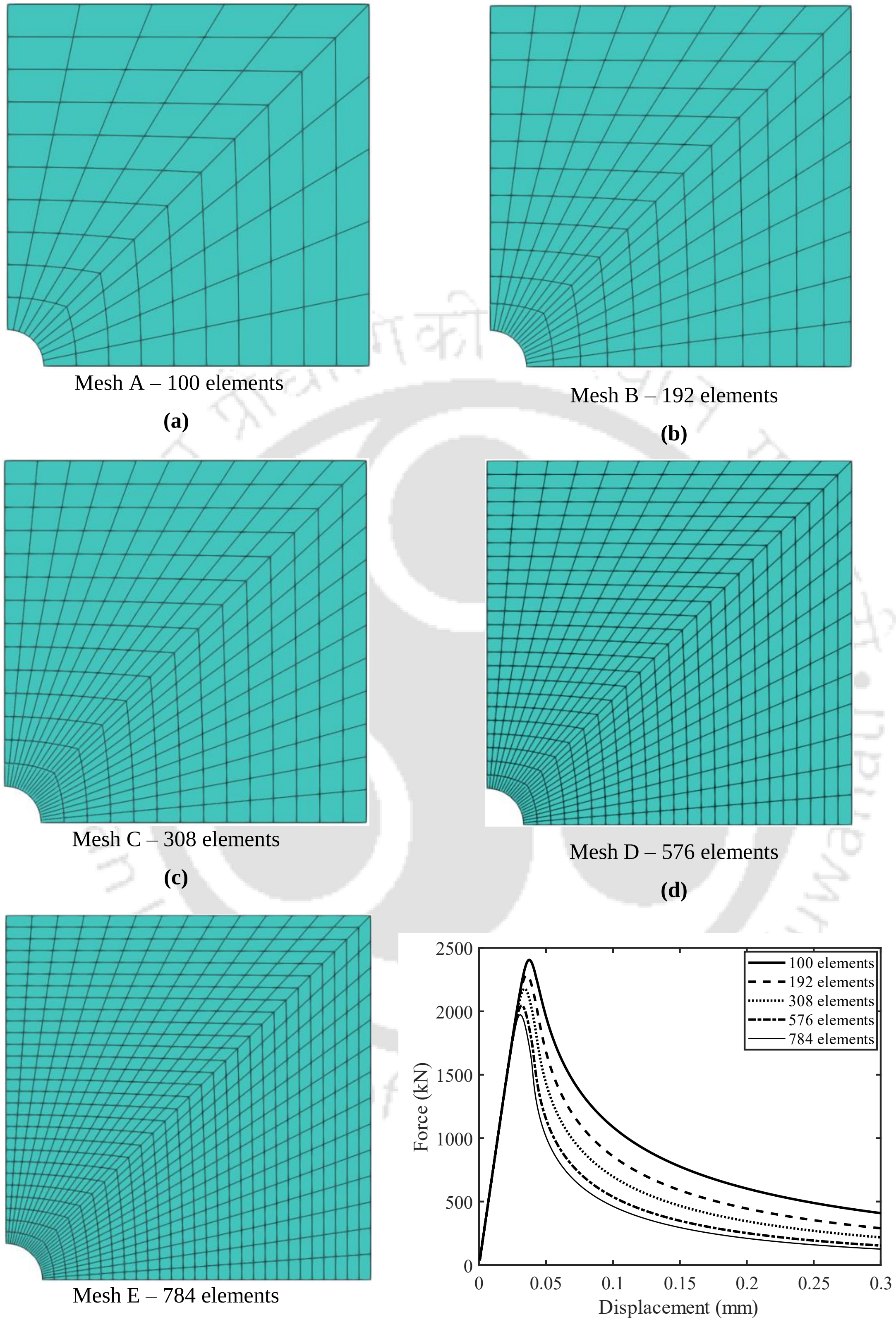

Fig. 5.2. (a)-(e) Various mesh discretizations of the geometry, and **(f)** force-displacement responses by standard FE analysis for meshes A, B, C, D, and E

Fig. 5.2(f) shows the load-displacement behaviour simulated by classical continuum damage theories through standard/local FEM. The results exhibit mesh sensitivity, particularly for meshes A, B, and C. There are relatively minor changes in the results for the other two meshes – D and E with a marginal decrease in the peak load. Notably, the latter set of meshes feature refined element sizes near the hole, aiding in achieving numerically converged responses.

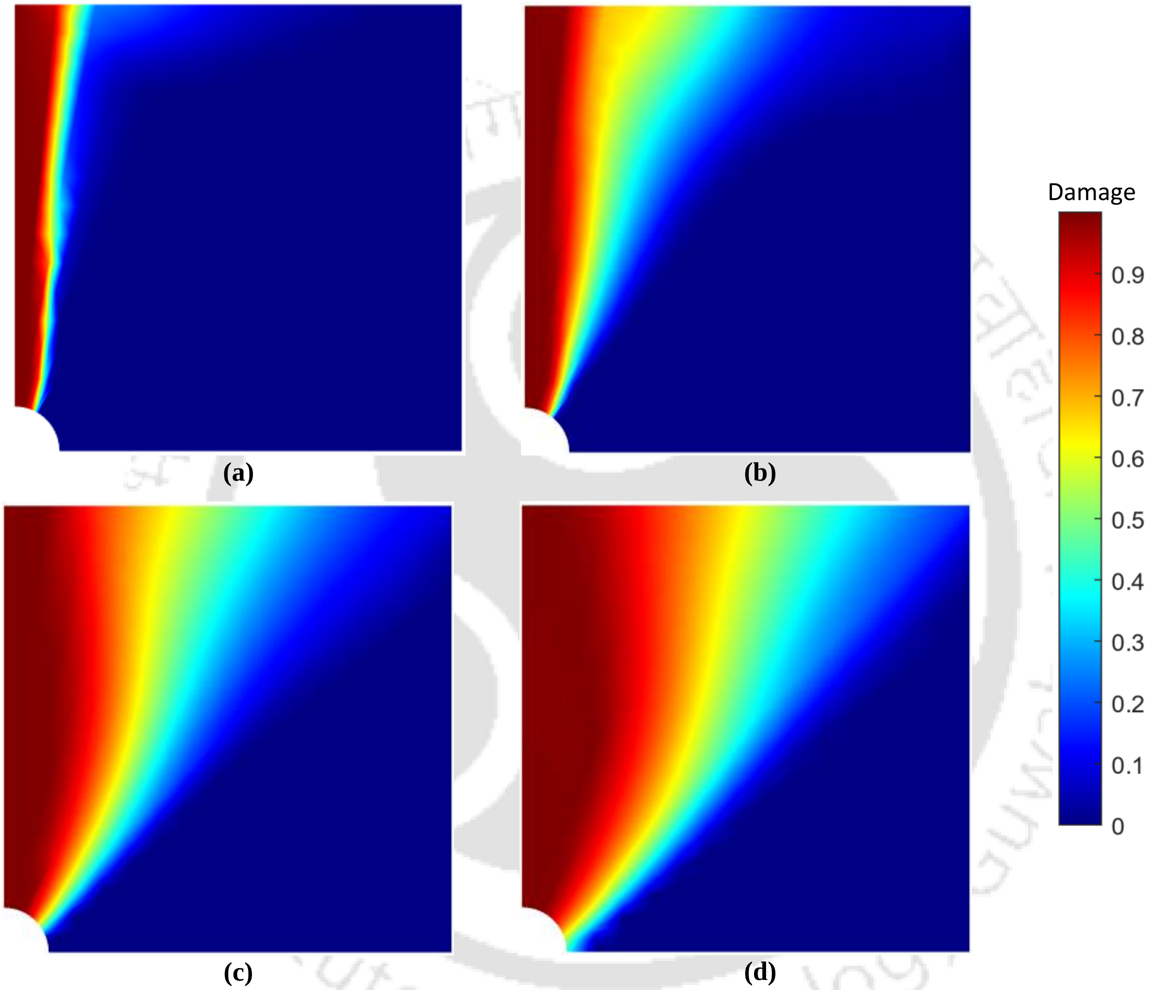

(a) **(b)**

(c) **(d)**

Fig. 5.3. Damage contours for mesh C: **(a)** $\alpha = 1$, **(b)** $\alpha = 10$, **(c)** $\alpha = 50$, and **(d)** $\alpha = 100$

In the present methodology, the parameter 'α' plays a significant role in distributing the nonlocal effects over the geometry. Fig. 5.3(a)-5.3(d) displays the damage contour plots of mesh C for different values of α. It is observed that, as α increases, there is a corresponding increase in damage localization and the extent of damage process zones, which are particularly noticeable for α values of 50 and 100. In these cases, the nonlocal distribution predominates, causing the material to behave in a ductile manner. On the contrary, for α values of 1 and 10, the damage localization area is nearly the same and almost aligns with practical studies. However, in the case of $\alpha = 1$, the damage process zone is minimal, whereas for $\alpha = 10$, it is negligible in regions with high strain gradients but gradually increases toward the free boundaries. Nevertheless, this effect is not as significant as that observed for α values of 50 and 100.

Fig. 5.4(a)-5.4(d) illustrates the load-displacement curves obtained using the strain difference-based nonlocal damage model for different values of α. These curves consistently predict a peak force that is independent of the mesh size in all four cases. When it comes to softening behaviour, there are not many significant changes observed with respect to the mesh size. However, it is notable that the softening response exhibits better convergence with increasing α, as evidenced by the error prediction of peak loads for various α values, as shown in Table 5.1.

Table 5.1. % Error of peak load values for various α's (with reference to peak load of 784 elements)

Elements	$\boldsymbol{\alpha = 1}$	$\boldsymbol{\alpha = 10}$	$\boldsymbol{\alpha = 50}$	$\boldsymbol{\alpha = 100}$
100	10.25	4.44	3.89	3.95
192	6.73	2.77	2.43	2.45
308	3.43	1.52	1.42	1.55
576	1.75	0.53	0.47	0.49

But, for values of $\alpha = 50$ and 100 (see Fig. 5.4(c) and 5.4(d)), the post-peak behaviour exhibits a distinct nature compared to the curves from classical CDM theories in Fig. 5.2(f). This behaviour can likely be attributed to the accumulation of damage in a large area after the peak force, as shown in Fig. 5.3(c) and 5.3(d). In this region, the material undergoes substantial stiffness degradation, leading to an increase in the damage rate. At the same time, due to the significant enlargement of the damage process zone, there is not much intensity in the softening response. Conversely, in the case of local modelling and for $\alpha = 1$, as discussed earlier, this damage process zone becomes quite negligible, resulting in an immediate drop in the nature of the curve after the peak force (see Fig. 5.4 (a)). Furthermore, for $\alpha = 10$, the softening response have balanced nonlocal effects (i.e., damage localization and damage process zones), resulting in a curve nature similar to that of local FE modelling (see Fig. 5.4(b)).

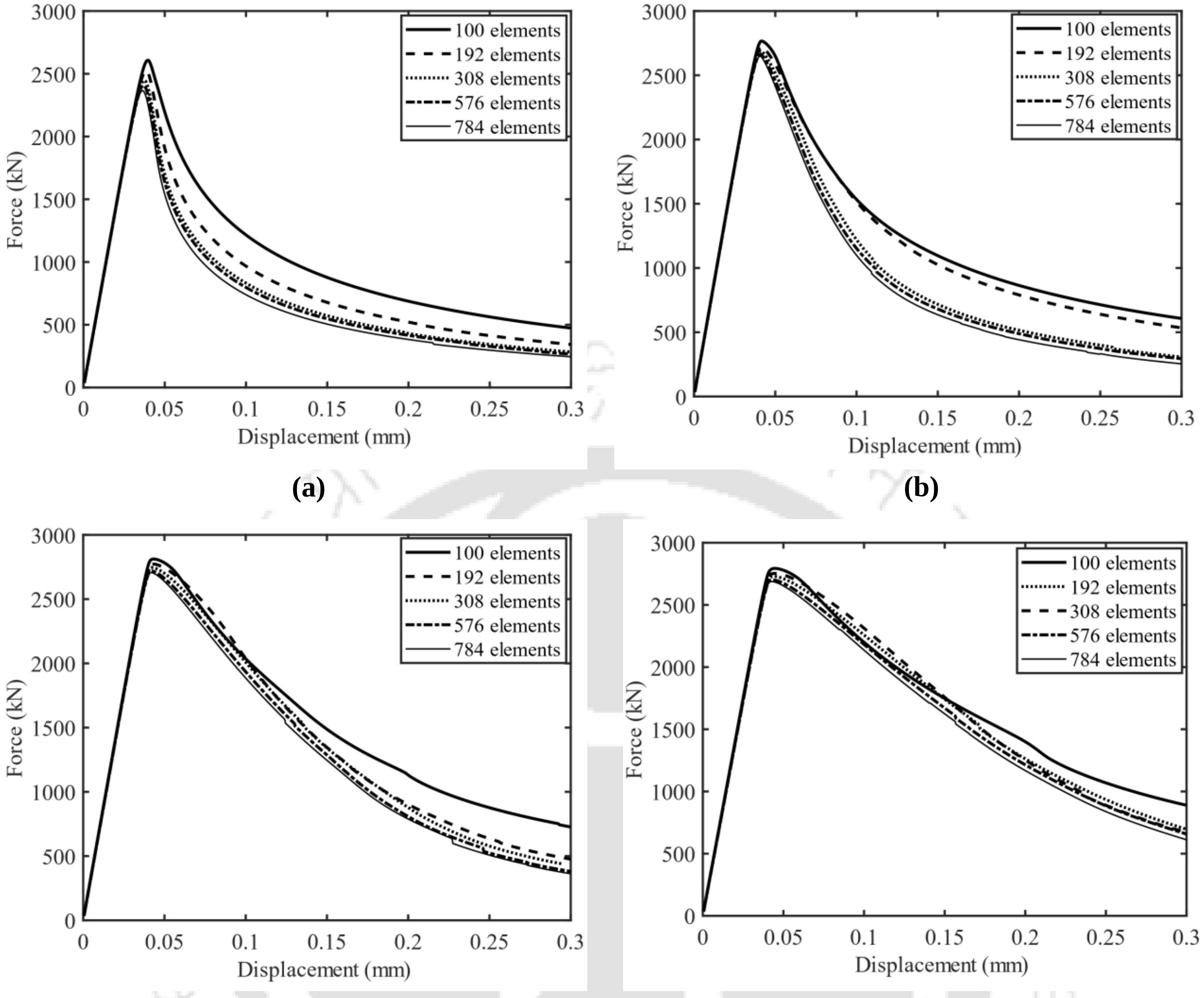

(a) **(b)**

(c) **(d)**

Fig. 5.4. Mesh sensitivity study and effect of **(a)** $\alpha = 1$, **(b)** $\alpha = 10$, **(c)** $\alpha = 50$, and **(d)** $\alpha = 100$ on peak load and softening behaviours

As discussed earlier in Section 3.2, it is important to note that the exponential attenuation function is defined by its unbounded support. Nevertheless, as the distance r increases, it consistently exhibits a decreasing pattern and eventually approaches zero at greater distances. This implies that regardless of the chosen kernel function, g, there will always be a corresponding interaction distance R at which g either vanishes or can be effectively considered as vanishing at all points beyond R. Therefore, for lesser computational costs, the nonlocal interaction radius $R = 6l_c$ is adopted [18] Simultaneously, to ensure the effectiveness of the nonlocal distributions, the authors deemed it reasonable to select $\alpha = 10$ for further examples.

5.4.2 Single-edge notched beam

In this example, numerical simulations of mode I failure of a single-edge notched beam subjected to three-point bending (TPB) is presented. The geometric details, boundary and loading conditions, shown in Fig. 5.5(a), are adopted from Petersson [233]. Due to symmetry considerations, only half of the geometry is modelled (see Fig. 5.5(c)), and a plane strain condition is assumed for the numerical analysis. The material properties used are as follows: $E = 30$ GPa, $\nu = 0.2$ and the damage parameters, for this example, achieved through trial and error analysis are given by $K = 5.8 \times 10^{-14}$ MPa, $c^{*} = 550$, $N = 11.74$. An internal characteristic length of 1.1 mm is chosen.

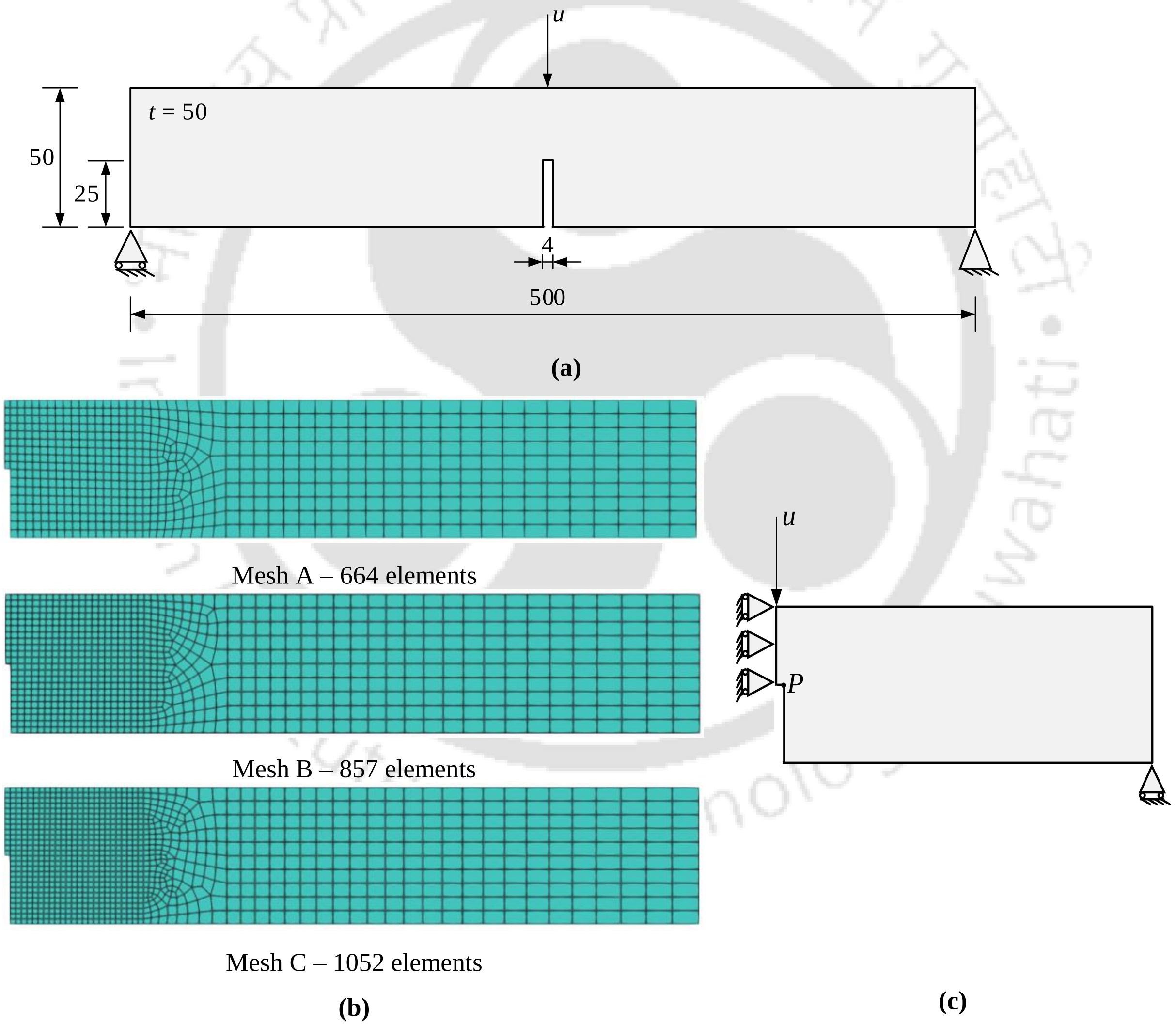

Fig. 5.5. (a) Single-edge notched beam, **(b)** FE meshes: A (664 elements), B (857 elements), C (1052 elements), and **(c)** symmetric beam model: boundary and loading conditions (all dimensions are in mm).

The numerical simulations of the notched beam are performed using three different finite element meshes, denoted as A, B, and C, each composed of four-node quadrilateral elements. Meshes A, B and C features 3 mm, 2.5 mm and 2 mm element sizes in the region where damage/crack propagation are anticipated (see Fig. 5.5(b)). Fig. 5.6 exhibits the damage contour plots for four distinct loading points: the first within the elastic regime, the second at the peak load, and the other two during the softening phase of the load–displacement curves obtained using the strain difference-based nonlocal damage model. The numerical analysis reveals a consistent linear path of damage/crack formation above the notch, extending from the notch's tip to the upper side of the beam. This observation aligns closely with practical studies.

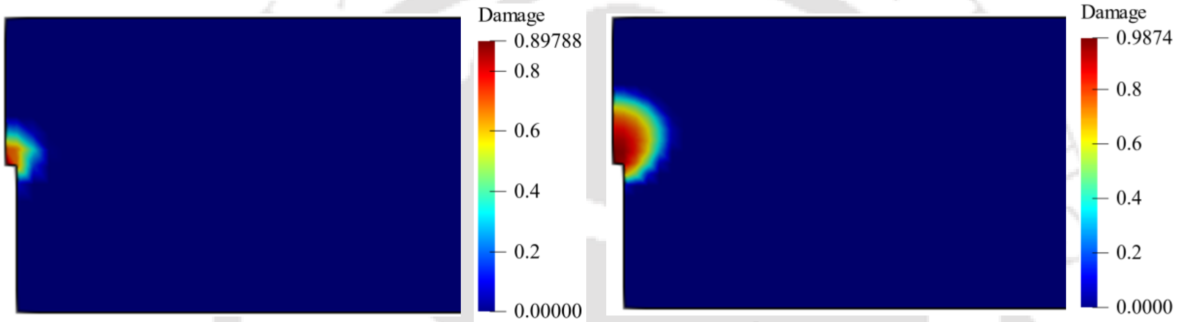

(a) u_y = 0.078 mm **(b)** u_y = 0.133 mm

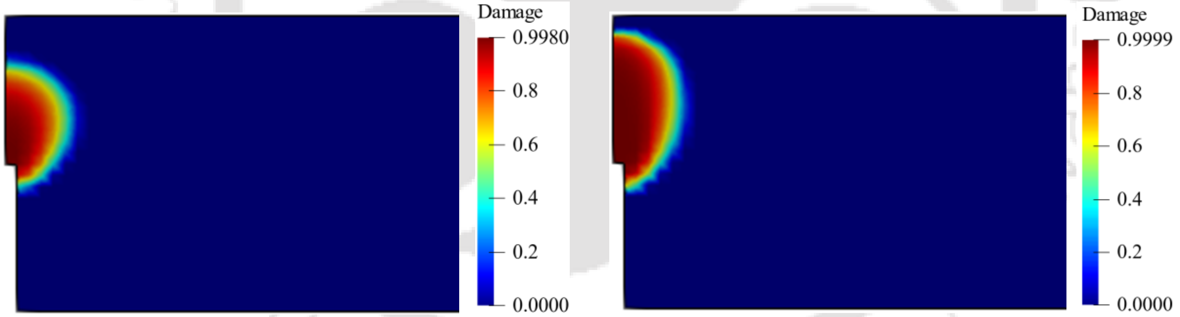

(c) u_y = 0.2 mm **(d)** u_y = 0.4 mm

Fig. 5.6. Damage profile with numerical damage/crack path at different displacement loading points for the three-point bending test using strain difference-based nonlocal damage model.

Similarly, contour plots illustrating stresses in the x-direction at the peak load and at 50% of the peak load ($u_y = 0.4$mm) are presented in Fig. 5.7(a) and 5.7(b). It is noticeable from both contour plots that the maximum tensile stresses progressively move away from the notch area with the increase in displacement loading. This is because the initiation, evolution, and propagation of the damage,as shown in Fig. 5.6, gradually degrades the stiffness of the affected region, thereby reducing the stresses in these regions. This is evident in Fig. 5.7(b). Conversely, the regions on the brink of damage initiation coincide with the locations experiencing maximum tensile stresses.

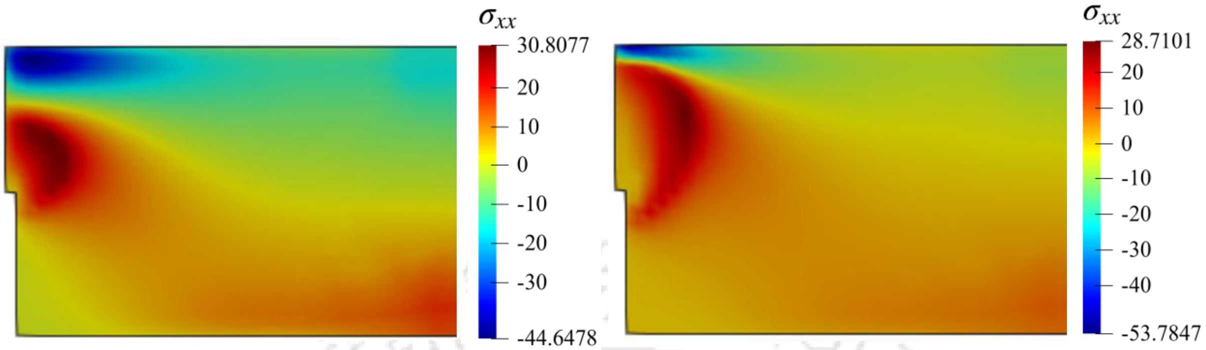

(a) $u_y = 0.133$ mm **(b)** $u_y = 0.4$ mm

Fig. 5.7. Contour plots of stresses in x-direction at peak load and at 50% of peak load for the TPB test.

A comparison of the structural responses predicted using meshes A, B, and C up to 50% peak load is illustrated in Fig. 5.8(a). It is observed that the load-deflection curves from various meshes show convergence, confirming the proposed methodology's independence from mesh-related issues. Additionally, a comparison between the numerical results and reference experimental data [233], reveals a favorable agreement, with only a 3% difference observed in the peak load for the refined mesh.

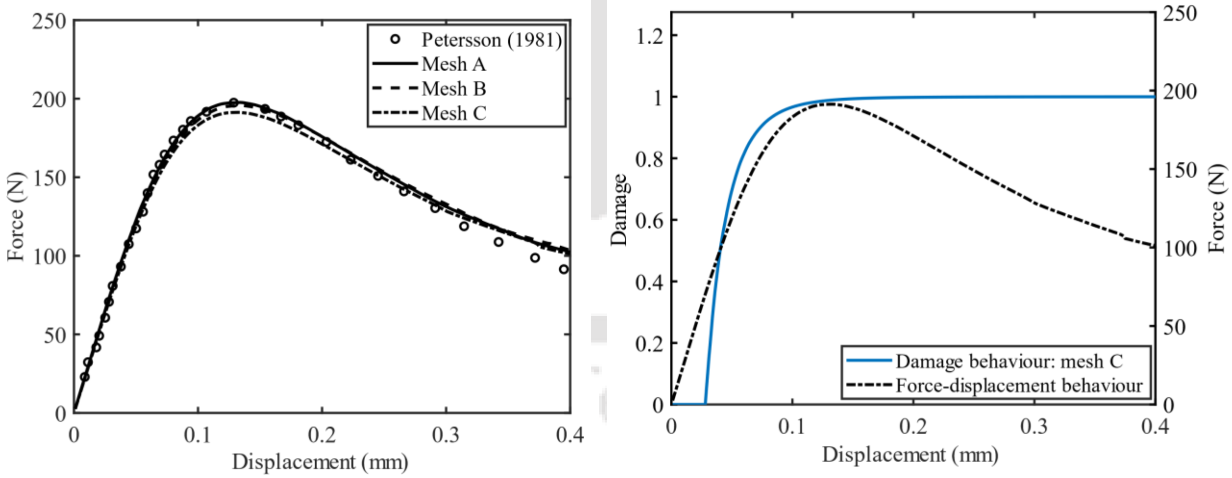

(a) **(b)**

Fig. 5.8. (a) Comparison between the structural responses: experimental and numerical results (showing mesh independency), and **(b)** damage behaviour at the sharp corner of the notch (point 'P') for the respective displacement loading.

In Fig. 5.8(b), the damage behaviour at the sharp corner of the notch, denoted by point 'P' (see Fig. 5.5(c)), is shown in relation to the prescribed displacement loading. It is noticed that damage initiates and undergoes rapid evolution up to the peak load, slowing down in subsequent stages. Similarly, a substantial portion of the material surrounding the notch experiences damage initiation and evolution even before reaching the peak load (see Fig. 5.6(b)). This results in a damage-dominant irreversible process, leading to immediate softening after the peak load.

The performance of the present strain difference-based methodology is evaluated against the nonlocal strain approach [234,235]. Both computational cost and accuracy are compared. Using Eringen's definition of nonlocal strain (Eq. 3.34), the constitutive equations are obtained within the thermodynamic framework, discussed in section 3.2. The weight function in Eq. (3.34) is replaced with Eq. (3.37) to eliminate the boundary effects in the geometry. Table 5.2 presents a comparison of the computational cost for both approaches for mesh A. Since the number of iterations per increment varies at different locations across the force-displacement curve, three specific displacement points are considered: one in the elastic regime, another at the peak load, and the last one in the softening zone. The proposed approach is executed on a PC Matlab R2022b platform, utilizing an Intel(R) Core(TM) i7-12700F processor clocked at 2.10 GHz, with 64 GB of RAM, and operating on Windows 10 Pro version 22H2.

Table 5.2. Comparison of the performance between the proposed methodology and the nonlocal strain approach in terms of computational cost.

	Strain difference-based approach (12.15 secs per iteration)	**Nonlocal strain approach (39.53 secs per iteration)**
Displacements	Total time (secs)	Total time (secs)
$u_y = 0.05$ mm	60.75	276.71
$u_y = 0.133$ mm	97.2	395.3
$u_y = 0.25$ mm	48.6	237.18

As seen in Table 5.2, the nonlocal strain approach requires 39.53 seconds per iteration employing identical nonlocal parameters. In contrast, the present methodology, benefiting from its symmetric nature, completes each iteration in 12.15 seconds. In terms of accuracy, the nonlocal strain approach tends to underpredict the peak load (see Fig. 5.9). However, the strain difference, an extension of the nonlocal strain approach, holds the advantage of enhancing nonlocal effects through the parameter α, as mentioned earlier, while maintaining accuracy. On the other hand, the strain difference approach, without invoking symmetry, requires 80% more computational effort compared to the case with symmetry.

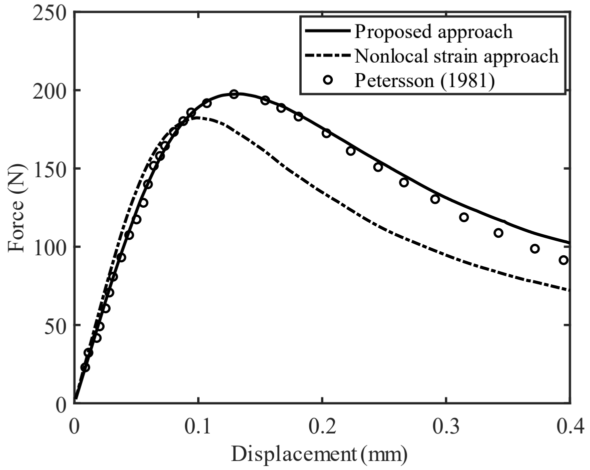

Fig. 5.9. Force-displacement responses for mesh A: showcasing the accuracy of proposed methodology over the nonlocal strain approach.

5.4.3 Four-edge notched specimen

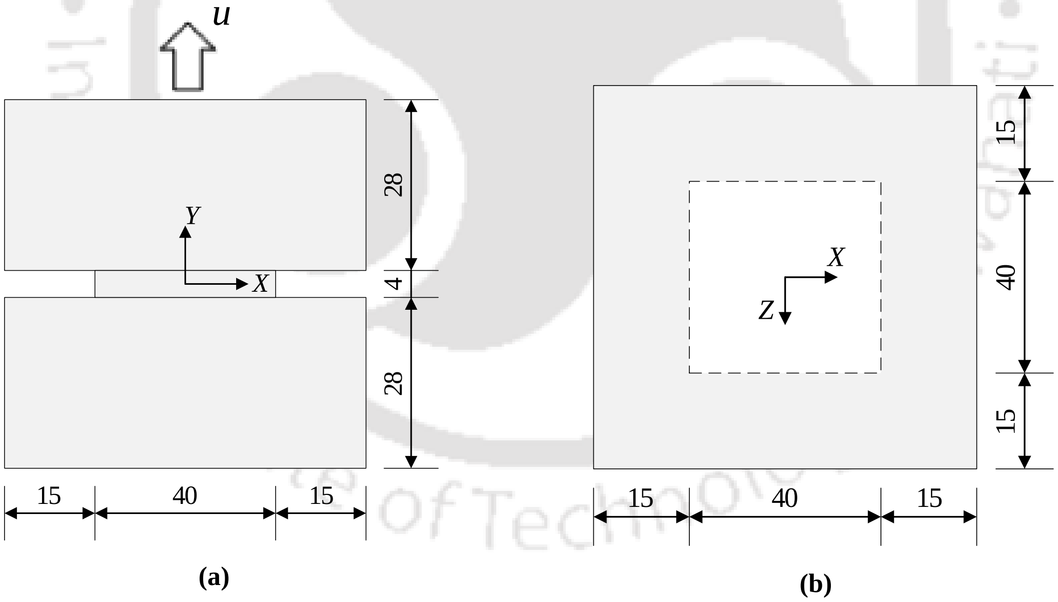

(a) **(b)**

Fig. 5.10. Geometry and dimensions of Four edge notched specimen (all dimensions are in mm)

Direct tension test on a four-edge notched specimen is a well-known concrete damage test first conducted by Hassanzadeh [236]. The Fig. 5.10(a) and 5.10(b) shows the geometry and dimensions of the plain concrete specimen, which includes four notches along its edges at the center. The bottom surface remains fixed, while tension is applied to the top surface using displacement control.

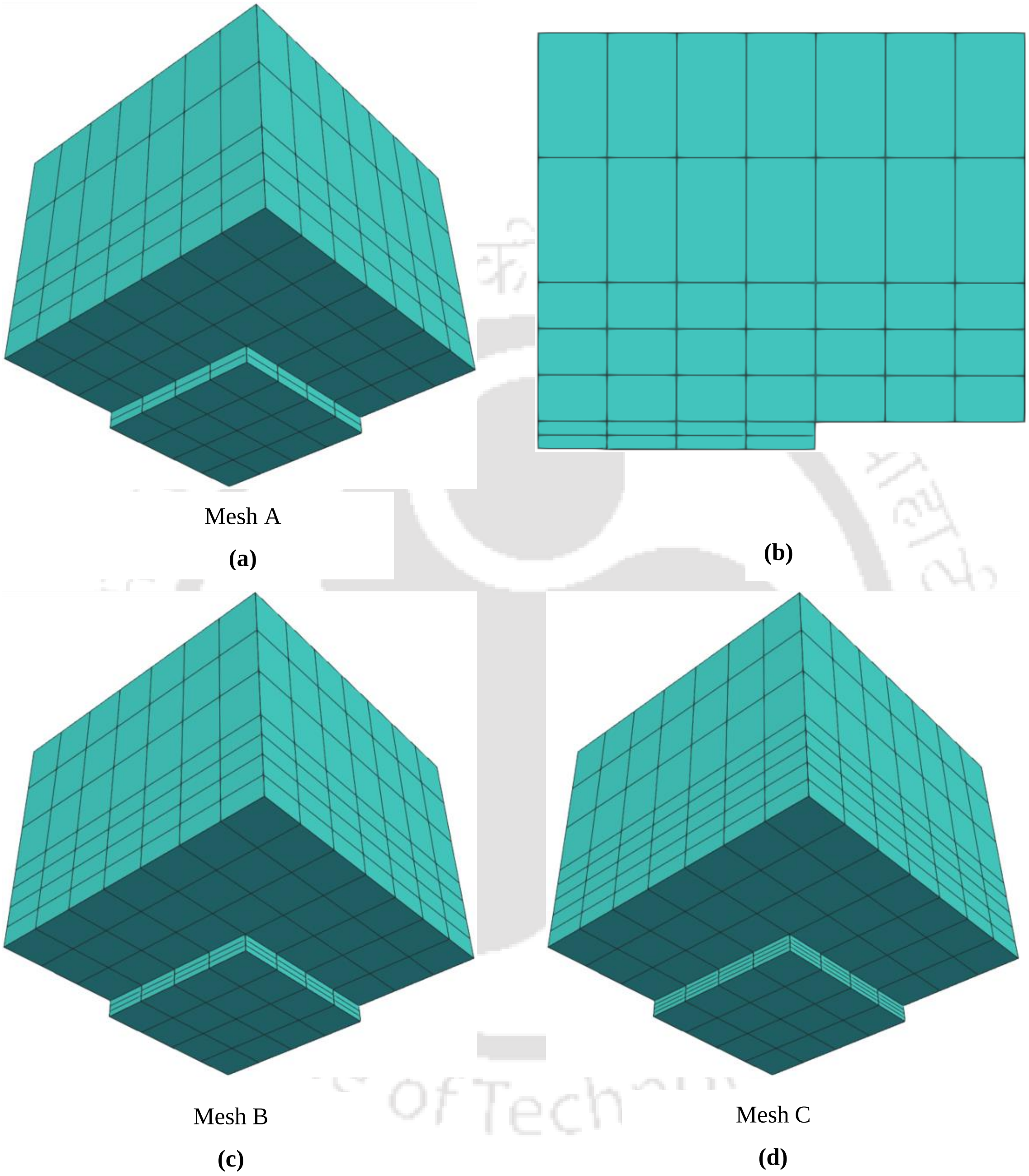

Fig. 5.11. Mesh discretization: **(a)** Mesh A (277 elements), **(b)** 2D representation of Mesh A, **(c)** Mesh B (391 elements), and **(d)** Mesh C (456 elements)

The main purpose of considering this numerical example is to validate the load-displacement behaviour obtained using the strain difference-based nonlocal damage model against experimental data, particularly for a coarse mesh. To achieve this, the present study focuses on analysing only one-eighth of the geometry, taking advantage of its inherent symmetry. Fig. 5.11(a), 5.11(c), and 5.11(d) illustrates the mesh discretizations of the specimen, employing 277, 391, and 456 solid brick elements distributed across three levels with varying sizes. Boundary and loading conditions are more effectively elucidated through a 2D representation, as depicted in Fig. 5.11(b). Symmetry-related boundary conditions are applied, with $u_x = 0$ on the left vertical surface and $u_y = 0$ on the bottom surface of the specimen. Displacement loading, u_y, is imposed on the top surface. The material properties and the damage parameters are given by [237]: $E =$ 36 GPa, $\nu = 0.15$, $K = 5.8 \times 10^{-14}$ MPa, $c^* = 405$, and $N = 12$. The internal characteristic length, $l_c =$ 1.1 mm is taken.

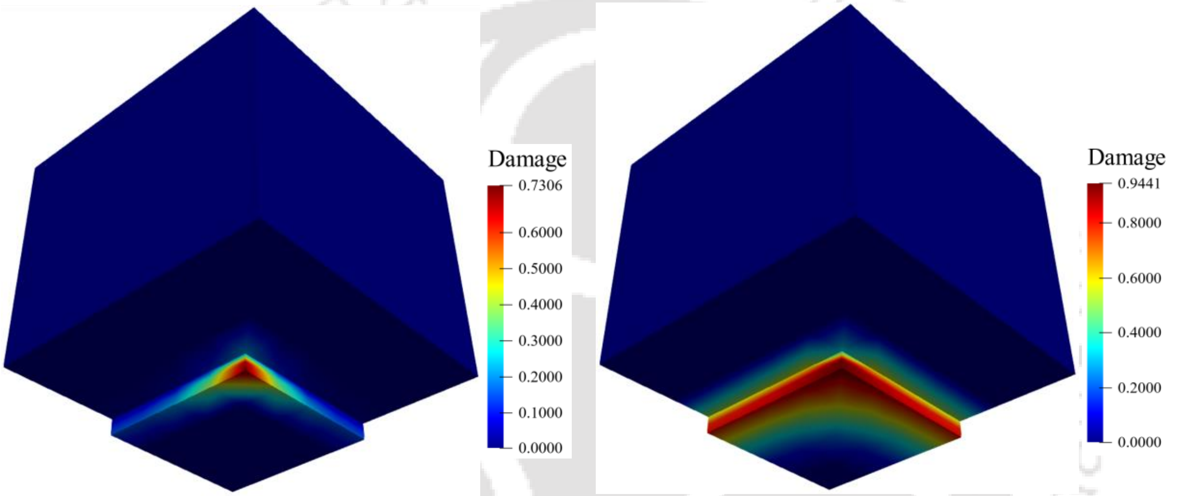

(a) u_y = 0.00244 mm

(b) u_y = 0.00453 mm

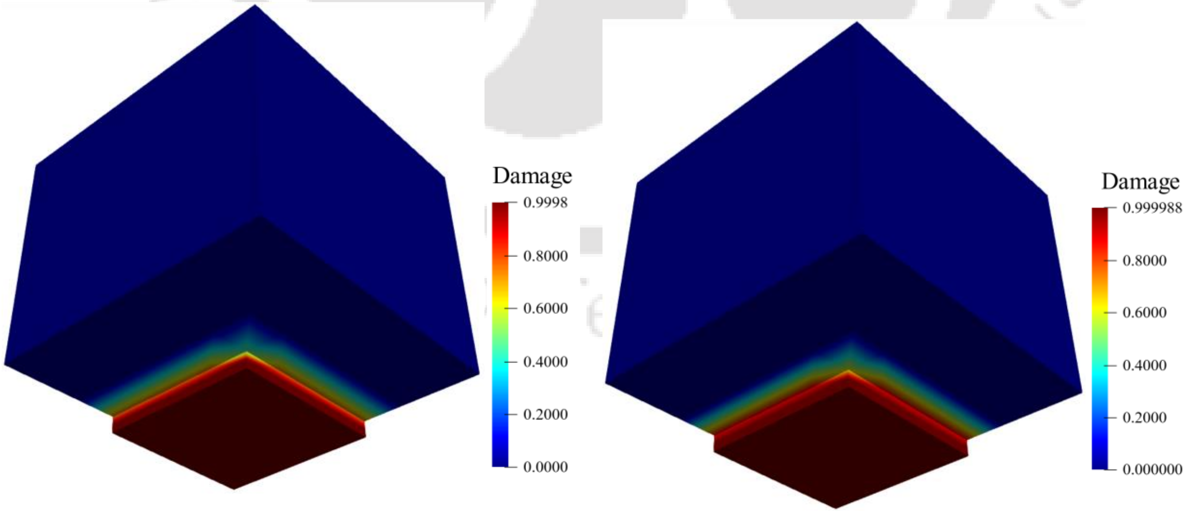

(c) u_y = 0.02621 mm

(d) u_y = 0.04 mm

Fig. 5.12. Damage profile with numerical damage/crack path at different displacement loading points for the direct tension test using strain difference-based nonlocal damage model

Fig. 5.12 displays the damage contour plots for four specific displacement loading points, as marked in the load-displacement curves (see Fig. 13(b)). As depicted in Fig. 5.12(a) and 5.12(b), the damage correctly initiates at the sharp tip of the notch and uniformly propagates in both directions from the tip under external loading. Fig. 5.12(b) also illustrates the damaged state of the specimen near its peak load. Fig. 5.12(c) and 5.12(d) are selected from the softening portion of the curve. They reveal significant damage in the bottom portion of the notch, gradually progressing toward the sharp corners between the notch and the top part of the specimen. Fig. 5.12(d) also portrays the final stages of the specimen's failure, and the numerical analysis is concluded at this displacement since the maximum damage is nearly 1.

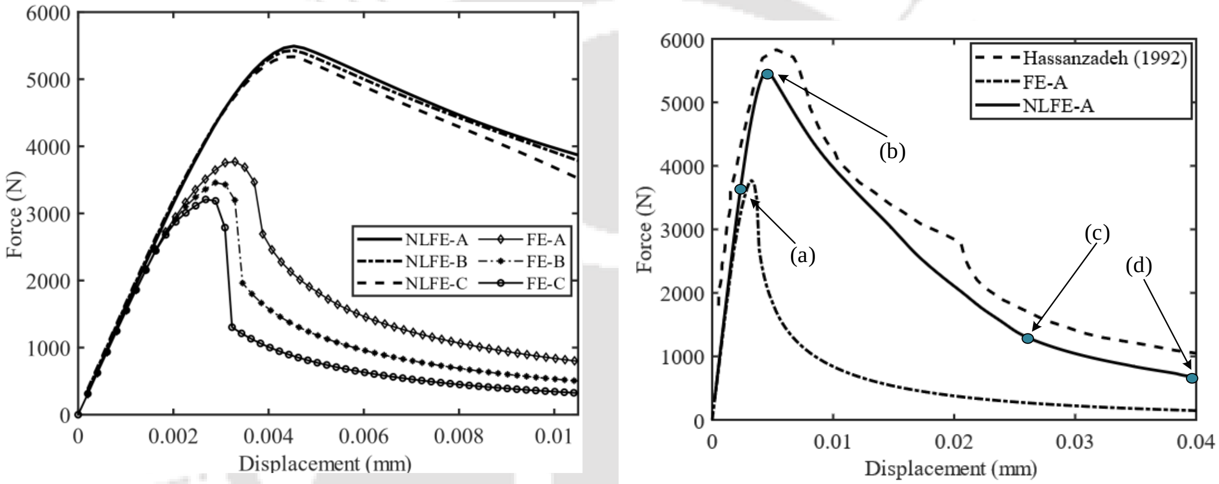

(a) **(b)**

Fig. 5.13. (a) Mesh convergence studies comparing local and proposed nonlocal FE analysis, and **(b)** Comparison between the experimental data [236] and the numerical structural response of the four-edge notched specimen (NLFE-A and FE-A refers to nonlocal and local FE analysis for mesh A)

Fig. 5.13(a) displays the structural responses obtained for meshes A, B, and C employing both local and proposed nonlocal FE approaches. Considering the computational cost associated with 3D fine mesh simulations, the mesh convergence studies have been performed up to 60% of the peak load. A mesh-sensitive nature is evident in the standard/local FE analysis. There is an observed sudden drop in load immediately after the peak point, and this intensity of drop in load is increasing with mesh refinement. In contrast, the proposed approach mitigates these issues and yields converged structural responses, with negligible changes in results for different mesh sizes.

On the other hand, Fig. 5.13(b) shows the comparison between the experimental data and the numerical structural response of the four-edge notched specimen. From the perspective of a coarse mesh, the numerical results show a reasonable alignment with the experimental data, exhibiting an approximate 4% error at the peak load, thus demonstrating the effectiveness of the strain difference-based nonlocal damage model. These results, while showing slight underprediction of the peak load, exhibited a similar softening nature. However, the analysis conducted using standard/local FE tends to underestimate the peak load.

5.5 Summary

A strain difference-based nonlocal damage model is proposed to study the failure behaviour of quasi-brittle materials. The formulation of the model operates within the framework of thermodynamics, leveraging the second principle to impose constraints on the constitutive relations. damage alone cannot account for the irreversible strains, the nonlocal energy residual function (P) in the present formulation aligns with those attained through a reversible process. In comparison, the previous works incorporated damage/damage energy release rate or equivalent strain as the regularization variable, where appropriate weight functions or associated flow rules are needed to preserve the symmetricity. The present methodology employs secant stiffness matrix for nonlocal FE analysis to account for material nonlinearity. The achieved converged results using the secant stiffness matrix remain ≤ 8 iterations per increment, maintaining computational efficiency. The model's effectiveness is demonstrated through mesh-independent results via % error prediction of peak load with respect to converged/reference results and force-displacement responses, accurate prediction of damage propagation paths for 2D and 3D case studies involving a crack and a hole.

Chapter 6

Ductile Damage Modelling in Nonlocal FEM Framework

This chapter introduces a novel ductile damage dissipation potential that incorporates the effects of isotropic hardening and scalar damage, providing an analytical expression that facilitates the straightforward determination of parameters. This formulation offers flexibility in selecting not only the isotropic hardening laws but also the power laws (such as the Ramberg-Osgood model) to contribute to the plasticity process. Moreover, the equivalent plastic strain, which significantly influences the damage evolution of ductile materials, has been treated as the nonlocal variable in the present work.

6.1 Introduction

As outlined in Chapter 2, significant advancements have been made in research concerning the development of damage evolution laws [19,20,90,179,206]. These laws are derived from the study of material degradation, often through multiple uniaxial tensile tests. However, it is noted that not all damage evolution laws are able to effectively capture all the damage patterns observed in ductile materials. Among them, the models proposed by [19] and Thakkar and Pandey [179] prove to be versatile by predicting damage in various types of ductile materials. As damage is known to strongly depend on plastic strain, these models are developed based on equivalent plastic strain, incorporating parameters related to power laws like Ramberg-Osgood law in the damage dissipation potential function. This actually restricts the application of the models when plasticity-related internal variables (isotropic and kinematic) responsible for hardening are involved, as it is crucial to discern the contribution of hardening to the plastic strain.

During uniaxial tensile tests, damage typically initiates in the early stages after reaching the yield limit. However, isotropic hardening in the material continues to have a significant contribution until the specimen reaches its ultimate strength. After necking, damage becomes dominant in the evolution of plastic strain. Furthermore, the effects of triaxiality are accounted for by considering it as a function of equivalent plastic strain. However, this approach not only necessitates for more number of material parameters but also applies primarily to high-stress triaxiality problems [179,238]. Bonora and Testa [239] recently reformulated his model by incorporating the triaxiality ratio and Lode angle parameter to capture the stress triaxiality effects across various ranges, from negative to positive values.

On the other hand, numerous research works have been conducted to address strain localization problems using nonlocal theories in ductile materials, as discussed in Section 2.3.2. In previous chapters, since permanent strain concepts are not included, the authors had the flexibility to experiment with various approaches to regularize the strain. However, in ductile materials, damage is significantly influenced by plastic strain and the damage energy release rate, which is a function of elastic strain. So, in this case, regularizing total strain is not a viable option. Moreover, Andrade et al. [240], in their comparative study, mentioned that the damage variable emerges as the most suitable choice for the nonlocal variable in implicit damage models, whereas it is not recommended for explicit damage models.

Therefore, building upon the aforementioned observations, as a preliminary step the authors propose a novel ductile damage dissipation potential that integrates the influences of isotropic hardening and scalar damage, offering an analytical expression that simplifies parameter determination. This formulation provides flexibility in the choice of isotropic hardening laws, as well as power laws (such as the Ramberg-Osgood model), to contribute to the plasticity process. Additionally, there has been limited exploration on failure analysis through the regularization of equivalent plastic strain, particularly within the class of Lemaitre's-based damage evolution laws. Thus, in the present work a nonlocal equivalent plastic strain is integrated with the proposed damage model to address the challenges associated with strain localization. The parameters required for the proposed damage model are identified through load-unload uniaxial tensile tests in which the damage evolution is measured through variation of elastic modulus concept.

6.2 Proposed continuum damage model: Local and Nonlocal

In this section, the mathematical formulation concerning the constitutive and evolution laws of coupled plastic-damage, considering the respective internal variables, is presented. Subsequently, a new closed-form expression for ductile damage is derived from the proposed damage dissipation potential function. Additionally, it is defined within a nonlocal framework by regularizing the equivalent plastic strain.

6.2.1 Constitutive laws

Considering small deformations, the Helmholtz free energy for ductile materials incorporates contributions from elastic-damage (ψ^{ed}) and isotropic hardening (ψ^{I}). It is defined as a function of respective constitutive variables, given by:

$$\psi = \psi^{ed}(\boldsymbol{\varepsilon}^e, D) + \psi^{I}(r) \tag{6.1}$$

$$\rho\psi^{ed}(\boldsymbol{\varepsilon}^e, D) = \frac{1}{2}\boldsymbol{\varepsilon}^e : (1-D)\mathbb{C} : \boldsymbol{\varepsilon}^e; \qquad \rho\psi^{I}(r) = R_\infty\left[r + \frac{1}{b}\exp(-br)\right] \tag{6.2}$$

where $\mathbb{C}$ is the fourth-order linear elasticity tensor, $\boldsymbol{\varepsilon}^e, r, D$ are the elastic strain tensor, isotropic hardening and damage variables, and R_∞, b are the hardening parameters.

Recalling the thermodynamic aspects of damaged materials, as discussed in Section 3.1.1, Eq. (3.12) for ductile damage is rewritten as:

$$\left(\boldsymbol{\sigma} - \rho\frac{\partial\psi^{ed}(\boldsymbol{\varepsilon}^e, D)}{\partial\boldsymbol{\varepsilon}^e}\right) : \dot{\boldsymbol{\varepsilon}^e} + \boldsymbol{\sigma} : \dot{\boldsymbol{\varepsilon}^p} - \rho\frac{\partial\psi^{I}(r)}{\partial r}\dot{r} - \rho\frac{\partial\psi^{ed}(\boldsymbol{\varepsilon}^e, D)}{\partial D}\dot{D} \geq 0 \tag{6.3}$$

Thus, the constitutive law by considering the reversible changes and also the thermodynamic conjugate forces for internal variables, r and D, is defined as:

$$\boldsymbol{\sigma} = \rho\frac{\partial\psi^{ed}(\boldsymbol{\varepsilon}^e, D)}{\partial\boldsymbol{\varepsilon}^e} = (1-D)\mathbb{C} : \boldsymbol{\varepsilon}^e \tag{6.4}$$

$$R = \rho\frac{\partial\psi^{I}(r)}{\partial r} = R_\infty[1 - \exp(-br)]; \qquad Y = -\rho\frac{\partial\psi^{ed}(\boldsymbol{\varepsilon}^e, D)}{\partial D} = \frac{1}{2}\boldsymbol{\varepsilon}^e : \mathbb{C} : \boldsymbol{\varepsilon}^e \tag{6.5}$$

Substituting Eqs. (6.4) and (6.5) in Eq. (6.3), reduces the dissipation inequality to

$$\boldsymbol{\sigma} : \dot{\boldsymbol{\varepsilon}^p} - R\dot{r} + Y\dot{D} \geq 0 \tag{6.6}$$

6.2.2 Evolution laws

From the theory of generalized standard materials, the evolution in the form of plastic strain and damage utilizes the normality law. Accordingly, the potential function F is additively decomposed into plastic (F^p) and damage dissipation potential function (F^D), postulated as:

$$F(\boldsymbol{\sigma}, r, Y, D) = F^p(\boldsymbol{\sigma}; r, D) + F^D(Y; D, r) \tag{6.7}$$

The coupled elasto-plastic model including the effect of damage is accomplished by substituting effective stress, $\tilde{\boldsymbol{\sigma}} = \frac{\boldsymbol{\sigma}}{1-D}$, in the definition of von Mises yield function:

$$F^p(\boldsymbol{\sigma}; r, D) = \frac{\sigma_{\boldsymbol{eq}}}{(1-D)} - \left(\sigma_{\boldsymbol{y_0}} + R\right) \tag{6.8a}$$

$$\dot{\boldsymbol{\varepsilon}}^p = \dot{\lambda}\frac{\partial F^p}{\partial \boldsymbol{\sigma}} = \frac{3}{2}\dot{\lambda}\frac{\boldsymbol{s}}{\sigma_{eq}} \tag{6.8b}$$

where the equivalent stress is defined as $\sigma_{eq} = \left(\frac{3}{2}\boldsymbol{s}:\boldsymbol{s}\right)^{\frac{1}{2}}$, and deviatoric stress $(\boldsymbol{s}) = \boldsymbol{\sigma} - \frac{1}{3}Tr(\boldsymbol{\sigma})\boldsymbol{I}$. $\sigma_{\boldsymbol{y_0}}$ and $\dot{\lambda}$ are the initial yield stress and plastic multiplier.

The inequality in Eq. (6.6) indicates that the dissipation due to damage must be positive, necessitating a convex potential function for damage. Considering the highly nonlinear nature of the damage evolution process, this work proposes a damage dissipation potential as a function of the isotropic hardening variable, the actual damage state, and the associated damage variable Y.

$$F^D = \frac{S}{2E^2(1-D)^{2s+1}\left(\sigma_{\boldsymbol{y_0}} + R\right)^{2s}(s+1)}\left(\frac{2E^2Y}{S}\right)^{s+1} \tag{6.9}$$

Damage energy release rate,

$$Y = \frac{\sigma_{eq}^2}{2E(1-D)^2}R_v; \qquad R_v = \frac{2}{3}(1+\nu) + 3(1-2\nu)\left(\frac{\sigma_H}{\sigma_{eq}}\right)^2 \tag{6.10}$$

where S and s are the damage parameters that are identified through the experimental data, R_v and $\frac{\sigma_H}{\sigma_{eq}}$ represents stress triaxial function and triaxiality ratio. Using the normality laws discussed in Section 3.1.1 and upon some mathematical operations, the kinetic laws of damage evolution is given by,

$$\dot{D} = \dot{\lambda}\frac{\partial F^D}{\partial Y} = \dot{p}\left(\frac{ER_v}{S(1-D)^2}\right)^s \tag{6.11}$$

6.2.3 Analytical expression for ductile damage

It can be observed that Eq. (6.11) is a direct application of variable separable approach. Thus, the above equation is integrated between (D_0, p_{th}) to (D_{cr}, p_{cr}), yields:

$$\frac{1}{(2s+1)}\left[-(1-D_{cr})^{(2s+1)}+(1-D_0)^{(2s+1)}\right]=\left(\frac{ER_v}{S}\right)^s(p_{cr}-p_{th}) \tag{6.12}$$

and for the integration between (D, p) and (D_{cr}, p_{cr})

$$\frac{1}{(2s+1)}\left[-(1-D_{cr})^{(2s+1)}+(1-D)^{(2s+1)}\right]=\left(\frac{ER_v}{S}\right)^s(p_{cr}-p) \tag{6.13}$$

where, D_0 represents the initial amount of damage within the material's microstructure, which is typically challenging to determine precisely and is often assumed to be zero. D_{cr} denotes the critical damage level, signifying the point at which the material fails due to the loss of its ability to withstand the external load, p_{th} represents the threshold plastic strain, indicating the onset of void nucleation and subsequent growth. Finally, p_{cr} corresponds to the effective accumulated plastic strain at the point of failure. Assuming the uniaxial loading or one-dimensional case, some of the important terms in above equations are redefined.

$$\frac{\sigma_H}{\sigma_{eq}}=\frac{1}{3}\Rightarrow\ R_v=1;\ \ p=\varepsilon^p, p_{th}=\varepsilon_{th}^p, p_{cr}=\varepsilon_{cr} \tag{6.14}$$

At the failure stage, elastic strain can be disregarded, allowing plastic strain to be substituted by the total uniaxial strain. Then, the Eqs. (6.12) and (6.13) are expressed as

$$\frac{1}{(2s+1)}\left[-(1-D_{cr})^{(2s+1)}+(1-D_0)^{(2s+1)}\right]=\left(\frac{E}{S}\right)^s(\varepsilon_{cr}-\varepsilon_{th}^p) \tag{6.15}$$

$$\frac{1}{(2s+1)}\left[-(1-D_{cr})^{(2s+1)}+(1-D)^{(2s+1)}\right]=\left(\frac{E}{S}\right)^s(\varepsilon_{cr}-\varepsilon^p) \tag{6.16}$$

A closed-form expression for the ductile damage using Eqs. (6.15) and (6.16) is derived as follows:

$$D=1-\left[(1-D_{cr})^{(2s+1)}+\left[-(1-D_{cr})^{(2s+1)}+(1-D_0)^{(2s+1)}\right]\frac{(\varepsilon_{cr}-\varepsilon^p)}{(\varepsilon_{cr}-\varepsilon_{th}^p)}\right]^{\frac{1}{(2s+1)}} \tag{6.17}$$

Similarly, in case of the multiaxial loading conditions, the expression for damage is derived using Eqs. (6.13) and (6.15).

$$D = 1 - \left[(1 - D_{cr})^{(2s+1)} + \left[-(1 - D_{cr})^{(2s+1)} + (1 - D_0)^{(2s+1)}\right] \frac{(p_{cr} - p)}{\left(\varepsilon_{cr} - \varepsilon_{th}^{p}\right)} (R_v)^s\right]^{\frac{1}{(2s+1)}} \tag{6.18}$$

It is well-known that an increase in triaxiality tends to make ductile materials more brittle and contributes to early fracture. Therefore, it is clear that p_{cr} is influenced by triaxiality, while p_{th} is assumed to be equal to the plastic strain threshold in the uniaxial case, neglecting any modifications[19,20]. Dividing Eq. (6.12) with (6.15),

$$\left(\varepsilon_{cr} - \varepsilon_{th}^{p}\right) = (R_v)^s (p_{cr} - p_{th})$$

$$p_{cr} = \varepsilon_{th}^{p}\left(1 + \frac{1}{(R_v)^s}\left(\frac{\varepsilon_{cr}}{\varepsilon_{th}^{p}} - 1\right)\right) \tag{6.19}$$

6.2.4 Nonlocal damage model

As mentioned earlier, since damage is significantly influenced by plastic strain, the nonlocal variable chosen is the equivalent plastic strain in the present work. Considering the insulation and locality recovery conditions during a uniform strain field, and substituting the equivalent plastic strain with its nonlocal counterpart in the evolution law, the derivation procedure of ductile damage follows the same steps as in the classical damage model.

$$\dot{D} = \dot{\bar{p}}\left(\frac{E R_v}{S(1 - D)^2}\right)^s \tag{6.20}$$

Nonlocal equivalent strain, $\bar{p}(\mathbf{x}) = \int_V W(\mathbf{x}, \mathbf{x}')\, p(\mathbf{x}') \mathrm{d}V(\mathbf{x}')$

For a uniaxial loading condition,

$$D = 1 - \left[(1 - D_{cr})^{(2s+1)} + \left[-(1 - D_{cr})^{(2s+1)} + (1 - D_0)^{(2s+1)}\right] \frac{(\varepsilon_{cr} - \bar{\varepsilon}^{p})}{(\varepsilon_{cr} - \varepsilon_{th}^{p})}\right]^{\frac{1}{(2s+1)}} \tag{6.21}$$

Since the threshold and critical parameters are determined from experimental data, the same parameters utilized in the local model are also applied here.

6.3 Methodology

This section delves into the numerical aspects, providing insights into the strategy utilized for conducting the simulations. It also outlines the materials, geometry, and procedures employed for the load-unload uniaxial tensile testing of the specimens, along with the calibration process used to determine the material parameters.

6.3.1 Numerical integration

In this study, the evolution of plastic strain, isotropic hardening, damage, and stress updating using the proposed elastoplastic damage constitutive model is computed through the forward Euler explicit integration scheme. This procedure is being employed due to its mathematical simplicity and convenience, especially in explicitly regularizing the equivalent plastic strain. When the updated stresses fall below the yield surface, the material at that point remains in the linear elastic regime. Conversely, when the stresses surpass the yield surface, plasticity effects are incorporated, initiating the process with a consistency condition.

$$\mathrm{d}F^p = \frac{\partial F^p}{\partial \tilde{\boldsymbol{\sigma}}} : \mathrm{d}\tilde{\boldsymbol{\sigma}} + \frac{\partial F^p}{\partial r} \mathrm{dr} = 0 \tag{6.22}$$

$$\frac{\partial F^p}{\partial \tilde{\boldsymbol{\sigma}}} : \mathbb{C} : (\mathrm{d}\boldsymbol{\varepsilon} - \mathrm{d}\boldsymbol{\varepsilon}^p) + \frac{\partial F^p}{\partial r} \mathrm{d}\lambda = 0 \tag{6.23}$$

By using Eq. (6.8b) and performing some mathematical operation to the above equation,

$$\mathrm{d}\lambda = \frac{\frac{\partial F^p}{\partial \tilde{\boldsymbol{\sigma}}} : \mathbb{C} : \mathrm{d}\boldsymbol{\varepsilon}}{\frac{\partial F^p}{\partial \tilde{\boldsymbol{\sigma}}} : \mathbb{C} : \frac{\partial F^p}{\partial \boldsymbol{\sigma}} - \frac{\partial F^p}{\partial r}} \tag{6.24}$$

where the terms $\frac{\partial F^p}{\partial \tilde{\sigma}}$ is defined similar to Eq. (6.8b), and $\frac{\partial F^p}{\partial r} = R_\infty b exp(-br)$. Then, the equation will be rewritten in Voigt form, which is the standard procedure in finite element analysis, to solve for the plastic multiplier. This aids in determining the evolution of internal variables at the next time step increment $t + \Delta t$.

$$\mathrm{d}\boldsymbol{\varepsilon}_t^p = d\lambda_t\left(\frac{3}{2}\frac{\mathbf{s}}{\sigma_{eq}}\right)_t ;\quad \mathrm{d}r_t = d\lambda_t;\quad \mathrm{d}p_t = \left(\frac{2}{3}\left(\mathrm{d}\boldsymbol{\varepsilon}_t^p\right)^{\mathrm{T}}\mathrm{P}^{\mathrm{T}}\mathrm{d}\boldsymbol{\varepsilon}_t^p\right)^{\frac{1}{2}} \tag{6.25}$$

$$\mathrm{d}\bar{p}_t = \sum_{n=1}^{ngp} w_n W(\mathbf{x}_n, \mathbf{x}_m)\,\mathrm{d}p(\mathbf{x}_m)\det(J(\mathbf{x}_m)) \tag{6.26}$$

$$\mathrm{d}D_t = \mathrm{d}\bar{p}_t\left(\frac{ER_v}{S(1-D)^2}\right)_t^s \tag{6.27}$$

$$\mathrm{d}\boldsymbol{\sigma}_t = \left(\mathbb{C}(1-D_t)\right)^{\mathrm{T}}\mathrm{d}\boldsymbol{\varepsilon}_t - \left(\mathbb{C}(1-D_t)\right)^{\mathrm{T}}\mathrm{d}\boldsymbol{\varepsilon}_t^p - \mathbb{C}^{\mathrm{T}}\left(\mathrm{d}\boldsymbol{\varepsilon}_t - \mathrm{d}\boldsymbol{\varepsilon}_t^p\right)\mathrm{d}D_t \tag{6.28}$$

where $\mathrm{P} = \begin{bmatrix} 1 & 0 & 0 \\ 0 & 1 & 0 \\ 0 & 0 & 2 \end{bmatrix}$. All the updated quantities at the end of the time step, Δt, may then be expressed as:

$$\begin{aligned} \boldsymbol{\sigma}_{t+\Delta t} &= \boldsymbol{\sigma}_t + \mathrm{d}\boldsymbol{\sigma}_t; &\qquad \boldsymbol{\varepsilon}_{t+\Delta t}^p &= \boldsymbol{\varepsilon}_t^p + \mathrm{d}\boldsymbol{\varepsilon}_t^p \\ r_{t+\Delta t} &= r_t + \mathrm{d}r_t; &\qquad D_{t+\Delta t} &= D_t + \mathrm{d}D_t \end{aligned} \tag{6.29}$$

6.3.2 Tangent stiffness matrix

In the field of FEA, capturing material nonlinearity typically involves the adoption of a consistent tangent stiffness matrix. This approach is favoured for its efficiency in achieving quadratic convergence while minimizing the number of iterations within incremental-iterative schemes. The equilibrium equation in the standard finite element discretized form is expressed as:

$$\mathbf{F}^{int} = \int_V \boldsymbol{B}^{\mathrm{T}}(\mathbf{x})\boldsymbol{\sigma}(\mathbf{x})\mathrm{d}V(\mathbf{x}) \tag{6.30}$$

Tangent Stiffness: $$\boldsymbol{K}_T = \frac{\partial \mathbf{F}^{int}}{\partial \mathbf{U}} = \frac{\partial}{\partial \mathbf{U}}\left(\int_V \boldsymbol{B}^{\mathrm{T}}(\mathbf{x})\boldsymbol{\sigma}(\mathbf{x})\mathrm{d}V(\mathbf{x})\right) \tag{6.31}$$

However, it can be seen that the relation between stress and strains are not directly related, instead stress is expressed as function of damage and elastic strain (see Eq. (6.4)). On the other hand, the constitutive law is indirectly nonlocal, where building the tangent stiffness is not as straightforward as the local theories for which the tangent moduli tensor is directly derived.

$$\frac{\partial \boldsymbol{\sigma}}{\partial \mathbf{U}} = \big(\mathbb{C}(1-D)\big)^{\mathrm{T}} \left(\frac{\partial \boldsymbol{\varepsilon}}{\partial \mathbf{U}} - \frac{\partial \boldsymbol{\varepsilon}^{p}}{\partial \mathbf{U}}\right) - (\mathbb{C})^{\mathrm{T}} \boldsymbol{\varepsilon}^{e} \frac{\partial D}{\partial \mathbf{U}} \tag{6.32}$$

where,

$$\frac{\partial D}{\partial \mathbf{U}} = \left(\frac{\partial D_n}{\partial \bar{p}_n} \frac{\partial \bar{p}_n}{\partial \boldsymbol{\varepsilon}_m}\right)^{\mathrm{T}} \frac{\partial \boldsymbol{\varepsilon}_m}{\partial \mathbf{U}} \tag{6.33}$$

Here, n and m are the source and neighbouring points. Expanding the expression of nonlocal equivalent plastic strain, the above equation further solved as:

$$\frac{\partial \bar{p}_n}{\partial \boldsymbol{\varepsilon}_m} = \int_V W(\mathbf{x}_n, \mathbf{x}_m) \frac{\partial p_m}{\partial \boldsymbol{\varepsilon}_m} \mathrm{d}V_m \tag{6.34}$$

By using Eq. (6.24),

$$\frac{\partial p_m}{\partial \boldsymbol{\varepsilon}_m} = \frac{\partial \lambda_m}{\partial \boldsymbol{\varepsilon}_m} = \left(\frac{\mathbb{C}^{\mathrm{T}} \dfrac{\partial F^p}{\partial \widetilde{\boldsymbol{\sigma}}}}{\left(\dfrac{\partial F^p}{\partial \widetilde{\boldsymbol{\sigma}}}\right)^{\mathrm{T}} \mathbb{C}^{\mathrm{T}} \dfrac{\partial F^p}{\partial \boldsymbol{\sigma}} - \dfrac{\partial F^p}{\partial r}} \right)_m \quad \text{and,} \quad \frac{\partial \boldsymbol{\varepsilon}_m}{\partial \mathbf{U}} = \boldsymbol{B}_m \tag{6.35}$$

Using Eqs. (6.32), (6.33), (6.34), and (6.35), the tangent stiffness matrix upon some mathematical operations elaborately written as,

$$\begin{aligned} \boldsymbol{K}_T = & \sum_{n=1}^{ngp} w_n \, \boldsymbol{B}_n^{\mathrm{T}} \big(\mathbb{C}_n(1-D_n)\big)^{\mathrm{T}} \boldsymbol{B}_n - \sum_{n=1}^{ngp} w_n \, \boldsymbol{B}_n^{\mathrm{T}} \big(\mathbb{C}_n(1-D_n)\big)^{\mathrm{T}} \frac{\partial \lambda_n}{\partial \boldsymbol{\varepsilon}_n} \boldsymbol{B}_n \\ & - \sum_{n=1}^{ngp} \sum_{m=1}^{ngp} w_n w_m W_{nm} \boldsymbol{B}_n^{\mathrm{T}} \mathbb{C}_n^{\mathrm{T}} \boldsymbol{\varepsilon}_n^{e} \left(\frac{\partial D_n}{\partial \bar{p}_n}\right)^{\mathrm{T}} \left(\frac{\partial p_m}{\partial \boldsymbol{\varepsilon}_m}\right)^{\mathrm{T}} \boldsymbol{B}_m \end{aligned} \tag{6.36}$$

6.3.3 Experiments and parameters identification

This section elaborates on the materials used, specimen geometry, and testing procedures employed for assessing mechanical properties, hardening characteristics, and damage. Furthermore, it includes a calibration procedure for identifying damage parameters. All tests conducted in this study are performed under quasi-static ($\dot{\boldsymbol{\varepsilon}} = 0.001 - 1s^{-1}$) and room temperature conditions.

6.3.3.1 Materials and Specimen geometry

The mechanical and damage behaviours of different materials, including SS316L and Al2024, are investigated in this study. Additionally, the damage behaviour of copper alloy is studied. The selection of these materials is based on their diverse damage responses to strain, demonstrating the material-independent nature of the proposed damage potential function.

The influence of stress triaxiality on material ductility and damage rate is widely acknowledged. Consequently, when determining the damage parameters, stress triaxiality is either kept constant or minimized within the region where damage is assessed. This necessitates prior knowledge of the strain and damage localization region. Bonora et al. [241] noted that tensile specimens with uniform geometry experience necking, resulting in non-uniform plastic strain distribution and increased stress triaxiality. To mitigate these effects, Lemaitre [183], Alves et al. [242], Gerbig et al. [243], and Sancho et al. [244] utilized hourglass specimens with round cross-sections. This design minimizes stress concentrations and confines necking to a defined range (see Fig. 6.1).

Following observations from the literature, a standard round bar (SRB) specimen (Fig. 6.2(a)), with a diameter of 12.5 mm and a gauge length five times the diameter (per ASTM-E8), is selected for extracting the material's mechanical properties and hardening parameters. Additionally, hourglass round bar (HGR) specimens, depicted in Fig. 6.2(b) along with their dimensions, are utilized for conducting damage monitoring tests.


(a) **(b)**

Fig. 6.1. (a) Geometry of copper specimens, and **(b)** geometry of Al2024 specimens (5 no.s of HGR and 2no.s of uniform round dia. specimens).

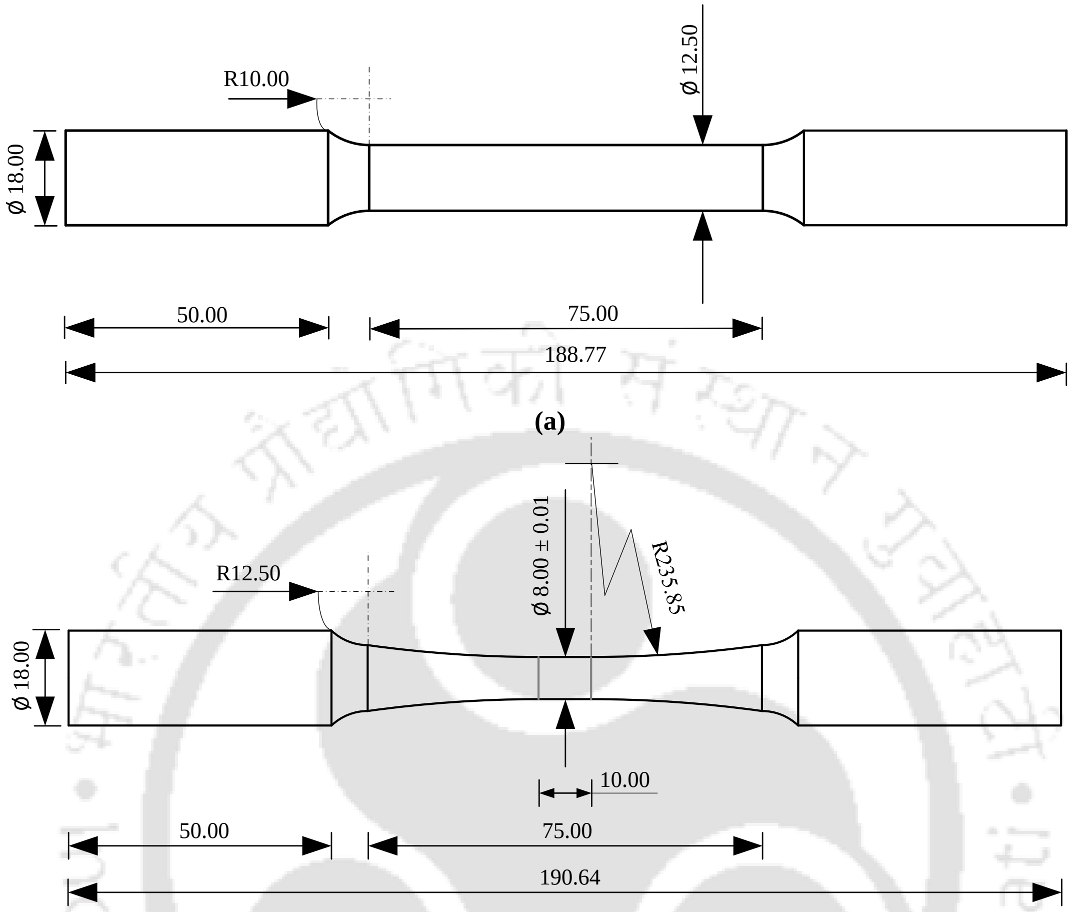

(a)

(b)

Fig. 6.2. (a) Smooth uniform round bar (SRB) specimen, and **(b)** Hour glass round (HGR) specimen geometry and dimensions.

6.3.3.2 Testing procedure

The experimental procedure is divided into following steps:

1. The SRB specimen is mounted in the Instron 100 KN servo-hydraulic dynamic testing machine (Fig. 6.3(a)) and adjusted into the loading fixtures.
2. An extensometer of gauge length 50 mm is positioned on the specimen to collect the strains in that region.
3. The displacement-controlled test is carried out till the failure of the material. Mechanical properties, including elastic modulus, yield strength, and ultimate tensile strength, are extracted from the collected data, with hardening parameters calculated accordingly. Reproducibility is ensured by testing at least two specimens for each material.

4. Following this, the HGR specimen is affixed within the same testing machine, with a 12.5 mm extensometer placed at the minimum cross-section region, as illustrated in Fig. 6.3(b).


(a) (b)

Fig. 6.3. (a) Instron 100 KN servo-hydraulic dynamic testing machine along with extensometer setup, and **(b)** positioning of extensometer (12.5 mm) at the minimum cross-section region

5. Similar to the SRB specimens, tensile tests are conducted on the HGR specimens until failure via displacement control. Intermediate data points are selected from the load versus displacement data for partial unloading operations.
6. The Load-Unload tests at the selected displacements are then conducted on a new HGR specimen to monitor the change in elastic modulus. These operations are repeated for approximately 8 to 10 cycles at regular intervals, each carried out at a low strain rate to neglect dynamic effects.

Thus, damage is measured using the expression

$$D = 1 - \frac{E}{E_0} \tag{6.37}$$

where E_0, E are initial and effective elastic modulus. The damage and plastic strain measurements of Al2024, copper alloy and SS316L materials are mentioned in Table 4.1.

Table 6.1 Damage growth and plastic strain of SS316L, Al2024, and copper alloy materials

S.No	**SS316L**		**Al2024**		**Copper alloy**	
	D	ε_p	D	ε_p	D	ε_p
1	0.01608	0.007971	0.0334	0.02417	0.0773	0.0180
2	0.01818	0.04228	0.0747	0.05113	0.1306	0.0472
3	0.03055	0.08822	0.08871	0.074	0.2305	0.1
4	0.04128	0.11622	0.1113	0.0923	0.3105	0.1402
5	0.04814	0.14654	0.1141	0.11198	0.3889	0.1778
6	0.08598	0.20971	0.12506	0.1121	0.4633	0.2117
7	0.1049	0.2223	0.13152	0.1263	0.5333	0.2418
8	0.1327	0.25648	0.13855	0.1328	0.6379	0.2833
9	0.19321	0.28628				

6.3.3.3 Identification of damage parameters

The procedure for determining the material parameters of the proposed damage growth law is discussed here. For the proposed model, data obtained from hour-glass round (HGR) bar specimens subjected to cyclic tensile load-unload tests (Table 4.1) is used for the calibration procedure. This calibration is aimed at determining the material parameters, including the damage exponent, s, denominator of the damage, S, and the critical damage D_{cr}. Additionally, parameters such as $\boldsymbol{\varepsilon}_{th}^{p}$ and $\boldsymbol{\varepsilon}_{cr}$ are determined for each material based on relevant information extracted from the stress-strain curves obtained from the experiments.

Determining the threshold plastic strain ($\boldsymbol{\varepsilon}_{th}^{p}$) poses a challenge, as measuring the initial damage is difficult (typically assumed as $D_0 = 0$). From the literature, it is understood that the bond between the particle and matrix is weak. Therefore, the threshold strain is considered to be of the same magnitude as the elastic proportional limit [19]. To address this, the specimen is first unloaded just after reaching the yield limit, and the reported plastic strain is then used as the threshold plastic strain ($\boldsymbol{\varepsilon}_{th}^{p}$).

$\boldsymbol{\varepsilon}_{cr}, D_{cr}$ - as discussed in Section 6.2.3, the plastic strain at failure is considered equal to the total strain, thereby neglecting the elastic strain. Unlike quasi-brittle materials, in these cases, experiments indicate that failure occurs before the damage reaches unity. Thus, the critical damage will always be less than one.

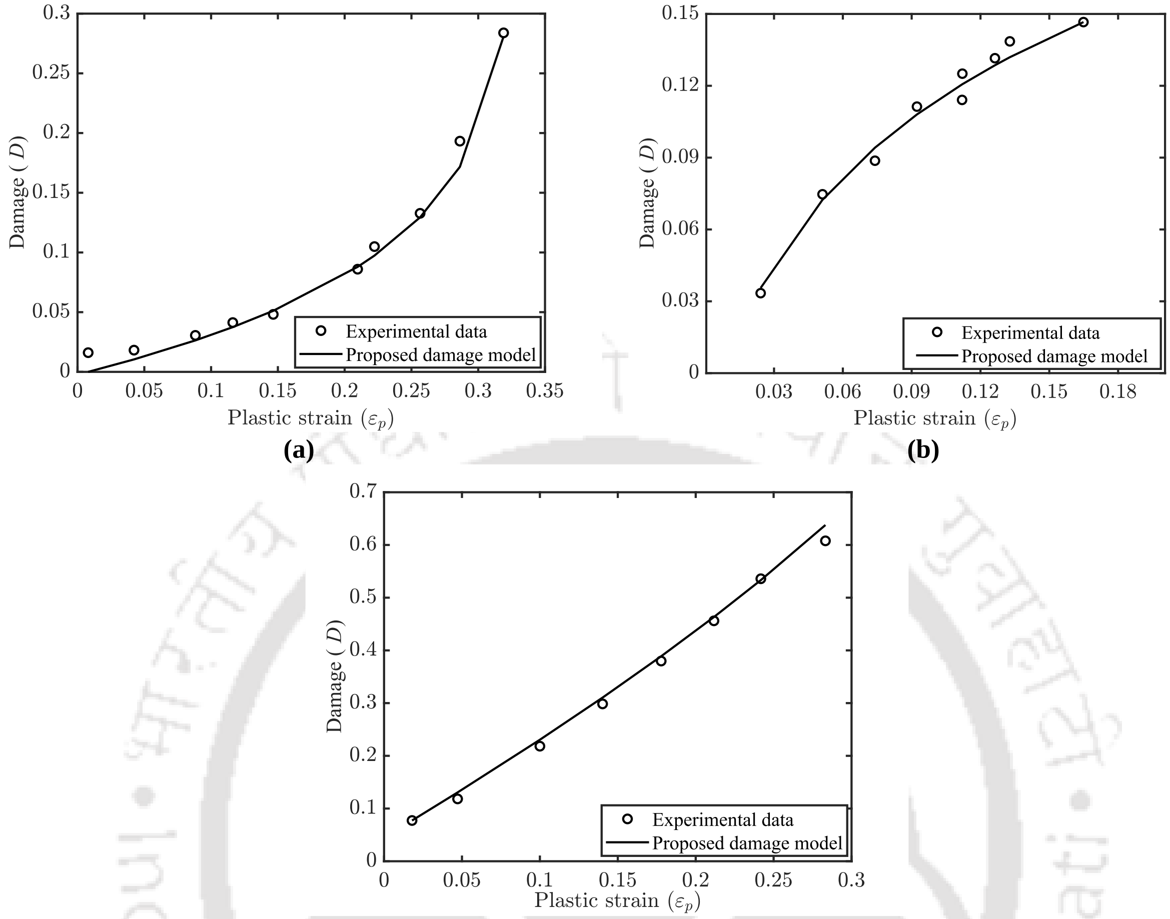

(a) **(b)**

(c)

Fig. 6.4. Fitting between numerical and experimental data **(a)** SS316L, **(b)** Al2024, and **(c)** Copper alloy

S, s, D_{cr} – the optimization approach, comprised of the least squares approach as the objective function and Nelder-Mead simplex search method is used for the calibration process [245]. This approach is readily implemented in MATLAB using the built-in function *fminsearch*. The optimization procedure tries to provide a close difference between the numerical and experimental results, which is measured through objective function. The set of material parameters utilised at the end of the optimization process are used as input parameters for the constitutive equations.

Table 6.2. Material parameters of aluminium alloy 2024

Material parameters		Al2024
Elastic modulus (GPa)	E	74.62
Yield stress (MPa)	σ_y	419
Hardening parameters	R_∞ (MPa)	303.6984
	b	8.8838
Critical strain	ε_{cr}	0.1649
Threshold plastic strain	ε_{th}^{p}	0.013
Damage exponent	s	-5.8322
Critical damage	D_{cr}	0.1466

Table 6.3. Material parameters of copper alloy

Material parameters		Copper
Elastic modulus (GPa)	E	120
Yield stress (MPa)	σ_y	240
Hardening parameters	R_∞ (MPa)	300
	b	4
Critical strain	ε_{cr}	0.33
Threshold plastic strain	ε_{th}^{p}	0.018
Damage exponent	s	0.2103
Critical damage	D_{cr}	0.7743

The detailed description of specimens shown in the Fig. 6.2, and also the data collected from the experimental results of Al2024, copper alloy and SS316L (see Table 6.1) are used. By fitting experimental data with a closed-form expression for damage (refer to Eq. (6.17)) and a constitutive equation (excluding damage), material parameters are determined. These parameters are then listed in Table 6.2, Table 6.3, and Table 6.4. The adequacy of the obtained parameters is validated by assessing the agreement between experimental and numerical responses for Al2024, copper alloy, and SS316L, as illustrated in Fig. 6.4.

Table 6.4. Material parameters of stainless-steel alloy 316L

Material parameters		SS316L
Elastic modulus (GPa)	E	200
Yield stress (MPa)	σ_y	700
Hardening parameters	R_∞ (MPa)	269.4582
	b	4.0525
Critical strain	ε_{cr}	0.3194
Threshold plastic strain	ε_{th}^{p}	0.007971429
Damage exponent	s	4.9051
Critical damage	D_{cr}	0.2839

6.4 Results and Discussions

In this section, the failure behaviour of Al2024 and SS316L SRB specimens under tensile tests is examined through 1D FE analysis. During the mesh discretization process, the area of the central element in the bar is intentionally reduced by 0.001% to initiate strain localization. This strain localization phenomenon is then addressed by applying nonlocal integral theories. Mesh convergence analysis is performed by varying the number of elements, namely 100, 200, and 400. Additionally, distributions of damage and nonlocal equivalent plastic strain along the length of the Al2024 bar are provided. Finally, numerical stress-strain responses are compared with experimental data to evaluate the accuracy of the simulation results.

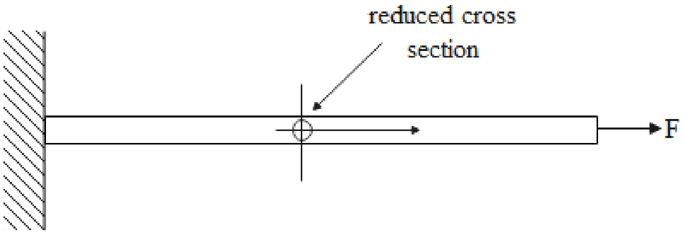

Fig. 6.5. 1D bar under tensile test

6.4.1 Aluminium alloy 2024

Using the mechanical properties, hardening, and damage parameters, the stress-strain and force-displacement responses of Al2024 are numerically predicted and compared with the experimental data, as depicted in Fig. 6.6(a) and 6.6(c). It can be observed that the 1D FE results exhibit good agreement with the uniaxial tensile data. The numerical analysis continues until the damage reaches its critical value, and it is observed that the critical damage parameter is reached approximately at the failure strain of the SRB specimen. This observation highlights the effectiveness of the proposed damage model.

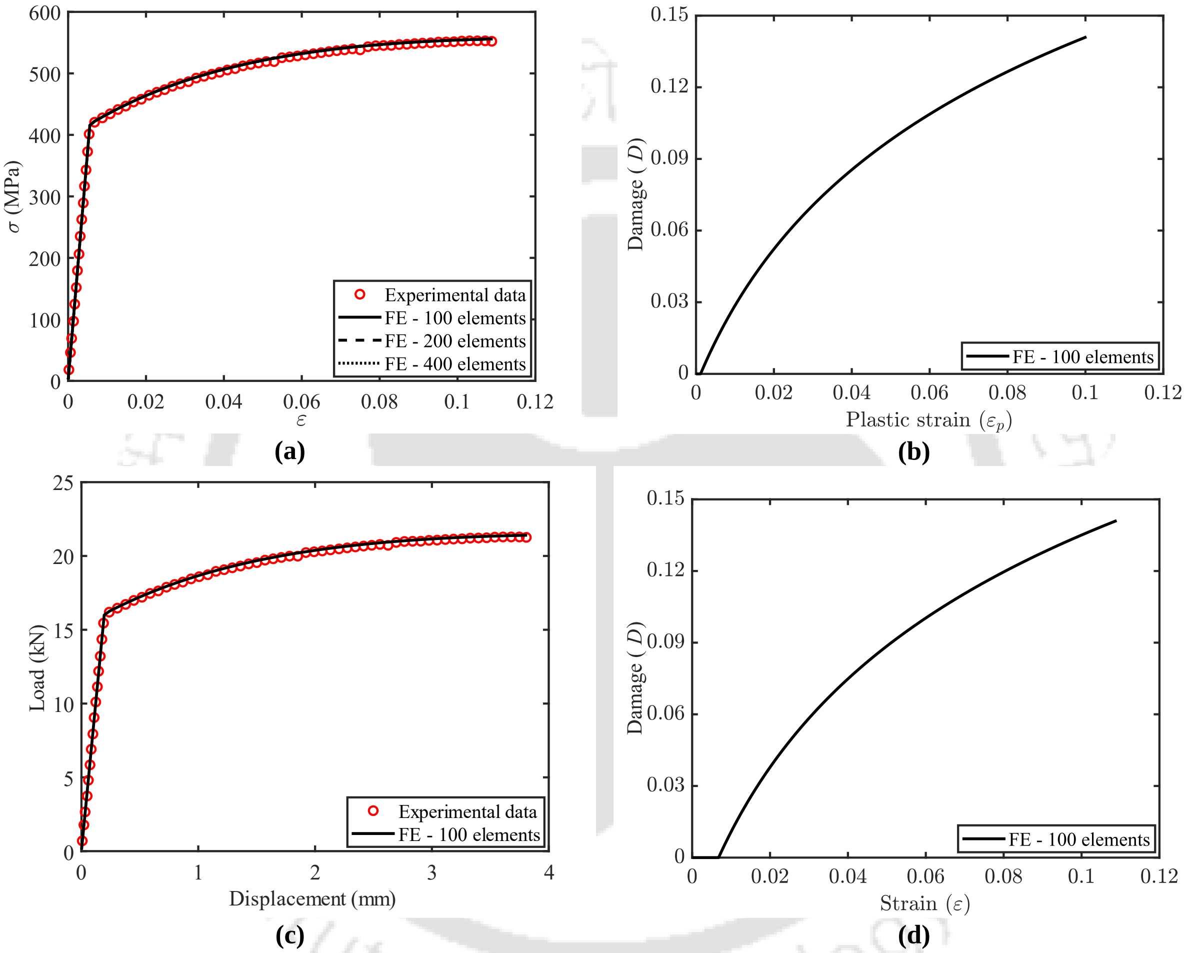

(a) **(b)** **(c)** **(d)**

Fig. 6.6. Al2024: **(a)** numerical and experimental results in the form of engineering stress vs strain, **(b)** damage vs plastic strain, **(c)** load-dispalcement response and **(d)** damage vs strain curves of SRB specimen.

As explained by Bonora [19], Al2024 exhibits a distinct pattern of damage accumulation concerning strain, with the nucleation phase playing a prominent role in the damage evolution. Upon reaching the threshold strain, numerous voids are nucleated. Subsequent strain increments lead to the formation of additional microvoids with limited growth in the already initiated voids. It is only when this process reaches saturation and the void spacing is significantly reduced that coalescence occurs, ultimately leading to specimen failure. This characteristic behaviour is evidently reflected in the predictions of the proposed damage model (refer to Fig. 6.6(b) and 6.6(c)). Because of this, from the initiation of damage until the failure point, the damage evolution progresses uniformly, preventing the material from entering the softening phase before failure occurs. Moreover, such failure behaviours are often predictable by the majority of models.

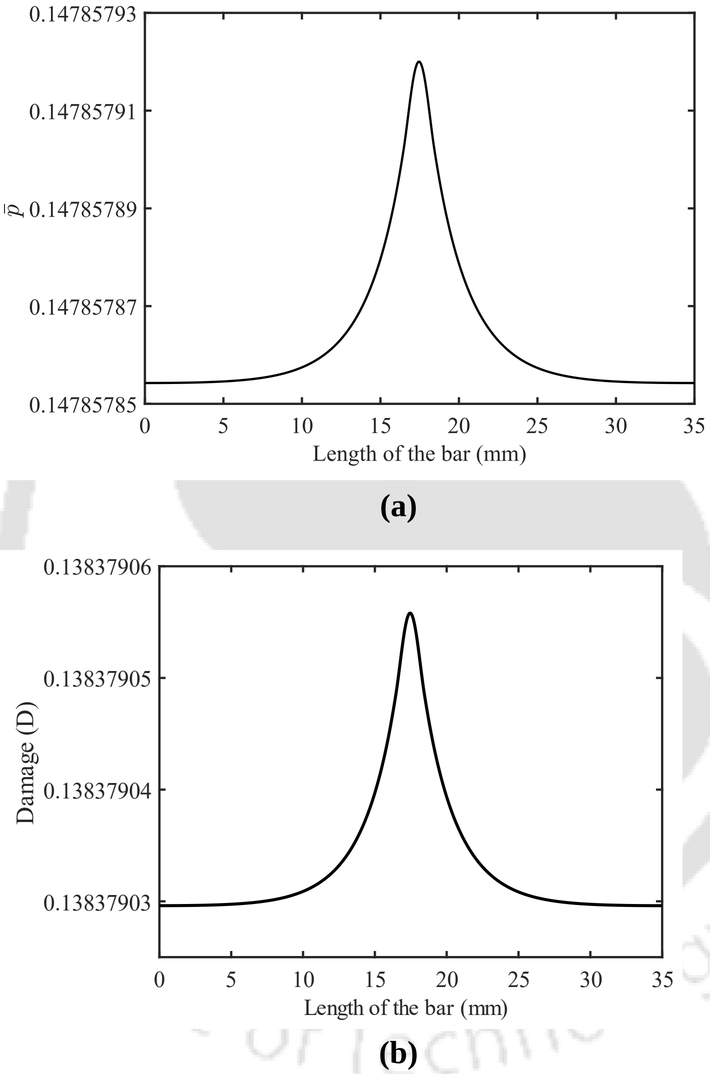

Fig. 6.7. Al2024: **(a)** nonlocal equivalent plastic strain profile, and **(b)** damage profile for a bar with 0.001% area reduction in central element for a FE mesh of 400 elements

In FEM, a sudden change in the cross-sectional area, commonly referred to as a weak discontinuity, leads to a discontinuous strain distribution within that respective region of the bar. In order to achieve an iteratively converged response, it often requires a greater number of elements. However, the nonlocal approach not only maintains a continuous nature, shown in Fig.

6.7(a), but also achieves iterative convergence with a relatively smaller number of elements. As damage evolution indirectly relies on the nonlocal equivalent plastic strain, it also exhibits a continuous nature (see Fig. 6.7(b)).

6.4.2 Stainless steel 316L

Experimentally, this is a special study, where instead of HGR only SRB specimens are considered with geometry shown in Fig. 6.8. The same procedure of load-unload cyclic tensile tests is carried out and parameters are identified, as already discussed in Section 6.3.3.

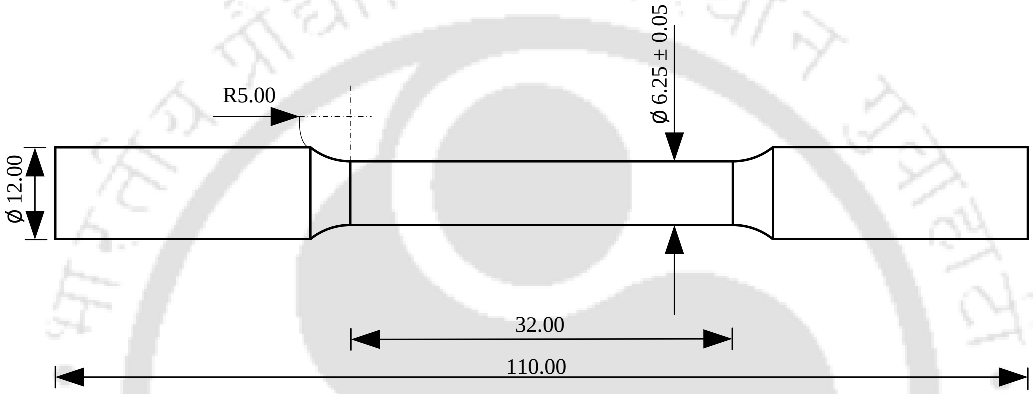

Fig. 6.8. Smooth uniform round bar specimen geometry and dimensions of SS316L.

Fig. 6.9(a) displays the stress-strain responses of stainless steel 316L, comparing the results obtained from numerical analysis with those from uniaxial tensile tests. It is evident that there is a strong agreement between both curves across the linear elastic, hardening, and softening phases. However, it is noted that there is a deviation in the numerical results beyond the ultimate strength, particularly in the softening regime. While this deviation is relatively small in this specific case, it is understood that materials of specimens with smooth, uniform geometries covering a significant area under the softening region may experience more substantial deviations between numerical and experimental results. This observation indicates the presence of significant stress triaxiality effects in the SRB specimens, an aspect that is not considered in this preliminary study.

For these steels, voids are nucleated both by the breaking of carbides and by their debonding from the ductile matrix. Bonora [19] observed that, all nucleated voids initially grow in the loading direction. It's only in a later stage that voids cease growing and begin to link due to necking of the ligament between them, allowing growth transverse to the load direction. This phenomenon can be observed by analyzing the results of the proposed damage model (see Fig.

6.9(b) and 6.9(c)). Specifically, it can be noted that after necking, the rate of damage evolution rapidly increases compared to before necking. This acceleration in damage evolution can be attributed to the coalescence of voids, as mentioned previously.

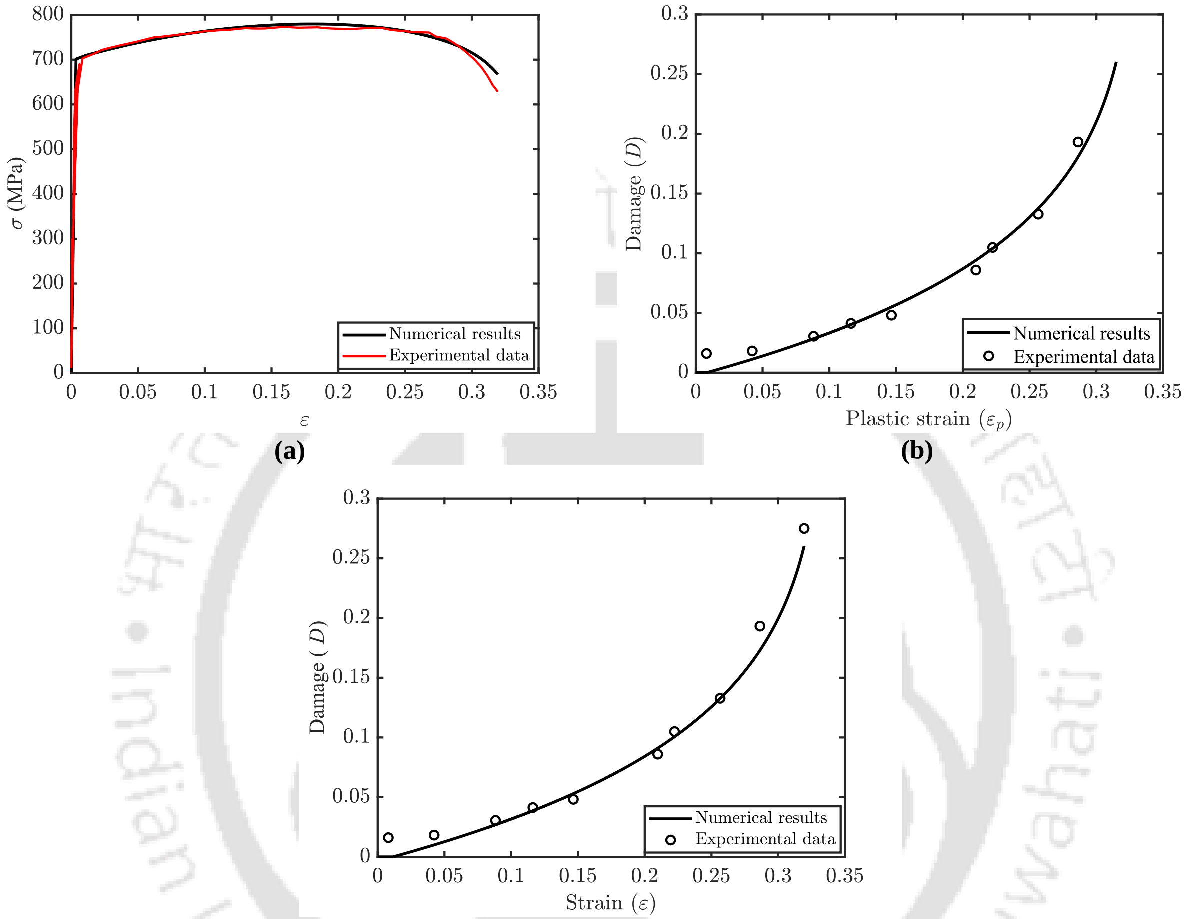

(a) **(b)**

(c)

Fig. 6.9. SS316L: **(a)** numerical and experimental results in the form of engineering stress vs strain, **(b)** damage vs plastic strain, and **(c)** Damage vs strain curves of SRB specimen.

6.5 Summary

In this work, it is proposed to incorporate the influence of internal variables such as isotropic hardening and damage into the damage potential function to more accurately predict nonlinear damage evolution. Following the testing procedure outlined in Section 6.3.3, the material's damage is assessed using the modulus of degradation approach. Based on the calibration condition, the damage parameters S and s, as well as the hardening parameters R_∞ and b, are determined by using the optimization technique, specifically the *fminsearch* tool in MATLAB. On the other hand, the equivalent plastic strain is explicitly regularized to deal with strain localization problems. The nonlocal tangent stiffness matrix and the implementation of explicit numerical integration procedures are presented. It is found that the numerically predicted stress vs strain, and damage vs strain curves for Al2024, and SS316L are in good agreement with the responses obtained through the experiments.

Chapter 7

Damage Modelling using CZM Approach in EFG Framework

In the present chapter, crack propagation in mode I and mode II problems are investigated using cohesive zone modelling (CZM) within the proposed modified EFGM framework. The modified EFG method incorporates both the diffraction method and the Heaviside enrichment function to handle crack tip solutions and represent crack discontinuities. The key highlights of this work include (i) the utilization of the generalized displacement control method (GDCM) to effectively tackle material nonlinearity that emerges during the evolution of damage in the cohesive layer, and (ii) the updating of tangent stiffness specifically for nodes enriched with the Heaviside function and those influenced by diffracted weight functions. To demonstrate the effectiveness of the proposed approach, it is applied to (1) uncracked three-point bending (TPB), (2) adhesively bonded: (a) cracked double cantilever beam (DCB), and (b) end-notched flexure (ENF) problems. Additionally, several parametric studies have been conducted on both the EFG method and GDCM.

7.1 Introduction

Numerous structural failures subjected to static and/or dynamic loading involve complex phenomena of onset, propagation, branching, merging, and arrest of cracks that are found throughout engineering history [246,247]. In nearly all materials, a fracture process zone (FPZ) exists near the crack tip, which exhibits localized yielding [248]. If the FPZ is not small, the cohesive zone modelling (CZM) is the simplest technique available to model crack propagation over the commonly used linear elastic fracture mechanics (LEFM) approach. CZMs are incorporated into the numerical techniques using the cohesive elements characterized by cohesive or traction-separation laws (TSL).

7.1.1 EFG in crack propagation using CZM approaches

Almost parallel to the XFEM, the meshfree methods (MMs) were developed to eliminate the issues inherent in meshing, where only nodes are present in the domain. The element-free Galerkin (EFG), which uses a global weak form [41] is a popular technique in dealing with solid and fracture mechanics. Weight function modification, intrinsic or extrinsic basis enhancement and partition-of-unity enrichment are some popular approaches to handling crack problems within the framework of the EFG method [31]. Belytschko et al., [160] analyzed the dynamic fracture in concrete using the CZMs through the EFG framework and proposed that the EFG method is reliable for this task. Subsequently, the methods like eXtended EFG (XEFG) and extrinsically enriched EFG methods were introduced, which will not be helpful in the absence of analytical solutions from which the branch enrichment functions are inspired.

7.1.2 Nonlinear solvers for strain softening phenomenon

In nonlinear separation, whenever the cohesive stress of the FPZs reaches its maximum, the crack gradually begins to open by degrading the stiffness of that region. This nonlinear softening nature was studied using the CZMs by employing various iterative techniques. Newton's method and extensions are load-controlled techniques that fail to converge at the limit points and are unsuitable for predicting post-peak responses [249]. These problems were addressed by displacement control techniques like the arc-length control method (ALCM), which uses a constraint equation based on a cylindrical/sphere/elliptical plane to control the equilibrium path. However, these methods face convergence issues near limit points of softening materials and fail to predict snapback behaviour [23,250,251]. Several alternatives, like modified arc-length methods [252–254], dynamic approach [255], the combination of arc-length and Newton-Raphson [256], etc., have been suggested to overcome the issues while studying the traction-separation behaviour. Notably, the sign of the load parameter in the ALCMs may change inaccurately because of higher gradients near the displacement limit points [257].

The generalized displacement control method (GDCM) proposed by Yang et al., [258] is the result of various limitations discussed until now used for nonlinear geometric problems. It can adjust the step size and is self-adaptive in changing the loading directions.

In this work, we combine the modified EFG method with the CZM approach that does not necessitate the usage of the branch enrichment functions to simulate the failure phenomenon owing to crack propagation in different geometries and material combinations. While meshfree methods offer robustness, their computational cost tends to be higher than that of FEM. Particularly, when addressing strain-softening problems that necessitate incremental-iterative techniques, further increases the computational expenses. Although the inherent computation time of EFG cannot be decreased, we can reduce the additional time consumed by iterative methods. Thus, the

Generalized Displacement Control method, which has received limited attention in applications involving material nonlinearity and fracture, was employed. One of the main advantages of this method is that it requires fewer incremental steps than others for the same value of the initial control factor and effectively maintains the accuracy of both the snapthrough and snapback behaviours. This approach will solve the nonlinear nature of the CZM based crack propagation problems by extracting the crack opening displacements (CODs) and updating the tangent stiffness matrix at the select region rather than the entire domain.

7.2 Governing equations and formulations for cohesive crack in modified EFG framework

The current section introduces the variational formulation and its algebraic representation within the modified EFG framework, specifically addressing the incorporation of the cohesive crack concept. Additionally, it delves into a detailed discussion of the constitutive law governing CZM.

7.2.1 Variational formulation

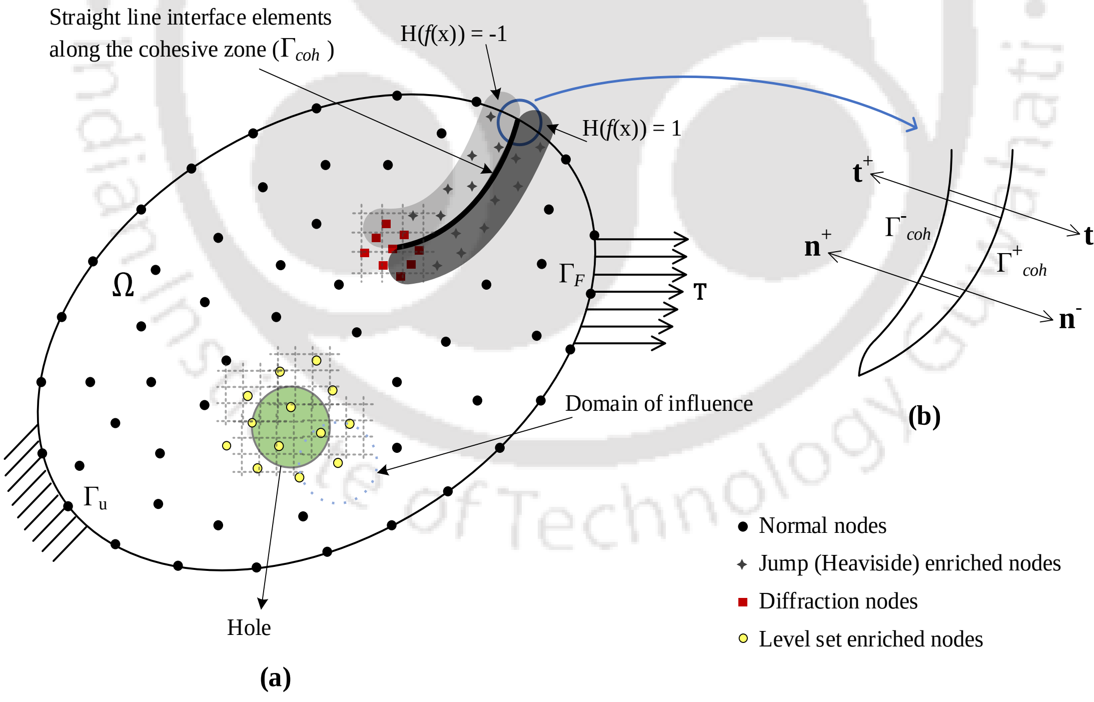

Fig. 7.1. (a) Geometry, boundary conditions, nodal discretization of a domain with strong and weak discontinuity, and **(b)** zoom in the region of cohesive crack propagation

Let us consider that the domain Ω with a crack Γ_c, as shown in Fig. 7.1, which has displacement constraints, $\mathbf{u}_\Gamma$, on Γ_u and subject to tractions, $\mathbf{T}$, on the boundary Γ_F. It contains an active cohesive zone, Γ_{coh}, within the crack surface where the upper and lower edges are subjected to tractions, $\mathbf{t}^+$and $\mathbf{t}^-$, respectively. The equilibrium equations of this problem are given by

$$\nabla.\boldsymbol{\sigma} = 0 \;\text{ on } \Omega \tag{7.1}$$

$$\boldsymbol{\sigma}.\mathbf{n}^+ = -\boldsymbol{\sigma}.\mathbf{n}^- = \mathbf{t}^+ = -\mathbf{t}^- = \mathbf{t} \;\text{ on }\; \Gamma_{coh} \tag{7.2}$$

where $\boldsymbol{n}^+$ and $\boldsymbol{n}^-$ are the normals at the crack surface. The obtained displacement solution should satisfy the following relations:

$$\mathbf{u} = \mathbf{u}_\Gamma \text{ on } \Gamma_u \in \Gamma\text{, and } \boldsymbol{\sigma}.\mathbf{n} = \mathbf{T} \text{ on } \Gamma_F \in \Gamma \tag{7.3}$$

By incorporating Eqs. (3.27), (3.28), and (3.30), which represent the strain-displacement relations, cohesive separation ($\mathbf{w}$), and the constitutive relations of both the cohesive zone and entire domain, respectively, the strong form of the equilibrium equations is transformed into the Galerkin weak form. This transformation allows for the construction of the discrete system of equations within the EFG framework. The displacement $\mathbf{u}$ belongs to a set of kinematically admissible displacement fields $\mathbf{v}$ such that $\mathbf{v} \in \mathcal{H}^1$ (Hilbert space). The Lagrange multiplier (λ) is utilized to impose the displacement boundary conditions since the shape functions of the EFG method obtained through the MLS procedure are approximants rather than interpolants. The weak form with Lagrange multipliers (λ) for the constraints for a 2D problem is given by:

$$\begin{aligned}\int_\Omega \delta(\mathbf{L}_d\mathbf{u})^{\mathrm{T}}\mathbf{C}(\mathbf{L}_d\mathbf{u})\,\mathrm{d}\Omega - \int_{\Gamma_u} \delta\lambda^{\mathrm{T}}(\mathbf{u} - \mathbf{u}_\Gamma)\mathrm{d}\Gamma - \int_{\Gamma_u} \delta\mathbf{u}^{\mathrm{T}}\lambda\mathrm{d}\Gamma \\ = \int_{\Gamma_F} \delta\mathbf{u}^{\mathrm{T}}\mathbf{T}\mathrm{d}\Gamma + \int_{\Gamma_{coh}^+} \delta(\mathbf{t}^+\mathbf{u}^+)\mathrm{d}\Gamma + \int_{\Gamma_{coh}^-} \delta(\mathbf{t}^-\mathbf{u}^-)\mathrm{d}\Gamma\end{aligned} \tag{7.4}$$

Then making use of the relations for crack face separation or the crack opening displacements and $\mathbf{t}^+ = -\mathbf{t}^- = \mathbf{t}$ on Γ_{coh}, rearranging Eq. (7.4), we get

$$\int_{\Omega} \delta(\mathbf{L}_d\mathbf{u})^{\mathrm{T}}\mathbf{C}(\mathbf{L}_d\mathbf{u})\,\mathrm{d}\Omega - \int_{\Gamma_u} \delta\lambda^{\mathrm{T}}(\mathbf{u}-\mathbf{u}_{\Gamma})\mathrm{d}\Gamma - \int_{\Gamma_u} \delta\mathbf{u}^{\mathrm{T}}\lambda\mathrm{d}\Gamma = \int_{\Gamma_F} \delta\mathbf{u}^{\mathrm{T}}\mathbf{T}\mathrm{d}\Gamma + \int_{\Gamma_{coh}} \delta\mathbf{w}^{\mathrm{T}}\mathbf{t}\mathrm{d}\Gamma \tag{7.5}$$

7.2.2 Modified EFG method

The modified EFG method does not require any enrichment functions to model the crack tip [259]. Instead, it combines the diffraction method and Heaviside functions while modelling the crack growth phenomena. The former characterizes the crack tip solution, whereas the latter represents the separation at the cohesive zone arising due to the damage propagation. The method also uses level set functions to model the material discontinuity occurring due to dissimilar material properties.

Consequently, the displacement approximation in the modified EFG method in the presence of a cohesive zone (displacement jumps) and the material interface present in a given geometry (see Fig. 7.1) takes the form

$$\mathbf{u}(\mathbf{x}) = \sum_{I\in S_N} \mathbf{\Phi}_I(\mathbf{x})\mathbf{u}_I + \sum_{I\in S_H} \mathbf{\Phi}_I(\mathbf{x})\{\mathbf{a}_I \mathrm{H}(f(\mathbf{x}))\} + \sum_{I\in S_L} \mathbf{\Phi}_I(\mathbf{x})\mathbf{c}_I\chi_I(\mathbf{x}) \tag{7.6}$$

where $\mathbf{a}_I$,$\mathbf{c}_I$, $\mathbf{u}_I$ represents Heaviside enriched, level-set enriched and regular nodal displacement vectors, the function $\chi_I(\mathbf{x}) = F^I(\mathbf{x}) - F^I(\mathbf{x}_I)$ is employed for displacement continuity across the interface with $F^I(\mathbf{x}) = \sum_{I\in S_L}|\zeta_I|\,\Phi_I(\mathbf{x}) - \left|\sum_{I\in S_L}\zeta_I\,\Phi_I(\mathbf{x})\right|$. ζ_I is the signed distance of node I from the interface [260]. The set S_H and S_L consists of Heaviside enriched and level set enriched nodes with a displacement continuity function.

Finally, the modified EFG approximation of the displacement is introduced in the weak form (Eq. (7.5)). To find the global stiffness matrix, integration is performed over the domain (Ω) and the cohesive layer (Γ_{coh}) by employing the background mesh and cohesive cells (straight-line segments). The final system of equations is given by

$$\underbrace{\begin{bmatrix}\mathbf{K} & \mathbf{G}\\ \mathbf{G} & 0\end{bmatrix}}_{\mathbf{M}}\underbrace{\begin{Bmatrix}\mathbf{U}\\ \lambda\end{Bmatrix}}_{\bar{\mathbf{U}}} = \underbrace{\begin{Bmatrix}\mathbf{F}\\ \mathbf{q}\end{Bmatrix}}_{\boldsymbol{\mathcal{F}}} \tag{7.7}$$

The expression of stiffness matrix (**K**), external force vector (**F**), matrix (**G**) and vector (**q**) are provided in Appendix A.

7.3 Numerical Implementation

This section explores the linearization process and employs a displacement-controlled solution technique to accurately capture the nonlinear response of both homogeneous and nonhomogeneous 2D geometries during cohesive crack propagation.

7.3.1 Linearization (Tangent stiffness matrix)

The displacements for the set of nodes, discussed in Section 7.2.2, are computed by solving the discrete system of equations. The stiffness matrix results from the entire domain being integrated using the Gauss quadrature scheme on the background mesh, which is triangular/quadrilateral in 2D geometry and a line segment in 1D. On the other hand, the straight-line cells are employed throughout the path where the cohesive crack grows, and the integration over the cohesive crack boundary performed on these cells is represented as part of the external force vector **F**.

With the aid of the constitutive relation or TSLs on Γ_{coh}, the behaviour of the cohesive cells can be recorded. When a line segment experiences maximum stress or traction, the damage is initiated and, on further evolution, degrades the element's stiffness and undergoes softening response, as shown in Fig. 3.4(a). During the cohesive crack growth, only the region close to the crack boundary is influenced, whereas the location far from the crack is assumed to continue in the elastic condition.

Therefore, the cohesive crack concept in the EFG framework has the advantage of updating only the stiffness of the straight-line segments at every iteration instead of the entire domain during the nonlinear softening. A pseudo-code for implementing this is shown in Box 7.1. Moreover, due to the MLS shape functions and the support domain, the stiffness matrix of straight-line elements considers only a set of nodes surrounding the crack that is either enriched with the Heaviside function or the nodes whose weight functions are modified by the diffraction method.

For a nonlinear problem, there exists the residual vector expressed as

$$\mathbf{R} = [\mathbf{K}]\{\mathbf{U}\} - \{\mathbf{F}\} \tag{7.8}$$

These residual forces must be reduced to zero ($\mathbf{R}(\mathbf{U}) = 0$) to solve the nonlinear system of equations, which is possible by establishing the linear approximation [261].

$$\mathbf{R}\,(\mathbf{U}_{i+1}) \approx \mathbf{R}\,(\mathbf{U}_i) + \mathrm{D}\mathbf{R}\,(\mathbf{U}_i)[\Delta\mathbf{U}] = \mathbf{0} \tag{7.9}$$

$$\mathrm{D}\mathbf{R}\,(\mathbf{U}_i)[\Delta\mathbf{U}] = \frac{\partial\mathbf{R}(\mathbf{U}_i)}{\partial\mathbf{U}}\Delta\mathbf{U}$$

where,

$$\mathbf{K}_{\mathbf{T}}(\mathbf{U}_i) = \frac{\partial\mathbf{R}(\mathbf{U}_i)}{\partial\mathbf{U}} = \mathbf{K} - \frac{\partial\mathbf{F}}{\partial\mathbf{U}} \tag{7.10}$$

$$\frac{\partial\mathbf{F}}{\partial\mathbf{U}} = 4\int_{\Gamma_{coh}}\left(\sum_{I\in S_H}\mathbf{\Phi}_I(\mathbf{x})\{\mathrm{H}(f(\mathbf{x}))\}\right)^{\mathrm{T}}\frac{\partial t}{\partial w}\boldsymbol{I}\,\mathrm{d}\Gamma \tag{7.11}$$

where D is the directional derivative, $\mathbf{U}_i$ represents the nodal displacement vector, $\mathbf{K}_{\mathbf{T}}$ is defined as tangent stiffness matrix, $\boldsymbol{I}$ is the second-order identity tensor, and $\frac{\partial t}{\partial w}$ represents the consistent tangent modulus for the traction-separation law, Eq. 3.20, which is expressed as:

$$\dot{t} = K(1-D)\dot{w} - Kw\dot{D} \tag{7.12}$$

The exponential damage evolution is used in the present work to predict the nonlinear softening behaviour of the specimen during crack propagation. By differentiating Eq. (3.22) with respect to time gives

$$\dot{D} = f(w)\dot{w}$$

$$f(w) = \left\{\frac{w_0}{w^2}\right\}\left\{1 - \frac{1-\exp\left(-\alpha\left(\frac{w-w_0}{w_f-w_0}\right)\right)}{1-\exp(-\alpha)}\right\} + \left\{\frac{w_0}{w}\right\}\left\{\left(\frac{\alpha}{w_f-w_0}\right)\left(\frac{\exp\left(-\alpha\left(\frac{w-w_0}{w_f-w_0}\right)\right)}{1-\exp(-\alpha)}\right)\right\} \tag{7.13}$$

Box 7.1. Pseudo-code for updating tangent stiffness matrix at every iteration

```
Calculate the 'w' (COD)by extracting the displacements from the jump and branch enriched nodes
if [$mode\ I\ \ \&\&\ \ COD >= w_0$ ]
    calculate $D, \frac{\partial D}{\partial w}$, and $\frac{\partial t}{\partial w}$ from Eqs. (3.22), (7.13), and (7.12)
elseif [$mode\ I$ ]
    $\frac{\partial t}{\partial w} = K_I$
elseif [$mode\ II\ \ \&\&\ \ COD >= w_0$ ]
    calculate $D, \frac{\partial D}{\partial w}$, and $\frac{\partial t}{\partial w}$ from Eqs. (3.22), (7.13), and (7.12)
elseif [$mode\ II$ ]
    $\frac{\partial t}{\partial w} = K_{II}$
end
Update $\frac{\partial \mathbf{F}}{\partial \mathbf{U}}$ and $\mathbf{K_T}(\mathbf{U}_i)$ using Eqs. (7.10) and (7.11)
```

7.3.2 Generalized displacement control method (GDCM)

The system of linear algebraic equations shown in Eq. (7.7) is solved until the cohesive zone reaches its full load-bearing capacity ($w = w_0$). However, damage begins immediately after this peak, resulting in stiffness degradation, whose failure or softening response is reflected as a nonlinear behaviour, effectively projected using displacement-controlled incremental-iterative approaches. According to Batoz and Dhatt [262], the linearized system of equations is expressed as:

$$[\mathbf{M}_\mathrm{T}]_{j-1}^{i}\left\{\Delta\hat{\hat{\mathbf{U}}}_j^{i}\right\} = \{\Delta\boldsymbol{\mathcal{F}}\} \tag{7.14}$$

$$[\mathbf{M}_\mathrm{T}]_{j-1}^{i}\left\{\Delta\tilde{\tilde{\mathbf{U}}}_j^{i}\right\} = \{\mathbf{R}_{j-1}^{i}\} \tag{7.15}$$

$$\{\mathbf{R}_{j-1}^{i}\} = \{\mathbf{F}_{j-1}^{i}\} - \{\mathbf{P}_{j-1}^{i}\} \tag{7.16}$$

$$\Delta\mathbf{U}_j^{i} = \Delta\gamma_j^{i}\left\{\Delta\hat{\hat{\mathbf{U}}}_j^{i}\right\} + \left\{\Delta\tilde{\tilde{\mathbf{U}}}_j^{i}\right\} \tag{7.17}$$

$$\{\mathbf{F}_j^{i}\} = \{\mathbf{F}_{j-1}^{i}\} + \Delta\gamma_j^{i}\{\Delta\boldsymbol{\mathcal{F}}\} \tag{7.18}$$

where, $[\mathbf{M}_\mathrm{T}] = \begin{bmatrix}\mathbf{K}_\mathrm{T} & \mathbf{G}\\ \mathbf{G}^\mathrm{T} & \mathbf{0}\end{bmatrix}$, $\left\{\Delta\hat{\hat{\mathbf{U}}}_j^i\right\}$ and $\left\{\Delta\tilde{\tilde{\mathbf{U}}}_j^i\right\}$ are tangential and residual nodal displacement vectors in incremental form, $\{\mathbf{R}\}, \{\mathbf{F}\}$, and $\{\mathbf{P}\}$ are residual, external and internal force vectors, respectively. $\Delta\gamma_j^i$ is defined as the incremental load parameter for i^{th} increment and j^{th} iteration.

In the present work, the above Eqs. (7.14) and (7.15) are solved using the GDCM due to its numerical stability at limit points (snap back and snap through), the automatic adjustment in the load increment, and flexibility in adjusting the loading direction at critical points [249,258]. The sign of the load parameter here depends on the generalized stiffness parameter (GSP), which represents the stiffness of the system. The GDCM algorithm for capturing the FPZ behaviour through exponential traction-separation law in the modified EFG method framework is presented in Box 7.2.

7.3.3 1D study on level set nodes: Friction stir welded (FSW) bar

7.3.3.1 Material, Geometry and nodal information

Consider a nonhomogeneous bar that is fabricated by friction stir welding of two dissimilar materials: aluminium (Al) and magnesium (Mg), each of length $L/2$, as shown in Fig. 7.2(a). The bar is subjected to uniaxial loading. Due to the nature of the problem, this can be simplified and solved using 1D analysis. This case study aims to demonstrate the usage of level-set enriched nodes for a multi-material scenario.

Box 7.2. Pseudo-code of generalized displacement control (GDC) technique

```
while [$displacement < \delta$] do
    $initial\_convergence = 1$
    $iteration = 1$
    Set Residual force $\{\mathbf{R}\} = 0$
    Set incremental load parameter for the initial step $(\Delta\gamma_1^1)$ between 0 and 1
    while [$initial\_convergence >$ convergence_criterion] do
        $\left\{\Delta\hat{\hat{\mathbf{U}}}_j^i\right\} = [\mathbf{M}_\mathrm{T}]^{-1}\{\Delta\boldsymbol{\mathcal{F}}\}$
        $\left\{\Delta\tilde{\tilde{\mathbf{U}}}_j^i\right\} = [\mathbf{M}_\mathrm{T}]^{-1}\{\mathbf{R}_{j-1}^i\}$
        if [$iteration = 1$]
            if [$increment = 1$]
                GSP = 1
                $\left\{\Delta\hat{\hat{\mathbf{U}}}_1^1\right\} = \left\{\Delta\hat{\hat{\mathbf{U}}}\right\}$
```

```
                else
                    $\mathrm{GSP} = \frac{\left|\left\{\Delta\hat{\bar{\mathbf{U}}}_1^1\right\}\right| \left\{\Delta\hat{\bar{\mathbf{U}}}_1^1\right\}^{\mathrm{T}}}{\left|\left\{\Delta\hat{\bar{\mathbf{U}}}_1^{i-1}\right\}\right| \left\{\Delta\hat{\bar{\mathbf{U}}}_1^i\right\}^{\mathrm{T}}}$
                end
                $\Delta\gamma_1^i = sign(\mathrm{GSP}) \times \Delta\gamma_1^1 |\mathrm{GSP}|^{\frac{1}{2}}$
            else
                $\Delta\gamma_j^i = -\frac{\left|\left\{\Delta\hat{\bar{\mathbf{U}}}_1^{i-1}\right\}\right|^{\mathrm{T}} \left\{\Delta\tilde{\bar{\mathbf{U}}}_j^i\right\}}{\left|\left\{\Delta\hat{\bar{\mathbf{U}}}_1^{i-1}\right\}\right|^{\mathrm{T}} \left\{\Delta\hat{\bar{\mathbf{U}}}_j^i\right\}}$
            end
            $\{\boldsymbol{U}\} = \{\boldsymbol{U}\} + \Delta\gamma_j^i \left\{\Delta\hat{\bar{\mathbf{U}}}_j^i\right\} + \left\{\Delta\tilde{\bar{\mathbf{U}}}_j^i\right\}$
            $\{\mathbf{F}_j^i\} = \{\mathbf{F}_{j-1}^i\} + \Delta\gamma_j^i \{\Delta\boldsymbol{\mathcal{F}}\}$
            Update $\mathbf{K}_{\mathrm{T}}$ and therefore $\mathbf{M}_{\mathrm{T}}$ for $i^{th}$ increment and $j^{th}$ iteration
            //Internal Force Vector $-$ $\{\boldsymbol{P}\}$//
            $\{\mathbf{P}_j^i\} = \{\mathbf{P}_{j-1}^i\} + [\mathbf{M}_{\mathrm{T}}]\,\{\Delta\mathbf{U}_j^i\}$
            $\{\mathbf{R}_j^i\} = \{\mathbf{F}_j^i\} - \{\mathbf{P}_j^i\}$
            $initial\_convergence = \frac{||\{\boldsymbol{R}_j^i\}||}{||\Delta\boldsymbol{\mathcal{F}}||}$
            $iteration = iteration + 1$
            update $cohesive\_displacement$
        end while
        $increment = increment + 1$
end while
```

This study considers the dimensions of tensile test samples prepared by Dorbane et al. [263] using the friction stir welded (FSW) Al and Mg sheets. The geometry of the 1D bar follows ASTM E8/E8M-15 specifications, whose dimensions are: gauge length $(L) = 25$ mm, thickness $(t) = 3$ mm and width $(w) = 6$ mm.

The nodal distribution along the bar is shown in Fig. 7.2(b). The blue colour nodes are the regular nodes. The jump nodes enriched by the Heaviside function are introduced to model the displacement discontinuity at the weld point. The level-set enriched nodes are introduced to account for the discontinuity in the axial strain across the weld or material interfaces. In the absence of level-set nodes that have a local character, the displacement field variable will show oscillations at the interfaces. This partition-of-unity approach is suitable for handling geometries with discontinuities in the EFG framework without much effort. The damage evolution at the weld interface is captured by assuming a cohesive zone where displacement jump, w, is controlled by the Heaviside enriched nodes.

The weak form for the 1D bar problem is given by,

$$\int_L \delta\left(\frac{\mathrm{d}u}{\mathrm{d}x}\right) E_x \left(\frac{\mathrm{d}u}{\mathrm{d}x}\right) A\mathrm{d}x - \delta\lambda^T (u - u_\Gamma)|_{(x=0)} - \delta u^T \lambda|_{x=0} = F|_{x=L} + t\delta w|_{x=L_{coh}} \tag{7.19}$$

The u-displacement is constrained at $x = 0$. This is imposed through the usage of the Lagrange multiplier.

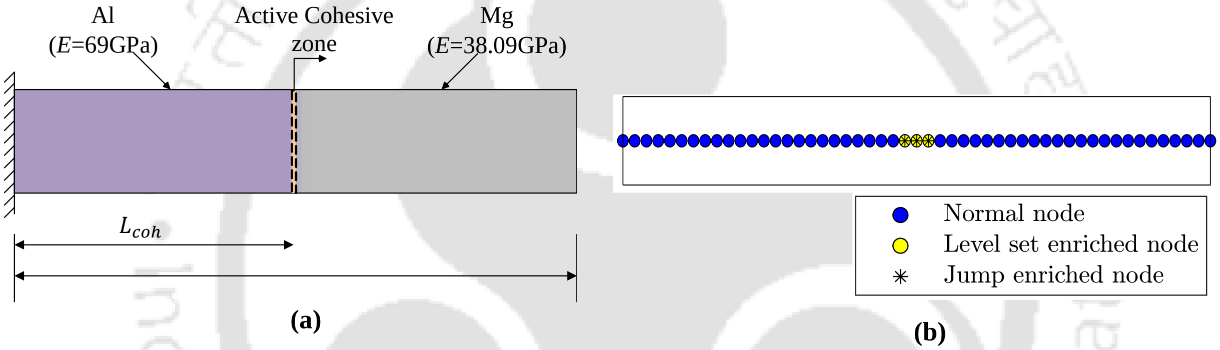

Fig. 7.2. (a) 1D friction stir welded (FSW) bar with geometry and boundary conditions, and **(b)** its regular nodal distribution

In the experimental reference results [263], only Young's modulus values are given. This study can also be performed using a 2D analysis, but that would require the knowledge of Poissons's ratio, particularly in the weld region, which is not available in the reference literature. To demonstrate the advantage of using level-set enriched nodes, we have resorted to simple 1D analysis. Here, different zones of weld have been replaced with a single homogenized weld region of constant elastic modulus.

7.3.3.2 Stress-strain response: without weld region

At the first attempt, the base metals properties (Young's modulus) of Al (69 GPa) and Mg (38.09 GPa) are considered at either side of the weld joint [263], and the cohesive zone (weld joint) is located exactly at $L_{coh} = 12.5$ mm. In the absence of a weld zone, i.e. considering only the parent materials with a cohesive zone, Fig. 7.3(a) compares the engineering stress versus strain response of the FSW welded tensile specimens obtained using the proposed numerical approach corresponding to cohesive stiffness of $100\ \mathrm{kN/mm^3}$ and the experiment results from the literature [263].

It is observed that the stiffness of the linear elastic portion for the numerical model and the experimental result is not matching. The difference in the linear elastic regime stiffness of the stress-strain curve between the experiment and the proposed approach continues to persist despite increasing the cohesive stiffness values. Even if the weld joint is replaced with a rigid material, the effective stiffness would only be $35.340\ \mathrm{kN/mm}$. However, the experimental findings show a higher value, i.e., the effective stiffness in the linear elastic region is $41.021\ \mathrm{kN/mm}$. In summary, though the stiffness of the stress-strain response is affected by the initial stiffness of the cohesive zone, there will not be any improvement in the global response even after significantly increasing the cohesive stiffness (see Fig. 7.3(b)).

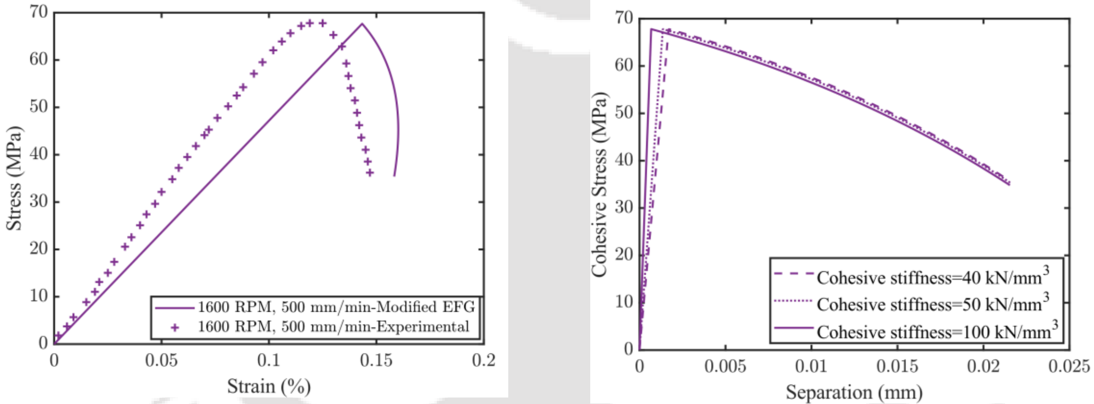

(a) **(b)**

Fig. 7.3. (a) Comparison of engineering stress-strain responses between modified EFG and uniaxial tensile test [263], and **(b)** cohesive behaviour for various initial stiffnesses

7.3.3.3 Stress-strain response: with weld region

In their study, Dorbane et al., [263] found that the region close to the weld, i.e. the heat affected zone (HAZ) does not retain its parent material properties. Therefore, this aspect is adopted in our study towards a better coupled EFG and CZ model. To this end, a weld region is employed in the 1D bar, as illustrated in Fig. 7.4(a), whose elastic modulus depends on the tool rotation and translation speeds [263]. The weld zone's length is 12.5 mm, close to the tool shoulder diameter of 10 mm. The nodal distribution consists of 51 nodes along the length of the bar. The nodes comprise normal nodes, level-set nodes near the interface between the base metal and weld region on either side of the bar, and the Heaviside enriched nodes located at the cohesive zone.

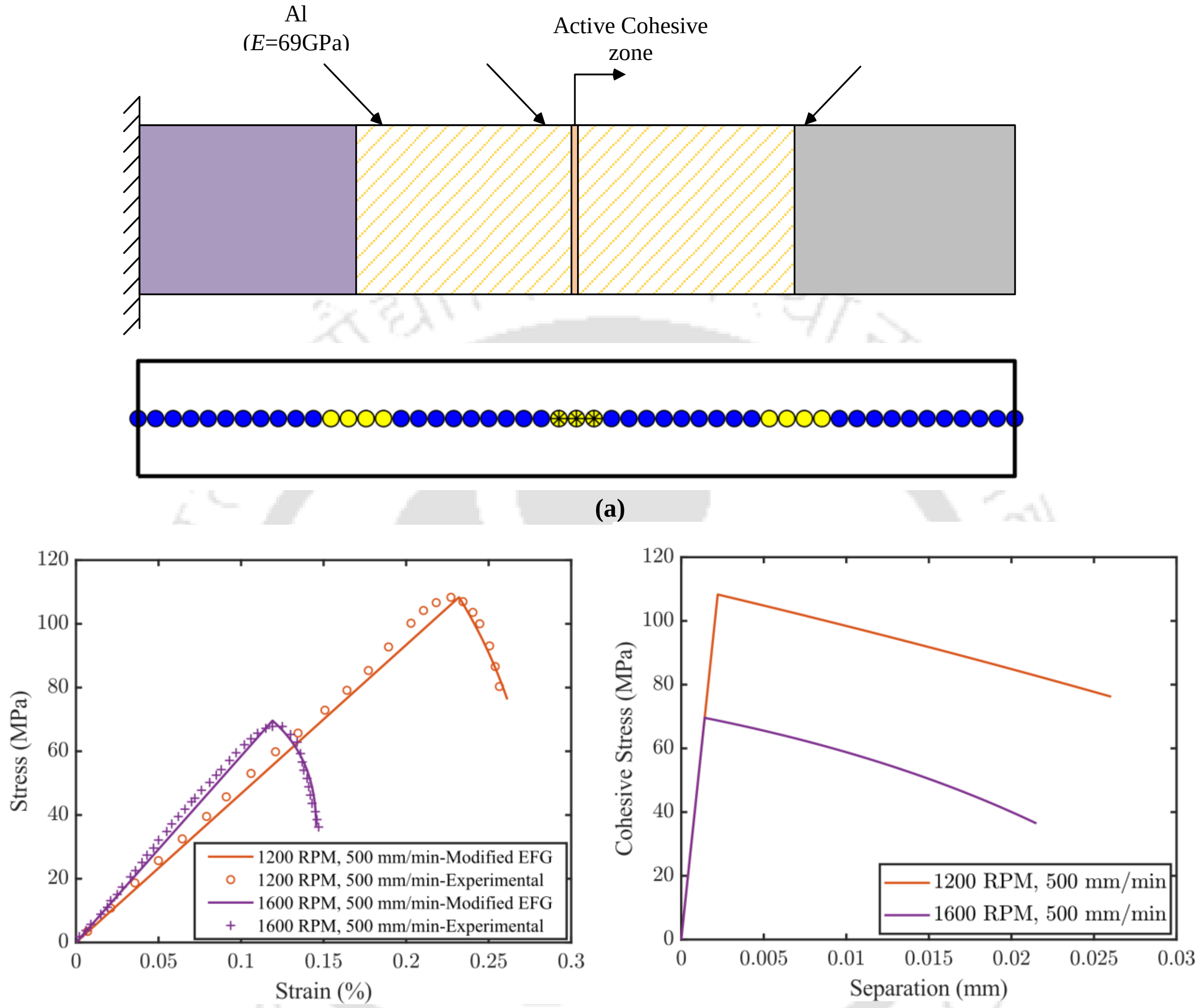

(a)

(b)

(c)

Fig. 7.4. (a) 1D friction stir welded (FSW) bar with geometry, boundary conditions, and its nodal distribution, **(b)** numerical and experimental validation of engineering stress-strain responses, and **(c)** cohesive behaviour at a constant tool translation speed

The elastic modulus and cohesive properties of the weld zone for constant translational speed (500 mm/min) with rotational speeds of 1200 and 1600 RPM are — (i) $E = 48\ \mathrm{GPa}$, $K = 49000\ \mathrm{N/mm^3}$, $w_0 = 0.00221\ \mathrm{mm}, w_f = 0.07\ \mathrm{mm}, and\ \alpha = -0.5$, and (ii) $E = 82\ \mathrm{GPa}$, $K = 49000\ \mathrm{N/mm^3}$, $w_0 = 0.00142\ \mathrm{mm}, w_f = 0.033\ \mathrm{mm}$, and $\alpha = -1.35$. Accordingly, Fig. 7.4(b) show the mechanical behaviour of the tensile specimens at constant tool translation speed and their comparison with the experimental data. The stress-strain plots at a constant translation speed of 500 mm/min show that the specimens subjected to the tool rotation of 1200 and 1600 RPM demonstrate a quasi-brittle behaviour though the parent materials are ductile. Between 1200 RPM and 1600 RPM, the latter results in a lower strength. Fig. 7.4(c) show the traction separation responses for the cohesive zone. The cohesive energy for the 1600 RPM is lower by approximately 50% compared to 1200 RPM.

7.4 Numerical Examples

This section discusses three numerical examples that show the wide range of applications of the cohesive crack concept in the modified EFG framework using the nonlinear solver –GDCM. Two-dimensional problems, such as three-point bending (TPB) specimen of brittle material without any initial crack, a double-cantilever beam (DCB) and an end-notched flexural (ENF) specimen of aluminium material adhesively bonded with Araldite subjected to pure mode I and mode II fracture, are analyzed.

The thickness of the adhesive in the case of the DCB and the ENF problem is considered to be zero. Considering a finite thickness of the adhesive will significantly increase the nodal density in the adhesive joint, making the nodal distribution in the overall geometry look non-uniform. A non-uniform nodal discretization will make the EFG shape functions highly irregular, requiring more background cells for accurate results [264,265]. It will be a limitation of the proposed methodology. However, it is to be noted that if the adhesive layer is very thin and for all practical purposes, the cohesive zone may be considered to be of zero thickness, whose constitutive response is commonly described in terms of a traction-separation law [196].

7.4.1 Three-point bending specimen

7.4.1.1 Material and Geometry data

The dimensions of the TPB specimen are width, $\mathrm{w} = 0.15\ \mathrm{m}$ and $L/\mathrm{w} = 4$. The specimen is subjected to displacement loading at point *A* and is constrained at two locations, *B* and *C*, as shown in Fig. 7.5(a). The material properties chosen are as follows [266]: $E = 36500\ \mathrm{MPa}\ , \nu = 0.1$. The cohesive properties are: $K_I = 100\ \mathrm{N/mm^3}, t_{max} = 1\ \mathrm{MPa},\ w_f = 0.05\ \mathrm{mm}$, and $\alpha = 6.5$. A plane strain condition is assumed. The specimen is discretized with 21x81 nodes, and the cohesive layer is employed between $\left(0, \frac{L}{2}\right)$ and $\left(0.9833w, \frac{L}{2}\right)$, as shown in Fig. 7.5(b). The region where the cohesive zone ends is refined with 11x11 nodes (see Fig. 7.5(c)) to capture the boundary effects.

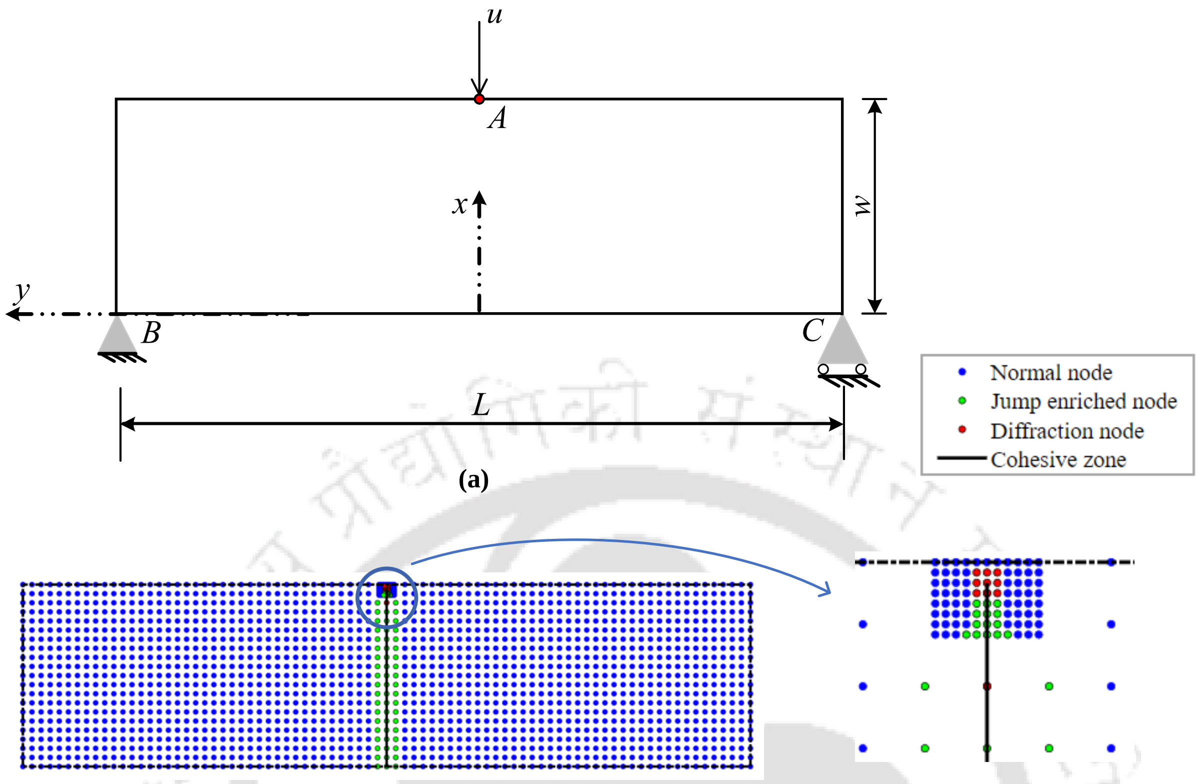

(a)

(b) (c)

Fig. 7.5. Three-point bending specimen (TPB): **(a)** geometry, dimensions and boundary conditions, **(b)** nodal discretization, and **(c)** nodal refinement at cohesive zone tip

7.4.1.2 Parametric studies: EFG

Fig. 7.6(a) shows that at 11 × 41 nodal discretization, the displacement is overpredicted, but from the next level of refinement, i.e. 21 × 81, the load vs displacement results converge. The difference in the mechanical response for the nodal densities such as 21 × 81, 31 × 121 and 41 × 161 are insignificant.

Therefore, 21 × 81 nodes are preferred for further case studies on the TPB specimen. Moreover, Fig. 7.6(a) also shows that the GDCM accurately predicts the asymptotic response towards the material failure regime. Fig. 7.6(b) however shows that the cohesive traction vs separation response is independent of the nodal discretization. On the other hand, through the studies on background cells for integration in the cohesive zone (10, 50, and 100), it is observed that the results obtained by the modified EFG method in virtue of the GDCM are independent of the cohesive cells for the present case, which is devoid of a starter crack. Hence, the proposed method needs less number of straight-line cohesive cells to predict the softening response accurately.

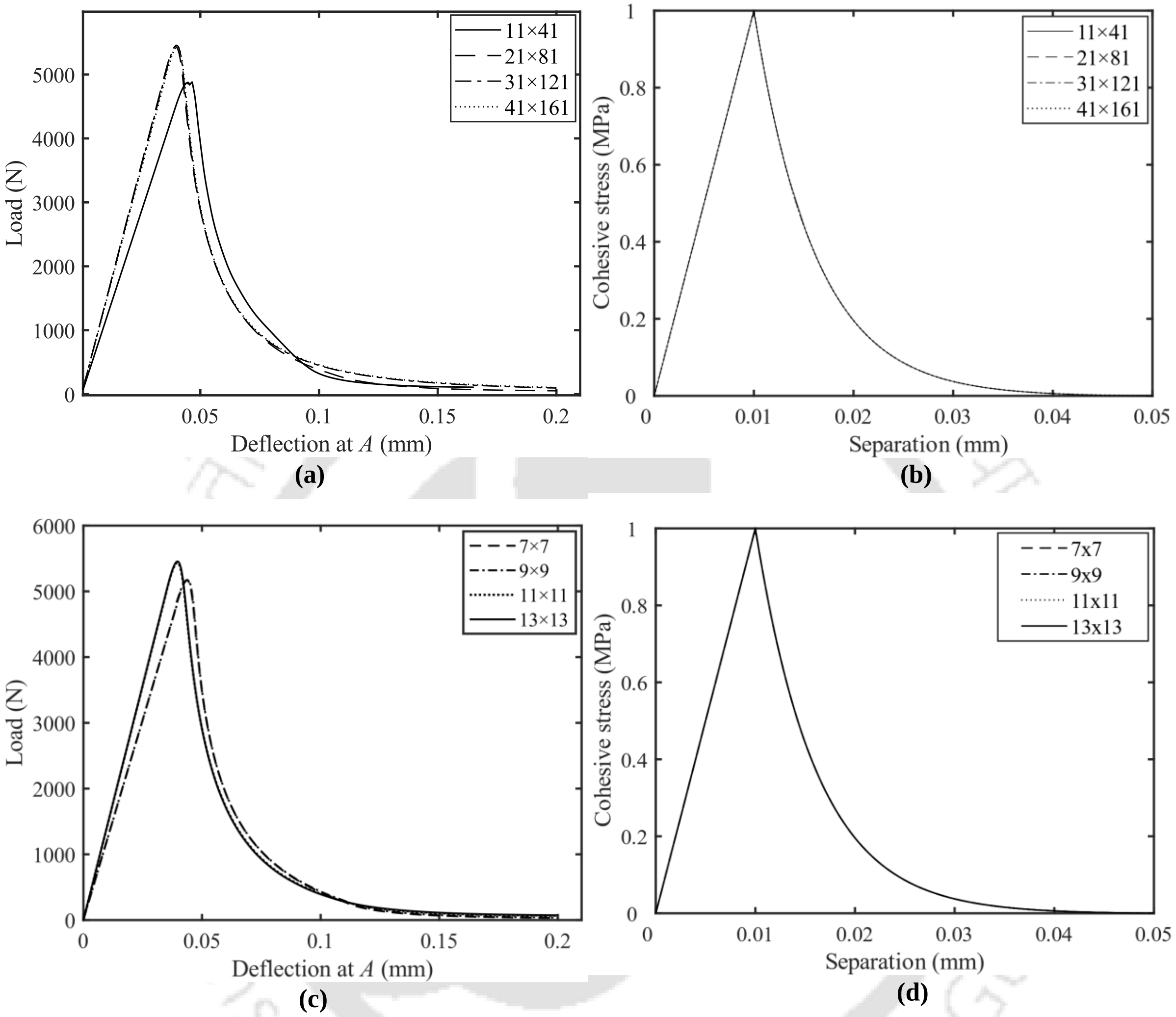

Fig. 7.6. Various nodal densities: **(a)** Load–deflection response at *A*, and **(b)** cohesive behaviour at (0,0), various nodal refinements: **(c)** Load–deflection response at *A*, and **(d)** cohesive behaviour at (0,0)

Fig. 7.6 (c) and 7.6 (d) show the effect of local nodal refinement at the boundary (See Fig. 7.5(c)) on global and cohesive responses at (0,0), respectively. While increasing the nodal density at location *A*, the nodal distribution in the cohesive zone is fixed with a global nodal discretization of 21×81. There is no change in the response of cohesive traction vs separation behaviour due to an increase in the nodes near the point of application load *A* (see Fig. 7.6(d)). However, it is not the same in the case of load-displacement behaviour (see Fig. 7.6(c)). This may be due to the proximity of the loading location to the nodal refinement region. The converged global response, however, is seen from a refinement of 11x11 nodes.

7.4.1.3 Parametric studies: GDCM

Fig. 7.7(a) and 7.7(b) shows parametric study of GDCM at reference load magnitude ΔF of 100 and 1000 N at A. The load-deflection curves are presented for various initial incremental load parameters ($\Delta\gamma_1^1 = 1, 0.5, 0.1, 0.01$). It is observed that the variation in the initial control factor at reference load 100 N (Fig. 7.7(a)) shows convergence for $\Delta\gamma_1^1 \leq 0.1$. The obtained responses corresponding to $\Delta\gamma_1^1 = 0.1$ are compared with the results of commercial FE ABAQUS® software, using 4599 plane strain (CPE4) and 20 cohesive (COH2D4) elements with MAXS damage criterion, and found to be in good agreement in linear elastic and softening regimes with error at the peak load of 0.9%.

However, the difference between load-displacement responses at $\Delta\gamma_1^1 = 0.1$ and $\Delta\gamma_1^1 = 1$, shows only a slight variation. Thus, either the initial control factor can be chosen flexibly at a reference load value of 100 N or a reference load value ≤ 100 N (0.1 times the peak load) can be flexibly chosen for $\Delta\gamma_1^1 = 1$ to obtain the converged solution. It is not, however, valid when the magnitude of the reference load at A increases, i.e., when the reference load increases to 1000 N, a large value of $\Delta\gamma_1^1 \geq 0.5$ lead to erroneous result (Fig. 7.7(b)). An increase in ΔF automatically necessitates the need to use smaller incremental load parameter $\Delta\gamma$ to achieve an accurate solution which increases the computation time.

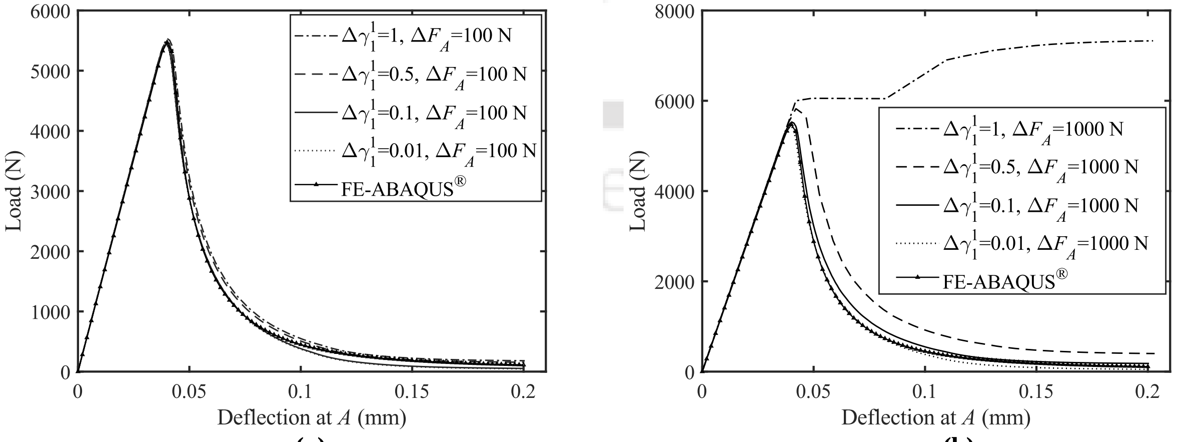

(a) **(b)**

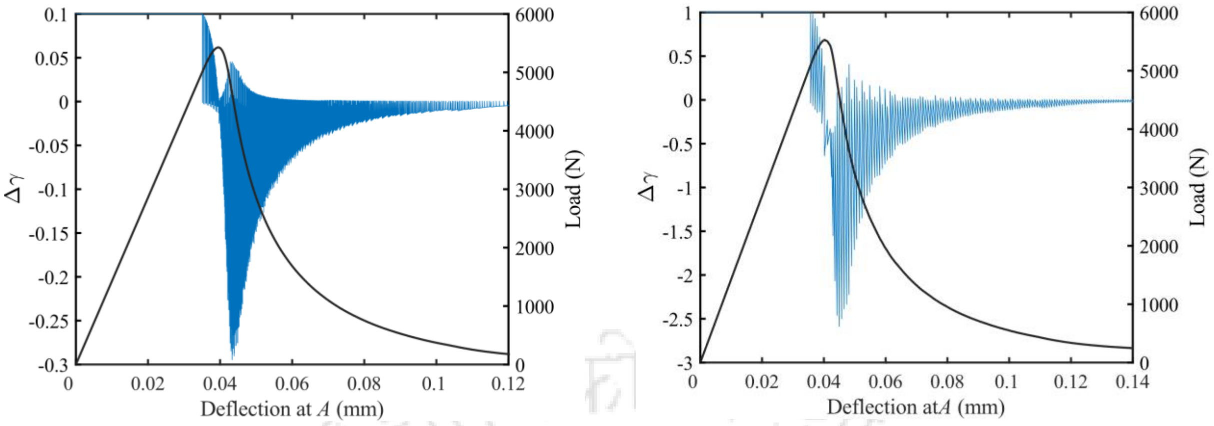

(c) **(d)**

Fig. 7.7. **(a)** Load–deflection response at A for various $\Delta\gamma_1^1$ at $\Delta F_A = 100$ N, and **(b)** $\Delta F_A = 1000$ N, **(c)** $\Delta\gamma$ responses in the softening region for $\Delta\gamma_1^1 = 0.1$, and **(d)** $\Delta\gamma_1^1 = 1$ at $\Delta F_\mathrm{A} = 100$ N

It is known that the maximum value of $\Delta\gamma$ corresponds to a higher gradient in the softening portion. Fig. 7.7(c) and 7.7(d) depict the $\Delta\gamma$ vs deflection behaviour and load–deflection response at A. Though the load-deflection behaviour is the same for both the initial control factors $\Delta\gamma_1^1 = 0.1$ and $\Delta\gamma_1^1 = 1$ at $\Delta F_A = 100$ N, it is observed that their incremental load parameters are different, causing significant differences in the number of incremental steps required to complete the solution process. While the maximum magnitude $\Delta\gamma_{max}$ attained for $\Delta\gamma_1^1 = 1$ is approximately ten times than for $\Delta\gamma_1^1 = 0.1$, the GDCM with parameters: $\Delta\gamma_1^1 = 1$, $\Delta F_\mathrm{A} = 100$ N dynamically adjusts without losing numerical stability by a few extra iterations. This demonstrates the effectiveness of the GDCM. The total number of iterations for $\Delta\gamma_1^1 = 1$ and $\Delta\gamma_1^1 = 0.1$ is 453 and 3250, respectively. It should be noted that the range of the control parameters of the GDCM for satisfactory results remains the same irrespective of the type and dimensionality of the problem. The same range of parameters was used in Section 7.3.3 for obtaining the results.

7.4.2 Double cantilever beam (DCB) specimen (mode I)

7.4.2.1 Material and Geometry data

The dimensions of the DCB problem considered in this case are taken from [267], as shown in Fig. 7.8(a). The length of the specimen is $L = 290$ mm, and the thickness of the beam is $h = 12.2$ mm. The DCB specimen has a starter crack of length $a = 50$ mm. There are two holes with a radius $R = 2$ mm in the specimen centered at A and B. The holes are located in the specimen in such a way that they do not influence the initial crack-tip stress field solution ($d_1 = 10.13$ mm and $d_2 = 6.1$ mm).

The displacement loading and boundary conditions are enforced at points A and B. The specimen is considered to be made of aluminium material with properties: $E = 70$ GPa, $\nu = 0.3$. The essential boundary conditions imposed on the DCB specimen are i) point A is subjected to transverse displacement loading of 1.9 mm and arrested in the x-direction, and ii) point B displacements are constrained in both directions. A plane strain condition is assumed.

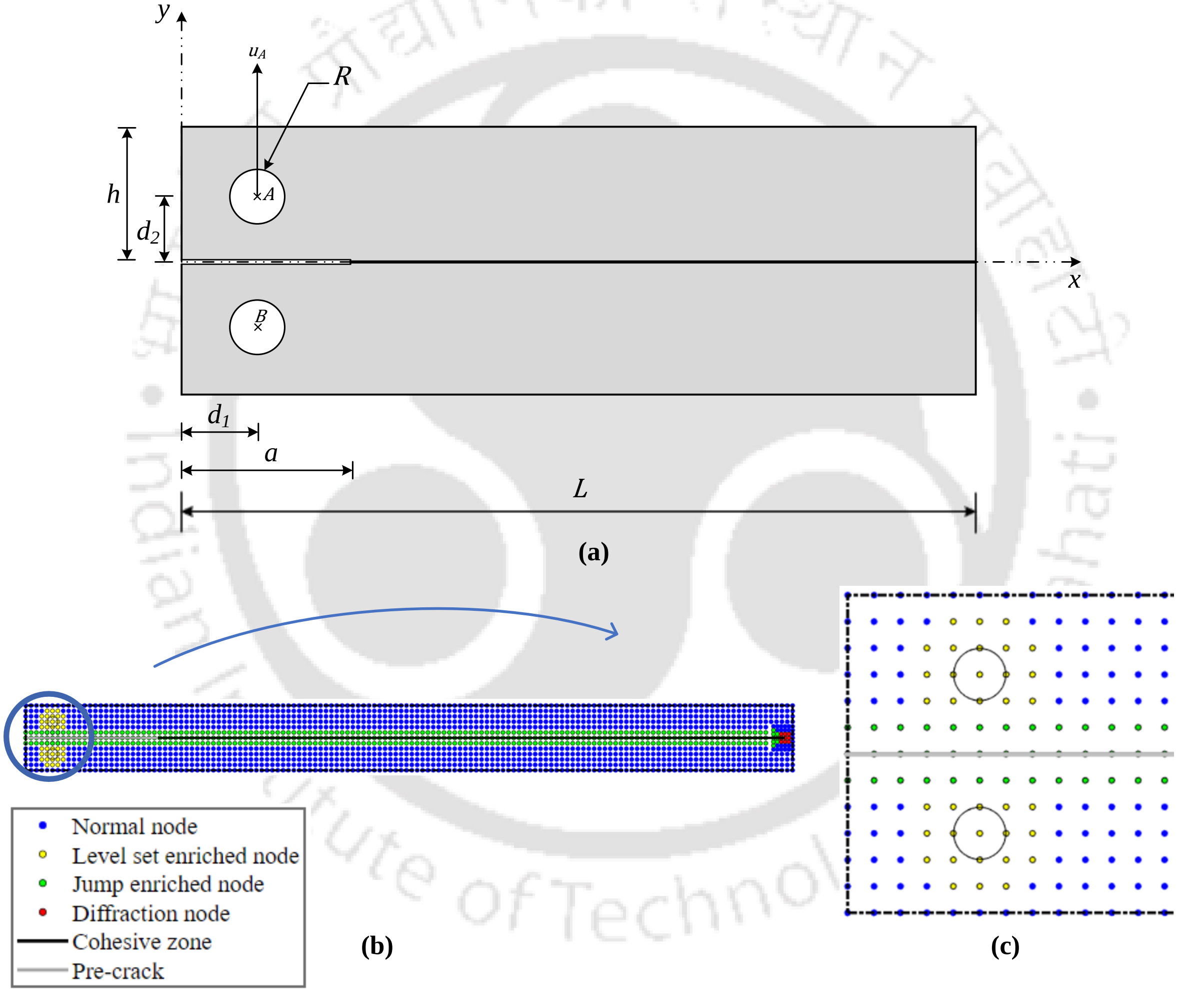

(a)

(b)

(c)

Fig. 7.8. Adhesively bonded double cantilever beam specimen (DCB): **(a)** geometry, dimensions and boundary conditions, **(b)** nodal discretization, and **(c)** level-set nodes

The presence of holes in the DCB specimen makes it non-homogenous and is conveniently dealt with by using level-set nodes (Fig. 7.8(b)), as discussed in section 7.2.2. The specimen is discretized with 13×144 nodes. Certain nodes between the starter crack and the holes act as regular nodes, enriched with both Heaviside and level-set functions (see Fig. 7.8(c)). A 1D cohesive zone in the form of straight-line segments is employed from $(0,0)$ to $(0.99L, 0)$. A zero traction is used from $(0,0)$ to $(a, 0)$ due to the presence of a starter crack. The cohesive stiffness corresponds to Araldite material [267]: $K_I = 8539.06\ \mathrm{N/mm^3}$. The other cohesive properties are taken as $t_{max} = 15$ MPa, $w_f = 0.107566$ mm, and $\alpha = 3.5$.

7.4.2.2 Results and Discussions

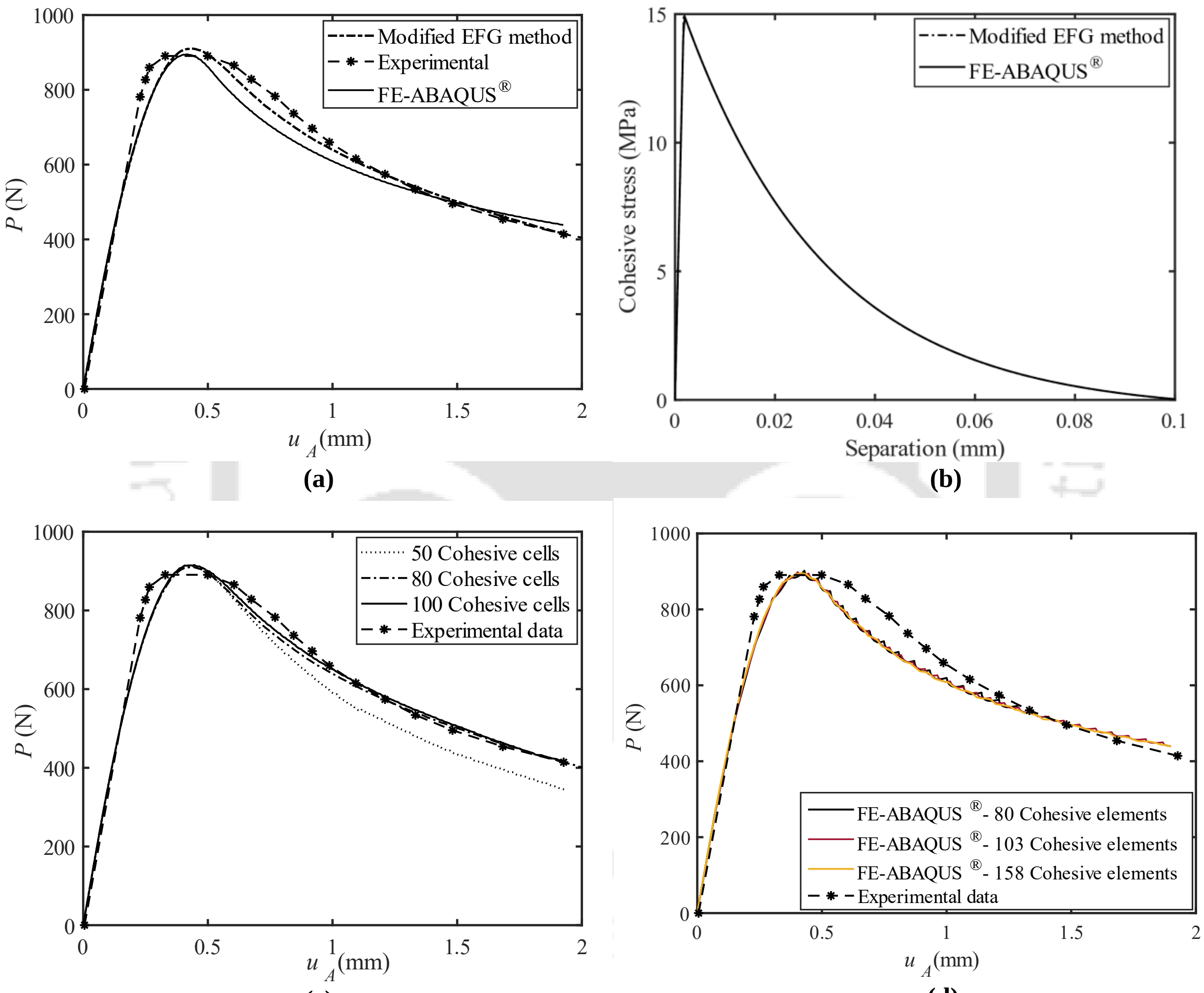

(a) **(b)** **(c)** **(d)**

Fig. 7.9. Comparison of **(a)** P versus u_A responses with experimental data, and **(b)** cohesive behaviour with ABAQUS®, **(c)** effect of number of cohesive elements on P versus u_A responses by modified EFG method, and **(d)** ABAQUS®

Similar to the TPB case study, a local nodal refinement is considered at $(0.99L, 0)$. The load P vs deflection u_A comparative study with experiments and ABAQUS® results is shown in

Fig. 7.9(a), where u_A is the imposed displacement, the load P is conveniently obtained from the Lagrange multiplier used to enforce the zero y-displacement at B. The mesh details for ABAQUS® simulations are taken from [267] and the numerical analysis is carried out upto 50% of the peak load in the softening zone. The numerical result obtained through the proposed approach is in good agreement with those obtained from the commercial FE software ABAQUS® result, as seen in Fig. 7.9(a). Fig. 7.9(b) shows the comparison of cohesive zone behaviour at (51,0) in the modified EFG framework and ABAQUS®. It is to be noted that the FE-ABAQUS® curve overlaps with the proposed methodology result.

Fig. 7.9(c) and 7.9(d) demonstrate the effect of the number of cohesive elements on the load-deflection behaviour using the modified EFG method and ABAQUS® software. The proposed approach encounters singularity when the cohesive cells are less than 50 and converges for 80 background integration cells for the cohesive zone. ABAQUS®, on the other hand, aborts the simulation prematurely for cohesive elements less than 103 and displays a smooth response from 158 elements. Here too, the number of background cells required for integration of the cohesive zone is less than in the FE method.

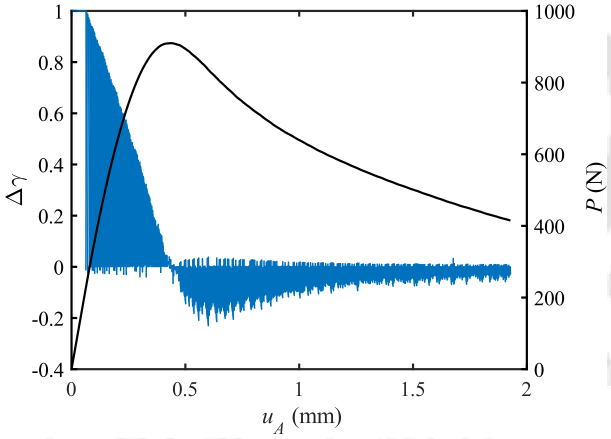

Fig. 7.10. Load – deflection response and $\Delta\gamma$ vs deflection at A for $\Delta\gamma_1^1 = 1$ and $\Delta F_A = 10$ N

Fig. 7.10 shows the variation of the incremental load parameter with the displacement u_A corresponding to the reference load magnitude, $\Delta F_{\mathrm{A}} = 10$ N and initial control factor, $\Delta\gamma_1^1 = 1$. The plot shows that $\Delta\gamma$ depends on the stiffness of the system. Unlike the TPB case study, the stiffness of the DCB problem gradually decreases as the damage accumulates, which occurs early compared to the TPB problem due to the presence of the starter crack. The incremental load parameter reflects almost a uniform pattern after the peak load as the load decreases gradually.

7.4.3 End-notched flexural (ENF) specimen (mode II)

7.4.3.1 Material and Geometry data

The end-notched flexural (ENF) specimen supported by two hinges at points B and C is subjected to displacement loading at point A, as shown in Fig. 7.11. The dimensions and material properties of the ENF specimen are similar to that of the DCB specimen considered in section 7.4.2. The cohesive properties are [267]: $K_{\mathrm{I}} = 3682.14\ \mathrm{N/mm^3}, K_{\mathrm{II}} = 108.698\ \mathrm{N/mm^3}, \sigma_c = 20.62$ MPa, and $\tau_c = 15.87$ MPa. A plane strain condition is assumed. The specimen is discretized with 11×120 nodes with a cohesive layer employed in the mid-section joining the two adherends. As in the previous case, the starter crack from (0, 0) to (a, 0) is modelled using a zero-traction cohesive layer.

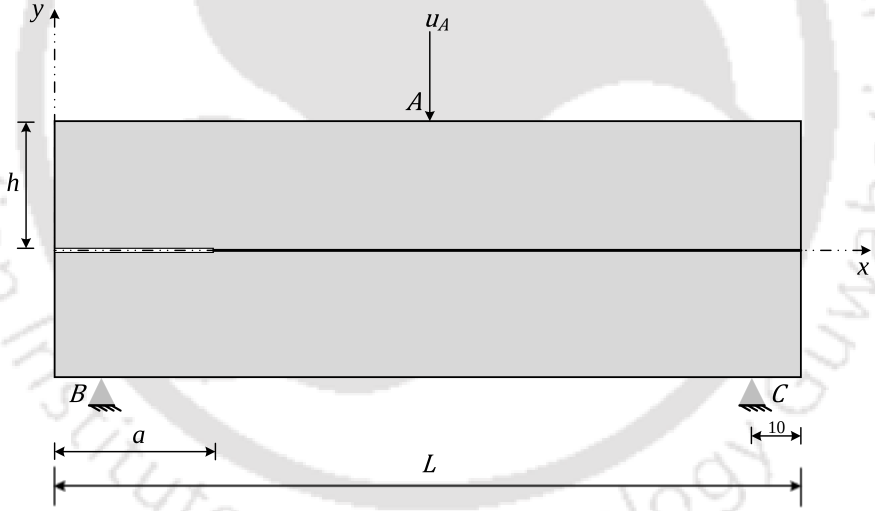

Fig. 7.11. Adhesively bonded end notch flexural specimen (ENF) with geometry and boundary conditions

The stiffness and the cohesive strength (mode I and mode II) correspond to the values used in Gheibi et al. [267], where Park-Paulino-Roesler (PPR) TSL was used. In the present work, only exponential TSL is considered, and accordingly, a cohesive energy of $2.418\ \mathrm{N/mm}$ was used, corresponding to a final separation of 0.306 mm. Through mesh convergence studies, Gheibi et al. [267] determined that around 400 cohesive elements are adequate for the FE modelling. In contrast, the present numerical scheme of the modified EFG framework uses only 200 background integration cells in the cohesive zone to capture the converged load-deflection response for $\alpha = 0.05$, as shown in Fig. 7.12(a). Fig. 7.12(b) shows the plot of the exponential TSL supplied to the ENF problem. Interestingly, the exponential TSL looks similar to the bilinear TSL when α is close to 0. The proposed methodology is capable of using any intrinsic TSL shape. Any change in the TSL affects only the constitutive behaviour of the cohesive zone and will have no adverse effect on the proposed numerical approach.

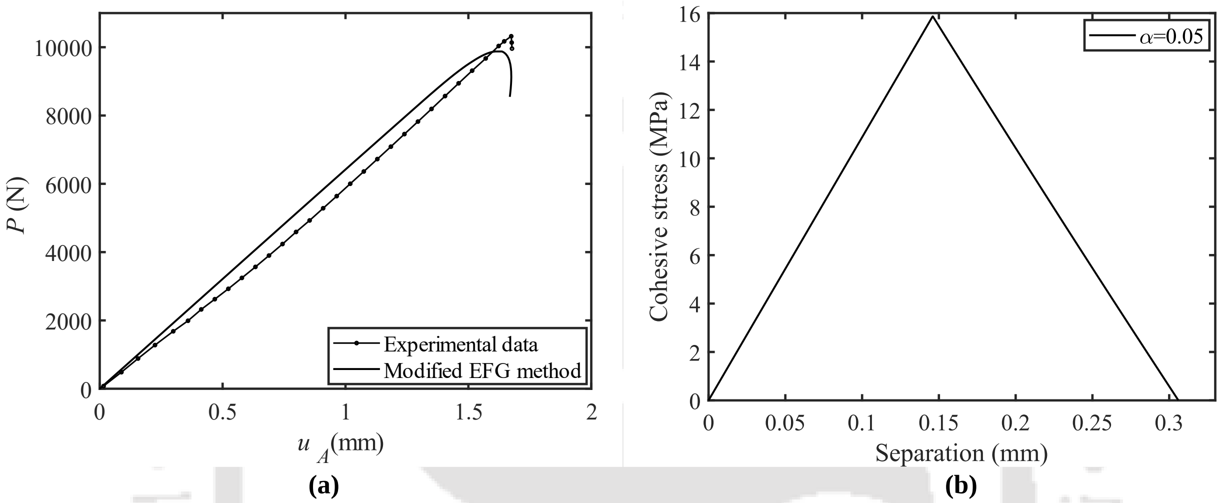

Fig. 7.12. For $\alpha = 0.05$, **(a)** Numerical and experimental validation of P versus u_A responses, and **(b)** cohesive behaviour at (50.5,0)

7.4.3.2 Comparison between GDCM and Newton Raphson technique

In most research works, the mode-independent and mixed-mode case studies are modelled in the FE framework through ABAQUS, which uses Newton-Raphson (NR) scheme as the default nonlinear solver. Here, the performance of the GDCM and NR techniques are compared for various values of α in the modified EFG framework. The performance of both the nonlinear solvers is quantitatively measured by the number of increments (Inc), the total number of iterations (Niter), and computational time (Time), as indicated in Table 7.1. The proposed approach is implemented on a PC Matlab R2021a platform supporting an Intel(R) Core(TM) i9-10900K processor running at 3.70 GHz using 64 GB of RAM, running Windows 10 Pro version 21H2.

The incremental parameters for GDCM: $\Delta F = -100$ N, $\Delta\gamma_1^1 = 1$ and NR: $\Delta u_A = -0.01$ are chosen as the best possible values that predict the converged load-deflection response. The best values correspond to obtaining accurate results with less computational effort.

Table 7.1. Comparison between GDCM and NR methods for various

	GDCM				NR technique			
	Incremental Parameters	**Inc**	**Niter**	**Time (Sec)**	**Incremental Parameters**	**Inc**	**Niter**	**Time (Sec)**
$\boldsymbol{\alpha = 2.5}$	$\Delta F = -100$ N, $\Delta\gamma_1^1 = 1$	132	224	128.86	$\Delta u_{\mathrm{A}} = -0.01$ mm	197	548	285.73
$\boldsymbol{\alpha = 3.5}$		133	226	126.36		197	548	286.06
$\boldsymbol{\alpha = 4.5}$		133	226	127.78		197	550	287.48
$\boldsymbol{\alpha = 6.5}$	$\Delta F = -10$ N, $\Delta\gamma_1^1 = 1$	1193	1757	688.49	$\Delta u_{\mathrm{A}} = -0.001$ mm	1701	3755	1240.1
$\boldsymbol{\alpha = 8.5}$		1194	1759	685.24		1701	3781	1258.5
$\boldsymbol{\alpha = 11}$		1191	1753	675.19		-	-	-

It is observed that the number of iterations and computing time required by the solver while employing GDCM is around half that of the Newton-Raphson approach. Generally, the incremental load parameter in GDCM varies with each iteration, allowing convergence to be reached in fewer iterations and thus resulting in less computation time. At the end of the simulation, as expected, both GDCM and NR produce identical load-deflection behaviour for various α values i.e., 2.5, 3.5, and 4.5 as shown in Fig. 7.13. *GDCM versus NR*: Load-deflection behaviour for various values of α.

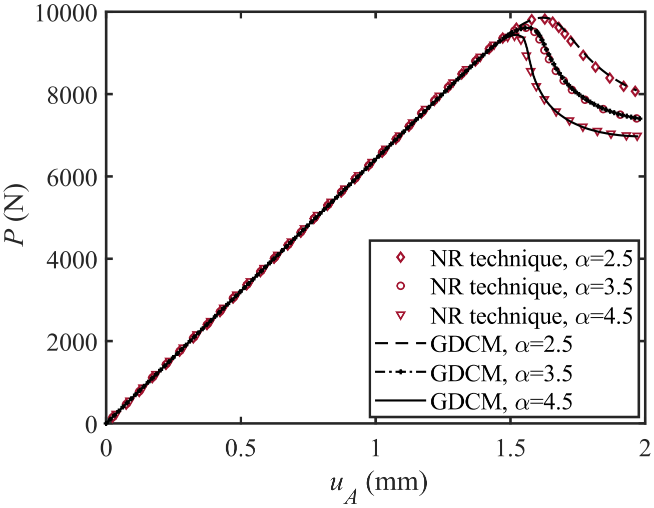

Fig. 7.13. *GDCM versus NR*: Load-deflection behaviour for various values of α

7.4.3.3 Snapback behaviour

In an exponential traction-separation law (TSL), increasing α\alphaα reduces the cohesive energy, which lowers the total energy available to resist separation. This higher α\alphaα value steepens the post-peak decline in cohesive traction, meaning that after the cohesive strength is reached, traction drops off more sharply. This accelerates the rate of damage evolution in the cohesive elements, particularly near the crack tip. As damage accumulates rapidly in this critical region, the resistance at that interface zone diminishes, leading to instability. Consequently, affects the load-displacement response, either as a sudden load drop with minimal displacement change at peak load or as snap-back behaviour, indicating brittle failure characteristics. It is known that the popular Newton-Raphson technique cannot predict the instability in the solution. Different types of snapback responses are studied for α values $6.5, 8.5$ and 11 using both GDCM and NR techniques, and their quantitative and qualitative performances are compared.

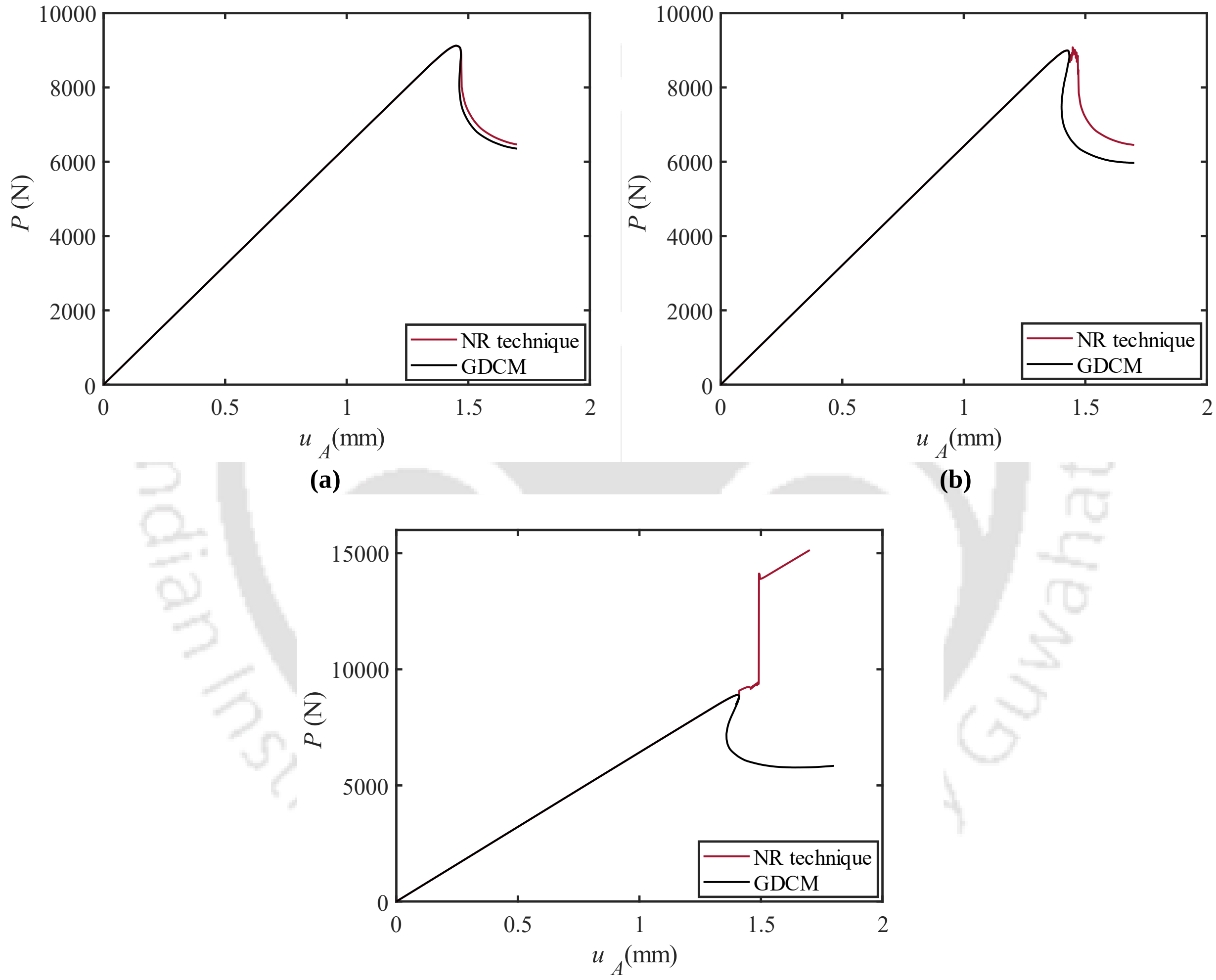

(a)

(b)

(c)

Fig. 7.14. *GDCM versus NR*: Load-deflection behaviour for **(a)** $\alpha = 6.5$, **(b)** $\alpha = 8.5$, and **(c)** $\alpha = 11$

The incremental parameters in both the nonlinear solver techniques have been chosen as smaller values to capture the instability, as the larger increments would not predict this phenomenon. It is to be noted that $\Delta\gamma_1^1 = 1,\ \Delta F = -100$ N can predict snapback behaviours till

$\alpha = 10$. Any further increase in α would increase the intensity of the snapback, necessitating a reduced value of ΔF or $\Delta\gamma_1^1$ to predict the snapback response accurately; in this case, we have used $\Delta F = -10$ N.

It can be seen that any difference in the response predicted by the NR compared to the GDCM begins after the peak load. Fig. 7.14(a) shows the load-deflection response at $\alpha = 6.5$ with a slight snapback. There is no appreciable difference between the predicted results after the peak load. However, for $\alpha = 8.5$, NR technique produces some oscillations immediately after the peak load, as seen in Fig. 7.14(b). Since the intensity of snapback is relatively small, the solution gets stabilized and shows a smooth response. Finally, when the intensity of snapback phenomenon is increased further by increasing α value to 11, the NR technique exhibits numerical instabilities and fails to predict the snapback behaviour, as evident from Fig. 7.14(c). In contrast, the GDCM anticipates all three snapback behaviours, demonstrating its adaptability in capturing a wide degree of snapback nonlinearities. This method can be efficiently explored in various applications, especially in adhesively bonded joints in composite materials involving delamination due to mode II and mixed-mode loading [268,269].

7.5 Summary

A modified EFG method involving diffraction technique, Heaviside and level-set functions is used to simulate mode I (DCB) and mode II (ENF) crack propagation problems. The level-set enrichement via a partition-of-unity scheme is particularly suitable to account for material interfaces without the need to alter the existing nodal distribution. The nonlinear nature of the problem arising due to damage evolution modelled by an exponential traction separation law (TSL) is solved by the generalized displacement control method (GDCM). This involves the determination of the tangent stiffness matrix at each iteration, which is conveniently established by considering the nodes that are enriched with the Heaviside function or whose weight function is modified by the diffraction technique. Three problems are solved succesfully: uncracked three-point bend specimen, pure mode I – double cantilever beam (DCB) and mode II – end-notched flexural (ENF) specimens. Satisfactory results are obtained with relatively lower nodal degress of freedom which is attributed to the higher order shape functions of the EFG method.

Chapter 8

Damage Modelling in EFG using Nonlocal Integral Approaches

The numerical prediction of the strain-softening behaviour using the CDM models is a well-known problem that produces mesh-dependent results in the standard FEM. This mesh sensitivity problem can be avoided using the element-free Galerkin (EFG) method, because of its higher-order continuous nonlocal shape functions. However, the shape function of the EFG method, obtained using the moving least squares (MLS) technique, poses difficulties during the convergence analysis due to the localization of the damage variable. In the present work, a nonlocal integral approach has been employed on the CDM models by regularizing the equivalent strain to overcome the convergence issues in the EFG method. The proposed methodology has been applied to model elastic damage in a one-dimensional problem.

8.1 Introduction

Askes et al. [270] examined the mathematical nonlocality of EFG interpolation functions to see if they introduce a mechanical nonlocality to the description, although their results indicate otherwise. Thus, EFG method is considered less effective than FEM in specific situations due to the inability of the smooth form functions generated by the Moving Least Squares (MLS) technique to adequately depict rapid shifts or discontinuities in the solution [171]. The EFG method successfully handles significant discontinuities, including crack propagations, by utilizing the cohesive crack idea. Nonlocal theories excel in addressing weak discontinuities like holes, notches, and rapid changes in area.

Fracture of heterogeneous materials is a complex process that often involves multiple stages. Standard continuum models, such as plasticity and damage, lead to the loss of mathematical well-posedness and dependence on the applied discretization in numerical simulations. Nonlocality can be included in the material model to avoid these deficiencies. Two main formats of nonlocality exist: gradient-type and integral-type nonlocality.

Comparative studies of second- and fourth-order gradient damage models against integral-type damage models in the EFG framework show no notable variations in behaviour. The presence of a fourth-order term in the gradient-type nonlocality has less impact on EFG than on FEM. This is due to the notable discrepancy in results between second-order and fourth-order derivatives in

FEM. In this study, a one-dimensional analysis is undertaken, considering the similarity between integral techniques and gradient theories, and the superior convergence behaviour of the EFG method over FEM. This analysis utilizes nonlocal integral theories in the EFG framework. These theories are specifically used in post-processing analysis due to their easy implementation, merging them with continuum damage mechanics principles. Moreover, due to the inherently demanding computational nature of the EFG technique, incorporating nonlocal theories explicitly helps reduce the extra computing time. The issue of strain localization is investigated by examining a concrete bar undergoing tensile deformation, with a rapid 1% decrease in area at the center of the bar. The paper examines the convergence of the nonlocal approach in both the FE and EFG frameworks. It specifically examines the behaviour of nonlocal equivalent stresses and damage when subjected to different displacement loadings.

8.2 Nonlocal damage mechanics

The Mazars model, a popular model to predict damage in both tension and compression of concrete material, is adopted in this work. Referring back to the damage model (see Eq. (2.5)), and its associated equations, such as the loading-unloading conditions of Eq. (2.2), the equivalent strain is replaced by the nonlocal equivalent strain.

$$\bar{\varepsilon}_{eq}(x) = \int_V W(x,x')\varepsilon_{eq}(x')\,Adx' \tag{8.1}$$

here, ε_{eq} represents the nonlocal equivalent strain. Accordingly, the modified loading-unloading conditions are given by

$$\bar{\varepsilon}_{eq}(\varepsilon) - \kappa \leq 0, \quad \dot{\kappa} \geq 0 \;\text{ and }\; (\bar{\varepsilon}_{eq} - \kappa)\dot{\kappa} = 0 \tag{8.2}$$

where, the internal variable κ represents the maximum previously reached value of the nonlocal equivalent strain ($\bar{\varepsilon}_{eq}$). Using those conditions and the variables, the damage model is expressed as follows.

$$D = 1 - \frac{\varepsilon_0(1 - A_t)}{\kappa} - \frac{A_t}{exp[B_t(\kappa - \varepsilon_0)]} \tag{8.3}$$

here, A_t and B_t are the damage parameters in tension, ε_0 is the strain where damage initiates. The regularization effects of nonlocal equivalent strain indirectly affect the load-displacement behaviour through damage and the constitutive equations. To streamline the computational process and minimize time consumption, the secant stiffness matrix is employed in this study, given its simplicity in handling the case study.

8.3 Numerical example

A 1D bar fixed at one end is subjected to uniaxial tension at the free end as shown in Fig. 8.1. The central portion of the bar is weakened (1% reduction in area) to trigger the localization.

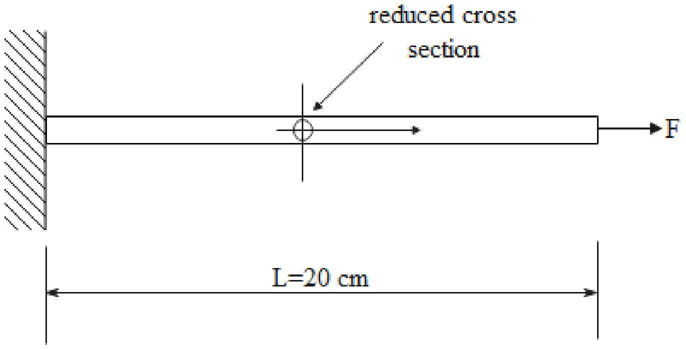

Fig. 8.1. Concrete bar subjected to extension

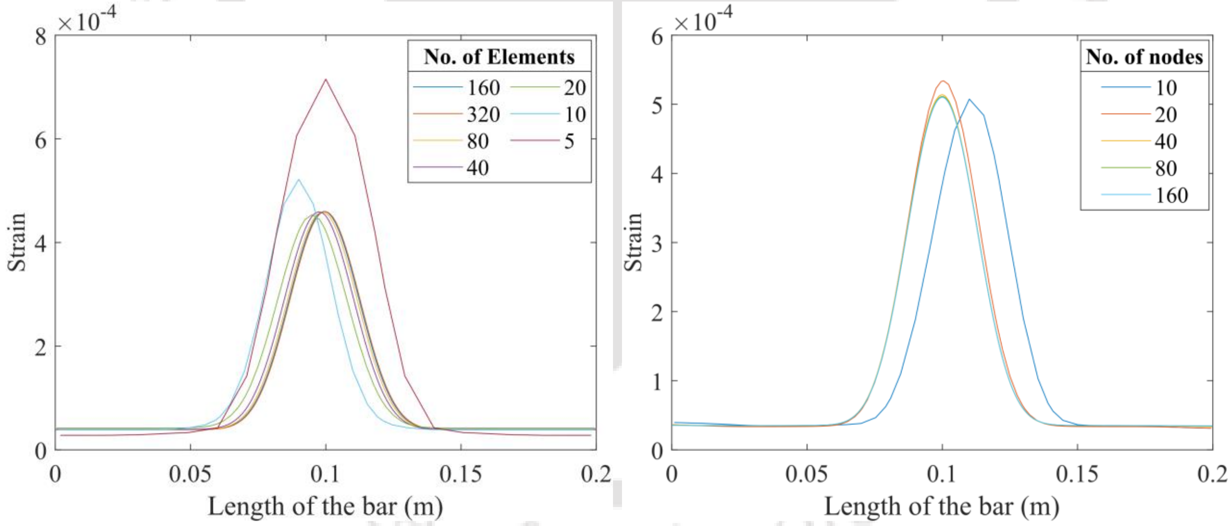

(a) **(b)**

Fig. 8.2. Convergence of strain profile employing nonlocal approach in **(a)** FEM and **(b)** EFG method

Fig. 8.2(a) and 8.2(b) illustrate the strain versus length of the bar that was obtained by the use of the FEM and EFG method. Both the numerical methods employ nonlocal approach that was discussed in the previous section. The EFG method is able to achieve strain convergence at a comparatively faster rate than the FEM. The reason for this can be traced to the higher-order shape functions that the EFG approach possesses in comparison to the FE method for degrees of freedom that are comparable. The two plots for ten degrees of freedom reflect this fact in their respective ways. Likewise, the strain variation obtained by the EFG method is somewhat smoother than the strain variation generated by the FEM, which exhibits some kinks in the area of the piece of the bar that has been weakened.

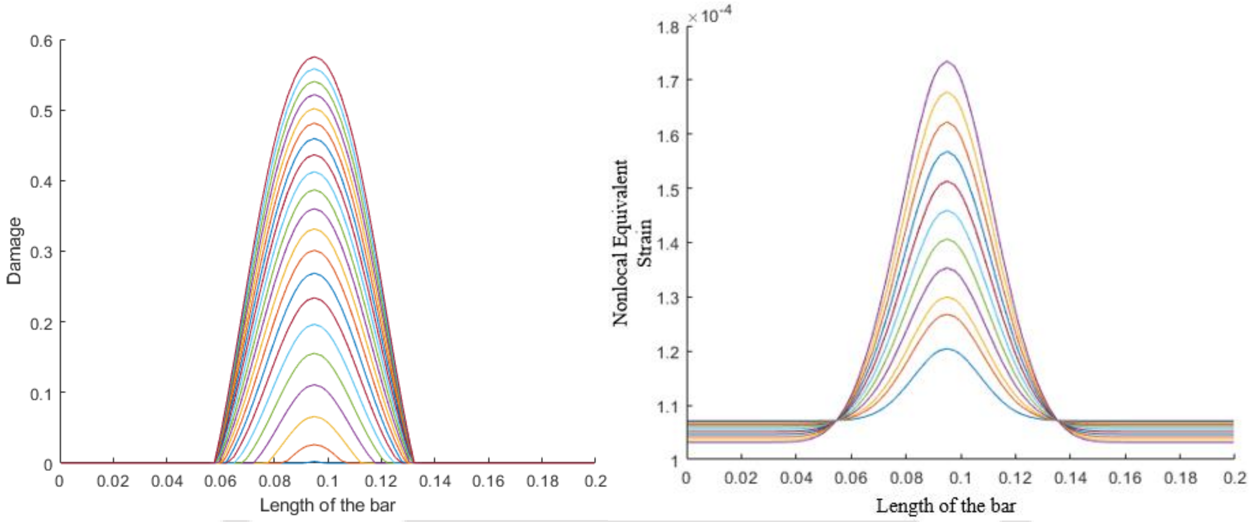

(a) **(b)**

Fig. 8.3. (a) Damage, and **(b)** nonlocal equivalent strain distributions within the bar

Fig. 8.3(a) and 8.3(b) show the evolution of damage and nonlocal equivalent strain with increments in force. As the magnitude of the force increases, the area under damage increases gradually. A bell-shaped damage profile centered around the weakened portion expands horizontally as the magnitude of the damage increases with load. The variation of damage is smooth with no kinks or sudden jumps. This is possible due to removal of the strain localizing effect. Another way to obtain the smooth variation of strain in FEM is by using the mixed FE involving displacement and strain as degrees of freedom. Even then, the total degrees of freedom will be significantly higher than the EFG method.

It is interesting to note that as the damage evolves the region outside the damaged portion undergoes stress relaxation. This is obvious since the weakened portion continues to get weaker under the action of the force. The same is reflected in the nonlocal equivalent strain evolution plot. Finally, the stress vs. strain plots for different combinations of the damage parameters - A_t and B_t, are plotted in Fig. 8.4. The parametric study on the model parameters revealed that adjusting A_t alters the softening behaviour of the material. Specifically, decreasing $\mathrm{A_t}$ broadens the softening response, which increases fracture energy. This is observed as A_t governs the softening behaviour, distinguishing various types within brittle materials. Meanwhile, varying B_t influences the rate of damage evolution; an increase in B_t leads to a faster rate of damage progression within the material.

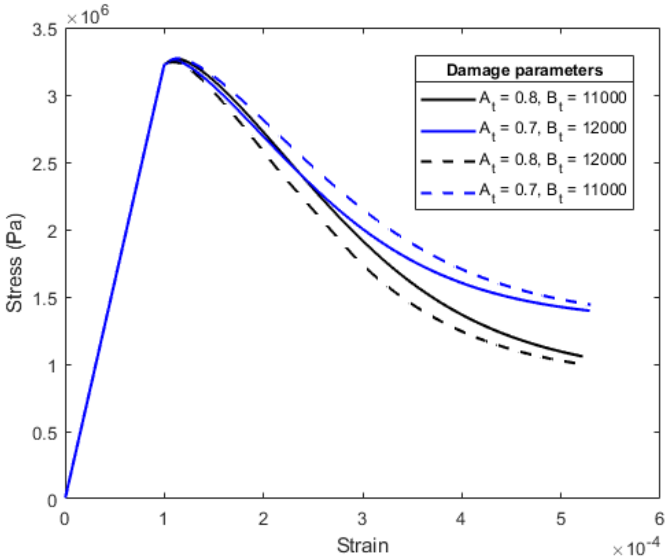

Fig. 8.4. Stress-strain responses of the bar for 80 nodal divisions

8.4 Summary

The higher-order shape functions which are generally smooth in nature limits their applicability while solving problems that possess sudden jumps. Therefore, this work integrates nonlocal approaches with the Element-Free Galerkin (EFG) method to handle such discontinuities effectively. The performance of the current approach is evaluated through a one-dimensional concrete bar example, focusing on the study of damage behaviour using Mazar's model, which assumes elastic-damage conditions. In this model, damage evolution is contingent upon the equivalent strain experienced by the specimen. Recognizing its significance, the equivalent strain is selected as the nonlocal variable. The results are also compared with nonlocal theories in the framework of FEM. The results are further compared with nonlocal theories within the FEM framework, revealing that the EFG method demonstrates superior convergence with fewer nodal divisions compared to FEM. The effectiveness of the method becomes evident as issues such as loss of ellipticity, mesh dependency, and the absence of the Kronecker delta property are eliminated.

Chapter 9

Hyperelasticity in EFG Framework

Most of the hyperelastic materials are nearly incompressible which poses challenges, i.e., volumetric locking during numerical modelling. There exist many formulations in the context of finite element method (FEM), among which the mixed displacement-pressure formulation is robust. On the other hand, such displacement-pressure formulation is less explored in meshfree methods which mitigates the problem associated with mesh distortion during large deformation.

This chapter proposes a two-field mixed variational formulation using the perturbed Lagrangian approach within the EFG framework. The key highlight of this work is the random distribution of the pressure nodes across the geometry by following specific guidelines, marking the first such attempt in the literature. A wide spectrum of problems involving bending, tension, compression and contact is solved using the proposed formulation involving regular and irregular pressure node distribution.

9.1 Introduction

Hyperelastic materials are utilized in various engineering fields due to their unique properties and behaviour. These materials are incompressible or nearly incompressible in nature and are mostly subjected to large deformations. When modelling such nearly incompressible materials using any standard displacement-based formulation a phenomenon of volumetric locking occurs, which causes an excessively stiff response [271]. There have been several methods introduced in the past to alleviate locking such as reduced/selective integration [272], B-bar technique [273,274], mixed formulations [275,276], assumed strain methods [277–280], and others[281–283].

9.1.1 Mixed displacement-pressure methods

In cases of incompressibility, the mixed displacement-pressure formulation stands out as computationally efficient option [284]. The mixed methods generally use the Lagrange multiplier approach to impose additional constraints. In FEM, the enforcement of constraints is typically performed on an element-by-element basis, accompanied by the utilization of local Lagrange multipliers. An intuitive approach involves attempting to eliminate the corresponding degrees of freedom at the element level [285]. However, this approach results in a saddle-point problem due to the non-positivity inherent in the element stiffness matrix, leading to numerical challenges.

Perturbed Lagrangian formulation [286,287] was introduced as a modification over mixed formulations which allows for eliminating the unwanted degrees of freedom at the elemental level. In a work by Brink and Stein [288] different mixed finite element methods for incompressible and nearly incompressible finite elasticity, were compared on some standard structural problems in a nonlinear framework. The observed results are consistent across all these methods when the stored energy function includes a volumetric contribution of $\left(\frac{1}{2\kappa}\right)(J-1)^2$, where J represents the volume dilatation (Jacobain determinant of the deformation), and κ is the bulk modulus.

9.1.2 EFG for locking issues in hyperelasticity

Due to mesh dependency in the finite element approaches, during large deformations, problems such as mesh distortion occurs which results in non-convergence [289]. Meshfree techniques have become more and more popular in recent years as a solution to this problem. A study conducted by Huerta and Fernández-Méndez [290] showed the locking phenomenon in the incompressibility limit for the EFGM. Chen et al. [291] proposed a pressure projection technique for the reproducing kernel particle method (RKPM) to alleviate volumetric locking where the dilatational component of the stiffness matrix is integrated using one-point quadrature in a background mesh. Later Dolbow and Belytschko [292] introduced a new formulation for the modelling of incompressible materials which employs a reduced integration technique within a mixed formulation of the EFGM. The use of nodal integration for the pressure contribution, in line with the mesh-free nature of the approach, is a key difference from Chen et al.'s work [291].

Resio et al. [293] introduced B-bar and enhanced strain methods in EFGM. A stabilization technique was implemented to avoid the hourglass effect. Graça et al. [294] blended the enhanced strain method (EAS) with EFGM to alleviate volumetric locking using a subspace analysis. A comparison between the proposed method and the B-bar technique was done and it was shown that the combined EFGM and EAS gave more flexibility to the solution for nearly incompressible materials. In a recent work by Cai et al. [289], the complex variable EFG method (CVEFG) based on complex variable moving least square (CVMLS) approximations to avoid mesh distortion for hyperelastic large deformation problems under non-conservative loads was used. The numerical examples discussed in the work showed that results obtained from the CVEFG method were closer to FE-ABAQUS® and the method was more efficient than EFGM.

The mixed displacement-pressure formulations are widely acknowledged as one of the most efficient and robust techniques for addressing volumetric locking issues associated with incompressibility conditions. Nevertheless, these formulations are predominantly applied in standard FE frameworks and have not been extensively explored in EFG frameworks, especially in the context of large deformation problems where challenges such as mesh distortion issues are more prevalent. In this chapter, a two-field (u/p) mixed variational formulation employing the perturbed Lagrangian approach is adopted within the EFGM framework to tackle the challenge of volumetric locking in hyperelastic materials. This study introduces a unique approach by randomly distributing pressure nodes across the geometry according to specific guidelines. This method is advantageous because the construction of EFGM shape functions relies solely on the distribution of displacement nodes. The primary intention of the authors in using irregular pressure nodal distribution is twofold: (a) to demonstrate that the accuracy of results is comparable to that of regular pressure nodal distribution, indicating that while irregular displacement nodes have certain limitations, this is not the case for pressure nodes, and (b) to use fewer pressure nodes than displacement nodes by ensuring proper distribution near critical regions in line with recommended guidelines, while still maintaining close accuracy. The proposed formulations are applied to solve various benchmark problems involving contact and stress gradients.

9.2 Two-field mixed displacement-pressure variational formulation in EFG framework

Consider the 2D body Ω, subjected to traction loads on boundary Γ_F and essential boundary conditions on the boundary Γ_u as shown in Fig. 9.1. The formulation entails selecting the closest pressure node, in addition to displacement nodes, within the support domain of each Gauss point. Employing the additive decomposition of the strain energy function (W),

$$W = \widetilde{W}(\boldsymbol{E}) + \frac{1}{2}\kappa[U(J)]^2 \tag{9.1}$$

here, κ represents the bulk modulus, which is required to be independent of deformation, $\widetilde{W}$is the deviatoric part of strain energy function and $\boldsymbol{E}$ denotes Green-Lagrangian strain. The volumetric component of strain energy (U) is exclusively dependent on the Jacobian $(J = det\boldsymbol{F})$. The classical Lagrange multiplier method poses a saddle-point problem susceptible to numerical challenges. To overcome this, a perturbed Lagrangian approach is employed, which alleviates the incompressibility constraint. The potential energy functional for the perturbed Lagrangian formulation is given as [287],

$$\Pi(\mathbf{u}, p, \lambda) = \int_{\Omega_0} \widetilde{W}(\boldsymbol{E})\, \mathrm{d}\Omega + \int_{\Omega_0} pU\big(J(\mathbf{u})\big)\, \mathrm{d}\Omega - \frac{1}{2}\int_{\Omega_0} \frac{p^2}{\kappa}\, \mathrm{d}\Omega$$
$$- \int_{\Omega_0} \mathbf{u}^{\mathrm{T}}\ \mathbf{f}^{\mathbf{b}}\, \mathrm{d}\Omega - \int_{\Gamma_F} \mathbf{u}^{\mathrm{T}}\ \mathbf{t}\, \mathrm{d}\Gamma - \int_{\Gamma_u} \lambda^T(\mathbf{u} - \mathbf{u}_\Gamma)\, \mathrm{d}\Gamma \tag{9.2}$$

where scalar p is a independent variable representing hydrostatic pressure, $\mathbf{f}^{\mathbf{b}}$ and $\mathbf{t}$ are the body force and traction vectors. The last term contains a Lagrange multiplier (λ) which is used to impose essential boundary conditions (EBC) in the EFGM framework.

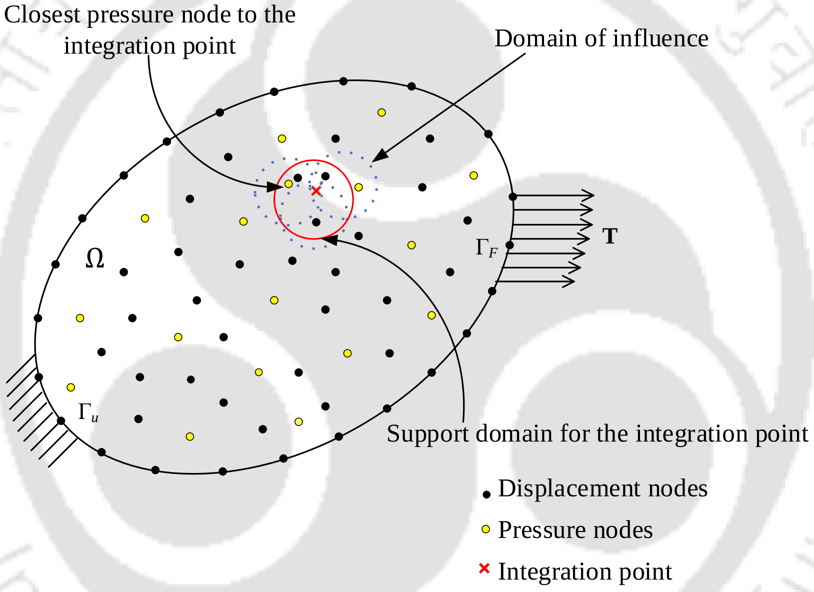

Fig. 9.1. Geometry, boundary conditions, and nodal discretization of an arbitrary body

Now, taking the directional derivative with respect to each variable as

$$\mathrm{D}_{\mathbf{u}}\Pi(\mathbf{u}, p, \lambda)\bar{\mathbf{u}} = 0,\ \ \mathrm{D}_p\Pi(\mathbf{u}, p, \lambda)\bar{p} = 0\ \ \text{and}\ \ \mathrm{D}_\lambda\Pi(\mathbf{u}, p, \lambda)\bar{\lambda} = 0$$

The resulting equations will be,

$$\int_{\Omega_0} \frac{\partial \widetilde{W}(\boldsymbol{E})}{\partial \boldsymbol{E}} : \bar{\boldsymbol{E}}\, \mathrm{d}\Omega + \int_{\Omega_0} pU'\big(J(\mathbf{u})\big) \frac{\partial J(\mathbf{u})}{\partial \boldsymbol{E}} : \bar{\boldsymbol{E}}\, \mathrm{d}\Omega$$
$$- \int_{\Omega_0} \bar{\mathbf{u}}^{\mathrm{T}}\ \mathbf{f}^{\mathbf{b}}\, \mathrm{d}\Omega - \int_{\Gamma_F} \bar{\mathbf{u}}^{\mathrm{T}}\ \mathbf{t}\, \mathrm{d}\Gamma - \int_{\Gamma_u} \bar{\mathbf{u}}^{\mathrm{T}}\ \lambda\, \mathrm{d}\Gamma = 0 \tag{9.3}$$

$$\int_{\Omega_0} \left[U(J(\mathbf{u})) - \frac{p}{\kappa}\right] \bar{p}\, \mathrm{d}\Omega = 0$$

$$\int_{\Gamma_u} \bar{\lambda}^T (\mathbf{u} - \mathbf{u}_\Gamma)\, \mathrm{d}\Gamma = 0$$

Now, employing the Taylor series expansion with respect to $\mathbf{u}, p,$ and λ, while neglecting the higher order terms, results linearization process, given by,

$$\begin{aligned} a_{(\mathbf{u},p,\lambda)}(\Delta\mathbf{u}, \bar{\mathbf{u}}) + b_{(\mathbf{u})}(\Delta p, \bar{\mathbf{u}}) - \int_{\Gamma_u} \bar{\mathbf{u}}^T \Delta\lambda\, \mathrm{d}\Gamma &= -\mathrm{D}_{\mathbf{u}}\Pi(\mathbf{u}, p, \lambda)\bar{\mathbf{u}} \\ b_{(\mathbf{u})}(\bar{p}, \Delta\mathbf{u}) + c_{(\mathbf{u})}(\bar{p}, \Delta p) &= -\mathrm{D}_p\Pi(\mathbf{u}, p, \lambda)\bar{p} \\ \int_{\Gamma_u} \bar{\lambda}^T \Delta(\mathbf{u} - \mathbf{u}_\Gamma)\, \mathrm{d}\Gamma &= -\mathrm{D}_\lambda\Pi(\mathbf{u}, p, \lambda)\bar{\lambda} \end{aligned} \tag{9.4}$$

where,

$$\begin{aligned} a_{(\mathbf{u},p,\lambda)}(\Delta\mathbf{u}, \bar{\mathbf{u}}) = & \int_{\Omega_0} (\bar{\boldsymbol{E}} : \boldsymbol{D}_d : \Delta\boldsymbol{E} + \boldsymbol{S}_d : \Delta\bar{\boldsymbol{E}})\, \mathrm{d}\Omega + \int_{\Omega_0} (\bar{\boldsymbol{E}} : p\, U^{'}(J(\mathbf{u})) \frac{\partial^2 J}{\partial\boldsymbol{E}\partial\boldsymbol{E}} : \Delta\boldsymbol{E})\, \mathrm{d}\Omega \\ & + \int_{\Omega_0} \left(\bar{\boldsymbol{E}} : p\, U''\big(J(\mathbf{u})\big) \frac{\partial J}{\partial\boldsymbol{E}} \otimes \frac{\partial J}{\partial\boldsymbol{E}} : \Delta\boldsymbol{E}\right) \mathrm{d}\Omega \\ & + \int_{\Omega_0} p U^{'}(J(\mathbf{u})) \frac{\partial J}{\partial\boldsymbol{E}} : \Delta\bar{\boldsymbol{E}}\, \mathrm{d}\Omega \\ b_{(\mathbf{u})}(\Delta p, \bar{\mathbf{u}}) = & \int_{\Omega_0} \Delta p U^{'}\big(J(\mathbf{u})\big) \frac{\partial J}{\partial\boldsymbol{E}} : \bar{\boldsymbol{E}}\, \mathrm{d}\Omega \\ c_{(\mathbf{u})}(\bar{p}, \Delta p) = & \int_{\Omega_0} \frac{1}{\kappa} \Delta p \bar{p}\, \mathrm{d}\Omega \end{aligned} \tag{9.5}$$

here, $\boldsymbol{S}_d$ and $\boldsymbol{D}_d$ are deviatoric part of second Piola-Kirchoff stress and material elasticity tensors. Firstly, the elemental matrices $\boldsymbol{K}_{uu}$, $\boldsymbol{K}_{up}$, and $\boldsymbol{K}_{pp}$ are assembled in their respective global matrices and expressed in algebraic form to determine the $\Delta\mathbf{d}^g, \Delta\mathbf{p}^g$, and $\Delta\lambda^g$:

$$\begin{bmatrix} \boldsymbol{K}_{uu}^{g} & \boldsymbol{K}_{up}^{g} & \boldsymbol{G} \\ \boldsymbol{K}_{pu}^{g} & \boldsymbol{K}_{pp}^{g} & \mathbf{0} \\ \boldsymbol{G}^{T} & \mathbf{0} & \mathbf{0} \end{bmatrix} \begin{bmatrix} \Delta\mathbf{d}^{g} \\ \Delta\mathbf{p}^{g} \\ \Delta\lambda^{g} \end{bmatrix} = \begin{bmatrix} \mathbf{f}_{res} - \boldsymbol{G}\lambda^{g} \\ \mathbf{f}_{p}^{g} \\ \Delta\mathbf{q}^{g} \end{bmatrix} \tag{9.6}$$

where superscript g represents global matrices and vectors. $\boldsymbol{f}_{res}^{g} = \boldsymbol{f}_{ext}^{g} - \boldsymbol{f}_{int}^{g}$ is the residual force and $\Delta\mathbf{d}^{g}$ is the incremental nodal displacement vector. The elemental matrices $\boldsymbol{K}_{uu}$, $\boldsymbol{K}_{up}$, and $\boldsymbol{K}_{pp}$ are expressed as,

$$\begin{aligned} \boldsymbol{K}_{uu} &= \int_{\Omega_0} \boldsymbol{B}_N^T(\boldsymbol{D}_d + \boldsymbol{D}_{vol})\boldsymbol{B}_N + \boldsymbol{B}_G^T(\boldsymbol{S}_d + \boldsymbol{S}_{vol})\boldsymbol{B}_G \,\mathrm{d}\Omega \\ \boldsymbol{K}_{up} &= \int_{\Omega_0} J\boldsymbol{B}_N^T\boldsymbol{C}^{-1}\mathrm{d}\Omega \\ \boldsymbol{K}_{pp} &= -\int_{\Omega_0} \frac{1}{\kappa}\mathrm{d}\Omega \end{aligned} \tag{9.7}$$

here, $\boldsymbol{B}_N$ and $\boldsymbol{B}_G$ represents the linear and nonlinear strain-displacement matrix, given by Eq. (3.77). The deviatoric parts, $\boldsymbol{S}_d$ and $\boldsymbol{D}_d$, are derived based on the hyperelastic material models, specifically the basic Mooney-Rivlin model has been considered in this work. The derivations of $\boldsymbol{S}_d$ and $\boldsymbol{D}_d$ are provided in Appendix B, while the volumetric parts of 2nd Piola-Kirchoff stress and elasticity tensors, from Eq. (9.5), are expressed as

$$\boldsymbol{S}_{vol} = pJ\boldsymbol{C}^{-1}; \qquad D_{vol} = pJ(\boldsymbol{C}^{-1} \otimes \boldsymbol{C}^{-1} - 2(\boldsymbol{C}^{-1} \otimes \boldsymbol{C}^{-\mathrm{T}})) \tag{9.8}$$

Similarly, the right-side vectors over the support domain take the form:

$$\begin{aligned} \mathbf{f}_{ext} &= \int_{\Omega_0} \boldsymbol{\Phi}^{\mathrm{T}}\,\mathbf{f}^{\mathbf{b}}\mathrm{d}\Omega + \int_{\Gamma_F} \boldsymbol{\Phi}^{\mathrm{T}}\,\mathbf{t}\,\mathrm{d}\Gamma + \int_{\Gamma_u} \boldsymbol{\Phi}_I^{\mathrm{T}}\,\lambda\,\mathrm{d}\Gamma \\ \mathbf{f}_{int} &= \int_{\Omega_0} \boldsymbol{B}_N^{\mathrm{T}}\,\{\boldsymbol{S}_d + \boldsymbol{S}_{vol}\}\,\mathrm{d}\Omega \\ \mathbf{f}_p &= \int_{\Omega_0} \left[U(J(\mathbf{u})) - \frac{p}{\kappa}\right]\mathrm{d}\Omega \\ \Delta\mathbf{q}^{g} &= \int_{\Gamma_u} \boldsymbol{N}^T\,(\mathbf{u} - \mathbf{u}_{\Gamma})\,\mathrm{d}\Gamma \\ \boldsymbol{G} &= -\int_{\Gamma_u} \boldsymbol{N}^T\boldsymbol{\Phi}\,\mathrm{d}\Gamma \end{aligned} \tag{9.9}$$

9.3 Guidelines for irregular pressure distribution

In the case of regular pressure distribution, the pressure nodes are positioned at the centroid of four uniformly distributed displacement nodes. However, in irregular distribution, the pressure nodes are randomly dispersed throughout the entire geometry. Despite its flexibility, adherence to certain guidelines is necessary to ensure stable and accurate results, as outlined below:

- It is essential to utilize all the pressure nodes distributed across the geometry; otherwise, it will lead to singularity issues from the initial iteration due to the rank of the tangent stiffness matrix being less than its size.
- Every Gauss point within its support domain should be associated with a pressure node. Although results can be obtained without following this guideline, it results in a substantial increase in the number of iterations needed for convergence, imposing a computational burden.
- Extending the above point, every geometry has critical regions, such as holes and cracks, which are typically the points of interest. In these areas, it is essential to have pressure nodes (at least one) within the support domain of each Gauss point. Otherwise, it may introduce uncertainties in the deformed shapes, particularly near those regions, and sometimes lead to convergence issues.

  Conversely, in regions far away from these critical areas, where coarse nodal discretization and larger support domains exist, the presence of pressure nodes in abundance is not necessarily required, especially in areas where stress gradients are less significant. This offers the advantage of employing an less number of pressure nodes without compromising the accuracy of the results (demonstrated in example 4).
- When immediate pressure nodes are present at the same location or in close proximity, some of these pressure nodes may distribute their intensity to a minimal number of nearest displacement nodes, and in certain instances, to only one displacement node, and vice versa. Consequently, a higher count of displacement nodes within a set for a corresponding pressure node leads to a decrease in intensity, as the pressure is evenly distributed among the displacement nodes. On the contrary, a smaller count of displacement nodes within a set localizes the intensity, resulting in higher pressure magnitudes compared to the

surrounding nodes. This leads to abnormal distribution of pressure over geometry which inturn effects the deformed shapes.

However, this effect becomes more prominent when immediate pressure nodes are situated near critical regions, emphasizing the importance of avoiding their placement in such areas. Conversely, locations distant from critical regions can accommodate immediate pressure nodes, provided that the pressure intensity in those areas is insignificant (discussed in example 2).

9.4 Contact problems: implementation in EFGM

The formulation of contact can be characterized by Signorini's law, which states that:

- The bodies are deemed to be in contact when the gap between them is zero, and contact forces are applied at the nodes where contact occurs.
- In the absence of contact, there is a non-zero gap between two objects, and contact forces remain zero across the entire region.

This definition can be mathematically expressed as a contact constraint using a gap function (g) and contact force (λ):

$$\text{No Penetration: } g \leq 0; \quad \text{Contact force: } \lambda \geq 0$$

Typically, the Lagrange multiplier and penalty methods are employed to enforce constraint conditions in numerical analyses. Since EFGM also utilizes the Lagrange multiplier method to impose essential boundary conditions, the imposition of contact conditions can be achieved more seamlessly compared to the FEM. Stick conditions (coefficient of friction (μ) is 1) are considered in this work, and the numerical implementation is provided in the form of an algorithm, as shown in Box 9.1.

Box 9.1: Algorithm for stick contact conditions in EFGM

```
for $i < loadsteps$ do
    Update $\boldsymbol{G}, \mathbf{q}$
    $[\mathbf{u}, err] \leftarrow$ Newton_Raphson_Solver($\mathbf{F}_i, \mathbf{u}$);        // if error $< 10^{-6}$ then $\mathbf{u}$ doesn't change
    Update $\boldsymbol{x}, \boldsymbol{y}$
    $n_{con} \leftarrow \boldsymbol{y} < 10^{-6}$                    // find contact nodes
```

```
    $\mathbf{u}_{ycorr} = \boldsymbol{Y}_{ground} - \boldsymbol{Y}_c$;        // update y-displacements of contact nodes to touch ground
    if $n_{con}$ is not empty then
        $n_{xy} \leftarrow n_{xy} \cup n_{con}$
        Update $\lambda$ size
    end
end
```

9.5 Numerical Examples

The present section elucidates the performance of the proposed formulation vis-à-vis the mixed EFG formulation incorporating a regular pressure nodal distribution, and its comparison with the mixed FE formulation. The method's accuracy under coarse nodal discretization, as well as its efficiency and robustness, are illustrated through the examination of various benchmark numerical examples. The first two examples not only showcase the superior accuracy in coarse nodal discretization achieved by the mixed EFG formulation but also highlight its adaptability in irregularly distributing pressure nodes while maintaining a convergence profile that is comparable to that observed with regular pressure node distribution. Subsequently, a simple yet well-established contact problem is presented to validate the effectiveness of the proposed formulations in addressing mesh distortion issues as compared to the FE formulation. Finally, a problem characterized by significant stress gradients and volumetric locking is solved to affirm the robustness of the proposed method.

The essential abbreviations employed in the subsequent examples are defined as follows: the ***FEM-U4P1*** describes the two-field mixed FEM formulation considering one pressure node for a four-node quadrilateral (Q4) element. ***mEFGr*** and ***mEFGir*** correspond to a two-field mixed EFGM formulation, where *r* and *ir* denotes regular and irregular pressure nodal distribution respectively. Further, N_{dof}^{u} signifies the degree of freedom related to displacement (u) nodes, while N_{dof}^{p} denotes the degree of freedom associated with pressure (p) nodes.

9.5.1 Cook's membrane

The first case study involves solving Cook's membrane to evaluate the performance of the proposed methodology under the influence of volumetric locking. The schematic of the problem along with the specified boundary and loading conditions is illustrated in Fig. 9.2. The left edge of the plate is entirely constrained, while the right edge is subjected to a load per unit length of $f_y = 6.25\ \mathrm{N/mm}$. The reference solution for the vertical displacement at the tip is 7 mm [295].

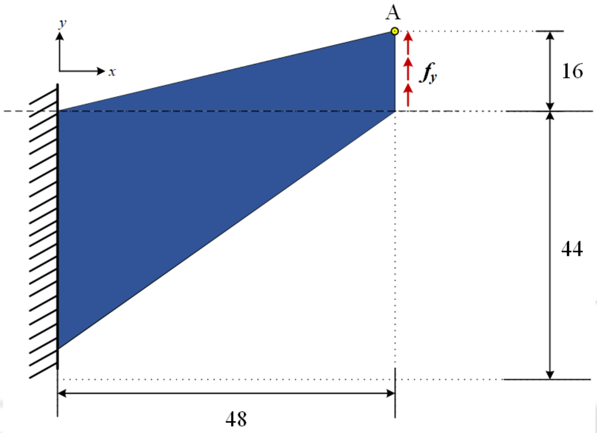

Fig. 9.2. Cook's membrane: geometry, boundary and loading conditions

The nearly incompressible Neo-Hookean model is employed, and the material properties taken are $C_{10} = 40.095\ \mathrm{MPa}$ and $\nu = 0.4999$. The results achieved through mixed EFG formulations are juxtaposed with those from mixed FEM (U4P1) analysis. To facilitate this comparison, a convergence study is conducted using various FE meshes, specifically with 2, 4, 8, 16, 32, and 64 elements per side. The nodal divisions in EFG follow a similar pattern, as depicted in Fig. 9.3. In addition to the displacements, nodes associated with pressure are discretized both regularly and irregularly. An example is illustrated for a 16×16 division in Fig. 9.3 (a) and 9.3(b) along with their corresponding deformed geometries in Fig. 9.3(c) and 9.3(d).

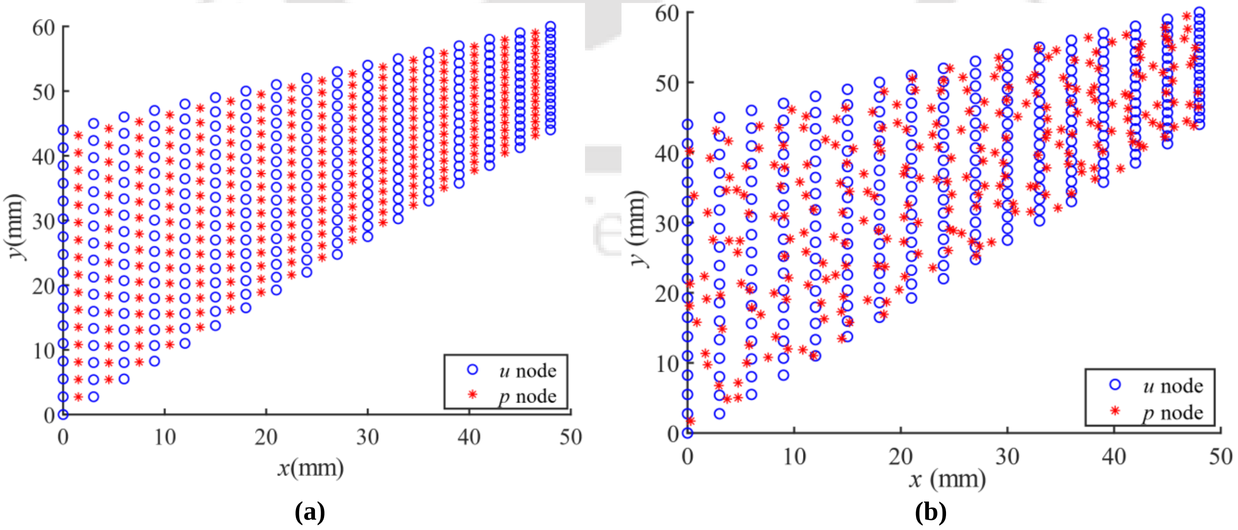

(a) (b)

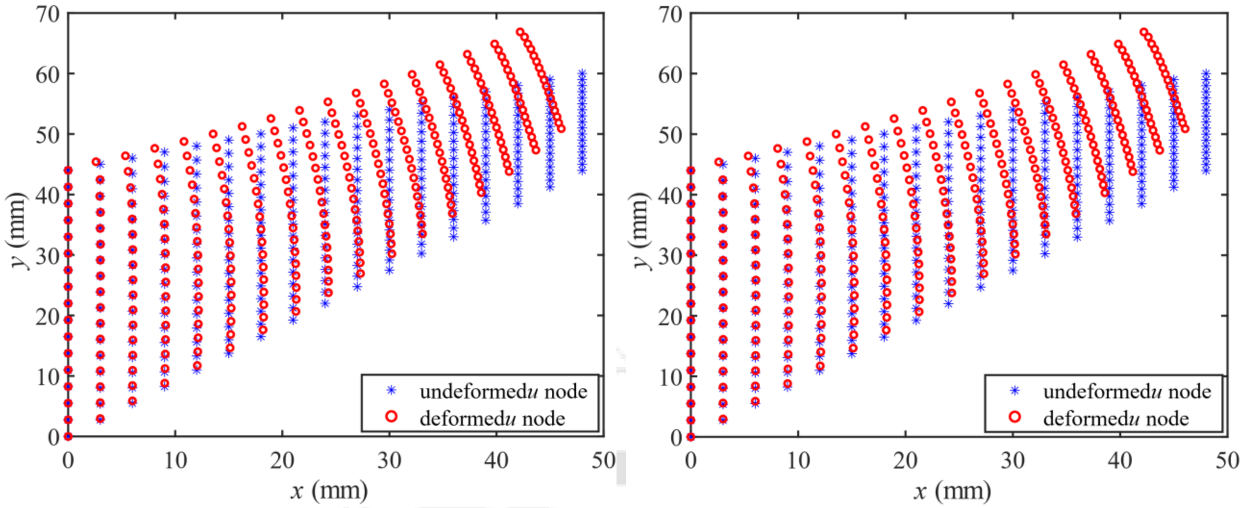

(c) **(d)**

Fig. 9.3. Cook’s membrane with 16 × 16 displacement nodal divisions distributed with **(a)** regular, **(b)** irregular pressures, and their corresponding deformed geometries **(c)**, and **(d)**

The problem is addressed to ascertain the vertical displacement at the tip. Fig. 9.4(a) presents normalized results against the reference solution, plotted in relation to the N_{dof}^{u}. It is widely acknowledged that the EFGM tends to exhibit improved performance compared to the FEM, particularly in scenarios involving coarse nodal divisions. The current example further illustrates this observation, showcasing the better convergence capabilities of the mixed EFGM (both ***mEFGr*** and ***mEFGir***) over the FEM-U4P1.

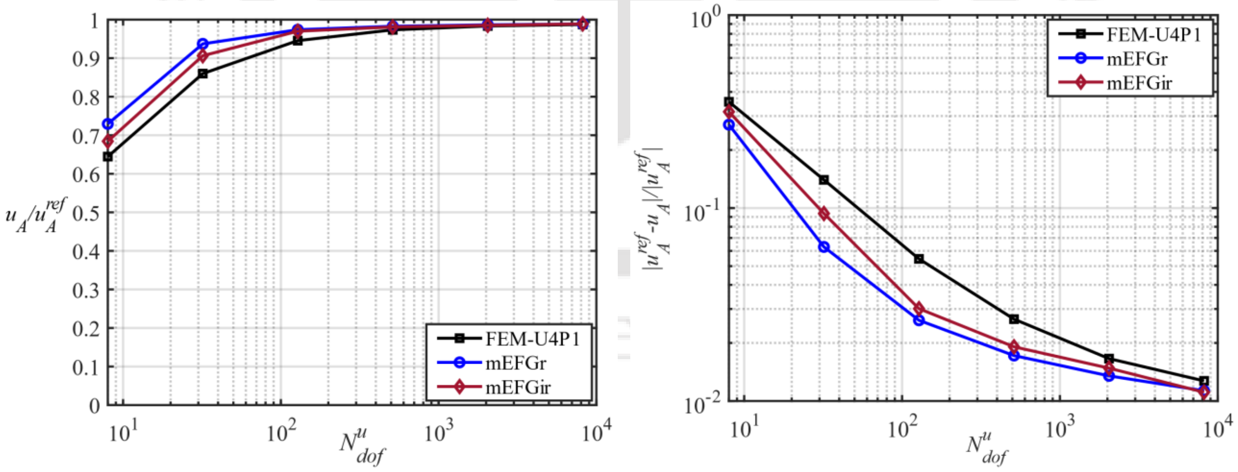

(a) **(b)**

Fig. 9.4. (a) Normalized vertical displacement at point ‘*A*’, and **(b)** relative error of displacement against the total degree of freedom for the Cook’s membrane example

Despite minor differences in the results obtained through mixed EFGM with irregular pressure distribution at coarse nodal divisions, it exhibits a convergence response similar to that of the regular distribution from 8 × 8 nodal divisions onward. This highlights the effectiveness of the current methodology, showcasing its flexibility in distributing pressure nodes across the geometry under the guidelines discussed in the earlier section. Fig. 9.4(b) shows the relative displacement error with N_{dof}^{u}, contributing to a more comprehensive understanding of the proposed methodology's performance compared to the mixed FEM formulation.

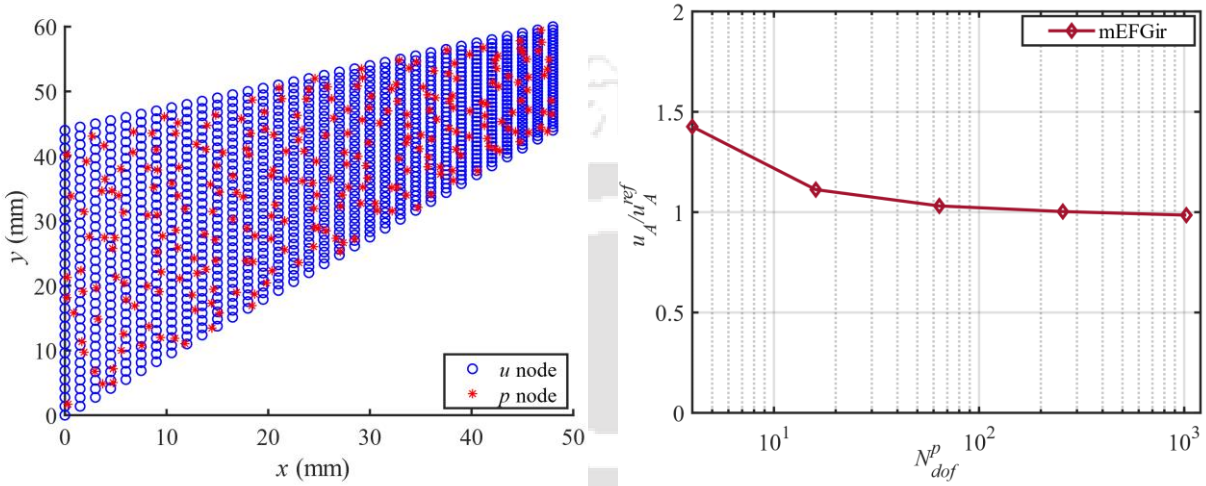

(a) **(b)**

Fig. 9.5. Cook's membrane with 32 × 32 displacement nodal divisions **(a)** distributed with 16 × 16 irregular pressure nodes, and **(b)** Normalized vertical displacement at point '*A*' for various '*p*' degrees of freedom

An additional convergence study, as depicted in Fig. 9.5, is conducted with a fixed displacement nodal division of 32 × 32, while varying the pressure nodes from 2 × 2 to 32 × 32. The attained converged results are noticeable from approximately 8 × 8 onward, indicating the capability of the proposed methodology to yield accurate results by employing less number of pressure nodes for irregular distribution, thereby reducing computational burden.

9.5.2 Partially loaded plane strain block

Here, a well-established benchmark problem involving a partially loaded block under compression is addressed to investigate the performance of formulations designed to handle near-incompressibility conditions in large deformations [296]. This problem involves a plane strain block of 20 × 10 mm^2 positioned on a rigid, frictionless surface and experiences pressure applied to its top edge at the central region. The geometry, boundary and loading conditions are shown in Fig. 9.6.

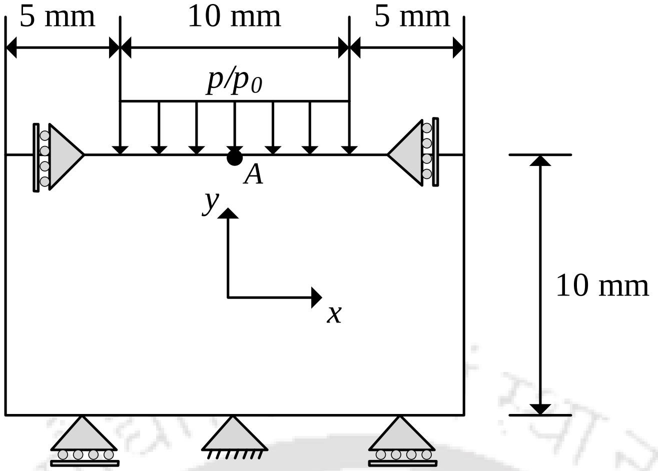

Fig. 9.6. Plane strain block under partial compression: Geometry, loading and boundary conditions

Because of symmetry in the geometry, only half of the model is taken into consideration for analysis. The nearly incompressible Neo-Hookean model is employed with the same constants as those used in the previous problem. The performance of the mixed EFGM formulations are compared with those derived from mixed FEM (U4P1) analysis under various load states, p/p_0, with $p_0 = 20\ \mathrm{N/mm^2}$. Similar to the Cook's problem, the FE meshes utilized are 4, 8, 16, and 32 elements per side. The nodal divisions used in EFGM (for both regular and irregular pressures) are identical to that of the FEM analysis. An example is illustrated for a 32 × 32 nodal division in Fig. 9.7(a) and 9.7(b).

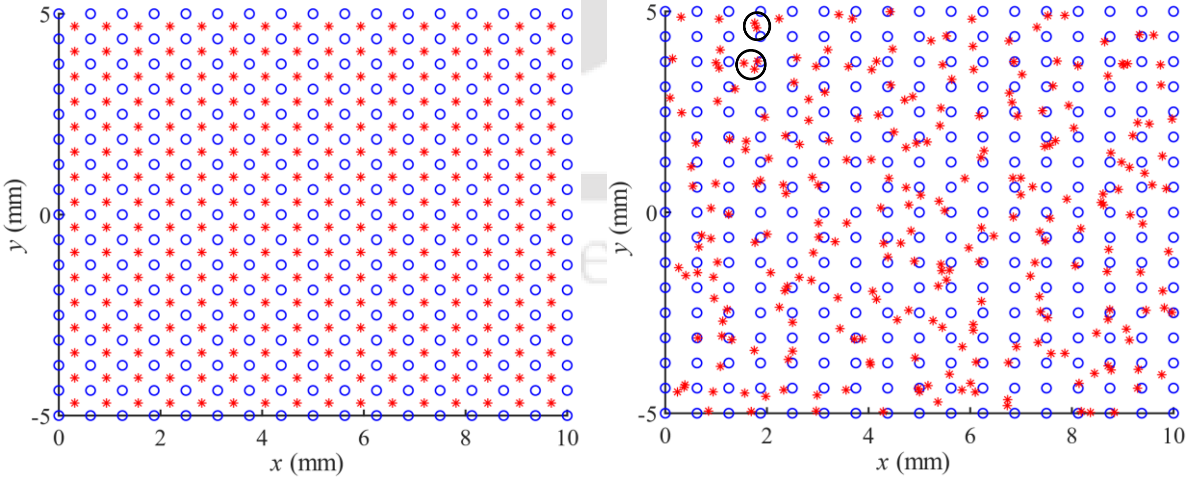

(a) **(b)**

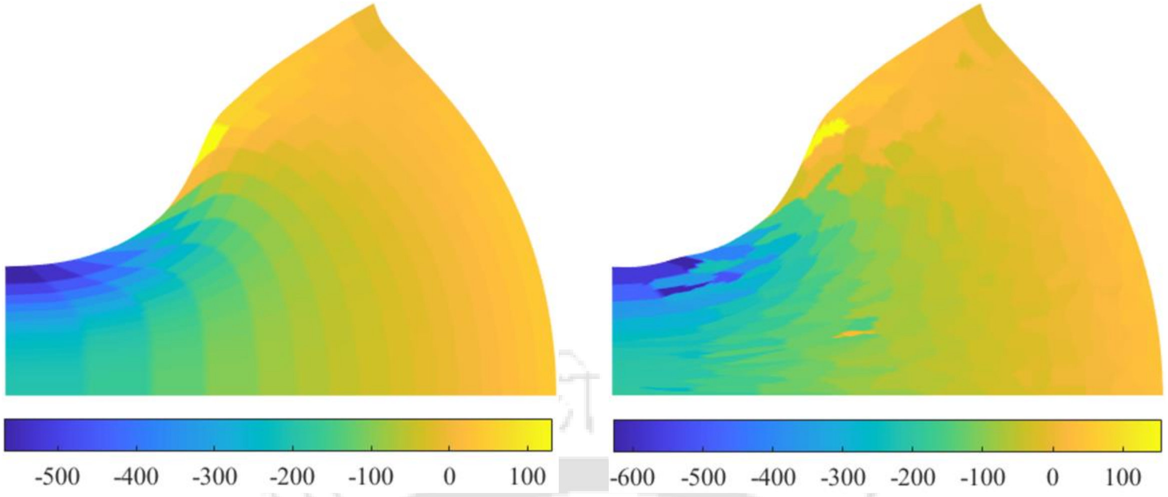

(c) (d)

Fig. 9.7. Plane strain block with 16×16 displacement nodal divisions distributed with **(a)** regular, and **(b)** irregular pressures and their corresponding pressure contour plots at $p/p_0 = 60$ in **(c)** and **(d)**

Fig. 9.7(c) and 9.7(d) display pressure contour plots for both regular and irregular distribution cases at $p/p_0 = 60$. It can be observed that the various pressure magnitudes across the geometry in both cases are identical. However, in the irregular case, the maximum pressure is slightly greater than that in the regular one. This difference arises from the presence of two adjacent pressure nodes near the top edge from the left side of the block (represented with circles in Fig. 9.7(b)). It is noted that one of the two immediate p-nodes has fewer nearest u-nodes, leading to localized intensity and consequently higher pressure magnitudes at that specific location (see Fig. 9.7(d)). However, the neighbouring regions around this location exhibit a uniform distribution of pressure. This observation aligns with the earlier discussion in the guidelines section. In this case study, as the intensity is not significant, the results remain unaffected. However, if there are more than two immediate p-nodes or if they are repeated at various locations near the top edge of the block, it would have substantially affected and compromised the performance of the present methodology. Hence, immediate pressure nodes are avoided near-critical regions, while locations far away from critical regions can accommodate them, given that the pressure intensity is insignificant, as shown in Fig. 9.7(d).

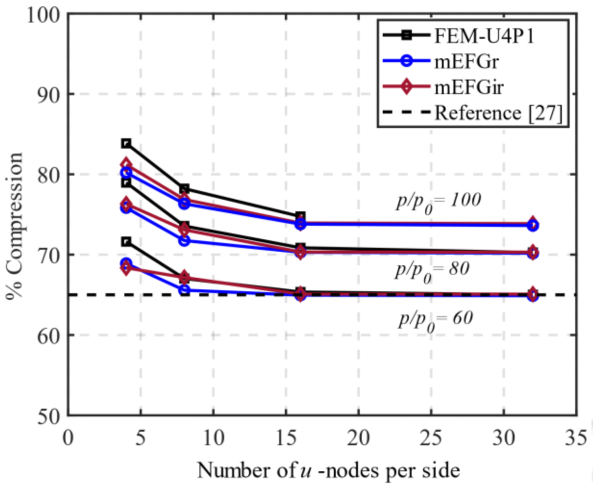

Fig. 9.8. Compression level of plane strain block at different load states using mixed EFGM and FEM

Fig. 9.8 shows the percentage compression at point A for load states (p/p_0) 60, 80, and 100. It is evident that the results obtained through the mixed EFGM, considering both regular and irregular pressure distribution, exhibit convergence with 16×16 nodal divisions and consistently maintain this convergence across all loading conditions. These plots also indicate that the results obtained at $p/p_0 = 60$ align well with the reference solution [297]. On the other hand, the mixed FEM (U4P1) formulation gradually loses its ability to achieve convergence as the p/p_0 increases, and it fails to produce results at $p/p_0 = 100$ for a 32×32 mesh. This is due to the gradual increase of the mesh distortion effect with the increase in load states. In the present case study, 20 load steps are considered for all values of p/p_0. Nevertheless, the 32×32 FE mesh is capable of producing results for $p/p_0 = 100$ when the load steps are increased substantially.

Table 9.1. Number of iterations at 20th load step by FEM-U4P1 at various load states

FEM-U4P1 (Elements)	$\boldsymbol{p/p_0 = 60}$	$\boldsymbol{p/p_0 = 80}$	$\boldsymbol{p/p_0 = 100}$
4 × 4	288	343	387
8 × 8	318	407	510
16 × 16	356	440	530
32 × 32	385	487	-

Furthermore, it is observed that although FEM-U4P1 successfully achieves convergence for $p/p_0 = 60$ and 80, it does so at the expense of a higher number of iterations, as depicted in Table 4.2. However, it is worth noting that the mEFGir formulation attains better convergence with a constraint of $<= 30$ iterations per load step. Therefore, employing mixed formulations in the EFG framework with irregular or regular pressure nodes yields stable and accurate results, requiring fewer load steps and iterations. Based on the numerical results, it has been observed that mEFGr would definitely give superior results. Nevertheless, the performance of mEFGir is close to mEFGr, which has flexibility in distributing pressure nodes. In order to demonstrate the advantage of mEFGir formulation the subsequent case studies are solved using irregular pressure distribution. The deformed geometries and pressure contour plots for 32×32 nodal divisions at $p/p_0 = 60, 80,$ and 100 are presented in Fig. 9.9.

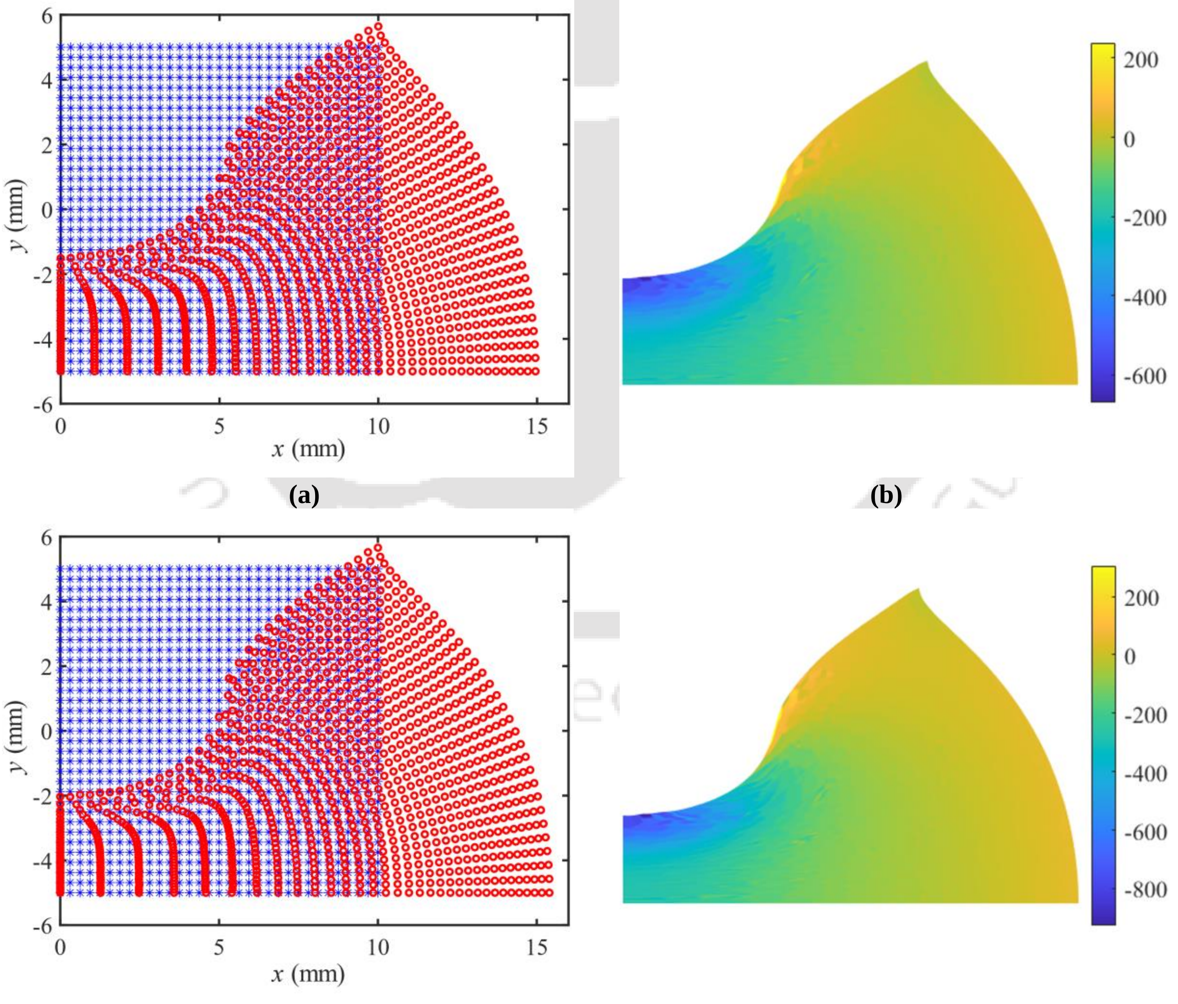

(a) **(b)**

(c) **(d)**

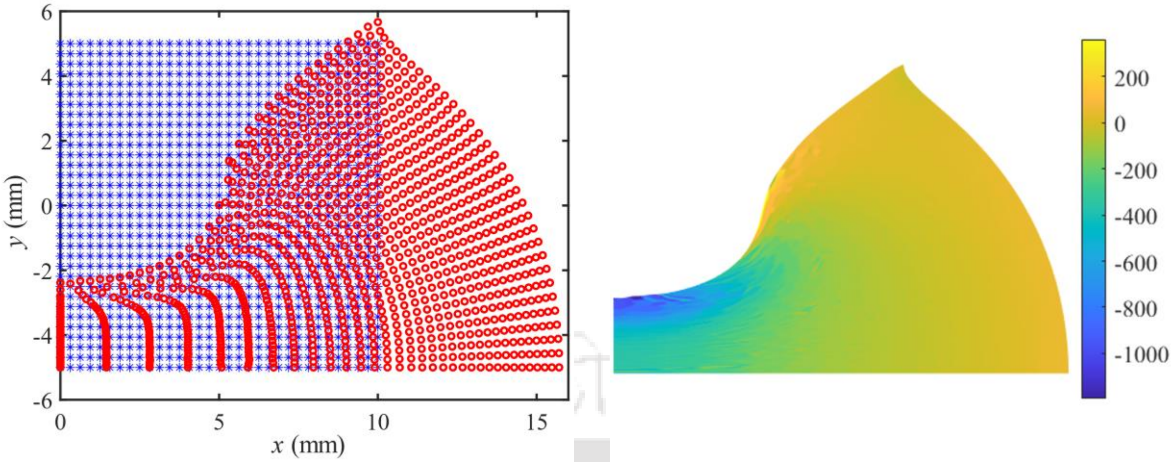

(e) **(f)**

Fig. 9.9. Partial compression of a plane strain block: deformed geometries (**(a)**, **(c)**, and **(e)**), and pressure contour plots (**(b)**, **(d)**, and **(f)**) using mEFGir for 32 × 32 nodal divisions for $p/p_0 = 60, 80$, and 100

9.5.3 Compression of a plate – Contact problem

The next example is just an extension to the previous problem with changes in boundary and loading conditions to address the severe mesh distortion issues. In this study, a plate resting on the ground undergoes 60% compression, i.e. $u_y = 6$ mm applied from its top edge. The boundary and loading conditions of the geometry are shown in Fig. 9.10. The nearly incompressible Neo-Hookean model is employed with the same constants as those used in the previous problem.

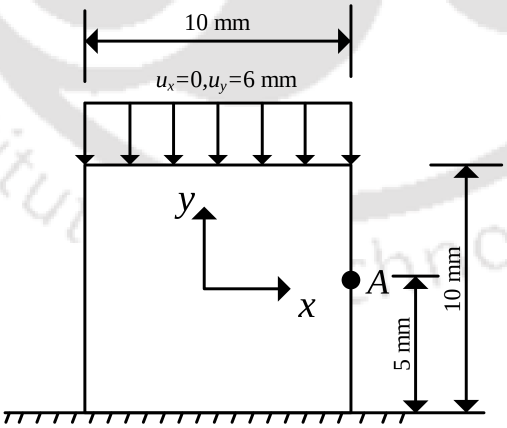

Fig. 9.10. Compression of a plate: geometry, boundary and loading conditions

During the compression of the geometry, the material in the plate attempts to bulge out from both vertical free sides, and some portions of it come into contact with the ground. This phenomenon is numerically simulated using both the FEM-U4P1 (with meshes of 10, 20, and 40 elements per side) and mEFGir formulations (employing the same nodal discretizations identical to FEM) involving contact formulations. The numerical analysis is conducted for 20 increments, limiting each load step to 40 iterations with a tolerance of 10^{-4}.

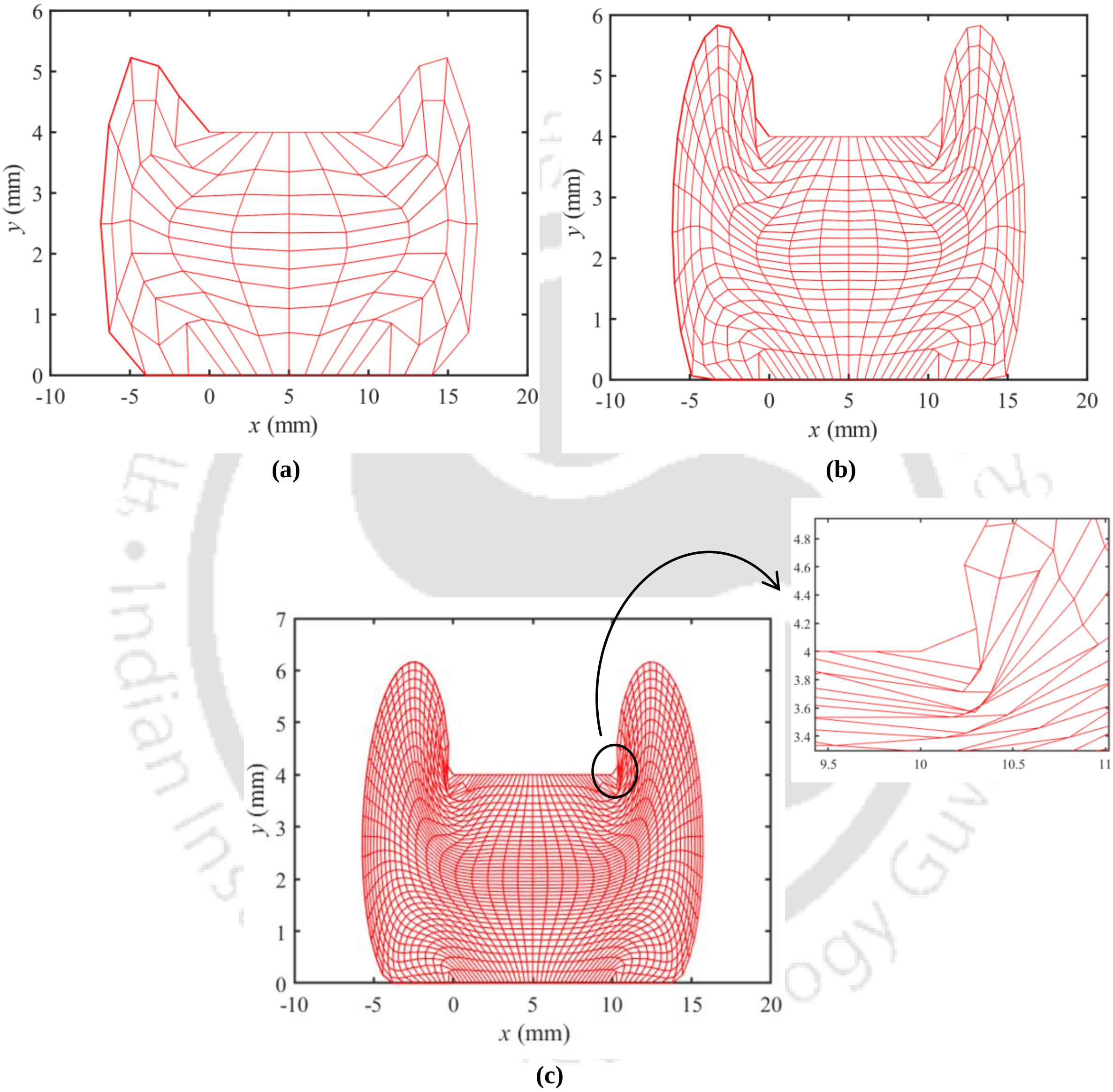

Fig. 9.11. Compression of a plate: deformed geometries of **(a)** 10×10, **(b)** 20×20, and **(c)** 40×40 meshes

Fig. 9.11(a)-9.11(c) visually present the deformed shapes of a plate for various FE meshes after undergoing a vertical compression of 6 mm. It is noted that there is an increase in the vertical expansion of the lateral sides with an increase in the number of elements. It is also observed that elements at the sharp corners near the top edge are interpenetrating in the case of the 40 × 40 mesh, rendering the results no longer reliable.

Table 9.2. Displacements at point *A* of a compressed plate for various meshes and nodal divisions

Elements/ nodal divisions	**FEM-U4P1**		**mEFGir**	
	u_x **(mm)**	u_y **(mm)**	u_x **(mm)**	u_y **(mm)**
10 × 10	6.836	-2.508	6.077	-1.409
20 × 20	6.029	-1.769	5.553	-1.282
40 × 40	5.579	-1.398	5.218	-1.126

Table 9.2 presents the displacements in both directions at point *A* (refer to Fig. 9.10) for a total compression of 6 mm from the top edge for various meshes and nodal divisions. It is observed that refining the mesh or nodal divisions results in an increase in displacements in the *y*-direction and a decrease in displacements in the *x*-direction. However, mEFGir exhibits superior convergence in displacements over FEM-U4P1 by avoiding severe mesh distortion problems. The undeformed and deformed geometries of the plate under compression for different nodal divisions are shown in Fig. 9.12(a)- 9.12 (c).

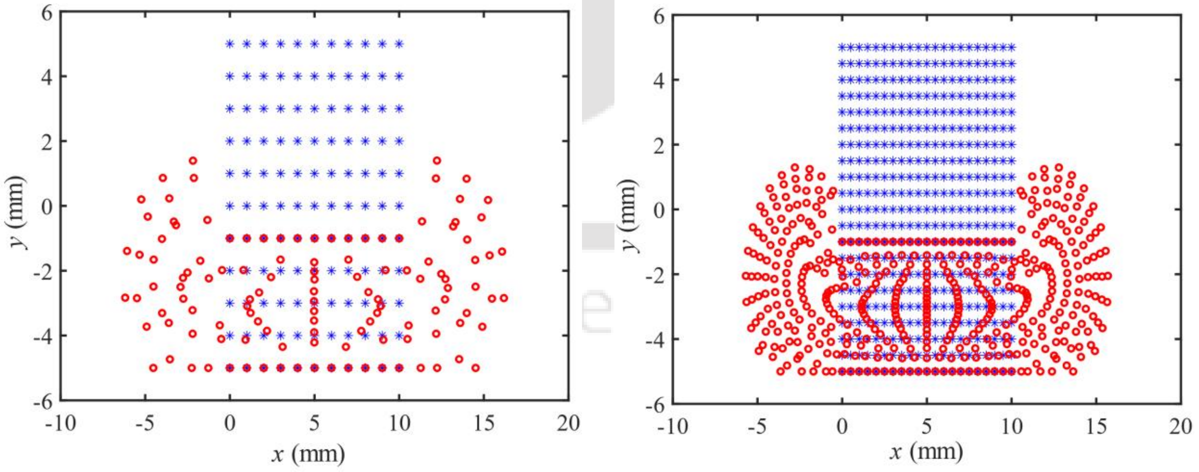

(a)

(b)

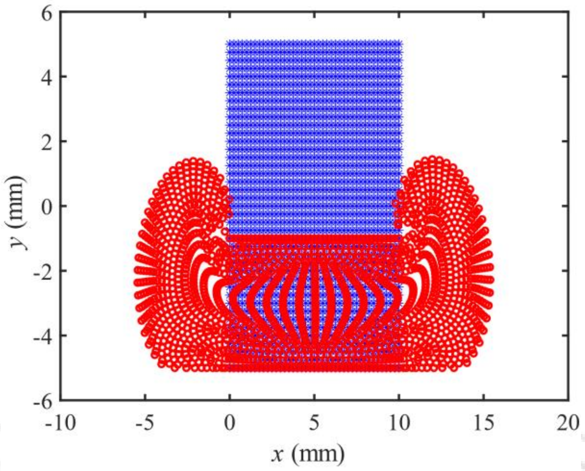

(c)

Fig. 9.12. Compression of a plate: deformed geometries of (a) 10 × 10, (b) 20 × 20, and (c) 40 × 40 nodal divisions using mEFGir

9.5.4 Infinite plate with a hole

The problem entails a two-dimensional infinite plate with a circular hole subjected to constant uniaxial in-plane tension [292]. Due to the symmetry of the problem, only a quarter portion of the plate is taken into consideration. The geometry, boundary and loading conditions are shown in Fig. 9.13(b), featuring symmetric boundary conditions on the edges with roller supports. This example is employed to investigate the variation of Cauchy stress (σ_{xx}) attributable to stress concentration at point *A*, influenced by the stretching in the plate.

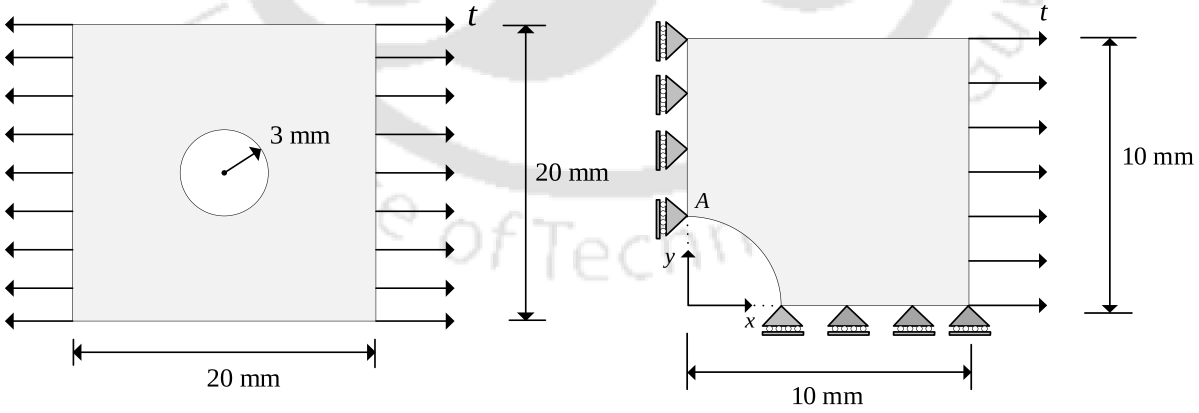

(a) **(b)**

Fig. 9.13. Infinite plate with hole subjected to uniaxial tension **(a)** Overall geometry, and **(b)** Quarter section

The Mooney-Rivlin material model is used here with the nearly incompressibility case. The material properties considered are $C_{10} = 25\,\text{MPa}$, $C_{01} = 7\,\text{MPa}$ and $D_1 = 6.25 \times 10^{-6}\text{MPa}^{-1}$ and a traction of $t = 100\ \text{N/mm}$ is applied. Initially, the problem is solved using FE-ABAQUS® with a hybrid formulation for a Q4 element [196], employing two sequences of meshes: 8×8 and 16×16. The simulation has been conducted for 10 load steps, and the stresses at point *A* are collected for each load step.

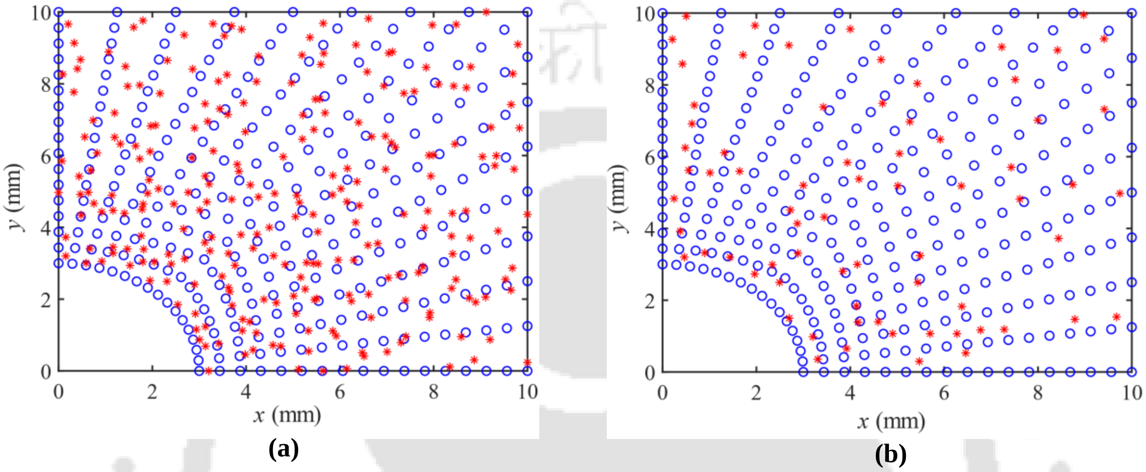

Fig. 9.14. Infinite plate with hole: irregular pressure distribution for 16×16 nodal divisions **(a)** 16×16, and **(b)** 71 pressure nodes

Fig. 9.14(a) and 9.14(b) shows the 16×16 displacement nodal divisions irregularly distributed with 16×16 and 71 pressure nodes, respectively. They are labeled as mEFgir-256 and mEFgir-71 to represent the results during stress analysis. The Cauchy stress (σ_{xx}) computed for each load step using the mEFGir formulation is compared with FE-ABAQUS® results, demonstrating good agreement, as illustrated in Fig. 9.15. It is observed that refining the mesh or nodal divisions results in a significant change in stresses at point *A* compared to the displacements.

Moreover, to demonstrate the flexibility of mEFGir formulation, the numerical analysis is also carried out by distributing the 71 irregular pressure nodes over 16×16 nodal divisions (see Fig. 9.15(b)). Adhering to the guidelines discussed, the pressure distribution process is carefully managed, ensuring that the support domain of each Gauss point in the background has at least one pressure node within it. It is observed that the results obtained using mEFGir-71 are well-aligned with those of mEFGir-256 *p*-nodes, showing a slight over-prediction in σ_{xx} with a 1.36% error.

Fig. 9.16 shows the contour plots of Cauchy stress in x-direction for mEFGr, mEFGir-256, and mEFGir-71 formulations with 16×16 nodal divisions.

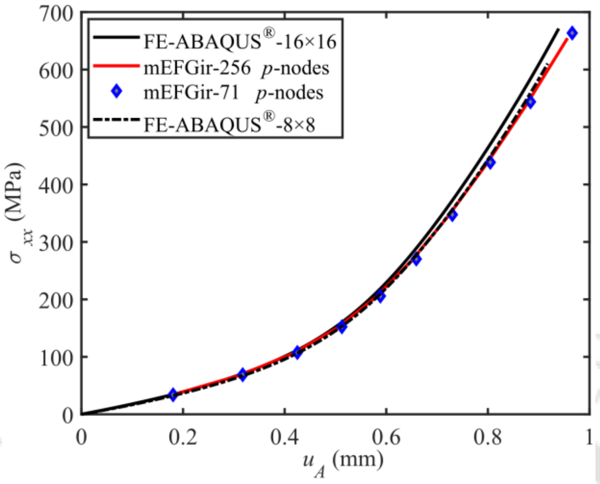

Fig. 9.15. σ_{xx} at point *A*: comparison between mEFGir and FE-ABAQUS® results

To ascertain the optimal number of pressure nodes for the given displacement degrees of freedom, the inf-sup stability condition must be satisfied. In FEM, each pressure node only influences the known finite region, i.e., the element, which remains constant throughout the geometry. Nevertheless, the present methodology offers flexibility by irregularly distributing pressure nodes, where each pressure node can influence several displacement degrees of freedom. This leads to a varying influence region throughout the geometry. So, the present work does not provide a basis to prescribe the ratio of the number of pressure nodes to the number of displacement nodes. However, it is observed that a decent number of irregularly distributed pressure nodes still yield accurate results.

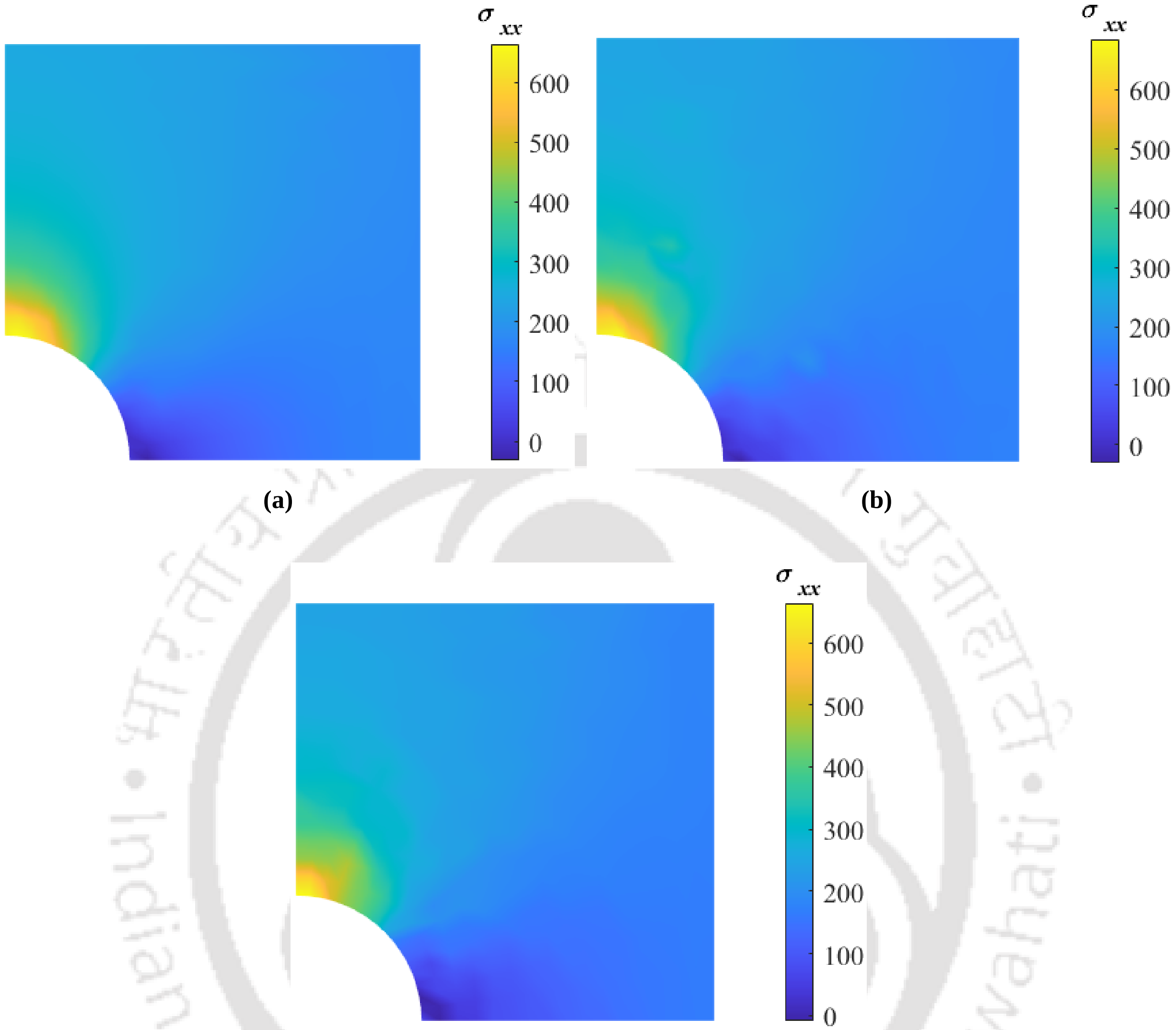

(a) (b)

(c)

Fig. 9.16. Stress (σ_{xx}) contour plots for 16 × 16 nodal divisions: **(a)** mEFGr, **(b)** mEFGir-256, and **(c)** mEFGir-71 formulations

9.6 Summary

In this chapter, a mixed displacement-pressure formulation is proposed in the EFG framework to alleviate volumetric locking in hyperelastic materials. The variational formulations and the linearization procedures are carried out considering the undeformed geometry as the frame of reference. Two mixed formulation approaches involving regular (mEFGr) and irregular (mEFGir) pressure node distributions have been used to solve different kinds of problems using the Neo-Hookean and Mooney-Rivlin models. Cook's membrane study indicates that there is a negligible difference in the results between mEFGr and mEFGir, though both of them show better convergence to the popular FEM-U4P1.

Though the mEFGir offers flexibility in pressure node distribution, the influence region of a pressure node could spread over a lot of displacement nodes. Specific guidelines are provided for distributing the pressure nodes arbitrarily in a regular displacement nodal distribution. In the case of plane strain compression of the block, the FEM did not provide results for higher pressures ($p/p_0 = 100$). This is attributed to increasing mesh distortion with increasing pressures, which is overcome in EFG method with a relatively smaller number of load steps and iterations. It is interesting to note for the plate with a hole subjected to tension, the Cauchy stress contour plot is almost the same for mEFGir-256 and mEFGir-71. This shows that the pressure nodal density can be comparatively less than the displacement nodal density. Nevertheless, the minimal ratio of pressure to displacement degrees of freedom for accurate results cannot be estimated for irregular pressure node distribution as the influence region of each pressure node can be arbitrary.

Chapter 10

Conclusions and Scope for Future Work

This chapter summarizes the key findings and conclusions derived from the work conducted to address each objective outlined in Section 1.4, subsequently presenting conclusions based on the contributions and outcomes derived from it. Finally, the chapter provides an outlook on various potential directions for future research, followed by a list of publications derived from the current work.

10.1 Damage modelling in adhesive bonded joints using nonlocal FEM

This work highlights the application of nonlocal integral theories in capturing the failure behaviour of adhesively bonded joints. While conventional FEM adeptly addresses regular benchmark problems and predicts their failure behaviour, there remains an untapped potential in exploring specific case studies that could enhance the performance of adhesive bonded joints. One such case study is the biadhesive single-lap joint, which mitigates stress concentrations by utilizing low modulus adhesive at the ends of the overlap and structural adhesive in the middle of the geometry. Numerical analysis to predict their failure behaviour is conducted using continuum damage models proposed by Chousal and de Moura [141] within a nonlocal FEM framework. Furthermore, the present work addresses the performance of joints with significant defects, such as cohesive cracks. The total strain is employed as the nonlocal variable, and ensuring thermodynamic consistency for successful derivation of a nonlocal constitutive law is achieved. Utilizing this proposed constitutive law, the construction and efficient implementation of the tangent stiffness matrix, crucial for capturing the material nonlinear behaviour of multimaterial systems, are demonstrated. Through the discussion and conclusions, the following points are highlighted:

1. Due to the specimen geometries, a large number of elements are required to ensure accurate response. However, a higher number of elements also results in increased computational time. To mitigate this issue and effectively utilize the proposed constitutive law, the tangent stiffness is computed for every iteration only in the adhesive and adhered regions influenced by them. The stiffness of the rest of the geometry remains constant throughout as they remain in the linear elastic regime.

2. Firstly, the numerical implementation procedure is validated by selecting a benchmark problem in mode I case. It is demonstrated that the nonlocal FEM yields the same response as that of the standard FEM, while also offering mesh-independent results. Moreover, the numerical procedure is extended to solve the mode I problem with a sharp crack, a scenario where FEM exhibits high mesh sensitivity and unreliable results. In contrast, the nonlocal approach circumvents these issues, yielding mesh-independent results with minimal variation in peak loads across all employed meshes.
3. Moreover, the failure behaviour of biadhesive single-lap joints is analyzed, revealing that FEM encounters severe iterative convergence issues for medium to fine mesh sizes and prematurely aborts the analysis. In contrast, the nonlocal approach, characterized by its inherent continuity even at sudden material changes, successfully completes the simulation for all meshes with minor variations in peak loads.

10.2 Damage modelling in quasi-brittle materials using strain difference-based nonlocal approach

Though from a physical perspective, it is reasonable to consider strain as a nonlocal variable due to its significant role in deformation processes, it still fails to accurately predict the structural response. Consequently, many research endeavors have shifted focus towards other internal variables responsible for damage, rather than relying solely on strain. Motivated to enhance the performance, a strain difference-based nonlocal constitutive model is employed within CDM framework to predict the structural response of quasi-brittle materials. The formulation of the model operates within the framework of thermodynamics, leveraging the second principle to impose constraints on the constitutive relations. The presented formulations, results, and discussions lead to the following conclusions.

1. The presented model's effectiveness is demonstrated through mesh-independent results via % error prediction of peak load with respect to converged/reference results and force-displacement responses, accurate prediction of damage propagation paths for 2D and 3D case studies involving a crack and a hole. A comparison of peak load numerical results with reference data for a coarse mesh indicated that % error is within 3%.

2. Another feature of the proposed methodology is the usage of strain difference as the regularization variable for damage propagation studies, which preserves the symmetricity of the nonlocal stiffness matrix. This is valuable in strain-softening problems where incremental-iterative techniques are employed until specimen failure.

3. The effect of nonlocal parameter α on the damage distribution while capturing the post-peak behaviours is studied. It is worth noting that the softening response exhibits better convergence with increasing α. However, due to the accumulation of damage in a large area, the post-peak behaviour is affected for values 50 and 100. Therefore, $\alpha = 10$ is chosen, which ensures balanced nonlocal effects — damage localization and damage process zones, and yields a softening response consistent with the reference results.

10.3 Ductile damage modelling in nonlocal FEM framework

Extending the work to ductile materials, a novel ductile damage dissipation potential is introduced, which accounts for isotropic hardening and scalar damage effects, providing a simplified analytical expression for parameter determination. Additionally, a nonlocal equivalent plastic strain is integrated with the proposed damage model to address the challenges associated with strain localization. The forward Euler explicit numerical integration scheme is employed for computing stress updates, plastic strain evolution, and other internal variables. This method is selected due to its ease of implementation and facilitates the explicit regularization procedure during post-processing. Following are some of the discussions and conclusions:

1. To reduce the influence of stress triaxiality on determining the damage parameters, a customized hour-glass round (HGR) specimen with a minimum cross-section at its central portion is designed and fabricated. This design is based on the adaptability of the tensile testing machine and the available extensometer range.

2. A closed-form expression is established to correlate damage with plastic strain. Critical and threshold plastic strains are directly inferred from the stress-strain response, under certain assumptions. Subsequently, parameters s and D_{cr} are determined through curve fitting, chosen for its simplicity over inverse analysis, though efficient yet tends to entail a more intricate parameter identification process.

3. To assess the versatility of the proposed damage evolution law, materials with diverse damage behaviours such as SS316L, Al2024, and copper alloy are selected. The damage model effectively predicts all three damage patterns, aligning well with the physical characteristics of the materials.

4. During loading, the tensile specimens undergo necking, resulting in strain localization. This phenomenon poses challenges for FEM, including convergence issues and strain discontinuity. Therefore, nonlocal equivalent plastic strain, known for its influence on damage evolution, is employed. Mesh convergence is validated using 100, 200, and 400 elements, demonstrating the continuous nature of strains. Additionally, numerical stress-strain responses of various materials are compared with tensile test data, showing good agreement.

10.4 Damage modelling using CZM approach in EFG framework

A modified EFG method involving diffraction technique, Heaviside and level-set functions is used to simulate mode I (DCB) and mode II (ENF) crack propagation problems. The level-set enrichment via a partition-of-unity scheme is particularly suitable to account for material interfaces without the need to alter the existing nodal distribution. The nonlinear nature of the problem arising due to damage evolution modelled by an exponential traction separation law (TSL) is solved by the generalized displacement control method (GDCM). This involves the determination of the tangent stiffness matrix at each iteration, which is conveniently established by considering the nodes that are enriched with the Heaviside function or whose weight function is modified by the diffraction technique. The following are the specific conclusions:

1. Based on the parametric studies of the GDCM, it is observed that the initial control factor ($\Delta\gamma_1^1$) can be chosen flexibly at a reference load value (ΔF) of 0.1 times the peak load. Alternatively, one can choose a lesser value of ΔF ($\leq$ 0.1 times the peak load) at $\Delta\gamma_1^1 = 1$ to obtain the converged solution.

2. For the mode I (DCB) problem, 80 background integration cells for the cohesive zone are required to get the converged results, but almost twice the number of cohesive elements are required in the case of FEM.

3. In the case of the mode II crack propagation problem (ENF), the performance of GDCM is twice as fast as the Newton-Raphson (NR) technique for different values of exponential TSL parameter α.

4. As α increases, the NR technique poses a challenge in capturing the snapback phenomenon, especially at $\alpha = 11$. The GDCM, on the other hand with the aid of incremental load parameter ($\Delta\gamma_j^i$), which adjusts automatically for every iteration based on the displacements, offers ease of handling the unstable nature in the solution arising due to crack propagation.

10.5 Alleviating locking using mixed formulations in EFG framework

A mixed displacement-pressure formulation is proposed in the EFG framework to alleviate volumetric locking in hyperelastic materials. The variational formulations and the linearization procedures are carried out considering the undeformed geometry as the frame of reference. Two mixed formulation approaches involving regular (mEFGr) and irregular (mEFGir) pressure node distributions have been used to solve different kinds of problems using the Neo-Hookean and Mooney-Rivlin models. The following are the specific conclusions:

1. Cook's membrane study indicates that there is a negligible difference in the results between mEFGr and mEFGir, though both of them show better convergence to the popular FEM-U4P1. Though the mEFGir offers flexibility in pressure node distribution, the influence region of a pressure node could spread over a lot of displacement nodes. Specific guidelines are provided for distributing the pressure nodes arbitrarily in a regular displacement nodal distribution.

2. In the case of plane strain compression of the block, the FEM did not provide results for higher pressures ($p/p_0 = 100$). This is attributed to increasing mesh distortion with increasing pressures, which is overcome in EFG method with a relatively smaller number of load steps and iterations.

3. It is interesting to note for the plate with a hole subjected to tension, the Cauchy stress contour plot is almost the same for mEFGir-256 and mEFGir-71. This shows that the pressure nodal density can be comparatively less than the displacement nodal density. Nevertheless, the minimal ratio of pressure to displacement degrees of freedom for accurate

results cannot be estimated for irregular pressure node distribution as the influence region of each pressure node can be arbitrary.

10.6 Summary of contributions of the thesis

The performance of the nonlocal integral approach is evaluated to address the challenges encountered by conventional FEM when dealing with complex case studies in adhesively bonded joints. The nonlocal constitutive law effectively addresses issues such as sharp cracks in adhesives and biadhesives-based joints by allowing simulations to run continuously until failure without abrupt interruptions. Additionally, it produces mesh-independent results, enhancing its reliability and applicability in various scenarios. Further, strain difference-based nonlocal model is employed to predict failure behaviour and damage propagation in quasi-brittle materials within the thermodynamic framework of CDM theories. The proposed constitutive law overcomes the accuracy issues encountered by nonlocal strain formulations. It demonstrates its effectiveness through reduced % error prediction of peak load with respect to converged/reference responses and accurate prediction of damage propagation paths for 2D and 3D case studies involving a crack and a hole. Extending the work to ductile materials, a nonlocal equivalent plastic strain is integrated with the proposed damage evolution law to address the challenges associated with strain localization. The nonlocal damage model demonstrates its adaptability in predicting damage across various types of ductile materials and addresses convergence and strain discontinuity issues.

Additionally, strong discontinuity studies are presented through the work which uses the modified EFG method that combines the Heaviside enrichment and diffraction method to study crack propagation problems by employing a CZM. The nonlinear nature of the problem arising due to damage evolution modelled by an exponential traction separation law (TSL) is solved by the GDCM. Subsequently, the strain localization due to the weak discontinuities are studied by employing a nonlocal integral approach on the CDM models by regularizing the equivalent strain to overcome the convergence issues in the EFG method. The proposed methodology has been applied to model the elastic damage in a one-dimensional problem. Finally, a mixed displacement-pressure formulation is proposed in the EFG framework to alleviate volumetric locking in hyperelastic materials. Taking advantage of the meshless nature of the EFG method, this work introduces a unique approach by randomly distributing pressure nodes across the geometry, following specific guidelines. FEM is attributed to increasing mesh distortion with increasing pressures, which is overcome in EFG method with a relatively smaller number of load steps and iterations.

10.7 Scope for future work

In the present section, various potential extensions and opportunities for the develop ment of the current research are discussed.

- The successful implementation of nonlocal integral approaches has demonstrated their effectiveness in addressing complex problems concerning adhesive bonded joints. Given that the majority of failure analysis related to defects are focused on adhesive bonded joints in composite materials, there's a clear rationale for extending nonlocal theories to investigate failure mechanisms in these joints within diverse orthotropic/anisotropic materials, which are frequently encountered in real-world scenarios.
- In the current study, we have employed a strain difference-based nonlocal approach, particularly suited for monomaterial geometries, providing the flexibility to utilize a secant stiffness matrix. However, when dealing with case studies involving multimaterial systems, the utilization of a tangent stiffness matrix becomes imperative. It has been noted that deriving the tangent stiffness matrix for the proposed nonlocal constitutive law presents significant mathematical complexity. Therefore, developing a simplified procedure to implement the tangent stiffness matrix while preserving symmetry would be an interesting work. This endeavour could streamline the computational process and enhance the applicability of the nonlocal constitutive law to a broader range of materials and geometries.
- The proposed ductile damage evolution model has demonstrated its effectiveness in accurately predicting the damage behaviour of various ductile materials and their mechanical response under constant stress triaxialities. By extending its applicability to diverse 2D and 3D case studies, the model can incorporate stress triaxiality and lode angle parameters to assess its performance across a wide range of triaxiality ratios.
- The exploration of strain localization issues in hyperelastic materials using nonlocal integral theories remains relatively limited, with few studies addressing this aspect comprehensively. Addressing strain localization in hyperelastic materials poses unique

challenges, including the presence of volumetric and shear locking phenomena, which complicate the modelling process. Implementing this study within both FEM and EFG frameworks presents both a challenge and an opportunity, offering an engaging investigation into the intricate nature of strain localization in hyperelastic materials.

List of publications

Journals

1. S. S. Kumar and N. Muthu, “Generalized displacement control technique for mode I/II fracture problems using cohesive zone model within a modified element-free Galerkin framework,” *Fatigue & Fracture of Engineering Materials & Structures*, vol. 46, no. 11, pp. 4119–4141, Nov. 2023, doi: 10.1111/FFE.14118.
2. S. S. Kumar and N. Muthu, “A thermodynamically consistent strain difference-based nonlocal damage mechanics approach for failure analysis of quasi-brittle materials”, *Theoretical and Applied Fracture Mechanics*, 131, 104351.
3. S. S. Kumar, A. Shaji, and N. Muthu, “A two-field mixed formulation with scattered pressure node distribution in element-free Galerkin method for alleviating volumetric locking in hyperelastic materials”, *Acta Mechanica Sinica*, vol. 41, p. 424446, Jan. 2025, doi. 10.1007/s10409-024-24446-x. (available online from January, 2025)
4. S. S. Kumar and N. Muthu, “A novel nonlinear ductile damage evolution law based on continuum damage mechanics approach”. **(Under preparation)**
5. S. S. Kumar, and N. Muthu, “Nonlocal approach for failure analysis of adhesively bonded joints with defects and bi-adhesive based single lap joints”. **(Under preparation)**

Book chapters

1. S. S. Kumar, A. Orepalli, and N. Muthu, “Hyperelastic Analysis of Adventitial Layer Using Isotropic Gent Model,” *Healthcare Research and Related Technologies*, pp. 405–417, 2023, doi: 10.1007/978-981-99-4056-1_28/COVER.

Conferences

1. Sai Kumar, S., Ashok, O., & Muthu, N., “Hyperelastic analysis of adventitial layer using isotropic Gent model”, North East Research Conclave, IIT Guwahati, May 20-22, 2022.
2. S. S. Kumar, and N. Muthu, “Application of damage model based on nonlocal equivalent strain in the element-free Galerkin method”, 12th International Conference on Structural Integrity and Failure SIF 2021, Monash University, Australia, 06 – 07 December, 2021.
3. S. S. Kumar, and N. Muthu, “Finite element implementation of elastic-plastic large deformation analysis for small strain problems”, 65th congress of the Indian Society of Theoretical and Applied Mechanics December 9-11,2020.
4. S. S. Kumar, and N. Muthu, “Modelling of damage behaviour in 1D composite bar using a novel continuum damage theory”, The proceedings of the International Conference and Exhibition on Reinforced Plastics, January 9-12, 2019.

Appendices

Appendix A.

Linear system of equations in modified EFG framework

To capture the nonlinear softening behaviour of both the cohesive zone and the specimen, displacement loading, i.e., Dirichlet boundary conditions, is prescribed instead of external forces on the Γ_F. Therefore, Eq. (7.5) can be rewritten as,

$$\int_{\Omega} \delta(\mathbf{L}_d\mathbf{u})^{\mathrm{T}}\mathbf{C}(\mathbf{L}_d\mathbf{u})\,\mathrm{d}\Omega - \int_{\Gamma_u} \delta\lambda^{\mathrm{T}}(\mathbf{u}-\mathbf{u}_{\Gamma})\mathrm{d}\Gamma - \int_{\Gamma_u} \delta\mathbf{u}^{\mathrm{T}}\lambda\,\mathrm{d}\Gamma = \int_{\Gamma_{coh}} \delta\mathbf{w}^{\mathrm{T}}\mathbf{t}\,\mathrm{d}\Gamma \qquad \text{(A.1)}$$

where,

$$\mathbf{L}_d\mathbf{u} = \mathbf{L}_d\left[\sum_{I\in S_N}\mathbf{\Phi}_I(\mathbf{x})\mathbf{u}_I + \sum_{I\in S_H}\mathbf{\Phi}_I(\mathbf{x})\{\mathbf{a}_I\mathrm{H}(f(\mathbf{x}))\} + \sum_{I\in S_L}\mathbf{\Phi}_I(\mathbf{x})\mathbf{c}_I\chi_I(\mathbf{x})\right] \qquad \text{(A.2)}$$

$$\mathbf{B}_I^N = \mathbf{L}_d\mathbf{\Phi}_I = \begin{bmatrix}\Phi_{I,x} & 0\\ 0 & \Phi_{I,y}\\ \Phi_{I,y} & \Phi_{I,x}\end{bmatrix} \qquad \forall I\in S_N$$

$$\mathbf{B}_I^H = \mathbf{L}_d\mathbf{\Phi}_I\mathrm{H}(\mathrm{f}(\mathbf{x})) = \begin{bmatrix}(\Phi_I\mathrm{H})_{,x} & 0\\ 0 & (\Phi_I\mathrm{H})_{,y}\\ (\Phi_I\mathrm{H})_{,y} & (\Phi_I\mathrm{H})_{,x}\end{bmatrix} \qquad \forall\, I\in S_H$$

$$\mathbf{B}_I^L = \mathbf{L}_d\mathbf{\Phi}_I\chi_I = \begin{bmatrix}(\Phi_I\chi_I)_{,x} & 0\\ 0 & (\Phi_I\chi_I)_{,y}\\ (\Phi_I\chi_I)_{,y} & (\Phi_I\chi_I)_{,x}\end{bmatrix} \qquad \forall\, I\in S_L$$

Now,

$$\mathbf{B}_I = [\mathbf{B}_I^N \quad \mathbf{B}_I^H \quad \mathbf{B}_I^L] \qquad \forall\, I\in S_N, I\in S_H, I\in S_L \qquad \text{(A.3)}$$

Using Eq. (A.2) and (A.3) in the first part of Eq. (A.1), gives

$$\int_{\Omega}\delta\left(\sum_{\substack{I\in S_N,\\ I\in S_H,\\ I\in S_L}}\mathbf{B}_I\,\mathbf{U}_I\right)^{\mathrm{T}}\mathbf{C}\left(\sum_{\substack{J\in S_N,\\ J\in S_H,\\ J\in S_L}}\mathbf{B}_J\mathbf{U}_J\right)\mathrm{d}\Omega = \delta\mathbf{U}^{\mathrm{T}}\mathbf{K}\mathbf{U} \qquad \text{(A.4)}$$

where,

$$\mathbf{U}_I = \begin{Bmatrix} \mathbf{u}_I \\ \mathbf{a}_I \\ \mathbf{c}_\mathrm{I} \end{Bmatrix}, \quad \text{and } \mathbf{K} = \begin{bmatrix} \mathbf{K}_{IJ}^{NN} \mathbf{K}_{IJ}^{NH} \mathbf{K}_{IJ}^{NL} \\ \mathbf{K}_{IJ}^{HN} \mathbf{K}_{IJ}^{HH} \mathbf{K}_{IJ}^{HL} \\ \mathbf{K}_{IJ}^{LN}\, \mathbf{K}_{IJ}^{LH}\, \mathbf{K}_{IJ}^{LL} \end{bmatrix} \tag{A.5}$$

Let us examine the second term in the LHS of the Eq. (A.1),

$$\begin{aligned}
&\int_{\Gamma_u} \delta\lambda^\mathrm{T}(\mathbf{u} - \mathbf{u}_\Gamma)\mathrm{d}\Gamma \\
&\quad = \int_{\Gamma_u} \delta\left(\sum_{I \in S_\lambda} \mathbf{N}_I \lambda_I\right)^\mathrm{T} \left[\sum_{I \in S_N} \boldsymbol{\Phi}_I(\mathbf{x})\mathbf{u}_I + \sum_{I \in S_H} \boldsymbol{\Phi}_I(\mathbf{x})\{\mathbf{a}_I \mathrm{H}(f(\mathbf{x}))\}\right. \\
&\quad \left. + \sum_{I \in S_L} \boldsymbol{\Phi}_I(\mathbf{x})\mathbf{c}_I \chi_I(\mathbf{x})\right] \mathrm{d}\Gamma - \int_{\Gamma_u} \delta\left(\sum_{I \in S_\lambda} \mathbf{N}_I \lambda_I\right)^\mathrm{T} \mathbf{u}_\Gamma \mathrm{d}\Gamma \\
&\quad = \sum_{I \in S_\lambda} \sum_{\substack{J \in S_N, \\ J \in S_H, \\ J \in S_L}} \delta\, \lambda_I^\mathrm{T} \underbrace{\left[\int_{\Gamma_u} \mathbf{N}_I^\mathrm{T} \boldsymbol{\Phi}_J \mathrm{d}\Gamma \quad \int_{\Gamma_u} \mathbf{N}_I^\mathrm{T} \boldsymbol{\Phi}_J \mathrm{H}(f(\mathbf{x}))\mathrm{d}\Gamma \quad \int_{\Gamma_u} \mathbf{N}_I^\mathrm{T} \boldsymbol{\Phi}_J \chi_I \mathrm{d}\Gamma\right]}_{-\boldsymbol{G}_{IJ}} \mathbf{U}_J \\
&\quad - \sum_{I \in S_\lambda} \delta\lambda_I^\mathrm{T} \underbrace{\int_{\Gamma_u} \mathbf{N}_I^\mathrm{T} \mathbf{u}_\Gamma \mathrm{d}\Gamma}_{-\boldsymbol{q}_I} = -\delta\lambda^\mathrm{T} \mathbf{G}^\mathrm{T} \mathbf{U} + \delta\lambda^\mathrm{T} \mathbf{q}
\end{aligned} \tag{A.6}$$

The last term in the LHS of the Eq. (A.1) is simplified to,

$$\begin{aligned}
&\int_{\Gamma_u} \delta\mathbf{u}^\mathrm{T} \lambda \mathrm{d}\Gamma \\
&= \sum_{\substack{I \in S_N, \\ I \in S_H, \\ I \in S_L}} \sum_{J \in S_\lambda,} \delta\, \mathbf{U}_I^\mathrm{T} \underbrace{\left[\int_{\Gamma_u} \boldsymbol{\Phi}_I^\mathrm{T} \mathbf{N}_J \mathrm{d}\Gamma \quad \int_{\Gamma_u} \left(\boldsymbol{\Phi}_I \mathrm{H}(f(\mathbf{x}))\right)^\mathrm{T} \mathbf{N}_J \mathrm{d}\Gamma \quad \int_{\Gamma_u} (\boldsymbol{\Phi}_I \chi_I)^\mathrm{T} \mathbf{N}_J \mathrm{d}\Gamma\right]}_{-\boldsymbol{G}_{IJ}} \lambda_J \qquad (\text{A.7}) \\
&= -\delta\mathbf{U}^\mathrm{T} \mathbf{G} \lambda
\end{aligned}$$

Assuming the cohesive tractions as the external force applied on the cohesive crack boundary, Γ_{coh}, is given by

$$\int_{\Gamma_{coh}} \delta \mathbf{w}^{\mathrm{T}} \mathbf{t} d\Gamma = \int_{\Gamma_{coh}} \delta \left(2 \sum_{I \in S_H} \mathbf{\Phi}_I(\mathbf{x}) \{ \mathbf{a}_I \mathrm{H}(f(\mathbf{x})) \} \right)^{\mathrm{T}} \mathbf{t} d\Gamma \tag{A.8}$$

$$= \delta \mathbf{a}^{\mathrm{T}} \mathbf{F} = \delta \mathbf{U}^{\mathrm{T}} \mathbf{F}$$

where, $$\mathbf{F} = 2 \int_{\Gamma_{coh}} \left(\sum_{I \in S_H} \mathbf{\Phi}_I(\mathbf{x}) \{ \mathrm{H}(f(\mathbf{x})) \} \right)^{\mathrm{T}} \mathbf{t} d\Gamma$$

Finally, using the Eqs.(A.4),(A.6), (A.7), and (A.8) in Eq. (A.1), obtains the form

$$\delta \mathbf{U}^{\mathrm{T}} [\mathbf{K}\mathbf{U} + \mathbf{G}\lambda] + \delta\lambda^{\mathrm{T}} [\mathbf{G}^{\mathrm{T}}\mathbf{U} - \mathbf{q}] = \delta \mathbf{U}^{\mathrm{T}} \mathbf{F}$$

As $\delta\mathbf{U}$ and $\delta\lambda$ are arbitrary, the above equation can be written in the discrete system of equations are satisfied only if

$$\begin{bmatrix} \mathbf{K} & \mathbf{G} \\ \mathbf{G}^{\mathrm{T}} & 0 \end{bmatrix} \begin{Bmatrix} \mathbf{U} \\ \lambda \end{Bmatrix} = \begin{Bmatrix} \mathbf{F} \\ \mathbf{q} \end{Bmatrix} \tag{A.9}$$

Appendix B.

Deviatoric part of 2nd Piola-Kirchoff stress and elasticity tensors

The deviatoric strain energy function of Mooney-Rivlin model is given by:

$$\widetilde{W} = C_{10} \left(\overline{I}_1^{\,C} - 3 \right) + C_{01} \left(\overline{I}_2^{\,C} - 3 \right) \tag{B.1}$$

here, the reduced invariants are defined as $\overline{I}_1^{\,C} = \frac{I_1^C}{J^{\frac{2}{3}}}$; $\overline{I}_2^{\,C} = \frac{I_2^C}{J^{\frac{4}{3}}}$; $J = \overline{I}_3^{\,C} = \sqrt{I_3} = \sqrt{\det \boldsymbol{C}}$. The deviatoric *second Piola-Kirchoff stress* derived from the strain energy function is given by,

$$\boldsymbol{S}_d = \frac{\partial \widetilde{W}}{\partial \boldsymbol{E}} = 2 \frac{\partial \widetilde{W}}{\partial \boldsymbol{C}} = 2 \left[\frac{\partial \widetilde{W}}{\partial \overline{I}_1^{\,C}} \frac{\partial \overline{I}_1^{\,C}}{\partial \boldsymbol{C}} + \frac{\partial \widetilde{W}}{\partial \overline{I}_2^{\,C}} \frac{\partial \overline{I}_2^{\,C}}{\partial \boldsymbol{C}} \right] \tag{B.2}$$

$$\frac{\partial \overline{I}_1^{\,C}}{\partial \boldsymbol{C}} = J^{-\frac{2}{3}} \boldsymbol{I} - \frac{1}{3} \overline{I}_1^{\,C} \boldsymbol{C}^{-1}$$

$$\frac{\partial \bar{I}_2^{\,C}}{\partial \mathbf{C}} = J^{-\frac{2}{3}}\,\bar{I}_1^{\,C}\,\mathbf{I} - J^{-\frac{4}{3}}\,\mathbf{C} - \frac{2}{3}\,\bar{I}_2^{\,C}\,\mathbf{C}^{-1}$$

$$\frac{\partial J}{\partial \mathbf{C}} = \frac{1}{2}J\mathbf{C}^{-\mathbf{1}}$$

$$\frac{\partial \bar{W}}{\partial J} = \frac{2}{D_1}\,(J-1)\,, \qquad \frac{\partial \bar{W}}{\partial \bar{I}_1^C} = C_{10}, \qquad \frac{\partial \bar{W}}{\partial \bar{I}_2^C} = C_{01}$$

Therefore,

$$\mathbf{S}_d = 2\left[C_{10}\left(J^{-\frac{2}{3}}\,\mathbf{I} - \frac{1}{3}\,\bar{I}_1^{\,C}\,\mathbf{C}^{-1}\right) + C_{01}\left(J^{-\frac{2}{3}}\bar{I}_1^{\,C}\,\mathbf{I} - J^{-\frac{4}{3}}\,\mathbf{C} - \frac{2}{3}\,\bar{I}_2^{\,C}\,\mathbf{C}^{-1}\right)\right] \tag{B.3}$$

Deviatoric constitutive Tensor ($\mathbf{D}_d$):

$$\mathbf{D}_d = \frac{\partial \mathbf{S}_d}{\partial \mathbf{E}} = 2\,\frac{\partial \mathbf{S}_d}{\partial \mathbf{C}} = 2\begin{bmatrix} C_{10}\left(\underbrace{\frac{\partial}{\partial \mathbf{C}}\left(2\,J^{-\frac{2}{3}}\,\mathbf{I}\right)}_{1^{\text{st}}\text{ term}} - \underbrace{\frac{\partial}{\partial \mathbf{C}}\left(\frac{2}{3}\,\bar{I}_1^{\,C}\,\mathbf{C}^{-1}\right)}_{2^{\text{nd}}\text{ term}}\right) \\ + \\ C_{01}\left(\underbrace{\frac{\partial}{\partial \mathbf{C}}\left(2J^{-\frac{2}{3}}\bar{I}_1^{\,C}\,\mathbf{I}\right)}_{3^{\text{rd}}\text{ term}} - \underbrace{\frac{\partial}{\partial \mathbf{C}}\left(2J^{-\frac{4}{3}}\,\mathbf{C}\right)}_{4^{\text{th}}\text{ term}} - \underbrace{\frac{\partial}{\partial \mathbf{C}}\left(\frac{4}{3}\,\bar{I}_2^{\,C}\,\mathbf{C}^{-1}\right)}_{5^{\text{th}}\text{ term}}\right) \end{bmatrix} \tag{B.4}$$

1st term:

$$\frac{\partial}{\partial \mathbf{C}}\left(2J^{-\frac{2}{3}}\mathbf{I}\right) = 2\,\left[-\frac{2}{3}\,J^{-\frac{5}{3}}\,\mathbf{I}\otimes\frac{\partial J}{\partial \mathbf{C}} + J^{-\frac{2}{3}}\,\frac{\partial \mathbf{I}}{\partial \mathbf{C}}\right] = -\frac{2}{3}J^{-\frac{2}{3}}\,\mathbf{I}\otimes\mathbf{C}^{-1} \tag{B.5}$$

2nd term:

$$\begin{aligned} \frac{\partial}{\partial \mathbf{C}}\left(-\frac{2}{3}\,\bar{I}_1^{\,C}\,\mathbf{C}^{-1}\right) &= -\frac{2}{3}\left[\mathbf{C}^{-1}\otimes\frac{\partial \bar{I}_1^{\,C}}{\partial \mathbf{C}} + \bar{I}_1^{\,C}\,\frac{\partial \mathbf{C}^{-1}}{\partial \mathbf{C}}\right] \\ &= -\frac{2}{3}\left[\mathbf{C}^{-1}\otimes\frac{\partial \bar{I}_1^{\,C}}{\partial \mathbf{C}} - \bar{I}_1^{\,C}\mathbf{C}^{-1}\otimes\mathbf{C}^{-\mathrm{T}}\right] \end{aligned} \tag{B.6}$$

3rd term:

$$\frac{\partial}{\partial \boldsymbol{C}}\left(2\,J^{-\frac{2}{3}}\;\overline{I}_1{}^{C}\,\boldsymbol{I}\right) = 2\left[-\frac{2}{3}\,J^{-\frac{5}{3}}\overline{I}_1{}^{C}\,\boldsymbol{I}\;\otimes\frac{\partial J}{\partial \boldsymbol{C}} + J^{-\frac{2}{3}}\;\boldsymbol{I}\otimes\frac{\partial \overline{I}_1{}^{C}}{\partial \boldsymbol{C}}\right]$$
$$= -\frac{2}{3}\,J^{-\frac{2}{3}}\,\overline{I}_1{}^{C}\,(\boldsymbol{I}\otimes\boldsymbol{C}^{-1}) + 2\,J^{-\frac{2}{3}}\left(\boldsymbol{I}\otimes\frac{\partial \overline{I}_1{}^{C}}{\partial \boldsymbol{C}}\right) \tag{B.7}$$

4th term:

$$\frac{\partial}{\partial \boldsymbol{E}}\left(-2J^{-\frac{4}{3}}\boldsymbol{C}\right) = \;-2\;\left[-\frac{4}{3}\,J^{-\frac{7}{3}}\;\boldsymbol{C}\otimes\frac{\partial J}{\partial \boldsymbol{C}} + J^{-\frac{4}{3}}\frac{\partial \boldsymbol{C}}{\partial \boldsymbol{C}}\right]$$
$$= \frac{4}{3}\,J^{-\frac{4}{3}}\,(\boldsymbol{C}\otimes\boldsymbol{C}^{-1}) - 2\,J^{-\frac{4}{3}}\,\mathbf{I} \tag{B.8}$$

5th term:

$$\frac{\partial}{\partial \boldsymbol{E}}\left(-\frac{4}{3}\;\overline{I}_2{}^{C}\;\boldsymbol{C}^{-1}\right) = -\frac{4}{3}\left[\boldsymbol{C}^{-1}\otimes\frac{\partial \overline{I}_2{}^{C}}{\partial \boldsymbol{C}} - \overline{I}_2{}^{C}\boldsymbol{C}^{-1}\otimes\boldsymbol{C}^{-\mathrm{T}}\right] \tag{B.9}$$

References

[1] W. Zhang, Numerical analysis of continuum damage mechanics, UNSW Sydney, 1992.

[2] E. de S. Neto, D. Peric, D. Owen, Computational methods for plasticity: theory and applications, 2011. https://books.google.co.in/books?hl=en&lr=&id=21Q0oLGFZuoC&oi=fnd&pg=PT7&dq=D+R+J+owen+2008&ots=CRpzqmvNTb&sig=-Z2DpRCOOi-u_Mxxs5bQF5Vn91E (accessed June 24, 2021).

[3] L. KACHANOV, Rupture time under creep conditions, in: 1958. https://www.sid.ir/en/journal/ViewPaper.aspx?ID=292195 (accessed June 22, 2021).

[4] Y. Rabotnov, Damage from creep, Zhurn. Prikl. Mekh. Tekhn. Phys 2 (1963) 113--123.

[5] D. Krajcinovic, Constitutive Equations for Damaging Materials, J Appl Mech 50 (1983) 355–360. https://doi.org/10.1115/1.3167044.

[6] D. Krajcinovic, Continuous Damage Mechanics Revisited: Basic Concepts and Definitions, J Appl Mech 52 (1985) 829–834. https://doi.org/10.1115/1.3169154.

[7] J. (Jean) Lemaître, J.-Louis. Chaboche, Mechanics of solid materials, Cambridge University Press, 1990.

[8] J. Lemaitre, R. Desmorat, M. Sauzay, Anisotropic damage law of evolution, European Journal of Mechanics - A/Solids 19 (2000) 187–208. https://doi.org/10.1016/S0997-7538(00)00161-3.

[9] J. Gelin, A. Mrichcha, Computational procedures for finite strain elasto plasticity with isotropic damage, Computational Plasticity: Fundamentals and Applications. II (1992) 1401–1412.

[10] F.X.C. Andrade, Non-local modelling of ductile damage: formulation and numerical issues, Universidade do Porto , 2011.

[11] G. Zi, T. Rabczuk, W. Wall, Extended meshfree methods without branch enrichment for cohesive cracks, Comput Mech 40 (2007) 367–382. https://doi.org/10.1007/s00466-006-0115-0.

[12] M. Shaat, E. Ghavanloo, S.A. Fazelzadeh, Review on nonlocal continuum mechanics: Physics, material applicability, and mathematics, Mechanics of Materials 150 (2020) 103587. https://doi.org/10.1016/J.MECHMAT.2020.103587.

[13] A. Egger, U. Pillai, K. Agathos, E. Kakouris, E. Chatzi, I.A. Aschroft, S.P. Triantafyllou, Discrete and Phase Field Methods for Linear Elastic Fracture Mechanics: A Comparative Study and State-of-the-Art Review, Applied Sciences 9 (2019) 2436. https://doi.org/10.3390/app9122436.

[14] J. Besson, Continuum Models of Ductile Fracture: A Review:, Http://Dx.Doi.Org/10.1177/1056789509103482 19 (2009) 3–52. https://doi.org/10.1177/1056789509103482.

[15] X. Pan, H. Yuan, Computational algorithms and applications of element-free Galerkin methods for nonlocal damage models, Eng Fract Mech 77 (2010) 2640–2653. https://doi.org/10.1016/J.ENGFRACMECH.2010.07.018.

[16] H. Askes, J. Pamin, R.E. De Borst, Dispersion analysis and element-free Galerkin solutions of second-and fourth-order gradient-enhanced damage models, Int J Numer Methods Eng 49 (2000) 811–832. https://doi.org/10.1002/1097-0207.

[17] A.C. Eringen, C.G. Speziale, B.S. Kim, Crack-tip problem in non-local elasticity, J Mech Phys Solids 25 (1977) 339–355. https://doi.org/https://doi.org/10.1016/0022-5096(77)90002-3.

[18] C. Polizzotto, P. Fuschi, A.A. Pisano, A nonhomogeneous nonlocal elasticity model, European Journal of Mechanics - A/Solids 25 (2006) 308–333. https://doi.org/10.1016/J.EUROMECHSOL.2005.09.007.

[19] N. Bonora, A nonlinear CDM model for ductile failure, Eng Fract Mech 58 (1997) 11–28. https://doi.org/10.1016/s0013-7944(97)00074-x.

[20] S. Chandrakanth, P.C. Pandey, An isotropic damage model for ductile material, Eng Fract Mech 50 (1995) 457–465. https://doi.org/10.1016/0013-7944(94)00214-3.

[21] S. Bordas, P.V. Nguyen, C. Dunant, A. Guidoum, H. Nguyen-Dang, An extended finite element library, Int J Numer Methods Eng 71 (2007) 703–732. https://doi.org/10.1002/NME.1966.

[22] T. Rabczuk, G. Zi, A Meshfree Method based on the Local Partition of Unity for Cohesive Cracks, Comput Mech 39 (2006) 743–760. https://doi.org/10.1007/S00466-006-0067-4.

[23] M.A. Crisfield, J. Wills, Solution strategies and softening materials, Comput Methods Appl Mech Eng 66 (1988) 267–289. https://doi.org/10.1016/0045-7825(88)90002-3.

[24] G. Alfano, M.A. Crisfield, Finite element interface models for the delamination analysis of laminated composites: Mechanical and computational issues, Int J Numer Methods Eng 50 (2001) 1701–1736. https://doi.org/10.1002/NME.93.

[25] W.K. Liu, S. Li, H.S. Park, Eighty Years of the Finite Element Method: Birth, Evolution, and Future, Archives of Computational Methods in Engineering 2022 29:6 29 (2022) 4431–4453. https://doi.org/10.1007/S11831-022-09740-9.

[26] J.N. Reddy, An introduction to the finite element method, McGraw-Hill , New York, 2005.

[27] K.J. Bathe, Finite element procedures, Prentice Hall Englewood Cliffs, NJ, 1996.

[28] A.E. Hatheway, Review of finite element analysis techniques: capabilities and limitations, Https://Doi.Org/10.1117/12.61113 10265 (1992) 335–365. https://doi.org/10.1117/12.61113.

[29] A. Srirekha, K. Bashetty, Infinite to finite: An overview of finite element analysis, Indian Journal of Dental Research 21 (2010) 425–432. https://doi.org/10.4103/0970-9290.70813.

[30] T. Belytschko, Y. Krongauz, D. Organ, M. Fleming, P. Krysl, Meshless methods: An overview and recent developments, Comput Methods Appl Mech Eng 139 (1996) 3–47. https://doi.org/10.1016/S0045-7825(96)01078-X.

[31] V.P. Nguyen, T. Rabczuk, S. Bordas, M. Duflot, Meshless methods: A review and computer implementation aspects, Math Comput Simul 79 (2008) 763–813. https://doi.org/10.1016/J.MATCOM.2008.01.003.

[32] T. Belytschko, T. Black, Elastic crack growth in finite elements with minimal remeshing, International Journal for Numerical Methods in Engineering 45 (1999) 601–620. https://doi.org/10.1002/(SICI)1097-0207(19990620)45:5.

[33] N. Moës, J. Dolbow, T. Belytschko, A finite element method for crack growth without remeshing, Int J Numer Methods Eng 46 (1999) 131–150. https://doi.org/10.1002/(SICI)1097-0207(19990910)46:1.

[34] S. Bordas, B. Moran, Enriched finite elements and level sets for damage tolerance assessment of complex structures, Eng Fract Mech 73 (2006) 1176–1201. https://doi.org/10.1016/J.ENGFRACMECH.2006.01.006.

[35] C. Dunant, V.P. Nguyen, M. Belgasmia, S. Bordas, A. Guidoum, Architecture tradeoffs of integrating a mesh generator to partition of unity enriched object-oriented finite element software, European Journal of Computational Mechanics 16 (2007) 237–258. https://doi.org/10.3166/REMN.16.237-258.

[36] L.B. Lucy, Lucy, L. B., A numerical approach to the testing of the fission hypothesis., AJ 82 (1977) 1013–1024. https://doi.org/10.1086/112164.

[37] J. Bonet, S. Kulasegaram, Correction and stabilization of smooth particle hydrodynamics methods with applications in metal forming simulations, International Journal for Numerical Methods in Engineering 47 (2000) 1189–1214. https://doi.org/10.1002/(SICI)1097-0207(20000228)47:6.

[38] L.D. Libersky, A.G. Petschek, T.C. Carney, J.R. Hipp, F.A. Allahdadi, High Strain Lagrangian Hydrodynamics: A Three-Dimensional SPH Code for Dynamic Material Response, J Comput Phys 109 (1993) 67–75. https://doi.org/10.1006/JCPH.1993.1199.

[39] G.R. Johnson, S.R. Beissel, Normalized smoothing functions for SPH impact computations, Int J Numer Methods Eng 39 (1996) 2725–2741. https://doi.org/10.1002/(SICI)1097-0207(19960830)39:16.

[40] B. Nayroles, G. Touzot, P. Villon, Generalizing the finite element method: Diffuse approximation and diffuse elements, Comput Mech 10 (1992) 307–318. https://doi.org/10.1007/BF00364252/METRICS.

[41] T. Belytschko, Y.Y. Lu, L. Gu, Element-free Galerkin methods, Int J Numer Methods Eng 37 (1994) 229–256. https://doi.org/10.1002/NME.1620370205.

[42] S.N. Atluri, T. Zhu, A new Meshless Local Petrov-Galerkin (MLPG) approach in computational mechanics, Comput Mech 22 (1998) 117–127. https://doi.org/10.1007/S004660050346/METRICS.

[43] W.K. Liu, S. Jun, Y.F. Zhang, Reproducing kernel particle methods, Int J Numer Methods Fluids 20 (1995) 1081–1106. https://doi.org/10.1002/FLD.1650200824.

[44] G.R. Liu, Y.T. Gu, A point interpolation method for two-dimensional solids, Int J Numer Methods Eng 50 (2001) 937–951. https://doi.org/10.1002/1097-0207(20010210)50:4.

[45] C.-D. Munz, R. Schneider, U. Voss, A finite-volume particle-in-cell method for the numerical simulation of devices in pulsed-power technology, Surveys on Mathematics for Industry, Springer-VERLAG 8 (1999) 243–257.

[46] S.G. Bardenhagen, J.U. Brackbill, D. Sulsky, The material-point method for granular materials, Comput Methods Appl Mech Eng 187 (2000) 529–541. https://doi.org/10.1016/S0045-7825(99)00338-2.

[47] N.R. Aluru, A point collocation method based on reproducing kernel approximations, International Journal for Numerical Methods in Engineering 47 (2000) 1083–1121. https://doi.org/10.1002/(SICI)1097-0207(20000228)47:6.

[48] T.-P. Fries, H.G. Matthies, Classification and overview of meshfree methods, Department of Mathematics and Computer Science, Technical University of Braunschweig 865 (2003).

[49] X. Zhuang, C. Heaney, C. Augarde, On error control in the element-free Galerkin method, Eng Anal Bound Elem 36 (2012) 351–360. https://doi.org/10.1016/J.ENGANABOUND.2011.06.011.

[50] N.M. Muthu, Studies in the use of the element-free galerkin method for linear elastic fracture mechanics, 2017. https://doi.org/10.4225/03/58B8AFDE5B7F4.

[51] M. Jirásek, B. Patzák, Consistent tangent stiffness for nonlocal damage models, Comput Struct 80 (2002) 1279–1293. https://doi.org/10.1016/S0045-7949(02)00078-0.

[52] M. Jirásek, Nonlocal damage mechanics, Revue Européenne de Génie Civil 11 (2007) 993–1021. https://doi.org/10.1080/17747120.2007.9692974.

[53] C. Oseen, The theory of liquid crystals, Transactions of the Faraday Society 29 (1933) 883–899.

[54] E. Kröner, Elasticity theory of materials with long range cohesive forces, Int J Solids Struct 3 (1967) 731–742. https://doi.org/10.1016/0020-7683(67)90049-2.

[55] A.C. Eringen, Linear theory of nonlocal elasticity and dispersion of plane waves, Int J Eng Sci 10 (1972) 425–435. https://doi.org/10.1016/0020-7225(72)90050-X.

[56] A.C. Eringen, D.G.B. Edelen, On nonlocal elasticity, Int J Eng Sci 10 (1972) 233–248. https://doi.org/10.1016/0020-7225(72)90039-0.

[57] C. Polizzotto, Nonlocal elasticity and related variational principles, Int J Solids Struct 38 (2001) 7359–7380. https://doi.org/10.1016/S0020-7683(01)00039-7.

[58] A.C. Eringen, On nonlocal plasticity, Int J Eng Sci 19 (1981) 1461–1474. https://doi.org/10.1016/0020-7225(81)90072-0.

[59] G. Pijaudier-Cabot, " S M Asce, Z.P. Basant, F. Asce, Nonlocal damage theory, J Eng Mech 113 (1987) 1512–1533. https://doi.org/10.1061/(ASCE)0733-9399(1987)113:10(1512).

[60] S. Murakami, Continuum damage mechanics, Springer Netherlands, Dordrecht, 2012. https://doi.org/10.1007/978-94-007-2666-6.

[61] K. Langenfeld, I.U. Handge, Continuum Modeling of Brittle and Ductile Damage: Theory and Computational Frameworks, Technische Universitat Dortmund, 2023.

[62] J. Mazars, A description of micro- and macroscale damage of concrete structures, Eng Fract Mech 25 (1986) 729–737. https://doi.org/10.1016/0013-7944(86)90036-6.

[63] J.C. Simo, J.W. Ju, Strain- and stress-based continuum damage models—I. Formulation, Int J Solids Struct 23 (1987) 821–840. https://doi.org/10.1016/0020-7683(87)90083-7.

[64] J. Lee, G.L. Fenves, Plastic-damage model for cyclic loading of concrete structures, J Eng Mech 124 (1998) 892–900. https://doi.org/10.1061/(ASCE)0733-9399(1998)124:8(892).

[65] L. Jason, A. Huerta, G. Pijaudier-Cabot, S. Ghavamian, An elastic plastic damage formulation for concrete: application to elementary tests and comparison with an isotropic damage model, Comput Methods Appl Mech Eng 195 (2006) 7077–7092. https://doi.org/10.1016/j.cma.2005.04.017.

[66] J. Mazars, J. Lemaitre, Application of continuous damage mechanics to strain and fracture behavior of concrete, Springer, 1985.

[67] W.A.M. Brekelmans, P.J.G. Schreurs, J.H.P. de Vree, Continuum damage mechanics for softening of brittle materials, Acta Mech 93 (1992) 133–143. https://doi.org/10.1007/BF01182579/METRICS.

[68] C. Comi, A non-local model with tension and compression damage mechanisms, European Journal of Mechanics-A/Solids 20 (2001) 1–22. https://doi.org/https://doi.org/10.1016/S0997-7538(00)01111-6.

[69] A.H. Al-Gadhib, M.H. Baluch, A. Shaalan, A.R. Khan, Damage Model for Monotonic and Fatigue Response of High Strength Concrete, Http://Dx.Doi.Org/10.1177/105678950000900105 9 (2000) 57–78. https://doi.org/10.1177/105678950000900105.

[70] M. Brünig, A. Michalski, A stress-state-dependent continuum damage model for concrete based on irreversible thermodynamics, Int J Plast 90 (2017) 31–43. https://doi.org/10.1016/J.IJPLAS.2016.12.002.

[71] M. Cervera, C. Tesei, G. Ventura, Cracking of quasi-brittle structures under monotonic and cyclic loadings: A d+/d− damage model with stiffness recovery in shear, Int J Solids Struct 135 (2018) 148–171. https://doi.org/10.1016/J.IJSOLSTR.2017.11.017.

[72] F. Ragueneau, R. Desmorat, F. Gatuingt, Anisotropic damage modelling of biaxial behaviour and rupture of concrete structures, Computers and Concrete, an International Journal 5 (2008) 417–434. https://hal.science/hal-00994323 (accessed March 29, 2024).

[73] J. Mazars, S. Grange, Simplified strategies based on damage mechanics for concrete under dynamic loading, Philosophical Transactions of the Royal Society A: Mathematical, Physical and Engineering Sciences 375 (2017). https://doi.org/10.1098/RSTA.2016.0170.

[74] R. Scotta, R. Vitaliani, A. Saetta, E. Oñate, A. Hanganu, A scalar damage model with a shear retention factor for the analysis of reinforced concrete structures: theory and validation, Comput Struct 79 (2001) 737–755. https://doi.org/10.1016/S0045-7949(00)00178-4.

[75] B.Z. George Voyiadjis, T.M. Abu-Lebdeh, Damage Model for Concrete Using Bounding Surface Concept, J Eng Mech 119 (1993) 1865–1885. https://doi.org/10.1061/(ASCE)0733-9399(1993)119:9(1865).

[76] X. Xue, X. Yang, A damage model for concrete under cyclic actions, International Journal of Damage Mechanics 23 (2014) 155–177. https://doi.org/10.1177/1056789513487084/ASSET/IMAGES/LARGE/10.1177_1056789513487084-FIG14.JPEG.

[77] L. Zhang, W. Yu, Constitutive modeling of damageable brittle and quasi-brittle materials, Int J Solids Struct 117 (2017) 80–90. https://doi.org/10.1016/J.IJSOLSTR.2017.04.002.

[78] A. Ibrahimbegović, D. Markovič, F. Gatuingt, A. Ibrahimbegovi´c, I.-D. Markovič, Constitutive model of coupled damage-plasticity and its finite element implementation, Revue Européenne Des Eléments 12 (2003) 381–405. https://doi.org/10.3166/REEF.12.381-405.

[79] B. Ahmed, G.Z. Voyiadjis, T. Park, Damaged plasticity model for concrete using scalar damage variables with a novel stress decomposition, Int J Solids Struct 191–192 (2020) 56–75. https://doi.org/10.1016/J.IJSOLSTR.2019.11.023.

[80] B. Alfarah, F. López-Almansa, S. Oller, New methodology for calculating damage variables evolution in Plastic Damage Model for RC structures, Eng Struct 132 (2017) 70–86. https://doi.org/10.1016/J.ENGSTRUCT.2016.11.022.

[81] F. Bourgeois, N. Burlion, J.F. Shao, Modelling of elastoplastic damage in concrete due to desiccation shrinkage, Int J Numer Anal Methods Geomech 26 (2002) 759–774. https://doi.org/10.1002/NAG.221.

[82] L. Contrafatto, M. Cuomo, A framework of elastic–plastic damaging model for concrete under multiaxial stress states, Int J Plast 22 (2006) 2272–2300. https://doi.org/10.1016/J.IJPLAS.2006.03.011.

[83] R. Faria, J. Oliver, M. Cervera, A strain-based plastic viscous-damage model for massive concrete structures, Int J Solids Struct 35 (1998) 1533–1558. https://doi.org/10.1016/S0020-7683(97)00119-4.

[84] P. Grassl, D. Xenos, U. Nyström, R. Rempling, K. Gylltoft, CDPM2: A damage-plasticity approach to modelling the failure of concrete, Int J Solids Struct 50 (2013) 3805–3816. https://doi.org/10.1016/J.IJSOLSTR.2013.07.008.

[85] N.R. Hansen, H.L. Schreyer, A thermodynamically consistent framework for theories of elastoplasticity coupled with damage, Int J Solids Struct 31 (1994) 359–389. https://doi.org/10.1016/0020-7683(94)90112-0.

[86] J.W. Ju, On energy-based coupled elastoplastic damage theories: Constitutive modeling and computational aspects, Int J Solids Struct 25 (1989) 803–833. https://doi.org/10.1016/0020-7683(89)90015-2.

[87] W.M. Garrison, N.R. Moody, Ductile fracture, Journal of Physics and Chemistry of Solids 48 (1987) 1035–1074. https://doi.org/10.1016/0022-3697(87)90118-1.

[88] A.P. Mouritz, Introduction to aerospace materials, Elsevier, 2012.

[89] J. Lemaitre, A Continuous Damage Mechanics Model for Ductile Fracture, J Eng Mater Technol 107 (1985) 83–89. https://doi.org/10.1115/1.3225775.

[90] Wei Hua Tai, Bing Xian Yang, A new microvoid-damage model for ductile fracture, Eng Fract Mech 25 (1986) 377–384. https://doi.org/10.1016/0013-7944(86)90133-5.

[91] M. Kumar, P.M. Dixit, A nonlinear ductile damage growth law, International Journal of Damage Mechanics 24 (2015) 1070–1085. https://doi.org/10.1177/1056789514561807.

[92] L. Malcher, E.N. Mamiya, An improved damage evolution law based on continuum damage mechanics and its dependence on both stress triaxiality and the third invariant, Int J Plast 56 (2014) 232–261. https://doi.org/10.1016/j.ijplas.2014.01.002.

[93] T.S. Cao, J.M. Gachet, P. Montmitonnet, P.O. Bouchard, A Lode-dependent enhanced Lemaitre model for ductile fracture prediction at low stress triaxiality, Eng Fract Mech 124–125 (2014) 80–96. https://doi.org/10.1016/J.ENGFRACMECH.2014.03.021.

[94] T.H.A. Nguyen, T.Q. Bui, S. Hirose, Smoothing gradient damage model with evolving anisotropic nonlocal interactions tailored to low-order finite elements, Comput Methods Appl Mech Eng 328 (2018) 498–541. https://doi.org/10.1016/J.CMA.2017.09.019.

[95] G.D. Nguyen, G.T. Houlsby, Non-local damage modelling of concrete: a procedure for the determination of model parameters, Int J Numer Anal Methods Geomech 31 (2007) 867–891. https://doi.org/10.1002/NAG.563.

[96] H. Amor, J.J. Marigo, C. Maurini, Regularized formulation of the variational brittle fracture with unilateral contact: Numerical experiments, J Mech Phys Solids 57 (2009) 1209–1229. https://doi.org/10.1016/J.JMPS.2009.04.011.

[97] C. Kuhn, A. Schlüter, R. Müller, On degradation functions in phase field fracture models, Comput Mater Sci 108 (2015) 374–384. https://doi.org/10.1016/J.COMMATSCI.2015.05.034.

[98] X. Zhang, C. Vignes, S.W. Sloan, D. Sheng, Numerical evaluation of the phase-field model for brittle fracture with emphasis on the length scale, Comput Mech 59 (2017) 737–752. https://doi.org/10.1007/S00466-017-1373-8/FIGURES/24.

[99] J.Y. Wu, V.P. Nguyen, A length scale insensitive phase-field damage model for brittle fracture, J Mech Phys Solids 119 (2018) 20–42. https://doi.org/10.1016/J.JMPS.2018.06.006.

[100] M. Jirásek, Computational aspects of nonlocal models, in: European Conference on Computational Mechanics, Germany, 1999.

[101] C. Comi, U. Perego, Numerical aspects of nonlocal damage analyses, Revue Européenne Des Éléments Finis 10 (2001) 227–242. https://doi.org/10.1080/12506559.2001.11869249.

[102] M. Jirásek, S. Marfia, Non-local damage model based on displacement averaging, Int J Numer Methods Eng 63 (2005) 77–102. https://doi.org/10.1002/NME.1262.

[103] G.D. Nguyen, A thermodynamic approach to non-local damage modelling of concrete, Int J Solids Struct 45 (2008) 1918–1934. https://doi.org/10.1016/j.ijsolstr.2007.11.001.

[104] C. Giry, F. Dufour, J. Mazars, Stress-based nonlocal damage model, Int J Solids Struct 48 (2011) 3431–3443. https://doi.org/10.1016/j.ijsolstr.2011.08.012.

[105] W. He, Y.F. Wu, Y. Xu, T.T. Fu, A thermodynamically consistent nonlocal damage model for concrete materials with unilateral effects, Comput Methods Appl Mech Eng 297 (2015) 371–391. https://doi.org/10.1016/J.CMA.2015.09.010.

[106] G. Borino, B. Failla, F. Parrinello, A symmetric nonlocal damage theory, Int J Solids Struct 40 (2003) 3621–3645. https://doi.org/10.1016/S0020-7683(03)00144-6.

[107] I. de-Pouplana, E. Oñate, Combination of a non-local damage model for quasi-brittle materials with a mesh-adaptive finite element technique, Finite Elements in Analysis and Design 112 (2016) 26–39. https://doi.org/10.1016/j.finel.2015.12.011.

[108] P. Grassl, M. Jirásek, Damage-plastic model for concrete failure, Int J Solids Struct 43 (2006) 7166–7196. https://doi.org/10.1016/J.IJSOLSTR.2006.06.032.

[109] M. Jirásek, R. Desmorat, Localization analysis of nonlocal models with damage-dependent nonlocal interaction, Int J Solids Struct 174 (2019) 1–17. https://doi.org/10.1016/j.ijsolstr.2019.06.011.

[110] B. V. Farahani, J. Belinha, F.M. Andrade Pires, A.J.M. Ferreira, P.M.G.P. Moreira, Extending a radial point interpolation meshless method to non-local constitutive damage models, Theoretical and Applied Fracture Mechanics 85 (2016) 84–98. https://doi.org/10.1016/J.TAFMEC.2016.08.008.

[111] R. Desmorat, F. Gatuingt, M. Jirásek, Nonlocal models with damage-dependent interactions motivated by internal time, Eng Fract Mech 142 (2015) 255–275. https://doi.org/10.1016/j.engfracmech.2015.06.015.

[112] B. Ahmed, G.Z. Voyiadjis, T. Park, Local and non-local damage model with extended stress decomposition for concrete, International Journal of Damage Mechanics 30 (2021) 1149–1191. https://doi.org/10.1177/1056789521998728.

[113] C. Su, D. Lu, X. Zhou, G. Wang, X. Zhuang, X. Du, An implicit stress update algorithm for the plastic nonlocal damage model of concrete, Comput Methods Appl Mech Eng 414 (2023) 116189. https://doi.org/10.1016/j.cma.2023.116189.

[114] F.X.C. Andrade, J.M.A. César De Sá, F.M. Andrade Pires, A Ductile Damage Nonlocal Model of Integral-type at Finite Strains: Formulation and Numerical Issues, Https://Doi.Org/10.1177/1056789510386850 20 (2011) 515–557. https://doi.org/10.1177/1056789510386850.

[115] F. Andrade, J.C. De Sá, F.A. Pires, Assessment and comparison of non-local integral models for ductile damage, International Journal of Damage Mechanics 23 (2013) 261–296. https://doi.org/10.1177/1056789513493103.

[116] M. Jirásek, S. Rolshoven, Comparison of integral-type nonlocal plasticity models for strain-softening materials, Int J Eng Sci 41 (2003) 1553–1602. https://doi.org/10.1016/S0020-7225(03)00027-2.

[117] G.D. Nguyen, A.M. Korsunsky, J.P.H. Belnoue, A nonlocal coupled damage-plasticity model for the analysis of ductile failure, Int J Plast 64 (2015) 56–75. https://doi.org/10.1016/J.IJPLAS.2014.08.001.

[118] A. V. Shutov, V.S. Klyuchantsev, Integral-based non-local approach to ductile damage and mixed-mode fracture, Eng Fract Mech 292 (2023) 109656. https://doi.org/10.1016/J.ENGFRACMECH.2023.109656.

[119] V.B. Pandey, I. V. Singh, B.K. Mishra, S. Ahmad, A. Venugopal Rao, V. Kumar, A new framework based on continuum damage mechanics and XFEM for high cycle fatigue crack growth simulations, Eng Fract Mech 206 (2019) 172–200. https://doi.org/10.1016/J.ENGFRACMECH.2018.11.021.

[120] C.H.M. Simha, S. Xu, W.R. Tyson, Non-local phenomenological damage-mechanics-based modeling of the Drop-Weight Tear Test, Eng Fract Mech 118 (2014) 66–82. https://doi.org/10.1016/J.ENGFRACMECH.2014.01.009.

[121] A. V. Shutov, V.S. Klyuchantsev, Large strain integral-based nonlocal simulation of ductile damage with application to mode-I fracture, Int J Plast 144 (2021) 103061. https://doi.org/10.1016/J.IJPLAS.2021.103061.

[122] V.S. Klyuchantsev, A. V. Shutov, A Comparative Analysis of Two Approaches to Nonlocal Ductile Damage Modeling, Journal of Engineering Physics and Thermophysics 95 (2022) 1634–1646. https://doi.org/10.1007/S10891-022-02632-6/METRICS.

[123] R. Adams, Adhesive bonding: science, technology and applications, 2021. https://books.google.com/books?hl=en&lr=&id=-AQhEAAAQBAJ&oi=fnd&pg=PP1&ots=pVytf7zSeK&sig=YBAJ8_D4Mt07YJSxit9Rjm6hAr8 (accessed March 30, 2024).

[124] R.J.B. Rocha, R.D.S.G. Campilho, Evaluation of different modelling conditions in the cohesive zone analysis of single-lap bonded joints, J Adhes 94 (2018) 562–582. https://doi.org/10.1080/00218464.2017.1307107.

[125] D. Álvarez, B.R.K. Blackman, F.J. Guild, A.J. Kinloch, Mode I fracture in adhesively-bonded joints: A mesh-size independent modelling approach using cohesive elements, Eng Fract Mech 115 (2014) 73–95. https://doi.org/10.1016/J.ENGFRACMECH.2013.10.005.

[126] D.C. O'Mahoney, K.B. Katnam, N.P. O'Dowd, C.T. McCarthy, T.M. Young, Taguchi analysis of bonded composite single-lap joints using a combined interface–adhesive damage model, Int J Adhes Adhes 40 (2013) 168–178. https://doi.org/10.1016/J.IJADHADH.2012.06.001.

[127] S. Sugiman, A.D. Crocombe, I.A. Aschroft, Modelling the static response of unaged adhesively bonded structures, Eng Fract Mech 98 (2013) 296–314. https://doi.org/10.1016/J.ENGFRACMECH.2012.10.014.

[128] T.N. Geleta, K. Woo, D.S. Cairns, D. Samborsky, Failure behavior of inclined thick adhesive joints with manufacturing defect, Journal of Mechanical Science and Technology 32 (2018) 2173–2182. https://doi.org/10.1007/S12206-018-0426-Z/METRICS.

[129] R.D.S.G. Campilho, M.D. Banea, J.A.B.P. Neto, L.F.M. Da Silva, Modelling of Single-Lap Joints Using Cohesive Zone Models: Effect of the Cohesive Parameters on the Output of the Simulations, J Adhes 88 (2012) 513–533. https://doi.org/10.1080/00218464.2012.660834.

[130] L.F.M. da Silva, R.D.S.G. Campilho, Advances in Numerical Modelling of Adhesive Joints, SpringerBriefs in Applied Sciences and Technology (2012) 1–93. https://doi.org/10.1007/978-3-642-23608-2_1.

[131] R.L. Fernandes, R.D.S.G. Campilho, Testing different cohesive law shapes to predict damage growth in bonded joints loaded in pure tension, J Adhes 93 (2017) 57–76. https://doi.org/10.1080/00218464.2016.1169176.

[132] R.L. Fernandes, R.D.S.G. Campilho, Accuracy of cohesive laws with different shape for the shear behaviour prediction of bonded joints, J Adhes 95 (2019) 325–347. https://doi.org/10.1080/00218464.2018.1438895.

[133] R.D.S.G. Campilho, M.D. Banea, J.A.B.P. Neto, L.F.M. Da Silva, Modelling adhesive joints with cohesive zone models: effect of the cohesive law shape of the adhesive layer, Int J Adhes Adhes 44 (2013) 48–56. https://doi.org/10.1016/J.IJADHADH.2013.02.006.

[134] U.T.F. Carvalho, R.D.S.G. Campilho, Validation of pure tensile and shear cohesive laws obtained by the direct method with single-lap joints, Int J Adhes Adhes 77 (2017) 41–50. https://doi.org/10.1016/J.IJADHADH.2017.04.002.

[135] J.M.D. Teixeira, R.D.S.G. Campilho, F.J.G. da Silva, Numerical assessment of the Double-Cantilever Beam and Tapered Double-Cantilever Beam tests for the GIC determination of adhesive layers, J Adhes 94 (2018) 951–973. https://doi.org/10.1080/00218464.2017.1383905.

[136] J.C.S. Azevedo, R.D.S.G. Campilho, F.J.G. da Silva, T.M.S. Faneco, R.M. Lopes, Cohesive law estimation of adhesive joints in mode II condition, Theoretical and Applied Fracture Mechanics 80 (2015) 143–154. https://doi.org/10.1016/J.TAFMEC.2015.09.007.

[137] J.C.P. Figueiredo, R.D.S.G. Campilho, E.A.S. Marques, J.J.M. Machado, L.F.M. da Silva, Adhesive thickness influence on the shear fracture toughness measurements of adhesive joints, Int J Adhes Adhes 83 (2018) 15–23. https://doi.org/10.1016/J.IJADHADH.2018.02.015.

[138] M.F.S.F. De Moura, J.A.G. Chousal, Cohesive and continuum damage models applied to fracture characterization of bonded joints, Int J Mech Sci 48 (2006) 493–503. https://doi.org/10.1016/j.ijmecsci.2005.12.008.

[139] Y. Hua, A.D. Crocombe, M.A. Wahab, I.A. Ashcroft, Continuum damage modelling of environmental degradation in joints bonded with EA9321 epoxy adhesive, Int J Adhes Adhes 28 (2008) 302–313. https://doi.org/10.1016/J.IJADHADH.2007.08.005.

[140] J.A. García, A. Chiminelli, B. García, M. Lizaranzu, M.A. Jiménez, Characterization and material model definition of toughened adhesives for finite element analysis, Int J Adhes Adhes 31 (2011) 182–192. https://doi.org/10.1016/J.IJADHADH.2010.12.006.

[141] J.A.G. Chousal, M.F.S.F. De Moura, Mixed-mode I+II continuum damage model applied to fracture characterization of bonded joints, Int J Adhes Adhes 41 (2013) 92–97. https://doi.org/10.1016/J.IJADHADH.2012.10.014.

[142] S.E. Stapleton, E.J. Pineda, T. Gries, A.M. Waas, Adaptive shape functions and internal mesh adaptation for modeling progressive failure in adhesively bonded joints, Int J Solids Struct 51 (2014) 3252–3264. https://doi.org/10.1016/J.IJSOLSTR.2014.05.022.

[143] S.E. Stapleton, A.M. Waas, B.A. Bednarcyk, Modeling Progressive Failure of Bonded Joints Using a Single Joint Finite Element, Https://Doi.Org/10.2514/1.J050889 49 (2012) 1740–1749. https://doi.org/10.2514/1.J050889.

[144] S. Sugiman, H. Ahmad, Comparison of cohesive zone and continuum damage approach in predicting the static failure of adhesively bonded single lap joints, J Adhes Sci Technol 31 (2017) 552–570. https://doi.org/10.1080/01694243.2016.1222048.

[145] A. Riccio, R. Ricchiuto, F. Di Caprio, A. Sellitto, A. Raimondo, Numerical investigation of constitutive material models on bonded joints in scarf repaired composite laminates, Eng Fract Mech 173 (2017) 91–106. https://doi.org/10.1016/J.ENGFRACMECH.2017.01.003.

[146] Q. Zhang, X. Cheng, Y. Cheng, W. Li, R. Hu, Investigation of tensile behavior and influence factors of composite-to-metal 2D-scarf bonded joint, Eng Struct 180 (2019) 284–294. https://doi.org/10.1016/J.ENGSTRUCT.2018.11.036.

[147] M.H. Kim, H.S. Hong, An adaptation of mixed-mode I + II continuum damage model for prediction of fracture characteristics in adhesively bonded joint, Int J Adhes Adhes 80 (2018) 87–103. https://doi.org/10.1016/J.IJADHADH.2017.10.008.

[148] H. Özer, Ö.Ö.-M.P. in Engineering, undefined 2014, A comparative evaluation of numerical and analytical solutions to the biadhesive single-lap joint, Hindawi.ComH Özer, Ö ÖzMathematical Problems in Engineering, 2014•hindawi.Com (n.d.). https://www.hindawi.com/journals/mpe/2014/852872/abs/ (accessed April 12, 2024).

[149] Ö. Öz, H. Özer, On the von Mises elastic stress evaluations in the bi-adhesive single-lap joint: a numerical and analytical study, J Adhes Sci Technol 28 (2014) 2133–2153. https://doi.org/10.1080/01694243.2014.948110.

[150] P.J. C das Neves, L.F. M da Silva, R.D. Adams, Analysis of Mixed Adhesive Bonded Joints Part I: Theoretical Formulation, J Adhes Sci Technol 23 (2009) 1–34. https://doi.org/10.1163/156856108X336026.

[151] S. Semerdjiev, Metal to metal adhesive bonding, London, Business Books. (1970).

[152] G. Narayana Naik, Single and dual adhesive bond strength analysis of single lap joint between dissimilar adherends, (2019). https://doi.org/10.1016/j.ijadhadh.2019.04.016.

[153] I. Pires, L. Quintino, J.F. Durodola, A. Beevers, Performance of bi-adhesive bonded aluminium lap joints, Int J Adhes Adhes 23 (2003) 215–223. https://doi.org/10.1016/S0143-7496(03)00024-1.

[154] M. You, P. Wang, H.Z. Yu, M. Li, Y.L. Zhao, Numerical analysis of bi-adhesive boded single lap composite joint with mechanics analysis, Adv Mat Res 644 (2013) 189–192. https://doi.org/10.4028/www.scientific.net/AMR.644.189.

[155] J. P-H Belnoue, S.R. Hallett, Cohesive/adhesive failure interaction in ductile adhesive joints Part I: A smeared-crack model for cohesive failure, (2016). https://doi.org/10.1016/j.ijadhadh.2016.03.009.

[156] P.P. Camanho, M.A. Bessa, G. Catalanotti, M. Vogler, R. Rolfes, Modeling the inelastic deformation and fracture of polymer composites-Part II: Smeared crack model, (n.d.). https://doi.org/10.1016/j.mechmat.2012.12.001.

[157] T. Pardoen, T. Ferracin, C.M. Landis, F. Delannay, Constraint effects in adhesive joint fracture, J Mech Phys Solids 53 (2005) 1951–1983. https://doi.org/10.1016/j.jmps.2005.04.009.

[158] N. Arnaud, R. Créac, J.Y. Cognard, A tension/compression-torsion test suited to analyze the mechanical behaviour of adhesives under non-proportional loadings, (2014). https://doi.org/10.1016/j.ijadhadh.2014.01.013.

[159] J.Y. Cognard, R. Créac'Hcadec, J. Maurice, P. Davies, M. Peleau, L.F.M. Da Silva, Analysis of the influence of hydrostatic stress on the behaviour of an adhesive in a bonded assembly, J Adhes Sci Technol 24 (2010) 1977–1994. https://doi.org/10.1163/016942410X507696.

[160] T. Belytschko, D. Organ, C. Gerlach, Element-free galerkin methods for dynamic fracture in concrete, Comput Methods Appl Mech Eng 187 (2000) 385–399. https://doi.org/10.1016/S0045-7825(00)80002-X.

[161] T. Rabczuk, T. Belytschko, Cracking particles: a simplified meshfree method for arbitrary evolving cracks, Int J Numer Methods Eng 61 (2004) 2316–2343. https://doi.org/10.1002/NME.1151.

[162] G. Ventura, J.X. Xu, T. Belytschko, A vector level set method and new discontinuity approximations for crack growth by EFG, Int J Numer Methods Eng 54 (2002) 923–944. https://doi.org/10.1002/NME.471.

[163] T. Rabczuk, G. Zi, S. Bordas, H. Nguyen-Xuan, A geometrically non-linear three-dimensional cohesive crack method for reinforced concrete structures, Eng Fract Mech 75 (2008) 4740–4758. https://doi.org/10.1016/J.ENGFRACMECH.2008.06.019.

[164] B. Chong, Simulation of Crack Growth Using Cohesive Crack Method, KSCE Journal of Civil Engineering 14 (2010) 765–772. https://doi.org/10.1007/S12205-010-1050-3/METRICS.

[165] A. Ghosh, P. Chaudhuri, Computational modeling of fracture in concrete using a meshfree meso-macro-multiscale method, Comput Mater Sci 69 (2013) 204–215. https://doi.org/10.1016/J.COMMATSCI.2012.11.025.

[166] M. Goudarzi, S. Mohammadi, Analysis of cohesive cracking in saturated porous media using an extrinsically enriched EFG method, Comput Geotech 63 (2015) 183–198. https://doi.org/10.1016/J.COMPGEO.2014.09.007.

[167] Y. Dong, S. Wu, S.S. Xu, Y. Zhang, S. Fang, Analysis of concrete fracture using a novel cohesive crack method, Appl Math Model 34 (2010) 4219–4231. https://doi.org/10.1016/J.APM.2010.04.019.

[168] S. Wang, Meshfree cohesive cracking method for dynamic material failure, International Journal of Mechanics and Materials in Design 6 (2010) 103–111. https://doi.org/10.1007/S10999-010-9109-3/FIGURES/11.

[169] V. Kumar, A. Ghosh, Non-linear dynamic fragmentation using Cracking Particles Method, Comput Mater Sci 98 (2015) 117–122. https://doi.org/10.1016/J.COMMATSCI.2014.10.004.

[170] M.A. Iranmanesh, A. Pak, Three-dimensional numerical simulation of hydraulically driven cohesive fracture propagation in deformable reservoir rock using enriched EFG method, Comput Geosci 27 (2023) 317–335. https://doi.org/10.1007/S10596-023-10198-2/METRICS.

[171] Milan Jirásek, Element-free Galerkin method applied to strain-softening materials, in: R. de Borst (Ed.), Proc. Computational Modelling of Concrete Structures (EURO-C), Austria, 1998.

[172] C. Comi, L. Driemeier, On gradient regularization for numerical analyses in the presence of damage, in: Material Instabilities in Solids, Wiley, 1998: pp. 425–440.

[173] B. Antonio Huerta, A. Member, G. Pijaudier-Cabot, Discretization Influence on Regularization by Two Localization Limiters, J Eng Mech 120 (1994) 1198–1218. https://doi.org/10.1061/(ASCE)0733-9399(1994)120:6(1198).

[174] T. Rabczuk, J. Eibl, Numerical analysis of prestressed concrete beams using a coupled element free Galerkin/finite element approach, Int J Solids Struct 41 (2004) 1061–1080. https://doi.org/10.1016/J.IJSOLSTR.2003.09.040.

[175] Y. Yang, A. Misra, Higher-Order Stress-Strain Theory for Damage Modeling Implemented in an Element-free Galerkin Formulation, Computer Modeling in Engineering and Sciences 64 (2010) 1–36. https://hal.science/hal-00556175 (accessed April 11, 2024).

[176] Y. Yang, W.Y. Ching, A. Misra, Higher-Order Continuum Theory Applied to Fracture Simulation of Nanoscale Intergranular Glassy Film, J Nanomech Micromech 1 (2011) 60–71. https://doi.org/10.1061/(ASCE)NM.2153-5477.0000030/ASSET/33890387-7836-49C2-9DBD-97E60445892C/ASSETS/IMAGES/LARGE/9.JPG.

[177] X. Pan, H. Yuan, Applications of meshless methods for damage computations with finite strains, Model Simul Mat Sci Eng 17 (2009) 045005. https://doi.org/10.1088/0965-0393/17/4/045005.

[178] L. Placidi, A. Misra, E. Barchiesi, Two-dimensional strain gradient damage modeling: a variational approach, Zeitschrift Fur Angewandte Mathematik Und Physik 69 (2018) 1–19. https://doi.org/10.1007/S00033-018-0947-4/METRICS.

[179] K.B. Thakkar, P.C. Pandey, A High-order Isotropic Continuum Damage Evolution Model, International Journal of Damage Mechanics 16 (2007) 403–426. https://doi.org/10.1177/1056789506065897.

[180] J. Lemaitre, J.-L. Chaboche, Phenomenological approach of damage rupture, Journal de Mecanique Appliquee 2 (1978) 317–365.

[181] Sumio, Murakami, Continuum Damage Mechanics, 1984.

[182] L. Kachanov, Introduction to continuum damage mechanics, Springer Science & Business Media, 1986. https://books.google.com/books?hl=en&lr=&id=gXnKpaCcgawC&oi=fnd&pg=PP13&dq=Kachanov,+L.+M.,+Introduction+to+Continuum+Damage+Mechanics.+Martinus+Nijhoff,+Boston,+1986.&ots=tGO1lVWv15&sig=vP9tkpSZKEPAC_S-O4HYVmx-K1k (accessed June 22, 2021).

[183] J. Lemaitre, A Course on Damage Mechanics, Springer Berlin Heidelberg, 1996. https://doi.org/10.1007/978-3-642-18255-6.

[184] D. Krajcinovic, Damage mechanics, Elsevier, 1996.

[185] J. Lin, Y. Liu, T.A. Dean, A Review on Damage Mechanisms, Models and Calibration Methods under Various Deformation Conditions, International Journal of Damage Mechanics 14 (2005) 299–319. https://doi.org/10.1177/1056789505050357.

[186] P.J. Rabier, Some remarks on damage theory, Int J Eng Sci 27 (1989) 29–54. https://doi.org/10.1016/0020-7225(89)90166-3.

[187] J., Lemaitre, Evaluation of dissipation and damage in metals submitted to dynamic loading, Proceedings of International Conference of Mechanical Behavior of Materials (1971). https://doi.org/10.11540/BJSIAM.5.4_329.

[188] J.L. Chaboche, Lifetime Predictions and Cumulative Damage under High-Temperature Conditions, ASTM Special Technical Publication STP 770 (1982) 81–104. https://doi.org/10.1520/STP32424S.

[189] P. Germain, The Method of Virtual Power in Continuum Mechanics. Part 2: Microstructure, Https://Doi.Org/10.1137/0125053 25 (2006) 556–575. https://doi.org/10.1137/0125053.

[190] J. Kestin, J. Rice, A critical review of thermodynamics, Mono Book Corp., Baltimore, Ch. Paradoxes in the Application of Thermodynamics to Strained Solids (1970) 275–298.

[191] L.E. Malvern, Introduction to the mechanics of a continuous medium, (1969) 713.

[192] J.R. Rice, Inelastic constitutive relations for solids: An internal-variable theory and its application to metal plasticity, J Mech Phys Solids 19 (1971) 433–455. https://doi.org/10.1016/0022-5096(71)90010-X.

[193] D.S. Dugdale, Yielding of steel sheets containing slits, J Mech Phys Solids 8 (1960) 100–104. https://doi.org/10.1016/0022-5096(60)90013-2.

[194] G.I. Barenblatt, The mathematical theory of equilibrium cracks in brittle fracture, Advances in Applied Mechanics 7 (1962) 55–129. https://doi.org/10.1016/S0065-2156(08)70121-2.

[195] A. Hillerborg, M. Modéer, P.E. Petersson, Analysis of crack formation and crack growth in concrete by means of fracture mechanics and finite elements, Cem Concr Res 6 (1976) 773–781. https://doi.org/10.1016/0008-8846(76)90007-7.

[196] C. User, ABAQUS 6.14 Analysis User Guide, Dassault System (2014).

[197] Z.P. Bažant, G. Pijaudier-Cabot, Measurement of characteristic length of nonlocal continuum, J Eng Mech 115 (1989) 755–767. https://doi.org/10.1061/(ASCE)0733-9399(1989)115:4(755).

[198] P. Kotronis, S. Al Holo, P. Bésuelle, R. Chambon, Shear softening and localization: modelling the evolution of the width of the shear zone, Acta Geotech 3 (2008) 85–97. https://doi.org/10.1007/S11440-008-0061-4/FIGURES/19.

[199] N. Challamel, C. Lanos, C. Casandjian, On the propagation of localization in the plasticity collapse of hardening-softening beams, Int J Eng Sci 48 (2010) 487–506. https://doi.org/10.1016/j.ijengsci.2009.12.002.

[200] M. Jirásek, Non-local damage mechanics with application to concrete, Revue Française de Génie Civil 8 (2004) 683–707. https://doi.org/10.1080/12795119.2004.9692625.

[201] B.Z. P., J. Milan, Nonlocal Integral Formulations of Plasticity and Damage: Survey of Progress, J Eng Mech 128 (2002) 1119–1149. https://doi.org/10.1061/(ASCE)0733-9399(2002)128:11(1119).

[202] G. Pijaudier-Cabot, Z.P. Bažant, Nonlocal damage theory, J Eng Mech 113 (1987) 1512–1533. https://doi.org/10.1061/(ASCE)0733-9399(1987)113:10(1512).

[203] C. Polizzotto, Unified thermodynamic framework for nonlocal/gradient continuum theories, European Journal of Mechanics - A/Solids 22 (2003) 651–668. https://doi.org/10.1016/S0997-7538(03)00075-5.

[204] C. Polizzotto, G. Borino, P. Fuschi, A thermodynamically consistent formulation of nonlocal and gradient plasticity, Mech Res Commun 25 (1998) 75–82. https://doi.org/10.1016/S0093-6413(98)00009-3.

[205] D.G.B. Edelen, N. Laws, Thermodynamics with internal variables, J Chem Phys 47 (1971) 597–613.

[206] J. Lemaitre, Coupled elasto-plasticity and damage constitutive equations, Comput Methods Appl Mech Eng 51 (1985) 31–49. https://doi.org/10.1016/0045-7825(85)90026-X.

[207] T. Beda, Modeling hyperelastic behavior of rubber: A novel invariant-based and a review of constitutive models, J Polym Sci B Polym Phys 45 (2007) 1713–1732. https://doi.org/10.1002/POLB.20928.

[208] A.F. Bower, Applied mechanics of solids, Applied Mechanics of Solids (2009) 1–795. https://doi.org/10.1201/9781439802489/APPLIED-MECHANICS-SOLIDS-ALLAN-BOWER.

[209] M.A. Fleming, The element-free Galerkin method for fatigue and quasi-static fracture, Northwestern University, 1997.

[210] G.R. Liu, Meshfree methods: moving beyond the finite element method, second edition, CRC Press, 2009. https://doi.org/10.1201/9781420082104/MESHFREE-METHODS-LIU.

[211] X. Zhuang, C. Heaney, C. Augarde, On error control in the element-free Galerkin method, (2011). https://doi.org/10.1016/j.enganabound.2011.06.011.

[212] J. Dolbow, T. Belytschko, Numerical integration of the Galerkin weak form in meshfree methods, Comput Mech 23 (1999) 219–230. https://doi.org/10.1007/S004660050403/METRICS.

[213] P. Lancaster, K. Salkauskas, Surfaces generated by moving least squares methods, Math Comput 37 (1981) 141–158. https://doi.org/10.1090/S0025-5718-1981-0616367-1.

[214] E. Oñate, S. Idelsohn, O.C. Zienkiewicz, R.L. Taylor, C. Sacco, A stabilized finite point method for analysis of fluid mechanics problems, Comput Methods Appl Mech Eng 139 (1996) 315–346. https://doi.org/10.1016/S0045-7825(96)01088-2.

[215] I. Milne, R.O. Ritchie, B. Karihaloo, Comprehensive Structural Integrity: Numerical and Computational Methods, Elsevier Pergamon, 2003.

[216] D. Hegen, Element-free Galerkin methods in combination with finite element approaches, Comput Methods Appl Mech Eng 135 (1996) 143–166. https://doi.org/10.1016/0045-7825(96)00994-2.

[217] Y.X. Mukherjee, S. Mukherjee, On boundary conditions in the element-free Galerkin method, Comput Mech 19 (1997) 264–270. https://doi.org/10.1007/S004660050175/METRICS.

[218] S.N. Atluri, S. Shen, The Meshless Local Petrov-Galerkin (MLPG) Method: A Simple & Less-costly Alternative to the Finite Element and Boundary Element Methods, Computer Modeling in Engineering & Sciences 3 (2002) 11–51.

[219] T. Rabczuk, S.P. Xiao, M. Sauer, Coupling of mesh-free methods with finite elements: basic concepts and test results, Commun Numer Methods Eng 22 (2006) 1031–1065. https://doi.org/10.1002/CNM.871.

[220] G.R. Johnson, Linking of Lagrangian particle methods to standard finite element methods for high velocity impact computations, Nuclear Engineering and Design 150 (1994) 265–274. https://doi.org/10.1016/0029-5493(94)90143-0.

[221] T. Belytschko, D. Organ, Y. Krongauz, A coupled finite element-element-free Galerkin method, Comput Mech 17 (1995) 186–195. https://doi.org/10.1007/BF00364080/METRICS.

[222] S.P. Xiao, T. Belytschko, A bridging domain method for coupling continua with molecular dynamics, Comput Methods Appl Mech Eng 193 (2004) 1645–1669. https://doi.org/10.1016/J.CMA.2003.12.053.

[223] M. Sauer, Adaptive Coupling of the Mesh-Free SPH-Method with Finite Elements for the Calculation of Impact Events, Universitaet der Bundeswehr Muenchen, , 2000.

[224] J.S. Chen, H.P. Wang, New boundary condition treatments in meshfree computation of contact problems, Comput Methods Appl Mech Eng 187 (2000) 441–468. https://doi.org/10.1016/S0045-7825(00)80004-3.

[225] J.S. Chen, C. Pan, C.T. Wu, Large deformation analysis of rubber based on a reproducing kernel particle method, Comput Mech 19 (1997) 211–227. https://doi.org/10.1007/S004660050170/METRICS.

[226] I. Kaljevic, S. Saigal, An improved element free Galerkin formulation, Int J Numer Methods Eng 40 (1997) 2953–2974. https://doi.org/10.1002/(SICI)1097-0207(19970830)40:16.

[227] F.C. Günther, W.K. Liu, Implementation of boundary conditions for meshless methods, Comput Methods Appl Mech Eng 163 (1998) 205–230. https://doi.org/10.1016/S0045-7825(98)00014-0.

[228] G. Borino, B. Failla, F. Parrinello, A symmetric nonlocal damage theory, Int J Solids Struct 40 (2003) 3621–3645. https://doi.org/10.1016/S0020-7683(03)00144-6.

[229] W. He, Y.F. Wu, Y. Xu, T.T. Fu, A thermodynamically consistent nonlocal damage model for concrete materials with unilateral effects, Comput Methods Appl Mech Eng 297 (2015) 371–391. https://doi.org/10.1016/J.CMA.2015.09.010.

[230] C. Polizzotto, P. Fuschi, A.A. Pisano, A strain-difference-based nonlocal elasticity model, Int J Solids Struct 41 (2004) 2383–2401. https://doi.org/10.1016/j.ijsolstr.2003.12.013.

[231] J. Lemaitre, Coupled elasto-plasticity and damage constitutive equations, Comput Methods Appl Mech Eng 51 (1985) 31–49. https://doi.org/10.1016/0045-7825(85)90026-X.

[232] T. Park, B. Ahmed, G.Z. Voyiadjis, A review of continuum damage and plasticity in concrete: Part I – Theoretical framework, International Journal of Damage Mechanics 31 (2022) 901–954. https://doi.org/10.1177/10567895211068174/ASSET/IMAGES/LARGE/10.1177_10567895211068174-FIG16.JPEG.

[233] P. Petersson, Crack growth and development of fracture zones in plain concrete and similar materials, Division of Building Materials, Lund Institute of Technology, 1981. https://inis.iaea.org/Search/search.aspx?orig_q=RN:13668228 (accessed November 4, 2023).

[234] M. Jirásek, Nonlocal models for damage and fracture: comparison of approaches, Int J Solids Struct 35 (1998) 4133–4145. https://doi.org/10.1016/S0020-7683(97)00306-5.

[235] X. Li, W. Gao, W. Liu, A mesh objective continuum damage model for quasi-brittle crack modelling and finite element implementation, International Journal of Damage Mechanics 28 (2019) 1299–1322. https://doi.org/10.1177/1056789518823876/ASSET/IMAGES/LARGE/10.1177_1056789518823876-FIG20.JPEG.

[236] M. Hassanzadeh, Behaviour of fracture process zones in concrete influenced by simultaneously applied normal and shear displacements, Division of Building Materials, Lund Institute of Technology, 1992.

[237] C. Comi, U. Perego, Criteria for mesh refinement in nonlocal damage finite element analyses, European Journal of Mechanics - A/Solids 23 (2004) 615–632. https://doi.org/10.1016/J.EUROMECHSOL.2004.03.006.

[238] N. Bonora, D. Gentile, A. Pirondi, G. Newaz, Ductile damage evolution under triaxial state of stress: theory and experiments, Int J Plast 21 (2005) 981–1007. https://doi.org/10.1016/J.IJPLAS.2004.06.003.

[239] N. Bonora, G. Testa, Plasticity damage self-consistent model incorporating stress triaxiality and shear controlled fracture mechanisms – Model formulation, Eng Fract Mech 271 (2022) 108634. https://doi.org/10.1016/J.ENGFRACMECH.2022.108634.

[240] F. Andrade, J.C. De Sá, F.A. Pires, Assessment and comparison of non-local integral models for ductile damage, Http://Dx.Doi.Org/10.1177/1056789513493103 23 (2013) 261–296. https://doi.org/10.1177/1056789513493103.

[241] N. Bonora, D. Gentile, A. Pirondi, Identification of the parameters of a non-linear continuum damage mechanics model for ductile failure in metals, Journal of Strain Analysis for Engineering Design 39 (2004) 639–651. https://doi.org/10.1243/0309324042379356.

[242] M. Alves, J. Yu, N. Jones, On the elastic modulus degradation in continuum damage mechanics, Comput Struct 76 (2000) 703–712. https://doi.org/10.1016/S0045-7949(99)00187-X.

[243] D. Gerbig, A. Bower, V. Savic, L.G. Hector, Coupling digital image correlation and finite element analysis to determine constitutive parameters in necking tensile specimens, Int J Solids Struct 97_98 (2016) 496–509. https://doi.org/10.1016/j.ijsolstr.2016.06.038.

[244] A. Sancho, M.J. Cox, T. Cartwright, C.M. Davies, P.A. Hooper, J.P. Dear, An experimental methodology to characterise post-necking behaviour and quantify ductile damage accumulation in isotropic materials, Int J Solids Struct 176–177 (2019) 191–206. https://doi.org/10.1016/j.ijsolstr.2019.06.010.

[245] J.C. Lagarias, J.A. Reeds, M.H. Wright, P.E. Wright, Convergence properties of the Nelder-Mead simplex method in low dimensions, SIAM Journal on Optimization 9 (1998) 112–147. https://doi.org/10.1137/S1052623496303470.

[246] K. Ravi-Chandar, Dynamic Fracture of Nominally Brittle Materials, Int J Fract 90 (1998) 83–102. https://doi.org/10.1023/A:1007432017290.

[247] K. Ravi-Chandar, W.G. Knauss, An experimental investigation into dynamic fracture: III. On steady-state crack propagation and crack branching, Int J Fract 26 (1984) 141–154.

[248] R. de Borst, Numerical aspects of cohesive-zone models, Eng Fract Mech 70 (2003) 1743–1757. https://doi.org/10.1016/S0013-7944(03)00122-X.

[249] M.A.M. Torkamani, M. Sonmez, Solution techniques for nonlinear equilibrium equations, in: Proceedings of 18th Analysis and Computation Speciality Conference - Structures Congress 2008: Crossing the Borders, American Society of Civil Engineers, 2008: pp. 1–17. https://doi.org/10.1061/41000(315)35.

[250] R. de Borst, Computation of post-bifurcation and post-failure behavior of strain-softening solids, Comput Struct 25 (1987) 211–224. https://doi.org/10.1016/0045-7949(87)90144-1.

[251] G. Alfano, M.A. Crisfield, Finite element interface models for the delamination analysis of laminated composites: mechanical and computational issues, Int J Numer Methods Eng 50 (2001) 1701–1736. https://doi.org/10.1002/NME.93.

[252] Z. Yang, J. Chen, Fully automatic modelling of cohesive discrete crack propagation in concrete beams using local arc-length methods, Int J Solids Struct 41 (2004) 801–826. https://doi.org/10.1016/J.IJSOLSTR.2003.09.033.

[253] Z.J. Yang, A.J. Deeks, Fully-automatic modelling of cohesive crack growth using a finite element–scaled boundary finite element coupled method, Eng Fract Mech 74 (2007) 2547–2573. https://doi.org/10.1016/J.ENGFRACMECH.2006.12.001.

[254] Y. Zhang, J. Huang, Y. Yuan, H.A. Mang, Cracking elements method with a dissipation-based arc-length approach, Finite Elements in Analysis and Design 195 (2021) 103573. https://doi.org/10.1016/J.FINEL.2021.103573.

[255] G.M. Chen, J.G. Teng, J.F. Chen, Q.G. Xiao, Finite element modeling of debonding failures in FRP-strengthened RC beams: A dynamic approach, Comput Struct 158 (2015) 167–183. https://doi.org/10.1016/J.COMPSTRUC.2015.05.023.

[256] L. Távara, V. Mantič, A. Salvadori, · Leonard, J. Gray, F. París, L. Távara, V. Mantič, · F París, F. París, A. Salvadori, L.J. Gray, Cohesive-zone-model formulation and implementation using the symmetric Galerkin boundary element method for homogeneous solids, Computational Mechanics 2012 51:4 51 (2012) 535–551. https://doi.org/10.1007/S00466-012-0808-5.

[257] S.E. Leon, G.H. Paulino, A. Pereira, I.F.M. Menezes, E.N. Lages, A unified library of nonlinear solution schemes, Appl Mech Rev 64 (2011) 040803. https://doi.org/10.1115/1.4006992/463373.

[258] Y. Bin Yang, M.S. Shieh, Solution method for nonlinear problems with multiple critical points, AIAA Journal 28 (1990) 2110–2116. https://doi.org/10.2514/3.10529.

[259] N. Muthu, S.K. Maiti, B.G. Falzon, W. Yan, Crack propagation in non-homogenous materials: Evaluation of mixed-mode SIFs, T-stress and kinking angle using a variant of EFG Method, Eng Anal Bound Elem 72 (2016) 11–26. https://doi.org/10.1016/J.ENGANABOUND.2016.07.017.

[260] N. Moës, M. Cloirec, P. Cartraud, J.F. Remacle, A computational approach to handle complex microstructure geometries, Comput Methods Appl Mech Eng 192 (2003) 3163–3177. https://doi.org/10.1016/S0045-7825(03)00346-3.

[261] J. Bonet, A.J. Gil, R.D. Wood, Nonlinear solid mechanics for finite element analysis: Statics, Cambridge University Press, 2016. https://doi.org/10.1017/9781316336144.

[262] J. -L Batoz, G. Dhatt, Incremental displacement algorithms for nonlinear problems, Int J Numer Methods Eng 14 (1979) 1262–1267. https://doi.org/10.1002/nme.1620140811.

[263] A. Dorbane, B. Mansoor, G. Ayoub, V.C. Shunmugasamy, A. Imad, Mechanical, microstructural and fracture properties of dissimilar welds produced by friction stir welding of AZ31B and Al6061, Materials Science and Engineering: A 651 (2016) 720–733. https://doi.org/10.1016/j.msea.2015.11.019.

[264] N. Muthu, B.G. Falzon, S.K. Maiti, S. Khoddam, Modified crack closure integral technique for extraction of SIFs in meshfree methods, Finite Elements in Analysis and Design 78 (2014) 25–39. https://doi.org/10.1016/j.finel.2013.09.005.

[265] Y. Cao, J.-L. Dong, L.-Q. Yao, A modification of the moving least-squares approximation in the element-free Galerkin method, J Appl Math 2014 (2014) 528082. https://doi.org/10.1155/2014/528082.

[266] N. Moës, T. Belytschko, Extended finite element method for cohesive crack growth, Eng Fract Mech 69 (2002) 813–833. https://doi.org/10.1016/S0013-7944(01)00128-X.

[267] M.R. Gheibi, M.H. Shojaeefard, H. Saeidi Googarchin, Direct determination of a new mode-dependent cohesive zone model to simulate metal-to-metal adhesive joints, Journal of Adhesion 95 (2019) 943–970. https://doi.org/10.1080/00218464.2018.1455145.

[268] F.P. van der Meer, L.J. Sluys, A phantom node formulation with mixed mode cohesive law for splitting in laminates, Int J Fract 158 (2009) 107–124. https://doi.org/10.1007/S10704-009-9344-5/METRICS.

[269] V.P. Nguyen, H. Nguyen-Xuan, High-order B-splines based finite elements for delamination analysis of laminated composites, Compos Struct 102 (2013) 261–275. https://doi.org/10.1016/J.COMPSTRUCT.2013.02.029.

[270] H. Askes, T. Bennett, S. Kulasegaram, Meshless discretisation of nonlocal damage theories, Solid Mechanics and Its Applications 5 (2007) 3–20. https://doi.org/10.1007/978-1-4020-6530-9_1.

[271] A. Ortiz, M.A. Puso, N. Sukumar, Maximum-entropy meshfree method for compressible and near-incompressible elasticity, Comput Methods Appl Mech Eng 199 (2010) 1859–1871. https://doi.org/10.1016/J.CMA.2010.02.013.

[272] T.J. Hughes, The finite element method: linear static and dynamic finite element analysis, Courier Corporation, 2012.

[273] G. Zhang, R. Alberdi, K. Khandelwal, On the locking free isogeometric formulations for 3-D curved Timoshenko beams, Finite Elements in Analysis and Design 143 (2018) 46–65. https://doi.org/10.1016/J.FINEL.2018.01.007.

[274] T.J.R. Hughes, Generalization of selective integration procedures to anisotropic and nonlinear media, Int J Numer Methods Eng 15 (1980) 1413–1418. https://doi.org/10.1002/nme.1620150914.

[275] F. Tian, J. Zeng, M. Zhang, L. Li, Mixed displacement–pressure-phase field framework for finite strain fracture of nearly incompressible hyperelastic materials, Comput Methods Appl Mech Eng 394 (2022) 114933. https://doi.org/10.1016/J.CMA.2022.114933.

[276] D.S. Malkus, T.J.R. Hughes, Mixed finite element methods — Reduced and selective integration techniques: A unification of concepts, Comput Methods Appl Mech Eng 15 (1978) 63–81. https://doi.org/10.1016/0045-7825(78)90005-1.

[277] J.F. Caseiro, R.J. Alves De Sousa, R.A.F. Valente, A systematic development of EAS three-dimensional finite elements for the alleviation of locking phenomena, Finite Elements in Analysis and Design 73 (2013) 30–41. https://doi.org/10.1016/J.FINEL.2013.05.006.

[278] J.C. Simo, M.S. Rifai, A class of mixed assumed strain methods and the method of incompatible modes, Int J Numer Methods Eng 29 (1990) 1595–1638. https://doi.org/10.1002/NME.1620290802.

[279] D.S. Bombarde, M. Agrawal, S.S. Gautam, A. Nandy, Development of quadratic enhanced assumed strain elements for three-dimensional linear elasticity, Comput Struct 291 (2024) 107217. https://doi.org/10.1016/J.COMPSTRUC.2023.107217.

[280] J. Wang, J. Chen, M. Li, URI 4-node quadrilateral element by assumed strain method for nonlinear problems, Acta Mechanica Sinica 20 (2004) 632–641. https://doi.org/10.1007/BF02485867/METRICS.

[281] Q. Xu, J. Liu, An improved dynamic model for a silicone material beam with large deformation, Acta Mechanica Sinica 34 (2018) 744–753. https://doi.org/10.1007/S10409-018-0759-Y/FIGURES/11.

[282] U. Heisserer, S. Hartmann, A. Düster, Z. Yosibash, On volumetric locking-free behaviour of p-version finite elements under finite deformations, Commun Numer Methods Eng 24 (2008) 1019–1032. https://doi.org/10.1002/CNM.1008.

[283] A. Bijalwan, B.P. Patel, M. Marieswaran, D. Kalyanasundaram, Volumetric locking free 3D finite element for modelling of anisotropic visco-hyperelastic behaviour of anterior cruciate ligament, J Biomech 73 (2018) 1–8. https://doi.org/10.1016/J.JBIOMECH.2018.03.016.

[284] O.C. Zienkiewicz, R.L. Taylor, The finite element method for solid and structural mechanics, Elsevier, 2005.

[285] C. Kadapa, M. Hossain, A linearized consistent mixed displacement-pressure formulation for hyperelasticity, Mechanics of Advanced Materials and Structures 29 (2022) 267–284. https://doi.org/10.1080/15376494.2020.1762952.

[286] M. Bercovier, Perturbation of mixed variational problems. Application to mixed finite element methods, RAIRO. Analyse Numérique 12 (1978) 211–236.

[287] C. Kadapa, Mixed Galerkin and least-squares formulations for isogeometric analysis, Swansea University, 2014.

[288] U. Brink, E. Stein, On some mixed finite element methods for incompressible and nearly incompressible finite elasticity, Comput Mech 19 (1996) 105–119. https://doi.org/10.1007/BF02824849.

[289] S. Cai, D.M. Li, J. xuan Xie, A complex variable EFG method for hyperelastic large deformation analysis under non-conservative loads, Appl Math Model 113 (2023) 596–612. https://doi.org/10.1016/J.APM.2022.09.024.

[290] A. Huerta, S. Fernndez-Mndez, Locking in the incompressible limit for the element-free Galerkin method, Int J Numer Methods Eng 51 (2001) 1361–1383. https://doi.org/10.1002/NME.213.

[291] J.S. Chen, S. Yoon, H.P. Wang, W.K. Liu, An improved reproducing kernel particle method for nearly incompressible finite elasticity, Comput Methods Appl Mech Eng 181 (2000) 117–145. https://doi.org/10.1016/S0045-7825(99)00067-5.

[292] J. Dolbow, T. Belytschko, Volumetric locking in the element free Galerkin method, Int J Numer Methods Eng 46 (1999) 925–942. https://doi.org/10.1002/(SICI)1097-0207(19991030)46:6.

[293] D.P. Recio, R.M. Natal Jorge, L.M.S. Dinis, Locking and hourglass phenomena in an element-free Galerkin context: the B-bar method with stabilization and an enhanced strain method, Int J Numer Methods Eng 68 (2006) 1329–1357. https://doi.org/10.1002/NME.1741.

[294] A. Graça, R.P.R. Cardoso, J.W. Yoon, Subspace analysis to alleviate the volumetric locking in the 3D solid-shell EFG method, J Comput Appl Math 246 (2013) 185–194. https://doi.org/10.1016/J.CAM.2012.09.013.

[295] E.A. De Souza Neto, D. Perić, M. Dutko, D.R.J. Owen, Design of simple low order finite elements for large strain analysis of nearly incompressible solids, Int J Solids Struct 33 (1996) 3277–3296. https://doi.org/10.1016/0020-7683(95)00259-6.

[296] S. Reese, M.K. Ussner, B.D. Reddy, A new stabilization technique for finite elements in non-linear elasticity, Int J Numer Methods Eng 44 (1999) 1617–1652. https://doi.org/10.1002/(SICI)1097-0207(19990420)44:11.

[297] C. Kadapa, W.G. Dettmer, D. Perić, Subdivision based mixed methods for isogeometric analysis of linear and nonlinear nearly incompressible materials, Comput Methods Appl Mech Eng 305 (2016) 241–270. https://doi.org/10.1016/J.CMA.2016.03.013.